



Universitat Autònoma de Barcelona

**ADVERTIMENT.** L'accés als continguts d'aquesta tesi queda condicionat a l'acceptació de les condicions d'ús establertes per la següent llicència Creative Commons:  [http://cat.creativecommons.org/?page\\_id=184](http://cat.creativecommons.org/?page_id=184)

**ADVERTENCIA.** El acceso a los contenidos de esta tesis queda condicionado a la aceptación de las condiciones de uso establecidas por la siguiente licencia Creative Commons:  <http://es.creativecommons.org/blog/licencias/>

**WARNING.** The access to the contents of this doctoral thesis it is limited to the acceptance of the use conditions set by the following Creative Commons license:  <https://creativecommons.org/licenses/?lang=en>

LAURA LÓPEZ MIR

TRANSPORT PHENOMENA AND MAGNETISM IN  
NANOSTRUCTURES OF LANTHANUM MANGANITE-BASED  
OXIDE THIN FILMS



TRANSPORT PHENOMENA AND MAGNETISM IN  
NANOSTRUCTURES OF LANTHANUM MANGANITE-BASED  
OXIDE THIN FILMS



LAURA LÓPEZ MIR  
Institut de Ciències de Materials de Barcelona (ICMAB-CSIC)

SUPERVISORS:  
Dr. Lluís Balcells  
Prof. Carmen Ocal  
Dr. Carlos Frontera

TUTOR:  
Prof. Jordi Sort

Universitat Autònoma de Barcelona  
Departament de Física



A thesis submitted for the degree of  
*Doctor of Philosophy in Physics*

Bellaterra, February 2018

Laura López Mir

*Transport Phenomena and Magnetism in Nanostructures of Lanthanum Manganite-based Oxide Thin Films*, February 2018

# ABSTRACT

---

Lanthanum manganite-based oxides conform an extensive family of compounds deriving from  $\text{LaMnO}_3$ : a perovskite with general formula  $\text{ABO}_3$ . Its physical properties can be drastically modified by cation substitution. In this thesis we explore two compounds obtained by A-site and B-site substitutions. On the one hand,  $\text{La}_2\text{Co}_{0.8}\text{Mn}_{1.2}\text{O}_6$  (LCMO), obtained by substitution of Mn by Co (B-site substitution), leads to a double perovskite structure with ferromagnetic insulating properties. On the other side, the  $\text{La}_{0.7}\text{Sr}_{0.3}\text{MnO}_3$  (LSMO) compound resulting from the partial substitution of La by Sr (A-site substitution) turns the material into a ferromagnetic half-metal.

The development of techniques for the growth of oxide materials in the form of thin films ease their integration in semiconductors technology and enable the design of micro and nanoscale devices with potential in spintronics and non-volatile memory applications. Nowadays, there is an increasing interest in the study of double perovskite thin films combining ferromagnetic and insulating properties due to their relatively high transition temperature and their integration on top of other perovskite oxides. The implementation of ferromagnetic insulators (FM-I) as substitutes of ferromagnetic metal-based devices can lead to much higher switching efficiency and less dissipative current transport. For instance, ultrathin films of (FM-I) might be used as spin-selective active tunneling barriers acting as spin-filters. Therefore, the main objective of the first part of this thesis has been to give a comprehensive understanding of LCMO physical properties and propose a guide to potential applications.

Firstly, we present a detailed study of the growth of the LCMO films as well as their structural and magnetic characterization. We demonstrate that we can obtain high quality thin films, with transition temperatures up to 230 K and with good cationic order despite a certain degree of off-stoichiometry. Then, we analyze magnetic anisotropy effects, focusing on the following aspects: i) the study of the appearance of strong perpendicular magnetic anisotropy (PMA) with large coercive and anisotropy fields, and ii) the relation of magnetic anisotropy strength and sign with lattice mismatches. In particular, we show that PMA appears for the tensile strain case while compressive strain produces in-plane easy axis. We also give a more detailed understanding of the origin of magnetic anisotropy using a simple atomistic model based on first-order perturbation theory calculations. We relate our predictions with X-ray magnetic circular dichroism (XMCD) experiments and evi-

dence that magnetic anisotropy in LCMO has a magnetocrystalline origin due to the strong spin-orbit coupling of  $\text{Co}^{2+}$  ions.

With the aim of integrating ferromagnetic insulating properties and PMA in a device, we have fabricated tunnel junctions using LCMO as a magnetically active barrier and have explored its spin-derived functionalities. We have found that the device provides high spin-filtering efficiency (of almost 100% of spin-polarization) as well as anisotropic sensing and memory functionalities. This is, the strong strain-induced PMA provokes a large difference between magnetoresistance curves measured with the magnetic field applied in the perpendicular or parallel directions, this phenomenon is the so called tunneling anisotropic magnetoresistance (TAMR). TAMR values as high as 20-30% have been found. Finally, we have proven that the device can be used as a magnetic memory as we can detect the existence of two non-volatile resistive state that switches depending on the direction of the magnetic field used to write it.

The last part of thesis presents results focused on the A-substituted manganite, LSMO, thin films. We show that growth instabilities can lead to the formation of double-terminated surfaces. Indeed, deviations from the ideal growth behaviour constitute a way to obtain spontaneously formed nanostructures with modulated local functional properties at the surface. The transport properties and the composition of these films have been analyzed by making use of scanning probe techniques and space-resolved photoemission electron microscopy, which are surface-sensitive techniques suitable to characterize properties at the nanoscale of this type of systems.

# RESUM

---

Els òxids basats en manganites de lantà formen una extensa família de compostos derivats del  $\text{LaMnO}_3$ : una perovskita de la forma general  $\text{ABO}_3$ . Les propietats físiques d'aquesta es poden modificar substancialment per substitució catiònica. En aquesta tesi estudiem dos compostos obtinguts per substitució dels cations A i B. D'una banda, el  $\text{La}_2\text{Co}_{0.8}\text{Mn}_{1.2}\text{O}_6$  (LCMO), obtingut per substitució del Mn per Co (catió B), que conforma una estructura doble perovskita amb propietats aïllants i ferromagnètiques. D'altra banda, el  $\text{La}_{0.7}\text{Sr}_{0.3}\text{MnO}_3$  (LSMO) format per substitució parcial de La per Sr (catió A) i que resulta en un material metàl·lic i ferromagnètic.

El desenvolupament de tècniques de creixement de materials òxids en forma de capes primes els dona un gran potencial per ser integrats en la tecnologia de semiconductors i per dissenyar dispositius micro i nanomètrics per a aplicacions en spintrònica i memòries no-volàtils. Actualment hi ha gran interès en l'estudi de capes primes de perovskites dobles amb propietats ferromagnètiques i aïllants, ja que tenen una temperatura de transició relativament alta i són fàcils d'integrar sobre altres òxids. La implementació d'aïllants ferromagnètics com a substituïts dels dispositius ferromagnètics basats en metalls pot conduir a una eficiència de commutació molt més gran i un transport de corrent menys dissipatiu. Assolir capes ultra primes d'aquests materials permetria obtenir una barrera túnel activa que selecciona l'espín, per tant actua com a filtre d'aquest. Així, l'objectiu principal de la primera part d'aquesta tesi és comprendre les propietats físiques del LCMO i obrir una via per futures aplicacions potencials.

En primer lloc, es presenta un estudi detallat del creixement i la caracterització estructural i magnètica de capes primes de LCMO. Demostrem que podem obtenir capes d'alta qualitat, amb temperatures de transició de fins a 230 K i amb un bon ordre catiònic tot i petites desviacions de l'estequiometria. A continuació, analitzem els efectes d'anisotropia magnètica centrats en els aspectes següents: 1) l'estudi de l'aparició d'una forta anisotropia magnètica perpendicular (PMA) amb un alt camp coercitiu i d'anisotropia, i 2) la relació del signe i la força de l'anisotropia magnètica amb els desajustos estructurals amb el substrat. En particular, la PMA apareix en el cas que la tensió sigui expansiva mentre que la tensió compressiva produeix un eix fàcil d'imantació dins el pla.

Per trobar una explicació a l'origen de l'anisotropia magnètica desenvolupem un model atòmic simple basat en càlculs de primer ordre de teoria de perturbacions. A més, relacionem les prediccions extreïdes amb experiments de dicroïsm magnètic



circular de raigs X (XMCD tot demostrant que l'anisotropia magnètica en l'LCMO té un origen magnetocristal·lí a causa del fort acoblament d'espín-òrbita del  $\text{Co}^{2+}$ .

Amb l'objectiu d'integrar les propietats aïllants ferromagnètiques i la PMA en un dispositiu, hem fabricat unions túnel utilitzant el LCMO com a barrera magnèticament activa i hem explorat les seves funcionalitats d'espín. Hem trobat que el dispositiu proporciona una alta eficiència de filtratge d'espín (gairebé el 100% de polarització) i funcionalitats de sensor i memòria anisotròpica. És a dir, que la forta PMA induïa per la tensió epitaxial provoca una gran diferència entre les corbes de magnetoresistència mesurades amb el camp magnètic aplicat perpendicular o paral·lelament; aquesta és l'anomenada magnetoresistència túnel anisotròpica (TAMR). S'han trobat valors de TAMR de 20-30%. Finalment, s'ha provat que el dispositiu pot funcionar com una memòria magnètica ja que podem detectar dos estat no volàtils de resistència ben diferenciats que s'*escriuen* canviant la direcció del camp magnètic aplicat.

En la darrera part de la tesi, s'han presentat resultats basats en l'altre sistema de manganita, el LSMO. Mostrem que les inestabilitats del creixement poden conduir a la formació de superfícies de doble terminació. Allunyar-se del comportament ideal de creixement constitueix una forma d'obtenir nanoestructures formades espontàniament amb propietats funcionals locals en superfícies. Les propietats de transport i la composició d'aquestes superfícies s'analitzen utilitzant tècniques de sonda d'escaneig i microscopia electrònica de fotoemissió amb resolució lateral. Aquestes tècniques sensibles a la superfície són adequades per caracteritzar les propietats a la nanoescala d'aquest tipus de sistemes.

# ACKNOWLEDGMENTS

---

En primer lloc vull agrair al Jacobo Santamaría, a la Neus Domingo i al Xavi Martí haver acceptat formar part del tribunal que valorarà aquesta tesi. En segon lloc, als meus directors en Lluís Balcells, la Carmen Ocal i en Carlos, per la dedicació i per la seva disponibilitat permanent. Per l'excellent tracte personal, per haver-me donat una formació molt àmplia i la possibilitat de fer estades a l'estranger i anar totes les conferències possibles. També, per l'esforç i les hores dedicades en la recta final, que ha permès acabar aquesta tesi i arribar en aquest punt on toca repassar a tothom que hi ha contribuït.

En particular, a en Lluís, per fer-me costat en tot moment, per ensenyar-me de tantes tècniques experimentals i a ser resolutive. Per baixar al laboratori al primer toc de telèfon i encarregar-se de fer reviure l'sputtering en totes les seves crisis.

A Carmen, le agradezco el apoyo, la positividad y sus consejos en momentos de desorientación, aunque mi tesis tomara caminos hacia tierras criogénicas, agradezco que haya seguido aportando ideas en todos los temas que he acabado estudiando.

A en Carlos, que em va liar a estudiar el lantà cobalt i va acabar essent un pilar fonamental de la meva tesi, i ell el meu tercer director. Moltes gràcies pel temps dedicat i pels coneixements transmesos, sempre generant claror enmig del caos. Espero que se'm quedi alguna cosa, sobretot de la seva rigurositat i perseverància. També li agraeixo que hagi supervisat el meu estat d'ànim i la meva dieta amb flux constant de xocolata i sobrassada.

Els agraïments també els vull estendre als col·laboradors que han contribuït en la realització dels experiments que formen part d'aquesta tesi:

Jose Santiso i Pablo García, de ICN2 per les mesures de XRR; Bernat Bozzo de l'ICMAB per les mesures d'SQUID i l'ajut amb el PPMS; Javier Herrero de l'ALBA pels experiments de XAS i XMCD; Sergio Valencia de BESSY II pels experiments X-PEEM i Xavier Llovet, dels Serveis Científico-tècnics de la UB per les mesures d'EPMA.

Del grup de magnètics, agraeixo al Benjamín Martínez haver-me donat la oportunitat de realitzar una tesi becada i haver confiat en mi al deixar-me en mans del nou AFM. A la resta de membres del grup que m'han ajudat d'una manera o altra: Alberto, Zorica, Elisa, Victor, Sergi,... Nogensmenys als primers companys de doctorat, quan el grup es disputava entre dofins i canams: Regina, Jose i Núria. A la Regina,

per resoldre tots els meus dubtes, pels beamtimes i congressos compartits i les dosis de positivisme. Al Jose per ser el meu mestre de l'sputtering, de les tècniques de litografia i moltes altres i per solucionar-nos tants problemes tècnics (beneïts siguin els enginyers electrònics!). I a la Núria pels cafés entre visites a l'ICN i a l'ICMAB.

Del grupo de AFM, gracias a Esther, Ana, Sonia, Rogger, Marcos, Adara y Francesco por escuchar mis charlas de óxidos de vez en cuando y enseñarme vosotros sobre celdas solares, moléculas y non-contact. También gracias por los buenos ratos, las cenas en restaurantes asiáticos y la reuniones anuales en la playa.

També agrair a la Neus i al Gustau els inicis, per fer-me descobrir el món dels òxids el qual vaig voler seguir explorant uns anys més. I a l'Albert, els inicis dels inicis, per deixar-me provar el que era treballar en un grup de recerca quan encara feia la carrera.

De les estades fetes:

I would like to thank Sergei for giving me the opportunity of working in his laboratory in ORNL for a short stay, and Rana, Qian and Evgeny for all the help. It was a really interesting experience for my formation. Also thanks to Jaume, Juan Carlos and Rohan to make my stay in the *Deep South* much more fun, showing me where to find IPA and Honky-Tonk bars.

Merci beaucoup to Karim for accepting supervising my stay in CNRS/Thales laboratory in Paris. For being so kind and teaching me a little of his magic tricks with Attocube. Thank you to all the other lab mates pour l'accueil très amical: Victor, Regina, Davide, Jacob, Miquel, Flavio, Mathieu, Danielles,...

Gracias a Carlos quien me acogió en mi corta visita a la Universidad Técnica Federico Santa María en Valparaíso. A Claudio por ayudarme en los intentos de crecer CoFeB y a los otros compañeros por tomarse los temblores tan poco en serio. Y a Roque por acompañarme en este viaje y en tantos otros, pasados o mentales, fuera Collserola o Leticia.

Així mateix també vull recordar-me del personal de l'ICMAB als que agraeixo la contribució al bon funcionament del centre. En especial en el promoure la interconnexió de grups als despatxos i l'acondicionament de les terrasses d'on n'han sortit grans companys. A en Blai, en Bernat, la Stefania, Ana, Juan Carlos, Greta, la Maria, l'Anna i demés, per haver format part dels millors moments extracurriculars i d'improductivitat, tan necessaris per trobar la inspiració. I tots els que han passat

pel despatx 3.17, actualment 100% femení, Maria, Marta, Cris, Ezhil, Sandra, Laura, Wenji, Magda i alguns nois, Hugo, Davide, Markus, agraeixo el caliu i la gula compartida. I igualment als companys de la resta del campus, els dinars puntuals a la una i els cafés al sol: James, Bernhard, Ashley, Ela, Pablo, Roberto, Kumara, Jacke, Alex, Fede, Mateo,...

A la meva família els he d'agraïr el carinyo i fer-me la vida tan fàcil. A la Berta, un cervell fugat, que encara que visqui lluny em recolza sempre que calgui. A ma mare, qui s'ha preocupat i m'ha animat constantment amb els seus savis consells per sobreviure al doctorat. Y a mi padre, que después de todo, tanto show en la cocina con botellas, palillos, pilas y imanes, de alguna cosa ha servido.



# CONTENTS

---

Introduction	1
1 INTRODUCTION	3
1.1 Motivation	3
1.2 Organization of the thesis	6
1.3 Electronic and magnetic properties of Transition Metal Oxides	6
1.3.1 Crystal Field	7
1.3.2 Exchange interactions	10
1.4 Lanthanum manganites perovskites	13
1.4.1 Mixed-valence perovskite manganites: $\text{La}_{0.7}\text{Sr}_{0.3}\text{MnO}_3$	15
1.4.2 Double perovskites: $\text{La}_2\text{CoMnO}_6$	15
1.5 Magnetic anisotropy	16
1.6 Charge carrier transport phenomenology	20
1.6.1 Magnetoresistive effects	20
1.6.2 Spin filtering	24
1.6.3 Transport mechanisms	26
1.6.4 Resistive Switching	28
2 EXPERIMENTAL TECHNIQUES	31
2.1 RF magnetron sputtering	31
2.2 Scanning probe microscopy	33
2.2.1 Contact mode. Friction Force Microscopy	34
2.2.2 Amplitude Modulation AFM. Phase lag	35
2.2.3 Conductive AFM	37
2.2.4 MFM	38
2.3 Structural and compositional characterization techniques	40
2.3.1 X-ray diffraction	40
2.3.2 Electron probe microanalysis	42
2.4 Magnetic characterization by SQUID	43
2.5 Electrical transport characterization	44
2.6 Synchrotron-based X-Ray Techniques	45
2.6.1 X-ray Absorption Spectroscopy	45
2.6.2 X-ray Magnetic Circular Dichroism	47
2.6.3 X-ray photoemission electron microscopy (X-PEEM)	50
2.7 Device fabrication	52

2.7.1	UV photolithography . . . . .	53
2.7.2	E-beam lithography . . . . .	53
2.7.3	Ion milling . . . . .	54
<b>Results</b>		<b>57</b>
3	TUNNING MAGNETIC ANISOTROPY BY STRAIN IN LCMO THIN FILMS	59
3.1	Introduction . . . . .	59
3.2	Growth and characterization of LCMO on STO . . . . .	61
3.2.1	Morphological, structural and magnetic characterization . .	61
3.2.2	Stoichiometry of the films . . . . .	67
3.3	Valence state studied with XAS . . . . .	68
3.4	Substrate mismatch strain effects on magnetic anisotropy . . . . .	73
3.4.1	Tensile strain case: LCMO/STO . . . . .	74
3.4.2	Compressive strain case: LCMO/LSAT and LCMO/LAO . . .	77
3.4.3	Thickness dependence . . . . .	80
3.5	Summary . . . . .	82
4	THE ORIGIN OF MAGNETIC ANISOTROPY IN LCMO	83
4.1	Introduction . . . . .	83
4.2	Magnetic anisotropy studied by XMCD . . . . .	84
4.3	Theoretical approach: Origin of PMA . . . . .	88
4.3.1	Effect of tetragonal crystal field (CF) and spin-orbit coupling (SOC) on $\text{Co}^{2+}$ in octahedral environment . . . . .	88
4.4	Summary . . . . .	98
5	SPIN DEPENDENT TRANSPORT ACROSS LCMO-BASED TUNNEL JUNC- TIONS	99
5.1	Introduction . . . . .	99
5.2	Growth and fabrication of the junction . . . . .	100
5.2.1	Fabrication of nanopillars . . . . .	101
5.3	Characterization of the tunnel junction by AFM . . . . .	102
5.4	Transport characterization of the junction by PPMS . . . . .	109
5.5	Magnetotransport phenomenology . . . . .	112
5.5.1	Estimation of spin filtering efficiency . . . . .	113
5.5.2	Theoretical calculations . . . . .	116
5.6	Angular dependence of the tunneling junction resistance. . . . .	118
5.6.1	Memory device . . . . .	123
5.7	Summary . . . . .	125
6	SURFACE CHEMICAL NANOSTRUCTURATION IN LSMO FILMS	127
6.1	Introduction . . . . .	127
6.2	$\text{SrTiO}_3$ substrates treatment . . . . .	128

6.3	Growth of $\text{La}_{0.7}\text{Sr}_{0.3}\text{MnO}_3/\text{SrTiO}_3$ films . . . . .	131
6.4	Surface characterization using Atomic Force Microscopy . . . . .	132
6.5	Surface characterization using X-PEEM . . . . .	136
6.6	Monte Carlo simulations . . . . .	140
6.7	Transport properties: Resistive Switching phenomena. . . . .	143
6.8	Summary . . . . .	147
	<b>Conclusions</b> . . . . .	149
7	CONCLUSIONS . . . . .	151
	List of Publications . . . . .	159
	BIBLIOGRAPHY . . . . .	177





# ACRONYMS LIST

---

- AF** Antiferromagnetic
- AFM** Atomic force microscopy
- AM-AFM** Amplitude modulation AFM
- AMR** Anisotropic magnetoresistance
- C-AFM** Conductive atomic force microscopy
- CF** Crystal field
- CFT** Crystal field theory
- CMR** Colossal magnetoresistance
- DFT** Density functional theory
- EBL** Electron beam lithography
- EPMA** Electron probe micro-analysis
- FC** Field cooled
- FM** Ferromagnetic
- FNT** Fowler-Nordheim tunneling
- FM-I** Ferromagnetic insulator
- GKA** Goodenough-Kanamori-Anderson
- GMR** Giant magnetoresistance
- H<sub>c</sub>** Coercive field
- HS** High spin
- HR** High resistance
- IP** In-plane
- JT** Jahn-Teller
- LAO** LaAlO<sub>3</sub>
- LCMO** La<sub>2</sub>Co<sub>0.8</sub>Mn<sub>1.2</sub>O<sub>6</sub>

- LMO**  $\text{LaMnO}_3$
- LSMO**  $\text{La}_{0.7}\text{Sr}_{0.3}\text{MnO}_3$
- LDA** Local Density Approximation
- LS** Low spin
- LR** Low resistance
- LSAT**  $(\text{LaAlO}_3)_{0.3}(\text{Sr}_2\text{AlTaO}_6)_{0.7}$
- MFM** Magnetic force microscopy
- MIM** Metal/insulator/metal
- MIS** Metal/insulator/semiconductor
- MR** Magnetoresistance
- MTJ** Magnetic tunnel junctions
- NM** Non-magnetic
- OOP** Out-of-plane
- PLD** Pulsed laser deposition
- PMA** Perpendicular magnetic anisotropy
- RF** Radio-frequency
- RMS** Root mean square
- RS** Resistive switching
- RSM** Reciprocal space map
- SOC** Spin-orbit coupling
- SQUID** Superconducting quantum interference device
- STEM** Scanning transmission electron microscopy
- STO**  $\text{SrTiO}_3$
- TAMR** Tunneling anisotropic magnetoresistance
- T<sub>c</sub>** Curie temperature
- TEY** Total electron yield
- TFY** Total fluorescence yield

- TMO** Transition metal oxides
- TMR** Tunneling magnetoresistance
- XAS** X-ray absorption spectroscopy
- XRD** X-ray diffraction
- XMCD** X-ray magnetic circular dichroism
- X-PEEM** X-ray photoemission electron microscopy
- XPS** X-ray photoelectron spectroscopy
- ZFC** Zero field cooled



# INTRODUCTION



# INTRODUCTION

---

## 1.1 MOTIVATION

A common characteristic of the development of future devices in spintronics and storage information applications is the drive towards smaller dimensions. The seek for improved performance is additionally enhanced by the discovery of size-dependent new properties and phenomena. In this sense, nowadays great scientific and technical efforts are dedicated to the development of experimental tools and modeling techniques to close the gap between the fundamental knowledge with the microscale.

Regarding fundamental science, this aim of miniaturization has required the understanding of elemental physical phenomena and the manipulation control of matter at the nanoscale. Therefore, in the last past years, experimental systems have been developed to design tailored nanostructures. Nanostructures refer to materials where one, two or the three dimensions are in the nanoregime leading to architectures as thin films, nanowires, nanoparticles, quantum wells, etc. Sometimes the challenge is to make every dimension as small as possible, as in nanodevices, but other times the purpose is to enlarge one dimension magnifying the surface area. The enlargement of surface-area-to-volume ratio is one of the main reasons for the appearance of unknown phenomena [1] and has triggered research fields as, for instance, surface and interface engineering in thin films. On the other hand, advances in the understanding of these phenomena have been possible mainly thanks to the development of novel characterization techniques such as atomic force and electron microscopies or X-ray based techniques.

Finding the right materials fulfilling the requirements for competitive technology is another challenging task. In this sense, transition metal oxides are one of the most exciting families of potential candidates as they present an incredibly rich spectrum of functionalities that can be tuned via structural, chemical modification or via external stimuli. Therefore, one-dimensional nanostructures of oxides conform thin



films, engineered interfaces or tunnel junctions and will be explored in the course of this thesis.

Among transition metal oxides (TMO), lanthanum manganite-based materials are one of the most extensively studied family of oxides since the discovery in the 90s of colossal magnetoresistive effects that can display. On the other hand, manganites exhibit other intriguing phenomena as half-metallicity, charge ordering, orbital ordering, metal-insulator transitions or multiferroic behaviour [2]. The parent compound of lanthanum manganites is  $\text{LaMnO}_3$  (LMO), a perovskite material with chemical formula  $\text{ABO}_3$  composed by  $A=\text{La}$  and  $B=\text{Mn}$ . It is an antiferromagnetic insulator whose properties can be substantially modified by cation substitution. In this thesis we explore, two kind of compounds obtained by A-site and B-site substitution. In particular, we study  $\text{La}_2\text{Co}_{0.8}\text{Mn}_{1.2}\text{O}_6$  (LCMO) obtained by substitution of Mn by Co which conforms a double perovskite structure, and  $\text{La}_{0.7}\text{Sr}_{0.3}\text{MnO}_3$  (LSMO) resulting from the partial substitution of La by Sr. In the first case, LCMO turns into a ferromagnetic insulator (FM-I) while in the second case, LSMO becomes a ferromagnetic half-metal. These physical properties make them potential materials for spintronics and memory applications.

Spintronics is expected to lead to future technologies of information processing and storage functionalities. Devices based on spin manipulation confer important advantages in front of conventional semiconductor devices: non-volatility, low power consumption, higher data processing speed and high integration densities [3]. Spin-polarized devices such as magnetic tunnel junctions (MTJ) are the main building blocks of spin-based electronic components such as magnetoresistive random-access memory (MRAM). Commonly, MTJs are composed by ferromagnetic metals separated by an ultrathin non-magnetic insulating barrier to tunnel through. With the discovery of tunneling magnetoresistance (TMR) these devices gained tremendous importance. This phenomenon implies that the relative orientation of the electrodes magnetization determines whether the MTJ exhibits a low or a high resistance state. As first approximation, the transport through this kind of junctions is extremely sensitive to interface effects such as interfacial chemical purity or interface scattering, thus the quality of the barrier becomes a major concern. Since then, other routes to use magnetoresistive effects in tunnel junctions have been explored, for instance, the tunneling anisotropic magnetoresistance (TAMR) effect. TAMR measures resistance changes that depend on the orientation of the magnetization of magnetic components in the tunnel junction with respect to its crystallographic axes [4, 5]. It arises from SOC effects and, unlike conventional TMR, it can be found in tunnel structures with only one magnetic electrode. In fact, TAMR seems to be a generic effect in ferromagnetic metals with SOC [6]. In particular, in this thesis we explore TAMR effects in a ferromagnetic insulating material. Additionally, ferromagnetic insulating mate-

rials can be used as spin selective barriers in spin filtering structures. The FM-I acts as a potential barrier whose height depends on the spin orientation of the carriers, so it actively filters the spin. Actually, the implementation of ferromagnetic insulators as substitutes of ferromagnetic metal-based devices can lead to much higher switching efficiency and less dissipative transport [7]. The main obstacle of FM-I is its scarcity in nature. LCMO is one of these rare materials and will be one of the topic of study of this thesis.

Remarkably we have found that LCMO presents strong perpendicular magnetic anisotropy (PMA) when grown on substrates that induce tensile strain. This property is of great interest for technology, for example, it enables to fabricate highly dense devices. Therefore, as an ultimate objective after LCMO thin film optimization, we seek for integrating FM-I and PMA properties in a device. The device is based on a LCMO barrier sandwiched between non-magnetic (NM) electrodes. In this sense, exploiting TAMR in junctions that could operate without magnetic electrodes represents an alternative of much easier technological implementation, avoiding the need of two magnetically decoupled ferromagnetic electrodes and coherent tunneling.

The last part of the thesis has been focused on the study transport properties in smaller nanostructures than tunnel junctions in LSMO thin films. The fabrication of epitaxial oxide thin films with well-defined atomically sharp interfaces requires thorough optimized conditions. Increasing interest in controlled thin film growth arises from the possibility of modulating the interface properties. Actually, interfaces between complex oxides comprise an extensive field due to the possibility of tailoring their electronic structures to display novel functionalities. Varying growth parameters (deposition rate, temperature, oxygen pressure,...) or inducing defects (cation excess, oxygen vacancies,...) can provoke local structural or stoichiometric deviations in the films and in their surfaces. In general, the reasons for instabilities in the growth process are mostly thermodynamic or kinetic. For instance, the formation of stacking faults is one frequent source of growth instability. Taking advantage of this fact, nanostructured LSMO films can be achieved without the need of special substrate preparation.

Getting away from then ideal growth behaviour constitutes a way to obtain spontaneously formed nanostructures leading to modulated local functional properties of thin film surfaces. Transport properties of these films are analyzed by making use of scanning probe techniques which are suitable to characterize materials at such nanosized level.

## 1.2 ORGANIZATION OF THE THESIS

Starting with this introductory chapter, we present general concepts of transition metal oxides particularly focusing on processes related to transport in certain manganite based oxides systems. Then chapter 2 briefly explains the most important facts of the experimental techniques used in the course of the thesis.

Chapter 3 and chapter 4 are centred in results related to ferromagnetic insulating lanthanum-cobalt manganite thin films (LCMO). In chapter 3 we present a detailed study of growth and structural and magnetic characterization of LCMO thin films. Firstly, we discuss about stoichiometry and cationic ordering of the films. Having proved that we can obtain high quality thin films with good cationic order despite a certain degree of off-stoichiometry, we analyze the appearance of strain-induced perpendicular magnetic anisotropy. Then, in chapter 4 we discuss about the origin of this strain tunable magnetic anisotropy using a theoretical approach and X-ray magnetic circular dichroism experiments.

In chapter 5, we explore the possibilities of using PMA in a spintronic device. Hence, we present the fabrication and evaluation of tunneling transport on a tunnel junction composed by LCMO barrier sandwiched between non-magnetic electrodes: metal/LCMO/Nb:SrTiO<sub>3</sub>. In particular, spin filtering effect and sensor and memory capabilities based on TAMR are analyzed.

In chapter 6, we examine double-terminated LSMO thin films making use of surface sensitive techniques such as Atomic force microscopy and X-ray photoemission electron microscopy. We relate local transport properties with different composition and explore the effect of the termination on resistive switching related phenomenology.

## 1.3 ELECTRONIC AND MAGNETIC PROPERTIES OF TRANSITION METAL OXIDES

Electronic and magnetic properties in most oxides are determined by its outermost electrons and the overlap of the orbitals where they are comprised. In particular, TMO are compounds whose emerging properties are governed by *d*-electrons and present a broad range of interesting functionalities, such as high temperature superconductivity, piezoelectricity, colossal magnetoresistance, fully spin-polarized currents, multiferroic properties, etc. The physics of these phenomena relies on the strong electronic correlations. Besides, the hybridization of the transition metal *d*-orbitals with the oxygen *p*-orbitals produce narrow energy bands where spin, charge and lattice degrees of freedom are coupled. Then emergent properties can be tuned

via strain, chemical doping or application of external fields, pressure or temperature. For its part, perovskite oxides have a simple crystalline structure that allows the epitaxial growth of thin films of them on top of each other. Hence oxide materials with different functionalities can be combined in thin film heterostructures giving rise to a great plethora of possibilities for new oxide devices.

### 1.3.1 *Crystal Field*

The first step to understand the properties of TMO is to examine how interactions with neighboring ions alter the configuration of partially filled  $d$ -levels. This has been addressed in the framework of crystal field theory (CFT). Within this theory, interactions with neighboring cations are modeled as static electric fields produced by them. The effects of the resulting electric field, known as CF depend crucially on the symmetry of the environment. TMO perovskites present octahedral coordination: the metal ion is placed in the center of a cube surrounded by 6 oxygen atoms forming an octahedron. The CF arises from Coulombic repulsion between electrons in  $3d$  orbitals of the metal ion and electrons in the  $2p$  orbital of oxygen and breaks the degeneracy of the  $d$ -levels depending on the symmetry of the orbitals. In particular, CF in perovskites with regular octahedral coordination splits the electronic levels into  $t_{2g}$  and  $e_g$  manifolds. As it is observed in Figure 1.1,  $t_{2g}$  are comprised by  $d_{xy}$ ,  $d_{xz}$  and  $d_{yz}$  orbitals and  $e_g$  by  $d_{x^2-y^2}$  and  $d_{z^2}$  ( $d_{3z^2-r^2}$ ). Electrons in  $e_g$  strongly interact with electrons in oxygen orbitals so they have higher energy than  $t_{2g}$ .

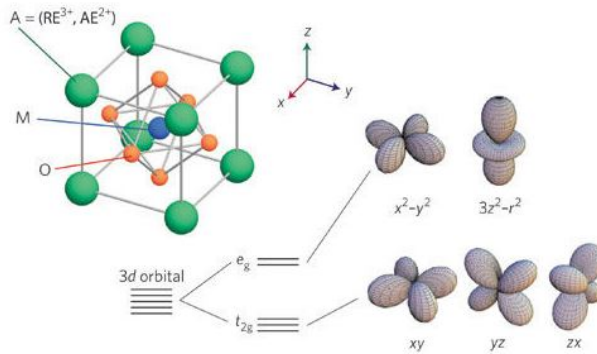


Figure 1.1: Perovskite structure and orbital energy levels under a cubic CF due to oxygen ions. M is a metal ion; RE, rare earth elements, and AE, alkaline earth elements. Figure reproduced from Ref. [8].

For completeness, in Figure 1.2 we show how the lobes of  $d$  orbitals are oriented relative to the negative charges at the corner of the octahedra: the lobes of the  $d_{z^2}$  and

$d_{x^2-y^2}$  orbitals (b and c) point toward the charges (so the repulsion force is higher) while the lobes of the  $d_{xy}$ ,  $d_{xz}$  and  $d_{yz}$  orbitals (d-f) point between the charges.

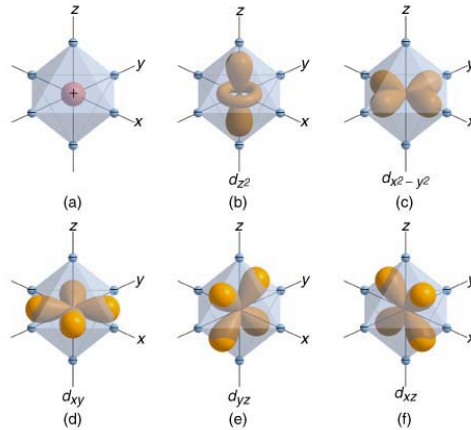


Figure 1.2: (a) Metal ion at the center of an octahedral array of negative charges. (b-f) The orientations of the  $d$  orbitals relative to the negatively charged ligands. Figure reproduced from Ref. [9].

In addition to CF effects, in general, other interactions must be taken into account to understand the properties of TMO. Of particular relevance in the framework of this thesis are the SOC and, under the application of a magnetic field, the Zeeman term.

CFT is useful to find the eigenstates and corresponding energy levels on the basis of the known symmetry of the system, treating these interactions as perturbation. Therefore in CFT one tries to find the solution of the Schrödinger equation with an interaction Hamiltonian described as:

$$H_i = H_0 + H_{CF} + H_{LS} + H_Z \quad (1.1)$$

where  $H_0$  is the Coulomb interaction,  $H_{CF}$  is the interaction with the CF,  $H_{LS}$  is the SOC interaction and  $H_Z$  accounts for the Zeeman effect.

It is important for the solution of this Hamiltonian to observe the energy scales. Thus, in transition metal oxides the magnitude of  $H_0$  lies between 1-10 eV,  $H_{CF}$  between 12.5 meV-1.25 eV,  $H_{LS}$  between 1.25-250 meV and  $H_Z$  is smaller than 1.25 meV [10]. On one hand, note that CF and SOC are always much larger than Zeeman effect, therefore it will be treated as a small perturbation. In particular, in this thesis we will see how magnetic properties of LCMO thin films system can be described solving a perturbative problem.

Having this in mind, the distribution of electrons in the orbitals will depend on the magnitude of the energies named above and also in intratomic exchange split-

ting ( $J_H$ ).  $J_H$  is the difference between spin-up and spin down levels due to Hund's coupling.

Three empirical rules were suggested by Friedrich Hund in 1925 for the energetic ordering and filling of electronic states in atoms. Hund's rules dictate the lowest-energy configuration for electrons in the  $3d$ -shell for a given electronic configuration. They originate from interatomic exchange interaction and SOC, hence, they are used to identify the ground state average spin (S), orbital (L) and total angular moments. Hund's rules state that:

1. The sum of the spin angular momentum (S) of all electrons in the shell is maximized, remembering that the orbitals can only accommodate one electron  $\uparrow$  and one electron  $\downarrow$  each according to Pauli exclusion principle.
2. Angular momentum (L) maximizes consistent with S. For a given spin arrangement, the configuration with the largest L is the lowest in energy.
3. L and S couple to form the total angular momentum J so that  $J=L-S$  if the shell is less than half-filled and  $J=L+S$  if the cell is more than half-filled. When it is exactly half-filled, then  $L=0$  and  $J=S$ .

For  $\Delta E_{CF} \ll J_H$  the Hund's rules are applicable while for  $\Delta E_{CF} \gg J_H$  only lowest levels are occupied. In the later case, orbital motion is impeded by the strong influence of the lattice. Then the L is quenched and S become the significant quantum number.

As a practical case, here we present the electronic structure for the three magnetic ions that comprise our materials of study:  $Mn^{3+}$ ,  $Mn^{4+}$  and  $Co^{2+}$ . Electronic configurations for each one are:  $[Ar]3d^4$  for  $Mn^{3+}$  and  $[Ar]3d^3$  for  $Mn^{4+}$  and  $[Ar]3d^7$  for  $Co^{2+}$ .

The distribution of electrons for each species is depicted in Figures 1.3 and 1.4. For the  $Mn^{4+}$  the three  $t_{2g}$  levels are completely filled and spins are parallel and coupled to  $S=3/2$  following Hund's interaction. The largest L compatible with this S is  $L=3$ . In  $Mn^{3+}$ , with 4 electrons in the  $d$ -level, three electrons fill  $t_{2g}$  levels and the remaining one is placed in one of the  $e_g$  levels. Again due to the strong Hund's interaction the electron spin remains parallel to the spins in  $t_{2g}$  electrons leading to a total spin moment of  $S=2$ . As all spins remain parallel, a high spin (HS) configuration is defined in both ions ( $Mn^{3+}$  and  $Mn^{4+}$ ). For  $Mn^{3+}$ , the largest L compatible with  $S=2$  is  $L=2$ .

Additionally, for  $Mn^{3+}$  electronic structure, we have to take into account Jahn-Teller (JT) effect. This effect leads to a distortion in the octahedron caused by the coupling of the  $e_g$  electron with the lattice. In a perfect octahedral environment, the  $e_g$  electron of  $Mn^{3+}$  can occupy either the  $d_{x^2-y^2}$  or the  $d_{z^2}$  orbital because in this

case levels are degenerate. In reality, the deformation of the octahedron produces a structural distortion which lowers the energy of one of these orbitals at expenses of raising the energy of the other, hence breaking the degeneracy [11]. As the raised orbital is unoccupied, there is a net lowering of the energy of the system, thus JT distortion yield to a more favorable energy state. The JT effect has important implications in the physical properties of manganites. For example, it is responsible of the orbital ordering phenomena and introduces strong interactions between electronic and lattice degrees of freedom in manganites.

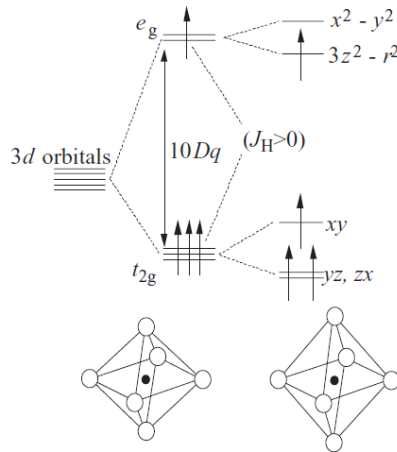


Figure 1.3: Energy splitting of the 3d-electron states in an octahedral CF ( $\text{Mn}^{4+}$ ) and due to the Jahn-Teller effect ( $\text{Mn}^{3+}$ ). Figure reproduced from Ref. [2].

From its part,  $\text{Co}^{2+}$  can show within the same oxidation state both HS ( $t_{2g}^5 e_g^2$ ) and low spin (LS) ( $t_{2g}^6 e_g^1$ ) configurations. This happens because  $J_H$ , which is the difference between spin up and spin down levels due to Hund's coupling, is comparable with  $\Delta E_{CF}$ .  $\Delta E_{CF} < J_H$  favors the filling of spin up band before the filling of  $t_{2g}$  spin down band as depicted in 1.4, yielding to a HS with  $S=3/2$ . Contrary, if  $\Delta E_{CF} > J_H$  the  $t_{2g}$  levels for both spin states are filled before  $e_g$  as they lie at lower energy, then six electrons occupy  $t_{2g}$  and the remaining one eventually occupies the  $e_g$ , defining a LS with  $S=1/2$ . When Hund's coupling dominates, the maximum angular momentum compatible with  $S=3/2$  is  $L=3$ .

### 1.3.2 Exchange interactions

Another factor that determines the electronic and magnetic properties of TMO, such as long range magnetic order, are the exchange interactions. Exchange interactions

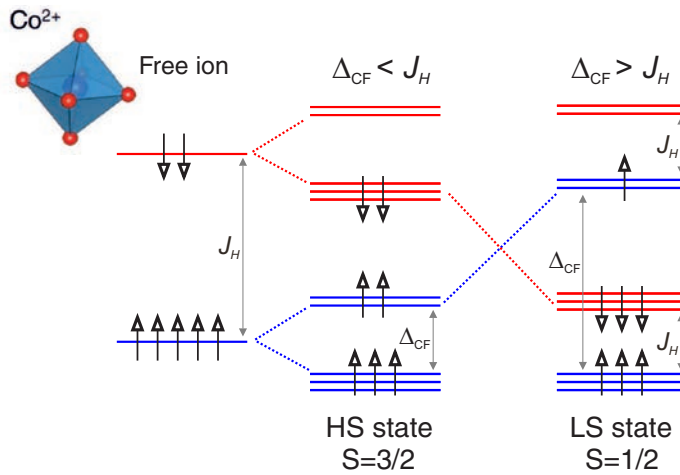


Figure 1.4: Energy splitting of the 3d-electron states in an octahedral CF for  $\text{Co}^{2+}$  in HS and LS configurations

are essentially electrostatic interaction arising because charges of the same sign bring up a gain of energy when they are apart and a cost of energy when they are close together. Exchange interactions depend on the overlap of magnetic ions wavefunctions which are exponentially decaying. Therefore, in perovskite oxides, there is small direct overlap of the wavefunctions of the nearest-neighbor cations (direct exchange), but can strongly overlap with the 2p-orbitals of the neighboring non-magnetic anions (indirect exchange). That is, direct exchange is very weak due to the localized nature of *d*-electrons and because magnetic cations are separated by a non-magnetic anion, thus too far apart to interact. Instead exchange interactions in oxides are indirect, mainly comprised by superexchange and double exchange, and use  $\text{O}^{2-}$  as intermediary to interact.

### *Superexchange*

Superexchange in oxides is the magnetic interaction between neighboring magnetic cations mediated by chemical bonding through oxygen where no real charge transport is involved. The interaction involves the virtual transfer of one electron. As depicted in Figure 1.5, when a 2*p*-electron of the oxygen transfers to a neighbouring Mn ion, the remaining unpaired *p*-electron of oxygen then enters into direct exchange with the other Mn ion. The sign of the magnetic interaction is then determined by the relative orientation of the spin of the virtually transferred oxygen *p*-electron with respect to the first Mn and the sign of the direct exchange between the oxygen and the second Mn. As *d*-orbitals can have different orientations and



configurations, different types of superexchange interactions can take place: ferromagnetic (FM) or antiferromagnetic (AF).

Goodenough [12], Kanamori [13] and Anderson [14] proposed a series of rules (GKA rules) that enable to determine the sign of the exchange integral and the type of interaction depending on the orbital configuration of the two Mn ions involved in the interaction. These rules, for octahedral-site cations in perovskite structures, are applicable for angles of  $180^\circ$  between the three ions. Then Goodenough-Kanamori-Anderson (GKA) rules state:

1. The interaction between two half-filled  $e_g$  orbital pointing toward each other is AF and strong.
2. The interaction between two  $t_{2g}$  orbitals pointing toward each other is AF and weak.
3. The interaction between one half-filled  $e_g$  and a  $t_{2g}$  orbitals (empty  $e_g$ ) pointing toward each other is FM.

LMO is an example of AF insulator compound with superexchange interaction at  $\text{Mn}^{3+}\text{-O-Mn}^{3+}$  bridges ( $e_g - 2p - e_g$ ) while LCMO is an example of a FM insulator due to ferromagnetic superexchange interaction between  $\text{Mn}^{4+}\text{-O-Co}^{2+}$  ( $t_{2g} - 2p - e_g$ ).

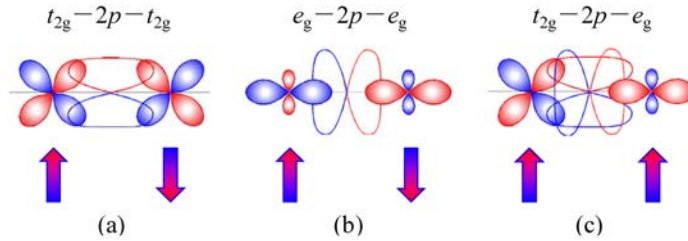


Figure 1.5: Schematic of  $180^\circ$  cation-anion-cation GKA rules governing magnetic interaction between transition metal cations ( $M, M'$ ) via oxygen. (a) AF interaction of  $M(t_{2g})\text{-O-M}(t_{2g})$ . (b) AF interaction of  $M'(e_g)\text{-O-M}'(e_g)$ . (c) FM interaction of  $M(t_{2g})\text{-O-M}'(e_g)$ . Figure reproduced from Ref. [15].

### Double exchange

Double exchange interaction is essentially a mechanism of superexchange that takes place in mixed valence materials, such as manganites, and implies the real transfer of

an electron, allowing electric conductivity. It was firstly proposed by Zener in 1951 [16]. It consist in the hopping of  $e_g$  electrons between neighboring Mn sites with distinct valence ( $\text{Mn}^{3+}$  and  $\text{Mn}^{4+}$ ) through the ligand oxygen ion. Therefore, there is a simultaneous charge transfer of the  $e_g$  electron of  $\text{Mn}^{3+}$  to  $\text{O}^{2-}$  and of one electron in the  $2p$  of  $\text{O}^{2-}$  to  $\text{Mn}^{4+}$  resulting in a net transport of charge. As Hund's coupling is very strong, the spin of the  $e_g$  electron going into  $\text{Mn}^{4+}$  must align its spin with those of the  $t_{2g}$  of the vacant site ion. Therefore, as  $t_{2g}$  electrons of  $\text{Mn}^{3+}$  ion are parallel to the  $e_g$  electron, the  $t_{2g}$  electrons of the two Mn ions must be aligned in the same orientation then, ferromagnetism is induced (see Figure 1.6).

The probability of hopping is dictated by the relative angle between the two Mn ions. Thus, the system can be described through the effective hopping ( $t_{eff}$ ) which is defined as:

$$t_{eff}(\theta) = t \cdot \cos(\theta/2) \quad (1.2)$$

where  $t$  is the hopping parameter and  $\theta$  is the angle between the  $t_{2g}$  spins of neighboring Mn ions. As a result hopping is maximum when  $\theta = 0$  and ions are ferromagnetically aligned, while  $t_{eff}=0$  when  $\theta = \pi$ , due to Pauli exclusion principle, and spins of the ions are AF aligned.

Double exchange is applied to extended system and drives ferromagnetism and half-metallicity: electrons of one kind of spin that are allow to hop through the whole system.

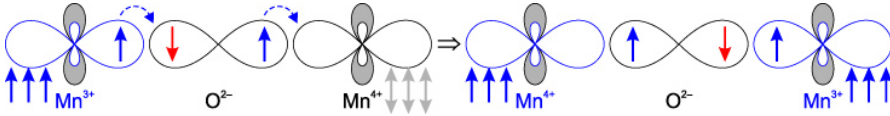


Figure 1.6: Double exchange between the  $3d_{z^2}$  orbital of  $\text{Mn}^{3+}$  and  $\text{Mn}^{4+}$  ion via the  $2p_z$  orbital of an  $\text{O}^{2-}$  ion. The  $3d_{x^2-y^2}$  orbital of Mn is shaded in grey. The core spin  $S = 3/2$  of the three (not-shown)  $t_{2g}$  orbitals of Mn is symbolized by triple arrows. The resulting interaction is ferromagnetic, mediated by the itinerant electron of  $\text{Mn}^{3+}$ . Figure reproduced from Ref. [17].

## 1.4 LANTHANUM MANGANITES PEROVSKITES

Lanthanum manganite perovskites are one of the most interesting complex oxides system studied so far. They exhibit unique electronic and magnetic properties which are determined by interactions between the lattice, charge, orbital, and spin degrees of freedom. Among this phenomenology we found effects as colossal magnetoresistance, half-metallicity, metal-insulator transitions, charge and orbital ordering ef-

fects or strong electron-phonon coupling [18]. Hence, an intense research effort has been devoted to study the interplay between structure, magnetism, and transport in perovskite manganites during the last twenty years.

Perovskites oxides adopt the general formula  $ABO_3$  and are mostly composed by a rare-earth (La, Sm, Pr, Nd) or alkali-earth metal (Ca, Sr, Ba) occupying A site, possessing oxidation states +3 or +2, respectively. Then the B site is composed by a transition metal oxide such as Mn, Fe, Co, Ni, Ir, Nb, Mo... which can have various oxidation states. The parent compound of lanthanum manganites is LMO composed by A=La and B=Mn. LMO is an antiferromagnetic insulator whose properties can be critically modified by cation substitution.

LMO has an AF ground state due to superexchange interactions when the metal-oxygen-metal bond angle is close to  $180^\circ$ . Upon full substitution of divalent cations,  $CaMnO_3$ ,  $SrMnO_3$  and  $BaMnO_3$ , Mn ion possesses +4 valence, hence, we also find an AF and insulating state. However, when doping at intermediate degrees  $La_xD_{1-x}MnO_3$  (D=divalent alkaline-earth cation), Mn ions acquire a mixed valence between +3 and +4, thus, the donor electrons can become delocalized and the material highly conductive and FM.

The crystalline structure of the perovskites consists in a 3D arrangement of  $BO_6$  linked by the vertex. A cations lie in the empty space between octahedra while B cations are placed at the center of the octahedra. The perovskite structure tends to suffer distortions with respect to the parent cubic structure that affect dramatically its properties. These distortions are mainly given by the relation between the ionic radius of the cations define by the tolerance factor:

$$t = \frac{r_A + r_O}{\sqrt{2}(r_B + r_O)} \quad (1.3)$$

where  $r_A$  and  $r_B$  are the ionic radii of the ions occupying A and B sites and  $r_O$  is the radius of the anion, i.e. oxygen. Tolerance factor is an indicator for the stability and distortion of crystal structures. When it equals to one, the perovskite exhibits a cubic structure. If  $t < 1$ , A cation is too small to fill the space between octahedra. As a result, octahedra rotate making this cavity smaller. These rotations imply a reduction of the symmetry of the structure that changes from cubic to rhombohedral, tetragonal, orthorhombic, monoclinic or even triclinic depending on octahedra tilting [19, 20]. In the unusual cases where  $t > 1$ , meaning that B cation is too small to fill the octahedra, an off-centering of the B cation takes place. The displacement of B cation is towards oxygen ions to compensate the valence. Hence, non-centrosymmetric structures, such as  $BaTiO_3$  are favored.

### 1.4.1 *Mixed-valence perovskite manganites: $La_{0.7}Sr_{0.3}MnO_3$*

As already stated, the substitution of trivalent La by divalent Sr in  $LaMnO_3$  produces a redistribution of charge in the compound and so, to fulfill charge neutrality a mixed valence state on Mn ions is introduced. That is, a certain proportion of  $Mn^{3+}$  converts to  $Mn^{4+}$ . The doping level ( $x$ ) establishes the proportion of each Mn valence:  $La_{1-x}^{3+}Sr_x^{2+}Mn_{1-x}^{3+}Mn_x^{4+}O_3^{2-}$ . Lanthanum manganite is an AF insulator for  $x = 0$ , while  $x = 0.3$  leads to a FM state with half-metallic character. Thus the mixed valence state provides a potential charge carrier path for electrical conduction via double exchange interactions. Due to double exchange Mn ions are aligned parallel producing ferromagnetism and consequently conduction. That is the reason why LSMO is additionally half-metallic, meaning that it is constituted by only one kind of electron spins at the Fermi level.

### 1.4.2 *Double perovskites: $La_2CoMnO_6$*

B-site substitution in  $ABO_3$  perovskites can yield to ordered double perovskite oxides with the general formula in  $A_2BB'O_6$ . Thus, the double perovskite structure is obtained by occupying the simple perovskite B-site with an alternate distribution of two different cationic species, B and B' as it is depicted in figure 1.7.

The unit cell of B-site-ordered double perovskite has in general four times larger volume than the cell of a simple perovskite, which corresponds to  $\sqrt{2}a_p \times \sqrt{2}a_p \times 2a_p$ , where  $a_p$  is the lattice parameter for a cubic perovskite. Besides, if cationic order is achieved the structure is in most of the cases defined by a rock salt-type lattice arrangement in which each B cation has only B' as nearest neighboring cations and viceversa. Cationic ordering depends on the ionic size of the cations and its oxidation state. In general, cationic order is favored for the largest differences in the ionic radii and in the oxidation state. Perfect cation ordering is difficult to obtain, specially when the valence difference is smaller than 3, and in many cases, some degree of cation mixing is present.

Moreover, the presence of multivalence cations such as Mn or Co is an additional drawback as they can stabilize in different valence states. Therefore the combination of cation capable of producing ordered double perovskite compounds is small and just a limited number of them has been fabricated to the date. Nevertheless, ordered double perovskite oxides can present unique properties not found in single perovskites. Some double perovskites exhibit FM-I properties with relatively high Curie Temperature ( $T_C$ ), e.g.  $La_2NiMnO_6$  ( $T_C \approx 280K$ ) [21],  $Ca_2CrReO_6$  ( $T_C \approx 360K$ ) [22]

Some double perovskites are half-metallic ferromagnets with very high  $T_C$ ,  $\text{Sr}_2\text{FeMoO}_6$  ( $T_C \approx 410$  K) [23] and  $\text{Sr}_2\text{CrReO}_6$  ( $T_C \approx 635$  K) [22]. Others can be ferroelectric as in the case of  $\text{Bi}_2\text{NiMnO}_6$  [24] or potential candidates for mixed oxide ion/electron conductor as  $\text{Sr}_2\text{MgMoO}_{6-\delta}$ . [25]

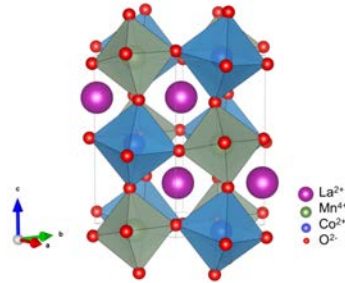


Figure 1.7: Double perovskite structure of  $\text{La}_2\text{CoMnO}_6$ .

The cobalt-substituted manganite,  $\text{La}_2\text{CoMnO}_6$ , subject of study in this thesis, presents special interest because the resulting compound exhibits FM-I character and relatively high  $T_C$  of 230 K, making it a promising materials for spintronic applications. Its magnetic properties strongly depend on cationic ordering. Since Mn and Co have stabilized different valences, it could be possible to obtain an ordered rock-salt structure with a strong net magnetic moment and a ferromagnetic ordering. When magnetic moments of Co and Mn order ferromagnetically, they give a  $T_C \approx 230$  K and an total magnetic moment of  $6 \mu_B/\text{f.u.}$ . It is generally accepted that in order to obtain cationic order Co adopts +2 oxidation state while Mn adopts +4. Then, the origin of ferromagnetism is attributed to superexchange interactions between  $\text{Co}^{2+}$  and  $\text{Mn}^{4+}$ . Disorder is associated with the presence of Mn and Co in +3 valence state, this may favor  $\text{Co}^{3+}\text{-Co}^{3+}$ ,  $\text{Mn}^{3+}\text{-Mn}^{3+}$  or  $\text{Mn}^{3+}\text{-Co}^{3+}$  interactions which are commonly antiferromagnetic. Then disordered  $\text{La}_2\text{CoMnO}_6$  will present lower  $T_C$  ( $\approx 150$  K [26]) and lower saturation magnetization. To obtain thin films with good ordering, growth conditions must be optimized. A common way to achieve cationic order is by proper annealing conditions as will be explained in chapter 3 of the thesis. The insulating behaviour in  $\text{La}_2\text{CoMnO}_6$  is driven by Coulomb-assisted spin orbit coupling within the  $\text{Co-}e_g$  states in the octahedral sites and the Coulomb correlations arising within CF splitting in Co  $d$ -mainfold [27].

## 1.5 MAGNETIC ANISOTROPY

Most ferromagnetic crystals, especially those that possess strong SOC, exhibit preferred crystallographic directions of magnetization, named "easy axes". Thus, mag-

netic anisotropy refers to the dependence of the magnetic properties on the direction of the applied field relative to the crystal axes. Magnetic anisotropy is closely related to phenomenology such as orbital moment formation, magnetoelasticity or magnetoresistance [28]. It has gain increasing attention in technology for application as magnetic information storage and magneto-optical recording [29]. Magnetic anisotropy can be classified by its physical origin. It can be a result of its crystal chemistry or its shape, or it can be induced by external factors such as strain or pressure. In systems of finite size there are two main contributions to magnetic anisotropy, named magnetocrystalline and shape anisotropy. The former is a bulk property and involves CF and SOC, while the later originates from magnetic dipole-dipole interaction and depends on the geometry of the sample. In thin films systems, its particular shape (2D dimensional) as well as the appearance of symmetry breaking elements in form of surfaces and interfaces confers the systems anisotropy properties different from bulk. In particular, the shape of a thin film always favors in-plane magnetization. However, in certain conditions, when the thickness of the film is further reduced, the preferential direction of magnetization can change from in-plane to out-of-plane. This is due to a surface anisotropy term.

The magnetic anisotropy energy can be expressed phenomenologically in terms of magnetization angle and anisotropy constants. The simplest anisotropy energy ( $E_a$ ) expression is:

$$E_a = K_1 V \sin^2 \theta \quad (1.4)$$

where  $V$  is the volume of the magnet,  $K_1$  the first-order uniaxial anisotropy constant and  $\theta$  is the angle between the magnetization and the film normal [28]. This expression is very limiting as excludes any higher order term, hence it is only useful for uniaxial magnetic anisotropy. In any case, the expression enables to interpret anisotropy direction in low-dimensional systems such as thin films. Thin films magnetic materials are treated as flattened cylinder because the thickness of the film is very small relative to lateral dimensions. Thus lateral dimensions are considered to be infinite and the symmetry axis correspond to the normal to its surface. If we inspect the sign of  $K_1$  we note that for positive  $K_1$ , the minima of energy will be found for  $\theta = (0, \pi)$ , implying that the easy axis will be parallel to the symmetry axis (perpendicular to the plane); while for negative  $K_1$ , the energy minimum will be at  $\theta = \pi/2$ , thus the in-plane direction.

Additionally in thin films, it is useful to define magnetic anisotropy  $K_1$  as the sum of volume ( $K_v$ , per unit volume) and interface ( $K_s$ , per unit area) contributions:

$$K_1 = K_v + 2 \frac{K_s}{t} \quad (1.5)$$

where  $t$  is the thickness of the system. The prefactor 2 accounts from assuming that the magnetic layer is bounded by two identical interfaces. This being pointed out, in the following, each of the possible anisotropy sources that concern the thin film systems presented in this thesis are briefly presented in some more detail.

### *Shape anisotropy*

Shape anisotropy is produced by long range magnetic dipolar interactions. If the sample is not spherical the magnetostatic energy of the system depends on the orientation of magnetic moments within the sample.

Then shape anisotropy is characterized by a shape-dependent demagnetizing field  $\vec{H}_d = -N\vec{M}$ , being  $N$  the demagnetizing tensor and  $\vec{M}$  the magnetization of the system per volume unit. Then the demagnetizing energy will be expressed as [30]:

$$E_d = \frac{\mu_0}{2V} \int \vec{M} \cdot \vec{H}_d dV \quad (1.6)$$

If the sample is an ellipsoid, it will be uniformly magnetized so the demagnetization field will be uniform and will be easily calculated using a demagnetization tensor where all the elements will be zero except the diagonals. In the case of thin films, all tensor elements will be zero except for the direction perpendicular to the layer, then anisotropy energy per unit volume will be expressed as <sup>1</sup> [30]:

$$E_d = \frac{1}{2} \mu_0 M_s^2 \cos^2 \theta \quad (1.7)$$

There is an energy saving if magnetization is kept in the plane. According to this equation, in-plane orientation of magnetization will be favored. As we have mentioned, thin films are treated as flattened cylinder in the continuum approach to calculate the integral above-written. Therefore this term only contributes to  $K_v$ . For ultrathin films, the number of elementary magnetic dipoles becomes countable. The calculation of the demagnetizing field will become a discrete sum of dipolar interactions. The symmetry of the surface will become important and anisotropy will be expressed by the sum of  $K_v$  and  $K_s$  contributions.

### *Surface anisotropy*

Louis Néel showed in 1954 that there must exist a surface anisotropy energy that depends on the orientation of the spontaneous magnetization with respect to the surface and it is not related to the classical phenomenon of the demagnetizing field

<sup>1</sup> Note that  $\cos^2 \theta = 1 - \sin^2 \theta$ , thus the contribution to  $K_v$  is  $-\frac{1}{2} \mu_0 M_s^2 < 0$ .

coming from the shape anisotropy [31]. Therefore, at the surface of a magnetic film, the absence of neighboring atoms in one of its interfaces critically modifies the magnetocrystalline anisotropy and occasionally causes the moments to align perpendicular to the surface (PMA). The great potential for application of PMA in spintronics has triggered the attention of studying these systems for its potentials for ultrahigh density recording. Nevertheless the nature of PMA is not always related with the surface anisotropy and can have a magnetocrystalline origin.

### *Magnetocrystalline anisotropy*

As already stated, the origin of magnetocrystalline anisotropy is the SOC interaction. The orbital moment of  $3d$ -electrons in TMO is generally coupled to the lattice through the CF at the same time that spins are coupled to the orbital moment via SOC.

The SOC can be approximated by a one-atom term  $\lambda \vec{L} \cdot \vec{S}$ , where  $\lambda$  is the SOC constant and is of the order of 0.05 eV in  $3d$  transition metals [32]. This is a small term as compared with CF energies of  $3d$  electron systems, of the order of 1 eV. Then SOC can be considered a small correction to the CF and consequently we can treat magnetocrystalline anisotropy as a perturbative problem, as we will see in chapter 4.

Therefore, in these systems, the total magnetic moment is coupled to the crystal axes so the energy required to rotate the spins away from the easy axis is the energy required to overcome SOC. This results in a total energy which depends on the direction of the magnetization and follows the same symmetry of the crystal. In some TMO the SOC is strong enough to produce sizable effects, e.g. the ones containing  $\text{Co}^{2+}$ . Once magnetized, a very large field in the direction opposite to the magnetization is needed to overcome the anisotropy and reverse the magnetization. The anisotropy holds the magnetization very strongly in the easy axis, and so the coercivity of the system is large.

### *Strain-induced magnetic anisotropy*

The coupling between magnetism and lattice strain gives rise to magnetoelastic effect in bulk samples. Magnetoelasticity is the inverse effect of magnetostriction, where the rotation of the magnetization creates a mechanical strain. In thin films epitaxial strain can critically influence the magnetic anisotropy. In particular, strain state can modify the CF. For instance, for cubic materials, such as perovskites, strain may lead to a tetragonal distortion of the lattice. As we have already explained, in transition metal oxide the  $d$ -orbitals are fixed by the CF. Thus, orbital occupation can,



in some cases, be tuned by strain with a strong influence on the orbital momentum  $\vec{L}$  of the unpaired electrons and change the SOC interaction, and consequently the magnetocrystalline anisotropy. Then, it is interesting to understand how the strain affects the magnetocrystalline part. Indeed, the way in which epitaxial strain can affect the magnetocrystalline anisotropy has been an intense subject of research. A prominent example of such investigations is the spinel compound  $\text{CoCr}_2\text{O}_4$ , which has a strong magnetostriction coefficient. In  $\text{CoCr}_2\text{O}_4$  thin films, it was proved that changing the sign of the strain leads from cooperation to competition of shape and magnetocrystalline anisotropies. Figure 1.8 has been reproduced here from Ref. [33] for comprehension.

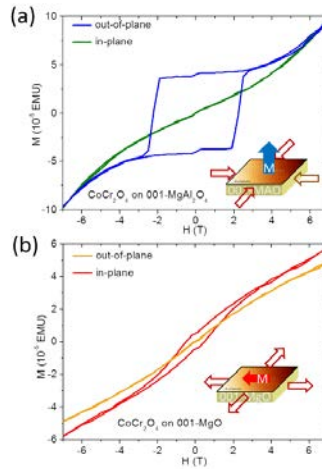


Figure 1.8: Magnetic hysteresis loops in the in-plane and out-of-plane direction of  $\text{CoCr}_2\text{O}_4$  on  $\text{MgAl}_2\text{O}_4$ , under compressive strain (a), and on  $\text{MgO}$ , under tensile strain. Figure reproduced from Ref. [33])

## 1.6 CHARGE CARRIER TRANSPORT PHENOMENOLOGY

### 1.6.1 *Magnetoresistive effects*

Magnetoresistance (MR) is a phenomenon that reflects the change of resistivity of a material when a magnetic field is applied:

$$MR(\%) = \frac{\rho_0 - \rho_H}{\rho_H} \times 100 \quad (1.8)$$

where  $\rho_0$  and  $\rho_H$  are the resistivities in the absence and presence of magnetic field, respectively. However, the effect in normal metals is usually very small, and does not have a technological application [11].

A bit larger magnetoresistive effects, of around 5%, were observed in ferromagnetic metal alloys of Ni-Fe and Ni-Co, in these cases, due to variations on the direction of the applied magnetic field [34]. This effect is known as anisotropic magnetoresistance (AMR) and accounts for an anisotropic resistance that depends on the orientation of the magnetic moments of ions in the system with respect to the electric current direction. The phenomenon originates from SOC interactions and was first reported by Lord Kelvin in 1856 [35]. Nevertheless, it was not until the discovery of giant magnetoresistance (GMR) in metallic multi-layers and colossal magnetoresistance (CMR) in perovskite manganites around 1990s that the study of MR effects became a field of major interest. Nowadays magnetoresistive materials are used in a great number of technologies, such as magnetic sensors, magnetic memories, and as the read head in magnetic recording structures.

In the next sections we describe some magnetoresistive phenomena, putting emphasis in the ones important for the understanding of the content of this thesis. Firstly, GMR and CMR are briefly revised. Then we present magnetoresistive effects that appear in metallic-insulator thin film systems such as TMR and TAMR.

### *Giant Magnetoresistance*

GMR was first discovered in 1988 in Fe-Cr-Fe superlattices which alternate FM with NM metals [36, 37]. It is defined as the ratio:

$$GMR = \frac{R_{\uparrow\downarrow} - R_{\uparrow\uparrow}}{R_{\uparrow\uparrow}} \quad (1.9)$$

Low resistance is found for parallel alignment ( $R_{\uparrow\uparrow}$ ) of the FM layers and high resistance for antiparallel alignment ( $R_{\uparrow\downarrow}$ ). A negative MR change around 20-50 % was observed in Fe-Cr multilayers [36, 37]. The orientation of magnetization is controlled, for example, by applying a magnetic field and fixed by given parameters as the thickness of the layers. For the discovery of this effect Fert and Grünberg obtained the 2007 Nobel Prize in Physics. The greatness of this phenomena lies in the fact that it enables to sense external magnetic field strengths in electrical magnitudes in between the two electric states of resistance. It was rapidly exploited technologically as the base of magnetic field sensors and hard-disk read-heads [38]. The origin of the effect is commonly attributed to the spin-dependent scattering that occurs in inhomogeneous systems. GMR was also found in granular systems and was described

as grains form ferromagnetic clusters embedded in a non-magnetic metal which interact forming a kind of superlattice [39].

### *Colossal Magnetoresistance*

CMR is an extremely large MR typically found in mixed-valence manganite perovskites where a transition to a FM state is accompanied by a transition to a metallic state or by a large reduction of the resistivity. CMR occurs near the paramagnetic-to-ferromagnetic transition due to the shift of  $T_C$  under a magnetic field. The larger values of CMR reported correspond to field-induced transitions from AF-insulating to FM-metallic states. Although large MR values in manganites were firstly reported in 1970 in (LaPb)MnO<sub>3</sub> compound [40], it is not until the 90s that the study of CMR in manganites became exhaustive [41–43]. The term CMR was introduced to distinguish the MR found in manganites from GMR observed in transition metal structures in multilayer or granular forms. An example is the case of La<sub>1-x</sub>Sr<sub>x</sub>MnO<sub>3</sub> ( $x=0.175$ ) depicted in Figure 1.9. The origin of CMR is quite different than in GMR. CMR effect is not related to a multilayer structure whereas it is an intrinsic property of materials.

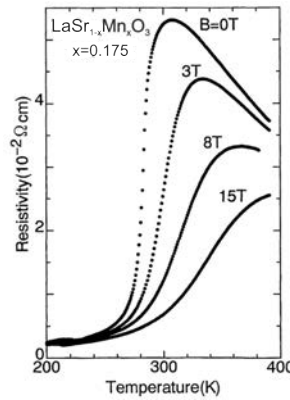


Figure 1.9: Colossal magnetoresistance (CMR) behaviour for the La<sub>1-x</sub>Sr<sub>x</sub>MnO<sub>3</sub> ( $x=0.175$ ) crystal. Figure reproduced from Ref. [44].

### *Tunneling Magnetoresistance*

Conventional MTJs consist of a non-magnetic insulator (NM-I) sandwiched between two ferromagnetic metals (FM-M). The resistance of the junction depends on the relative alignment of the magnetic moments of the ferromagnetic electrodes, phe-

nomenon known as TMR. The orientation of magnetization can be changed by applying a magnetic field. Then TMR, in analogy with GMR, is defined as the relative difference between the resistance of the system when ferromagnetic electrodes are aligned parallel or anti-parallel.

$$TMR = \frac{R_{\uparrow\downarrow} - R_{\uparrow\uparrow}}{R_{\uparrow\uparrow}} \quad (1.10)$$

One way to interpret TMR is by Jullière's model. The density of states at the Fermi level of magnetic materials,  $N_i(E_F)$ , is spin dependent resulting in an unequal filling of the bands for spin-up and spin-down electrons, one being the majority and the other the minority charge carrier electrons. Then the spin polarization can be defined by Jullière's formula as:

$$P_i = \frac{N_{i\uparrow}(E_F) - N_{i\downarrow}(E_F)}{N_{i\uparrow}(E_F) + N_{i\downarrow}(E_F)} \quad (1.11)$$

where  $N_{i\uparrow(\downarrow)}(E_F)$  is the density of spin-up (spin-down) states at the Fermi level.

Then TMR can be also expressed as function of spin polarization of the electrodes:

$$TMR = \frac{2P_1P_2}{1 - P_1P_2} \quad (1.12)$$

It is worth noting that the most successful approach to obtain large TMR ratios will be through coherent tunneling between half-metallic electrodes [45].

### *Tunneling Anisotropic Magnetoresistance*

In magnetically anisotropic systems the resistance of the tunneling junction can depend on the magnetization direction of each ferromagnetic layer. This effect is known as TAMR and measures the dependence of the magnetoresistance on the orientation of the magnetization with respect to the crystallographic axes [4, 5, 46]. We define TAMR ratio as:

$$TAMR(\theta) = \frac{R(\theta) - R(\theta_{min})}{R(\theta_{min})} \quad (1.13)$$

where  $\theta$  is the position of the sample with respect to the magnetic field and  $\theta_{min}$  the angle where the resistivity is minimum.

SOC is a source of TAMR. The analogue effect in bulk is the above mentioned AMR, but in tunneling junction can be highly enhanced as SOC effects can be much significant at the interfaces and have a larger contribution [47]. The effect was initially described in magnetic semiconductors and tunneling junctions with FM metal electrodes [48, 49]. TAMR, unlike TMR, can also be found in tunnel structures with only

one magnetic component. It has been measured in structures where only one of the electrodes is ferromagnetic [50, 51], and in this thesis we will show that it can be measured in a device with a FM-I barrier as the only magnetic component.

Moreover, TAMR in thin film systems can be found in two different configurations depending on the plane in which the magnetization is rotated. In-plane (IP) configuration is defined for the magnetization rotating parallel to the sample surface (renamed  $\phi$  in Figure 1.10) and out-of-plane (OOP) when magnetization is rotated within the angle between surface plane and the normal direction.

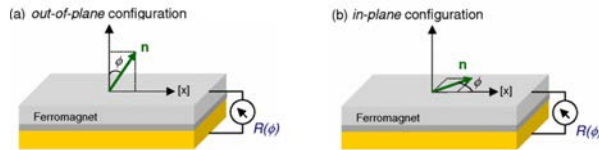


Figure 1.10: Schematic of OOP (a) and IP (b) configurations used for measuring TAMR in a MTJs with just one ferromagnetic layer.  $x$  is the reference crystallographic axis and  $z$  the normal axis,  $\vec{n}$  indicates magnetization orientation. Figure reproduced from Ref. [46].

### 1.6.2 Spin filtering

Spin filtering consists in spin selective tunneling through a magnetically active barrier sandwiched between two metals. As schematically depicted in Figure 1.11, the barrier height is sensitive to spin orientation and, due to exchange splitting, two different barrier heights for spin-up and spin-down electrons,  $\Phi_{\uparrow}$  and  $\Phi_{\downarrow}$ , will be formed.

The current density of spin-up and spin-down electrons depends exponentially on the barrier height [52]:

$$J_{\uparrow(\downarrow)} \propto e^{-d\sqrt{\Phi_{\uparrow(\downarrow)}}} \quad (1.14)$$

As a consequence, a small difference in barrier height results in very efficient spin selection, and the tunnel current can become spin-polarized even for nonmagnetic electrodes. Therefore spin-filtering efficiency (or polarization) of the tunnel barrier can be expressed as:

$$P = \frac{J_{\uparrow} - J_{\downarrow}}{J_{\uparrow} + J_{\downarrow}} \quad (1.15)$$

A spin-filter tunnel barrier is sandwiched between two metal electrodes. If the counter-electrode is magnetic and magnetically decoupled from the magnetic insulator spin polarization can be directly detected using TMR measurements. The

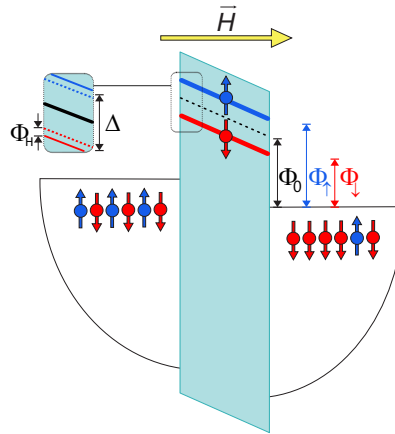


Figure 1.11: Schematic diagram of the spin filtering effect. Electrons with randomly oriented spins tunnel from the Fermi level of the metal through the spin-selective barrier resulting in a highly spin-polarized current.  $\Phi_0$  is the mean tunneling barrier which is split into  $\Phi_\uparrow$  and  $\Phi_\downarrow$ . In the zoom,  $\Delta$  is the exchange splitting and  $\Phi_H$  is the additional splitting of the barrier under an applied magnetic field.

method consist in collecting the transmitted current with the ferromagnetic electrode while playing with respective coercive fields of the magnetic elements. If the FM-I is a harder magnet than the FM electrode, the electrode can be flipped with a small magnetic field after fixing polarization of the FM-I with a higher magnetic field. Spin polarization can be extracted through Jullière's formula:

$$TMR = \frac{2P_{electrode}P_{barrier}}{1 - P_{electrode}P_{barrier}} \quad (1.16)$$

Then the total current density depends on the relative orientation of the magnetization direction in the spin-filter barrier and in the magnetic electrode. For parallel alignment, there are empty states available for the majority spin electrons that experience the lower barrier height, leading to a large tunnel current and a low barrier resistance. For antiparallel alignment, there are more states available for the minority spin electrons, but due to the larger barrier height, the tunnel current is substantially reduced and the resistance is high. The Meservey-Tedrow technique is another method to measure the spin polarization. It uses a superconducting counter-electrode instead of a ferromagnetic metal as spin detector [53]. In an applied magnetic field, the junction conductance as a function of bias voltage reveals the unequal densities of spin-up and spin-down electrons states as an asymmetry in the conductance-voltage curve [54], from which the spin polarization can be inferred. However this technique is limited to very low temperatures.

### *Two-current model*

If the electrodes are non-magnetic spin-filtering efficiency can be estimated using the two-current model. This model assumes two differentiated tunneling channels for the spin-down and spin-up electrons and an additional splitting of the bands due to a Zeeman term when an external magnetic field is considered. This method has been used in systems such as  $\text{Fe}_3\text{O}_4/\text{Nb}:\text{SrTiO}_3$  and  $\gamma\text{-Fe}_2\text{O}_3/\text{Nb}:\text{SrTiO}_3$  [55–57]. In these works they use two-current model to treat the magnetic field dependence of the tunneling current through the Schottky barrier formed at metal-semiconductor contacts systems.

According to two-current model spin-down and spin-up conduction bands of the insulating barrier lie at different energies due to the exchange splitting. When a magnetic field is applied those energies change in opposite directions and the tunneling barrier must be described as:

$$\Phi_{\uparrow(\downarrow)} = \Phi_0 \pm \Delta/2 \pm \Phi_H \quad (1.17)$$

where  $\Phi_0$  is the average barrier height,  $\Delta$  is the exchange splitting of the conduction band, and  $\Phi_H$  accounts for the effect of magnetic field on this band (see Figure 1.11). Note the exchange splitting is much larger than the Zeeman field.

Describing an spin-dependent barrier, we can determine spin-up and spin-down current densities from magnetotransport curves, and using an adequate expression for the current density, generally described in eq. 1.14, estimate the spin filtering efficiency using eq. 1.15.

## 1.6.3 *Transport mechanisms*

MTJs in MRAM and Resistive switching (RS) memory cells in RRAM are commonly built in metal-insulator-metal (MIM) or metal-insulator-semiconductor (MIS) structures. Transport in these structures are usually interpreted either by a tunneling current or by a Schottky thermionic emission current models [58]. In the next section we will present the theoretical basis for the understanding of the main mechanisms of transport in tunnel junction and RS systems.

### 1.6.3.1 *Tunnel junctions*

Tunnel junctions are the main building blocks for spintronic devices. Tunnel barriers in MIS structures are useful to avoid the conductivity mismatch between electrodes that diminished the effectiveness when injecting and detecting spin-polarized current [59]. The study of  $I$ - $V$  characteristics of this type of structure is important for

understanding spin dependent transport phenomena studied in this thesis. In this section we focus on explaining the basis of transport in MIS system interpreted through thermionic-field emission theory.

Transport through a barrier will occur in two possible ways: carriers surmounting the barrier by thermal activation or by tunneling through it. These mechanisms are known as thermionic emission and field emission, respectively [60, 61]. For simplicity, to build a qualitative picture, we consider a metal/semiconductor interface. Then current density in thermionic emission ( $J_{TE}$ ) is described as:

$$J_{TE} = J_s \left[ \exp \left( \frac{eV}{nk_B T} \right) - 1 \right] \quad (1.18)$$

where  $e$  is the electron charge,  $V$  the applied voltage,  $k_B$  the Boltzmann constant,  $T$  the temperature,  $n$  the ideality factor and  $J_s$  is the saturation current expressed as:

$$J_s = A^* T^2 \exp \left( \frac{-q\Phi_0}{k_B T} \right) \quad (1.19)$$

where  $A^*$  is the Richardson constant, and  $\Phi_0$  is the barrier height.

On the other hand, current density for field emission ( $J_{FE}$ ) is expressed as:

$$J_{FE} = J_s \left[ \exp \left( \frac{eV}{E_{00}} \right) - 1 \right] \quad (1.20)$$

$E_{00}$  is the characteristic energy at 0 K. It represents transmission probability of an electron from the bottom of the conduction band. It is defined as

$$E_{00} = \frac{\hbar}{2} \sqrt{\frac{N_D}{m^* \epsilon_S}} \quad (1.21)$$

$\hbar$  is the Planck constant,  $N_D$  is the doping density,  $m^*$  is the effective mass of the electrons and  $\epsilon_S$  the dielectric constant.

Hence,  $E_{00}$  is a parameter that enables to differentiate transport regimes. If it is compared with thermal energy  $k_B T$ , when  $E_{00} \gg k_B T$  pure tunneling occurs, thus field emission dominates. When  $E_{00} \ll k_B T$ , is dictated by the Schottky barrier with thermionic emission prevailing. Then when  $E_{00} \sim k_B T$  thermionic-field emission dominates which refers to the tunneling of thermally excited carriers.

In addition, tunneling conduction process strongly depends on the bias voltage. At low voltages it is described as direct tunneling. Field emission, which corresponds to high voltages regimes, is described by Fowler-Nordheim tunneling (FNT) formalism. So the tunneling current density will follow the next equation [63]:

$$J_{FNT} = \frac{e^3 V^2}{8\pi \hbar t^2 \Phi_0} \exp \left( -\frac{t}{V} \frac{8\pi \sqrt{2m^*} \Phi_0^{\frac{3}{2}}}{3eh} \right) \quad (1.22)$$



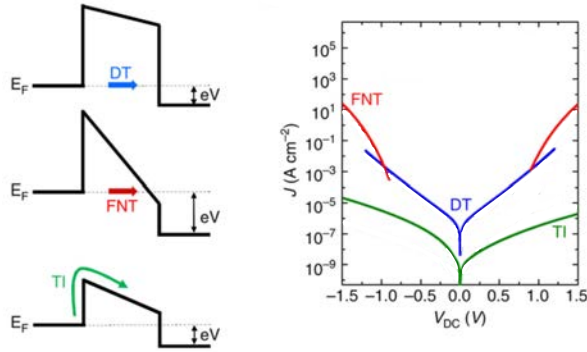


Figure 1.12: (*Left*) Diagram of three possible transport mechanisms through ultrathin barrier: direct tunnelling (DT), Fowler-Nordheim tunnelling (FNT) and thermionic emission (TE). (*Right*) Current densities ( $J$ ) versus voltage ( $V_{DC}$ ) of the contributions from DT, FNT and TI through an insulating barrier. Figure adapted with permission from Ref. [62]

where  $\Phi_0$  is the barrier height,  $h$  is the Planck constant and  $t$  is the barrier thickness.

Each transport mechanism can be identified through temperature or voltage dependencies. In particular, thermionic emission is a thermally activated process that should lead to strong variations with temperature, while field emission should be constant with temperature variations. For its part, FNT current will have a particular dependence as  $\ln \frac{J}{V^2} \propto V^{-1}$ . This approach will be more deeply analyzed and applied in chapter 5.

#### 1.6.4 Resistive Switching

Resistive switching (RS) refers to a voltage-induced change in the resistance state of the so called memristive devices, where the state of internal resistance can be retained until another electrical pulse with particular characteristics is applied. Memristive devices have great potential for non-volatile memories as they can be scaled down to less than 10 nm and offer fast and low-energy electrical switching [64]. The most simple RS device is a two-terminal MIM or MIS structure and typically the sandwiched layer between the electrodes is an oxide. Conventionally, RS implies high to low resistance transition and requires an initial step of electroforming to activate the switching property. There are particular cases, as in the case of manganites, where the initial state is conductive and the switching leads to a high resistance state without the need of an electroforming process.

In the basis of  $I$ - $V$  characteristics, the switching operation mode can be bipolar or unipolar. As depicted in Figure 1.13a-b, bipolar switching requires opposite volt-

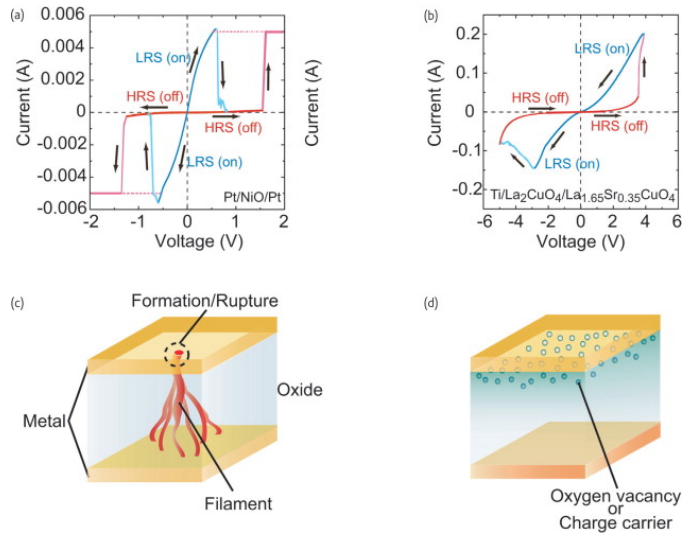


Figure 1.13:  $I$ - $V$  curves for (a) unipolar switching in a Pt/NiO/Pt cell and (b) bipolar switching in a Ti/La<sub>2</sub>CuO<sub>4</sub>/La<sub>1.65</sub>Sr<sub>0.35</sub>CuO<sub>4</sub> cell. In unipolar switching, the switching direction depends on the amplitude of the applied voltage. Bipolar switching depends on the polarity of the applied voltage. Mechanisms for RS can be classified according to their conducting path either (c) a filamentary, or (d) an interface-type. Figure reproduced from Ref. [65].

age polarities to switch between ON (set) and OFF (reset) states, whereas unipolar switching can be induced with both voltage polarities (it only depends on the amplitude of the applied voltage). The type of switching depends on the material but principally on the structure of the device: asymmetric electrodes typically lead to bipolar cases.

The different RS mechanisms have been a matter of intense discussion and there is not a unequivocal theory of the origin of the underlying mechanisms. It seems that each kind of material has its own. Still it is widely accepted that the mechanism behind RS in transition metal oxides is a redox reaction, induced by oxygen-ion migration [64–67].

To simplify a plausible picture to understand the effect, TMO-based switching can additionally be classified in terms of the conducting paths: filamentary or interface-type (see Figure 1.13c-d). Filamentary-type occurs in insulating materials and requires the formation/rupture and reconstruction of conducting filaments of metallic cations or oxygen vacancies (more likely in TMO). Filaments are localized channels with lower concentration of oxygen that enable electrical conductivity between two electrodes. Oxidize cations from the electrode or oxygen vacancies are able to migrate through the conduction filaments towards the other electrode that becomes

reduced. On the other hand, interface-type switching emerges at the oxide/electrode interface. The accumulations of oxygen vacancies at the metal/oxide interface act as donor dopants. The resulting local dopant distribution modifies the Schottky barrier at the interface with the top electrode and leads to a low resistance (LR) state. The reset process consists in recovering the high resistance (HR) state with opposite bias by reoxidizing the switching area. As a consequence, oxygen concentration is modulated along the thickness of the resistive layer and across the whole electrode area. To distinguish between these two types of RS one can consider the area dependence of the cell resistance. Filamentary switching, due to its local nature, is not dependent on the area of the electrode while interface-type leads to a more uniform effect that scales with electrode area.

Focusing on RS in the LSMO system [68–70], the underlying effect cannot be based on dielectric breakdown via the formation of conducting filaments as LSMO is a conducting oxide. Nowadays, the most plausible mechanism to explain RS in LSMO-based cells is the electric-field driven migration of oxygen vacancies occurring primarily at the interface [67]. It is discussed for other manganite systems that the consequent formation of an interfacial transition oxide layer between a reactive metal electrode and an insulating or conducting oxide is the key component for RS [71–74].

Recently, numerous local spectroscopies [67] as well *in-situ* transmission electron microscopy (TEM) [75] have emerged as powerful techniques for the analysis of structural features and redox processes following the application of voltage pulses. A glaring example of direct observation of RS switching in LSMO thin films has been published by Yao *et al.*. They give evidence that the resistive transition originates from a reversible horizontal migration of oxygen vacancies within the manganite film, driven by combined effects of Joule heating and bias voltage, that finally triggers a structural transition to brownmillerite phases [75]. Indeed, LSMO with a brownmillerite structure consists in a superstructure with ordered oxygen vacancy planes and is a mixed ionic-electronic conductor whose resistance, at room temperature, tends to be higher than that of the original perovskite structure.

## EXPERIMENTAL TECHNIQUES

---

This chapter includes a brief explanation of the experimental techniques used in this thesis that include thin film growth, morphological, structural, compositional and physical properties characterization.

### 2.1 RF MAGNETRON SPUTTERING

Manganite epitaxial thin films studied in this thesis have been grown using radio-frequency (RF) sputtering technique. Sputtering is a deposition method classified as a physical vapor technique together with pulsed laser deposition (PLD) or molecular beam epitaxy, in which chemical species are physically evaporated by means of ion bombardment. It is advantageous in terms of large area coverage and wide range of available materials. Hence, it is one of the preferred techniques for growing high quality thin films for industrial use. Sputtering consists in ejecting components from a target source of the desired material onto a substrate (see Figure 2.1). Substrates are placed in a vacuum chamber and evacuation of gases is firstly conducted. In our sputtering we operate at a vacuum level around  $10^{-6}$  Torr.

Secondly, high purity gases as oxygen and argon are introduced at a controllable pressure. Complex oxides films can be grown at a wide range of oxygen pressures from very low  $5 \cdot 10^{-3}$  Torr to high as 0.5 Torr. In particular, for the growth of manganite thin films, high oxygen pressure are used (190 mTorr for LSMO and 400 mTorr for LCMO) which enable low growth rates, so the control of very small thicknesses. So, when a constant flow of gas is reached, a plasma with positively charged oxygen (or argon) ions is created by the application of a high negative voltage (of hundreds of volts) to a target material. Oxide material target are dense ceramic pellets of 1.3" which are often attached to the backside of a magnetron. This consist in an arrangement of permanent magnets that can create a magnetic field near the target surface that confine the plasma, increase the probability of collision of the ions and accel-

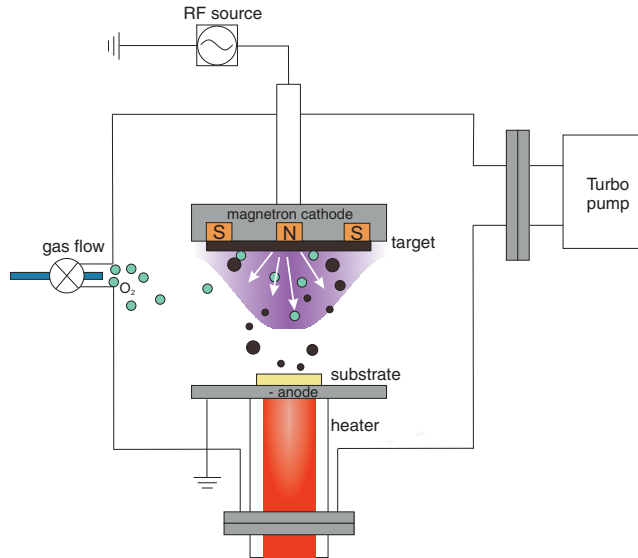


Figure 2.1: Schematic of a sputtering system.

erates them against the cathode. This greatly increases the efficiency of sputtering achieving high degrees of ionization even for very low pressures.

Therefore, a plasma is created by the application of a high voltage between the anode beneath the target and the cathode behind the substrate, formed by accelerated positively ionized atoms of the chamber gas up to kinetic energies of 0.1-1 keV [76]. Then, momentum of these ions is transferred to the atoms at the surface of the target material atoms are ejected. The ejected particles expand away, with high kinetic energies of several eV, until they are deposited on the surface of the substrate. The deposited atoms and molecular are sometimes trapped at a local minimum energy state rather than lying at a global minimum state. This can lead to the formation of metastable phases [77].

The plasma is stoichiometrically similar to the target, one can achieve thin films of practically the same composition as the target. If the target is insulating, an accumulation of charges can appear on its surface. For this reason, for oxides and/or insulators a RF power supply is used. For conducting materials, as metal coatings, DC voltage is more adequate. In RF, during part of the cycle, oxygen ions bombard the target and for the rest of the cycle, electrons neutralize the build up of positive charge.

In general, for epitaxial growth of crystalline structures, substrates are previously heat to temperatures around 700-900°C. Such high temperature assures high diffusivities for the ions on the surface, yielding an ordered growth process of the films. Finally, after sputtering step an *in-situ* post annealing treatment in high pressure

oxygen atmosphere is commonly carried in order to achieve the correct oxygen stoichiometry in the deposited material. At high temperatures, the ease of diffusion of oxygen ions in the crystal enables to reach thermal equilibrium between the sample and the atmosphere at certain  $p_{O_2}$ .

## 2.2 SCANNING PROBE MICROSCOPY

Atomic force microscopy (AFM) is a powerful technique for characterizing surface properties of materials within a range from few nanometers to hundreds of micrometers. AFM was invented by Binnig, Quate and Gerber in 1986 [78]. Resolution of the order of the ångström can be achieved in the vertical scale. The lateral resolution is limited by the convolution with the tip but less than tens of nm can be reached. Nowadays, the technique enables to detect several kinds of interactions such as van der Waals forces, capillary forces, chemical bonding, electrostatic forces, magnetic and electrical forces, electromechanical responses, etc. [79].

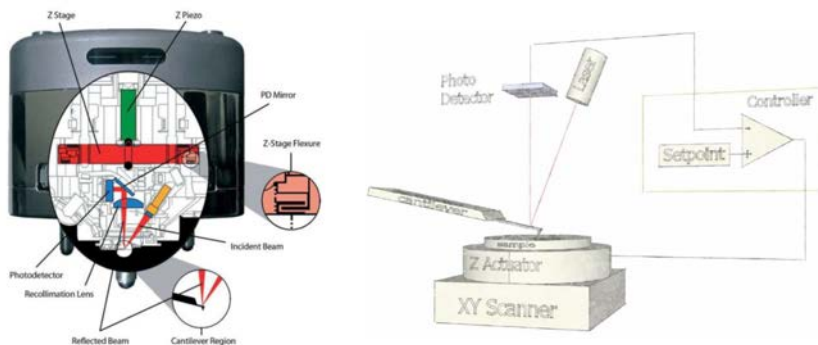


Figure 2.2: (left) Schematic illustration of an AFM head (Asylum Research MPF-3D) and its working principle (right). The Z-piezo adjust the tip-sample distance in order to keep cantilever deflection/oscillation amplitude at a given setpoint. Figure reproduced from Ref. [80].

The basic operating principle for AFM consists of a physical probe that is scanned over a sample mapping out the surface topography in three dimensions. The probe consists of a silicon or silicon nitride cantilever with a sharp integrated tip at one end. The vertical bending (deflection) or lateral bending (torsion) of the cantilever due to forces acting on the tip is detected by a laser focused on the metallic back side of the cantilever. The laser is reflected by the cantilever onto a four sectors photodetector. The movement of the laser spot on the photodetector gives a measurement of the movement of the probe. The probe is moved over the sample by a XYZ scanner,

typically a piezoelectric element, which can make extremely precise movements. The detected signal is controlled by means of an electronic feed back on the Z-piezo that compares the signal at each point with a pre-established set-point value. If they are not equal, a voltage is applied to the scanner in order to move the probe either closer to or farther from the sample surface to bring the error signal back to zero.

The combination of the sharp tip, the very sensitive optical lever, and the highly precise scanner, combined with the careful control of probe-sample forces by a feedback electronics provides the extremely high resolution and sensitivity of the AFM.

The original measuring mode, the so-called contact mode, is based in monitoring of the deflection of the cantilever due to repulsive/attractive forces. Later on, dynamic AFM modes were developed in which the cantilever is used as a mechanical resonator and brought to oscillate very close to the surface. Interactions of the resonator probe with the surface lead to changes in the amplitude, phase, and frequency of the oscillation. These changes are used as imaging parameters.

Simultaneously with the acquisition of high-resolution images of surface topography, secondary or even a ternary signal can be measured revealing other properties of the sample. Some examples are compositional mapping of laterally heterogeneous surfaces or local electromechanical, electrical and magnetic properties. Each of the measuring modes used in this thesis is briefly introduced here.

In this thesis AFM experiments have been performed with an MFP-3D AsylumResearch AFM (Oxford Instruments) for the majority of measurements and an Attocube for MFM measurements at low temperature

### 2.2.1 *Contact mode. Friction Force Microscopy*

In contact AFM, topography images are achieved from accurate measurement of the deflection of the cantilever at each position. Every elevation on the sample causes the tip to move up and bend the cantilever upward and every depression makes the cantilever move down. As schematized in Figure 2.2, the diode records vertical changes with respect to an initial pre-defined deflection point (the setpoint). Then, the original deflection of the cantilever is restored via a feedback loop by motion of the scanner in the  $z$  direction. The changes in the scanner position are recorded and used as the topography image.

When the tip is brought into close proximity to the sample surface, the cantilever bends up due to repulsive interactions. If the bending of the cantilever is  $z$ , then the force exerted on the sample surface follows Hooke's law  $F = -kz$ , where  $k$  is the spring constant of the cantilever. The force exerted by the cantilever can take values from 1 nN to several  $\mu\text{N}$ . Typically, for contact mode AFM imaging, soft cantilevers

with spring constant in a range within 0.01-10 N/m are used to prevent sample damage while scanning.

### Friction Force Microscopy

Commonly, the photodiode consist in four quadrants, allowing the detection of the longitudinal bending as well as the lateral torsion of the cantilever. Therefore, when scanning in contact mode, in addition to cantilever normal deflection (topography), the cantilever torsion caused by friction can be monitored as a lateral deflection of the reflected laser beam in a secondary channel.

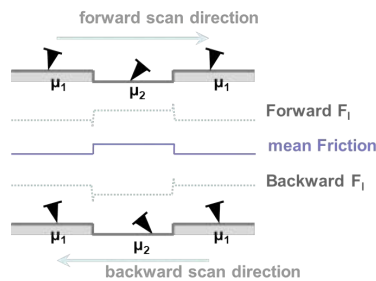


Figure 2.3: Schematics of mechanism of formation of friction image by subtracting lateral force backward scan line from forward scan line.

In this case, the laser beam moves sideways and by comparing the signals from the right and left segments of the photodiode, a map of the friction can be derived. The local friction signal is defined as half the amplitude of the so-called friction loop,  $F = 1/2[F_l(\text{forward}) - F_l(\text{backward})]$  where  $F_l$  is the lateral force signal for forward and backward scans (see Figure 2.3). Applying this line by line procedure to the lateral force images, a friction map is derived. This mode, also known as Friction Force Microscopy (FFM), is useful to highlight differences in composition of diverse surface regions [81].

#### 2.2.2 Amplitude Modulation AFM. Phase lag

Amplitude modulation AFM (AM-AFM) is a dynamic intermittent-contact technique commonly known as *tapping* mode. It maps topography by slightly tapping the surface with an oscillating probe.

The cantilever is mechanically excited at a frequency close to its resonance frequency ( $f_{res}$ ) with a free oscillation amplitude ranging between 5 and 100 nm [82].



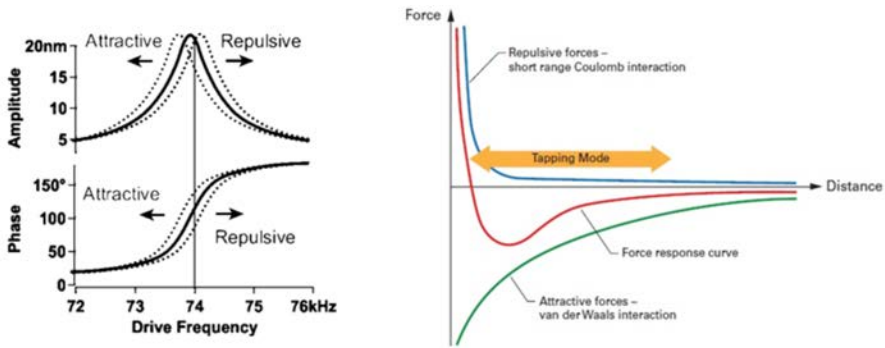


Figure 2.4: Force dependence on tip-to-sample separation distance.

At resonance the harmonic oscillator is very sensitive to perturbations. As depicted in Figure 2.4, in response to tip-sample interactions,  $f_{res}$  (and as a consequence the amplitude and phase) of the cantilever shifts: amplitude and  $f_{res}$  decrease if the interaction is attractive and increase if its repulsive. Shifts will be used as measurement parameters for acquiring images.

In AM-AFM, one uses a fixed amplitude as a setpoint, so the error signal of the amplitude monitored by the photodiode is used as feedback loop to adjust the tip-sample distance. Thus, one can obtain topography, amplitude and phase lag images. Cantilevers for *tapping* typically have spring constants within a range of 10-100 N/m and resonant frequencies of 100-500 kHz. As the cantilever resonant frequency goes up, they get stiffer and have a higher quality factor,  $Q$ . Higher  $Q$  provides greater amplitude amplification and better frequency discrimination for small shifts [83].

Depending on the amplitude of the probe oscillations, the tip-sample interaction will range over a wide distribution of forces, from attractive to repulsive forces (see the force-distance-to-surface dependence depicted in Figure 2.4). What one measures is thus a convolution of the force-distance curve with the oscillation trajectory. The interpretation of AM-AFM measurements is complicated as they cannot be converted to a force-distance curve and numerical simulations are required to a better understanding of the complex relationship between forces and oscillation parameters. Although AM-AFM is not suitable to obtain quantitative information of tip-sample force interaction, a qualitative interpretation is possible thus, the technique appears very useful for imaging exerting minimal damage on the sample.

### 2.2.2.1 Phase lag

Phase imaging consists in mapping the phase lag of the cantilever oscillation relative to the external driving oscillation [84]. Phase lag is a useful tool to distinguish different materials in heterogeneous samples which present, for example, variation in the composition. However, composition changes are only interpretable as phase shifts in repulsive mode regime. In repulsive mode, different materials will produce changes in the tip oscillation due to unequal adhesion, friction or viscoelastic forces [85]. These changes can be indistinct in the amplitude signal but produce large in the phase contrast due to the sharpness of the phase signal, when transiting between attractive and repulsive regime regions.

### 2.2.3 Conductive AFM

When using a conductive tip in the contact AFM mode, one can simultaneously map the topography and measure the current distribution over the sample surface. Thus, Conductive atomic force microscopy (C-AFM) is technique to characterize local variations of electrical properties in resistive samples. In C-AFM the topography information is completely separated from the electrical part. Topography maps are acquired using the deflection of the cantilever as the monitoring parameter while the electric conductivity is measured through an electric current amplifier attached either to the conducting tip or to the sample. Apart from 2D current images, one can perform  $I$ - $V$  characteristic curves at specific points of the sample surface which give greater insight of the transport properties of materials revealing the corresponding behaviours: ohmic, Schottky barriers, resistive switching behaviours, etc.

In this thesis measurements are performed using an MFP-3D Asylum Research AFM (Oxford Instruments) system equipped with an ORCA module with a specially-designed cantilever holder that encloses two different amplifiers (one with a gain of  $10^9$  V/A and another of  $10^6$  V/A).

The tip is brought into contact with the surface at a prefixed load and a bias voltage ( $V_{Bias}$ ) is applied between the conductive AFM tip and the sample. For  $I$ - $V$  curves the voltage is ramped to a pre-set value and with a certain rate. In our measuring set-up the  $V_{Bias}$  is applied directly to the sample and, as the tip is mounted in a virtual ground, a potential difference between the tip and sample equal to the applied  $V_{Bias}$  value is produced. The sample is usually mounted on a sample holder using conductive silver paste to ensure good electrical contact.

Transport measurements based on the use of a conductive AFM tip as a top electrode are strongly affected by the conductive tip properties and the contact resistance. One seeks to have a tip-sample electrical contact as small and stable as possi-

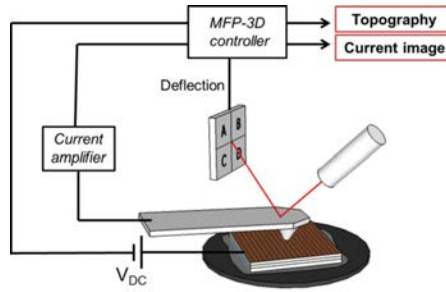


Figure 2.5: Schematics of C-AFM experimental setup in the AFM system in our laboratory.

ble. For semiconductor samples, a Schottky barrier between the semiconductor surface and the metallic tip appears, and strongly depends on the work function of the metal used for the conductive coating. There are various available conductive probes for C-AFM. Metal-coated probes with coatings made of PtIr, TiN, Au and probes with conductive diamond coating (B-doped diamond) are the most commonly used tips for the technique. Wear resistance and quality of conduction, thus low resistivity, are the most important aspects for the choice of the tip. Metal-coated probes present lower resistivity but higher ease to wear while diamond-coated tips show higher resistance to wear but also higher electrical resistivity, of the order of tens of  $k\Omega$ . Moreover, the radius of curvature is smaller for metal-coated tips (typically 35 nm compared to 100 nm for diamond-coated probes [86]) so they provide better lateral resolution.

## 2.2.4 MFM

In MFM, probes coated with a ferromagnetic or a superparamagnetic material are used. Then one measures the stray field generated from the sample that couple with the magnetic coating of the cantilever via the magnetostatic interaction. Generally, MFM is a two-pass technique (see Figure 2.6). In the first pass the surface is scanned in AM-AFM mode to measure surface topography. The tip is kept close to the sample, so that the tip-sample interaction is dominated by short-range interactions, and the tip measures topography rather than longer-range interactions. In the second pass the topography signal from first pass is used to control the Z-position (feedback loop on the amplitude is turned off, so the cantilever is in free oscillation), keeping the tip at a fixed height, generally further away from the surface. Here, tip-sample interaction is dominated by long-range forces, such as those arising from the electric or magnetic field of the sample. Thus, magnetic forces induces a phase shift of the can-

tiler resonance if the driving frequency is held constant. Phase shifts are directly related to the net force acting on the probe and by mapping them one obtains an image of the magnetic domain structure.

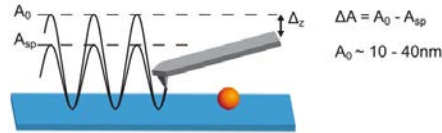


Figure 2.6: Sketch of second pass method for MFM imaging.

The shape of conventional cantilever tip favors magnetization to be perpendicular to the sample surface, hence, conventional cantilever tips are most sensitive to perpendicular fields generated from the sample. As depicted in Figure 2.7, samples with an in-plane magnetic configuration of domains will show only magnetic contrast at a domain wall where the magnetization partially or fully rotates out-of-plane. Perpendicularly magnetized samples, exhibit more direct imaging of up and down domains (black or white contrast in the Figure).

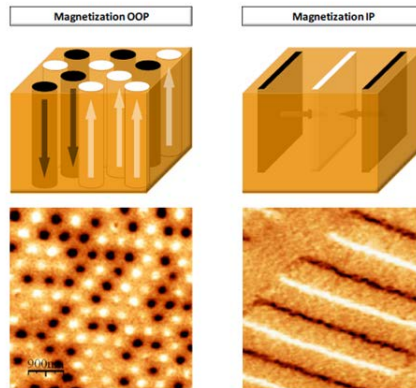


Figure 2.7: (left) Contrast observed when imaging samples with an OOP magnetization accounts for magnetic domains. (right) In the case of IP magnetization, it highlights the presence of domain walls (Figure reproduced from Ref. [87]).

## 2.3 STRUCTURAL AND COMPOSITIONAL CHARACTERIZATION TECHNIQUES

### 2.3.1 X-ray diffraction

X-ray diffraction is the most established method for structural analysis of thin film materials. It is useful to determine structural phases, the degree of epitaxy, film thickness, presence of parasitic phases and defects, structural distortion, etc. Diffraction technique uses low energy X-rays which interact with matter non-destructively. As these X-rays wavelengths (0.5-10 Å) are comparable with interatomic distances (1-4 Å), the scattered radiation from a periodic array of atoms composing a crystal will suffer interferences with itself. The coherent (or elastic) scattering leads to diffraction patterns from where one extracts the structural information.

In this thesis we present two types of XRD measurement:  $\theta - 2\theta$  scans and reciprocal space map (RSM). Measurements have been acquired at the Institut Català de Nanociència i Nanotecnologia (ICN2), using a PANalytical X'Pert Pro MRD diffractometer (Cu  $K_{\alpha}$  radiation). This diffractometer is composed by a four-circle goniometer as it is depicted the schematic in Figure 2.8.

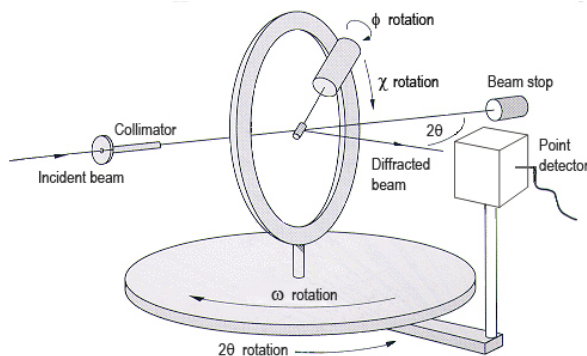


Figure 2.8: Schematic representation of four-circle goniometer. Figure reproduced from Ref. [88]).

In this scheme,  $\omega$  is the angle between the incident beam and the direction defined by the intersection between the surface and the diffraction plane (the diffraction plane is the plane defined by the incident and the diffracted beams).  $\chi$  is the angle formed between the diffraction plane and the normal to the surface. Also referred to  $\psi$  ( $\psi = 90^\circ - \chi$ ).  $\phi$  defines the rotation of the sample around the normal axis to the surface plane. Finally,  $2\theta$  is the relative angle between the incident beam and the diffracted beam.

Symmetric reflexions, for those where the incident beam is symmetric to the reflected one with respect to the normal to the surface, are easily measured with  $\theta - 2\theta$  scans. On the other hand, to be able to map asymmetric reflexions (not symmetric to the surface normal), one needs to play with  $\chi$  and  $\phi$  angles. For instance, RSM one can access to these reflexions by fixing one of this angles and scanning along another angle, normally  $\omega$ .

All measurement in this thesis were performed keeping the diffraction plane perpendicular to the film surface.

### 2.3.1.1 $\theta - 2\theta$ scan

$\theta - 2\theta$  scans are line scans in which the  $\omega$  angle is fixed to one half of the diffraction angle  $2\theta$ . These line scans are only able to detect diffraction produced by crystallographic planes parallel to the film surface. The corresponding reflections are called symmetric reflections and satisfy the Bragg's law:

$$n\lambda = 2d_{hkl} \sin \theta \quad (2.1)$$

where  $n$  is a positive integer defining the order of diffraction,  $\lambda$  is the wavelength of the characteristic X-ray beam,  $\theta$  is half of the dispersion of angle  $2\theta$ ,  $d_{hkl}$  the interplanar distance between the atomic planes defined by Miller indices  $(hkl)$ . The intensity of the diffraction peaks obtained by scanning over  $\theta$  can be related to Bragg's law to obtain interplanar spacing. If the film is single oriented, then the out-of-plane lattice parameter can be determined. As an example, (001)-oriented STO single crystals are one of the most employed substrates for epitaxial thin film growth. A  $\theta - 2\theta$  of a manganite film grown (001)-oriented on top of (001)STO will only give diffraction peaks in the (00l) reflections. Additionally, if films have a high degree of crystallinity and the sample is well aligned, depletion and boardening of the recorded peaks can give information about the strain state.

In this thesis, for high resolution  $\theta - 2\theta$  XRD data analysis, we have used the approach presented by Pesquera *et al.* in Ref. [89]. They propose that for an accurate description of the diffraction patterns, the superposition of the scattered waves by the substrate and film should be considered rather than a simple addition of intensities. Using this approach, accurate out-of-plane cell parameters and the thickness of the films can be extracted.

### 2.3.1.2 RSM

RSM measurements are useful to determine the in-plane and out-of-plane lattice parameter of films and to study degree of epitaxy and the influence of strain on the film. An RSM measurement is composed by successive  $2\theta$  scans for different  $\omega$  at a certain region around a selected diffraction peak. It usually requires a careful alignment of the sample around the substrate peak close to the film reflection.

In order to plot the diffraction peaks, a 2-D map is constructed with respect to the reciprocal space lattice vectors  $q_{\parallel}$  and  $q_{\perp}$ . Then, the positions in the reciprocal space for the chosen reflection are given by:

$$\begin{aligned} q_{\parallel} &= 2/\lambda \cdot \sin\theta \sin(\theta - \omega) \\ q_{\perp} &= 2/\lambda \cdot \sin\theta \cos(\theta - \omega) \end{aligned} \quad (2.2)$$

The cell parameters can be obtained from the position of the diffraction peak and the Miller indices of the reflection. As an example, in a tetragonal system, with lattice parameters  $a = b \neq c$ , the in-plane (normally,  $a$ ) and out-of-plane ( $c$ ) parameters can be calculated as:

$$\begin{aligned} a &= \frac{\sqrt{h^2 + k^2}}{q_{\parallel}} \\ c &= \frac{l}{q_{\perp}} \end{aligned} \quad (2.3)$$

### 2.3.2 Electron probe microanalysis

Electron probe micro-analysis (EPMA) is a widely used technique for determining the elemental composition of solid samples. It consists in bombarding a micrometer volume of a sample with a focused electron beam; then, the X-ray photons emitted by the various elements are collected by energy and dispersive spectrometers. EPMA instruments possess both wavelength dispersive spectrometers (WDSs) and energy dispersive spectrometers (EDSs). WDS detectors are the ones that confer the analytical power to the technique that enables accurate quantitative analysis. WDS identifies the emitted X-rays according to their wavelengths while EDS according to their energies. WDS gives much better spectral resolution ( $\sim 5$ - $10$  eV) than energy-dispersive spectroscopy ( $\sim 120$ - $130$  eV), however data collection is slower [90].

EPMA determines the concentration of the elements based on the intensities of the emitted X-rays. The results are commonly displayed as weight percentages of elements. First the entire energy spectrum is collected with EDS (or WDS) to identify the major elements contained in a specimen. Then quantitative analysis is performed with the WDSs. Each WDS contains diffracting crystals dedicated to a given

range of X-ray wavelengths. X-ray intensities for all the elements identified are compared with standards of known composition after correcting effects of fluorescence, absorption and atomic number.

## 2.4 MAGNETIC CHARACTERIZATION BY SQUID

Superconducting quantum interference device (SQUID) magnetometry is one of the most sensitive methods to measure magnetization. In particular, it allows direct determination the overall magnetic moment of a sample in absolute units. SQUID system used in ICMAB is a Quantum Design MPMS-XL. It enables to measure magnetic moments as small as  $10^{-6}$  emu with magnetic fields up to 9 Tesla and at temperatures between 2 and 380 K.

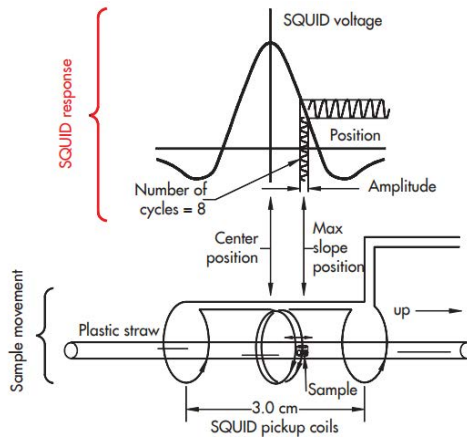


Figure 2.9: Schematics of SQUID magnetometer with longitudinal pickup coils. Reproduced from Ref. [91].

SQUID is mounted in a magnetometer with a sensor consisting in a superconducting ring with one or more Josephson junctions that act as resistive barriers that separate superconducting regions. The sensor is connected to a pickup coil with four windings (see Figure 2.9). When the sample is moved up and down it produces an alternating magnetic flux in the pick-up coil which leads to a small alternating output voltage when transferred to a flux-to-voltage converter. This voltage is then amplified and read out as a voltage that is proportional to the magnetic moment of the sample.

The magnetic properties of a material are commonly identified through magnetization *vs.* field and magnetization *vs.* temperature measurements. The magnetic moment of the film is then normalized by its volume to determine its magnetization.



It is typically measured in  $\text{emu}/\text{cm}^3$ . The signal of a thin film is generally weak (of the order of  $10^{-5}$  emu) and has a diamagnetic contribution coming from the substrate which is not negligible. When measuring hysteresis loops, the diamagnetic contribution gives a negative slope at high magnetic fields. This slope should be subtracted by adjusting the slope of the cycle at high fields. Sometimes saturation at high fields is not reached and diamagnetism cannot be accurately corrected. To solve this, an hysteresis loop over critical temperature can be measured and use the resulting slope to do the corrections.

## 2.5 ELECTRICAL TRANSPORT CHARACTERIZATION

Electrical transport measurements are used to determine the resistance and magnetoresistance of thin films and tunnel junction structures. Measurements were performed on a Quantum Design Physical Property Measurement System with magnetic fields up to 9 Tesla and over a temperature range of 2-300 K. To determine in-plane transport properties of the thin films, the four point method is used with 4-inline bar geometry. In this geometry, four parallel Pt stripes are deposited by sputtering using a shadow mask. Current is passed through the outer bars, I+ and I-, inducing a voltage between the inner bars, V+ and V-. Then resistance is calculated using Ohm's Law.

In tunnel junctions, a two-point method is used to measure the current flowing through pillar structures in an OOP configuration. To ensure that the resistance accurately reflects that of the junction, the magnitude of the electrode resistance must be orders of magnitude less than the junction. We can simultaneously extract bias dependence characteristics with field- and temperature-dependent measurements. Additionally, using a rotating holder we can measure the magnetoresistance dependence with the orientation with respect to the magnetic field (TAMR).

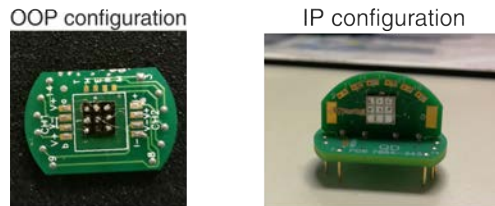


Figure 2.10: Sample holders used in PPMS for OOP and IP configurations.

## 2.6 SYNCHROTRON-BASED X-RAY TECHNIQUES

### 2.6.1 *X-ray Absorption Spectroscopy*

X-ray absorption spectroscopy (XAS) enables to obtain valence and site symmetry information about the atomic species of a compound. In XAS, core electrons are excited into empty states above the Fermi energy, thus probing specifically the unoccupied density of states. As X-ray energy is tuned to a characteristic element absorption edge, only one atom species is excited because each element has specific excitation energies. Therefore to measure different states one needs a tunable radiation source, as the one we found available in a synchrotron.

The required energy for an absorption process is defined as  $E_{abs}=E_f - E_i$  where  $E_f$  is the energy of the excited final state with the core electron into the conduction band and  $E_i$  is the energy of the not excited initial state. Allowed transitions are mainly governed by the dipole selection rules (Fermi golden rule): only transitions which change the angular momentum  $l$  of the excited electron by one can occur ( $\Delta l = \pm 1$ ). The spin momentum  $s$  is conserved ( $\Delta s = 0$ ), so that the  $z$ -component of the orbital momentum  $m$  must obey  $\Delta m = 0, \pm 1$ . In particular,  $\Delta m = \pm 1$  corresponds to left- and right-hand circularly polarized light and  $\Delta m = 0$  for linearly polarized light.

The energy range of soft X-rays is well-controlled for  $2p$  to  $3d$  transitions in  $3d$  transition metals. The spectra of these elements typically exhibit two broad peaks which arise from spin-orbit interactions that split the  $2p$  core states into  $2p_{3/2}$  and  $2p_{1/2}$  states; thus, leading to the  $L_3$  and  $L_2$  edges, respectively. These spectra exhibit fine structure as the empty states of  $3d$  are affected by crystal field and other interactions, for example from SOC. An understanding of the fine structure can be gathered from simulations using multiplet-based software. However, it is often sufficient to perform a qualitative analysis and compare it to published spectra to identify the valence and site symmetry of an element.

XAS experiments gathered in chapter 4 were performed on BOREAS beamline at ALBA synchrotron in Cerdanyola del Vallès. In our measurements we use two different detection modes: total electron yield (TEY) and total fluorescence yield (TFY). The core holes created by absorption processes are subsequently filled by an electron with lower binding energy resulting in either the emission of a fluorescence photon or the emission of an Auger electron.

On one hand, TEY method takes advantage of the avalanche of low kinetic energy secondary electrons produced through inelastic scattering processes from the emitted photoelectrons. The resulting photoelectron current is measured with a picoam-

perimeter that measures the electrons flowing back into the sample from ground. TEY is extremely surface-sensitive with a probing depth of 2-5 nm (see in section 2.6.3 more discussion about the relation between the penetration depth and the kinetic energy of detected electrons).

On the other hand, in TFY one measures the intensity of radiant recombination. Fluorescent photons have a large escape depth and render probing depth  $\approx 100$  nm. Thus, TFY is useful to explore bulk properties in XAS experiments.

### 2.6.1.1 Self-absorption correction in TFY mode

TFY measurements of films frequently exhibit distortions due to "self-absorption effects". They are caused by the absorption of both the exciting photons that penetrate the sample and the absorption of the generated fluorescence radiation when escaping the sample. As shown in Figure 2.11, in a grazing-incidence geometry, all incoming photons are absorbed close to the sample surface compared to the photon penetration length. Nearly all generated fluorescence photons contribute to the signal which is less affected for the absorption coefficient. On the contrary, in normal incidence the absorption of the generated fluorescence radiation substantially attenuates the detected signal.

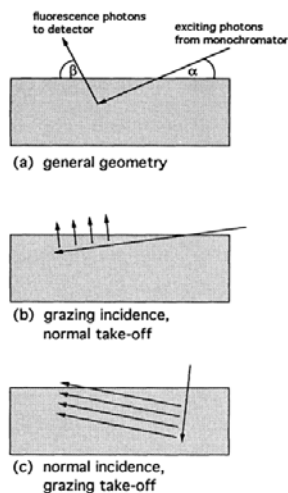


Figure 2.11: (a) General geometry for measuring TFY spectra: incident radiation enters the sample under the glancing angle  $\alpha$ , and produce fluorescence radiation detected under the angle  $\beta$ . Two possible configurations: (b) in grazing-incidence and (c) in normal incidence. Reproduced from Ref.[92].

The absorption of the photons and the angular dependence can be described analytically. Eisebitt *et al.* reported a methodology to correct self-absorption [92] and derive the real absorption coefficient. It consist in measuring at two different incidence angles ( $\alpha_1$  and  $\alpha_2$ ): one nearly normal and one in grazing incidence. The total absorption coefficient ( $\mu_{abs}$ ) can be calculated using the following expression:

$$\mu_{abs}(E) = \mu_{abs}(E_f) \frac{g_2 I_2(E) - g_1 I_1(E)}{I_1(E) - I_2(E)} \quad (2.4)$$

$E$  in the incident photon energy,  $I_i$  the measured intensity and  $g_i = \frac{\sin(\alpha_i)}{\sin(\beta_i)}$ . As in our setup  $\alpha_i + \beta_i = 90^\circ$ , then  $g_i = \tan(\alpha_i)$  which is directly determined. Then, the absorption coefficient can be evaluated relative to  $\mu_{tot}(E_f)$ .

This procedure is exemplified in Figure 2.12. We show the correction procedure used to obtain TFY spectra for LCMO and LSMO spectra presented in 3.7 in chapter 3.

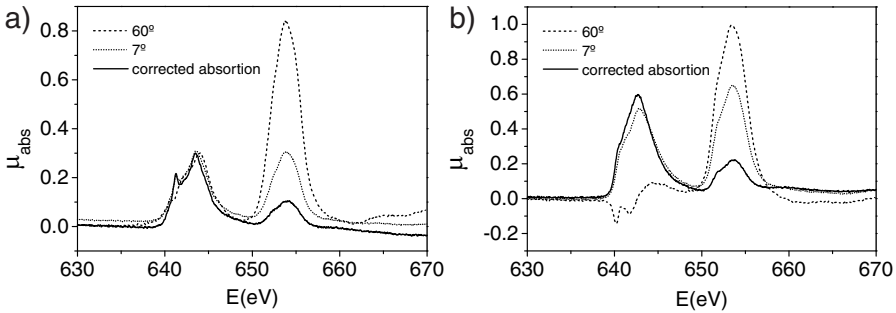


Figure 2.12: a) Corrected Mn L-edge TFY-XAS spectra for (a) LCMO and (b) LSMO samples at  $60^\circ$  (dashed line) and  $7^\circ$  (dots) incidence angles and their corrected curve (continuous line).

## 2.6.2 X-ray Magnetic Circular Dichroism

XMCD is obtained from the difference in intensity of XAS spectra when measured at alternating polarization of circularly polarized light in systems where magnetic moments are aligned.

Left- and right-circularly polarized light confers X-rays opposite angular momenta which are transferred to the excited photoelectron. The excitations are spin-selective, thus leading to spin-dependent absorption processes. This difference is measured by the spin dependent absorption coefficients  $\mu_+$  and  $\mu_-$  for circular polarized light with parallel (+) and antiparallel (-) helicity with respect to the majority

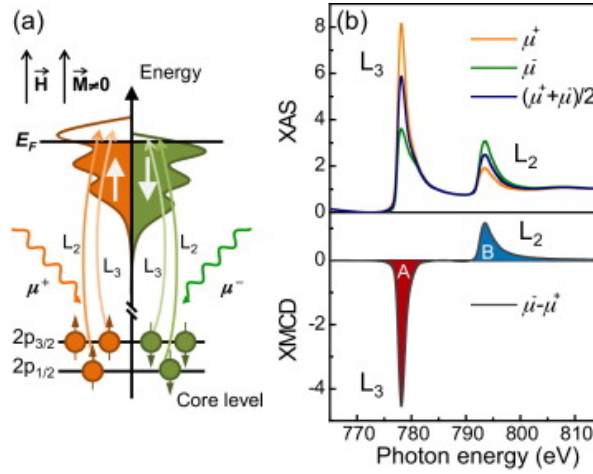


Figure 2.13: a) Diagram of the helicity dependent excitation process of a  $3d$  magnetic material in an XMCD experiment . b) XAS spectra at the Co  $L_{3,2}$ -edges for right ( $\mu_+$ ) and left ( $\mu_-$ ) circularly polarized light. The difference spectrum, thus, the XMCD is shown on the bottom. Figure reproduced from Ref. [93].

spin. An intense magnetic field should be applied to make sure that the spins are parallel or antiparallel aligned to the direction of propagation of the light.

In a simple picture, XMCD can be described as a two-step process. As depicted in Figure 2.13, the  $2p$  core state of a  $3d$  metal is split, due to SOC in a  $j = 3/2$  level ( $2p_{3/2}$  or  $L_3$ -edge) and  $j = 1/2$  level ( $2p_{1/2}$  or  $L_2$ -edge) with its spin coupled parallel and antiparallel, respectively. In the first step, the emission with the light helicity vector parallel (antiparallel) to the  $2p$  orbital moment results in excited electrons of preferred spin up (down) direction. In the first step, circularly polarized light excites a spin polarized electron from the  $2p$  level. From the  $2p_{3/2}$  level X-rays with positive helicity (+) excite 62.5% spin up electrons and those with negative helicity (-) excite 37.5% spin-up electrons, while the  $2p_{1/2}$  level (-) gives 25% spin-up and (+) gives 75% spin-up. In the second step, the excited electron has to find a place in the unoccupied  $3d$  valence band, and if there are less spin-up than spin-down holes available, the XMCD spectrum has a net negative  $L_3$  and positive  $L_2$  peak.

X-ray magnetic circular dichroism (XMCD) is an element-specific magnetic characterization technique and enables to estimate orbital and spin magnetic moments ( $m_L$  and  $m_S$ , respectively) using the so-called magneto-optical sum rules. Sum-rules

derived by Thole *et al.* [94] relate the integrated intensity of the XMCD signal directly to the expected value of the orbital moment,  $\langle L_z \rangle$ , which can be written as:

$$\langle L_z \rangle = -\frac{2 \int_{(L_3+L_2)} (\mu_+(E) - \mu_-(E)) dE}{3/2 \int_{(L_3+L_2)} (\mu_+(E) + \mu_-(E)) dE} N_h \quad (2.5)$$

where  $\mu_-$  and  $\mu_+$  are left- and right-circularly polarized light (for a Poynting vector along  $z$ ),  $\mu_z$  for  $z$ -polarized light, and  $N_h$  the number of holes.

On the other hand, Carra *et al.* [95] derived another sum rule which enables to determine the expected value for the spin,  $\langle S_z \rangle$ , and the magnetic-dipole moment,  $\langle T_z \rangle$ :

$$2\langle S_z \rangle + 7\langle T_z \rangle = \frac{3 \int_{L_3} (\mu_+(E) - \mu_-(E)) dE - 2 \int_{L_2} (\mu_+(E) - \mu_-(E)) dE}{3/2 \int_{(L_3+L_2)} (\mu_+(E) + \mu_-(E)) dE} N_h \quad (2.6)$$

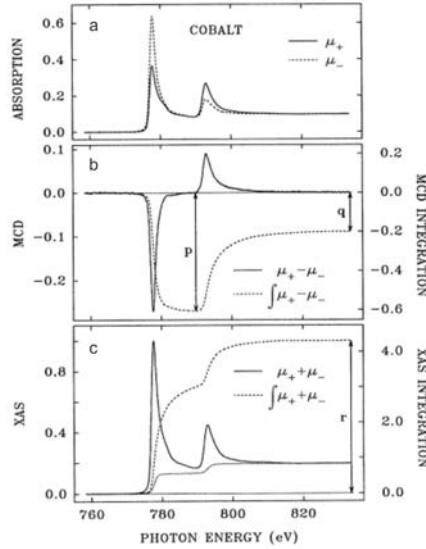


Figure 2.14: Cobalt  $L_{2,3}$ -edge (a) XAS, (b) MCD spectra and (c) summed XAS with corresponding integration with dashed lines. The dotted line shown in (d) is the two-step-like function for edge-jump removal before the integration. The  $p$ ,  $q$  and  $r$  are the three integrals numbers needed in for sum-rule analysis. Figure adapted from Ref. [96].

For the sum rule one can derive the ratio  $m_L/m_{S_{eff}}$ :

$$\frac{m_L}{m_{S_{eff}}} = \frac{\langle L_z \rangle}{\langle 2S_z + 7T_z \rangle} = \frac{-2 \int_{(L_3+L_2)} (\mu_+ - \mu_-) dE}{3 \int_{L_3} (\mu_+ - \mu_-) dE - 2 \int_{L_2} (\mu_+ - \mu_-) dE} \quad (2.7)$$

The integral curves are used to set the correct limits to calculate integrals for sum rules. Chen et al. [96] introduced an alternative notation using  $p = \Delta L_3$ ,  $q = \Delta L_2 + \Delta L_3$ , and  $r = \mu_+ + \mu_-$ , which rewrites the sum rules as:

$$m_L = \frac{4}{3} \frac{q}{r} N_h \quad (2.8)$$

$$m_{S_{eff}} = \frac{3p - 2q}{r} N_h \quad (2.9)$$

Then, the integral numbers  $p$ ,  $q$  and  $r$  are graphically depicted in Figure 2.14. In order to use sum rules one needs to estimate the denominator; thus, the volume of the spectrum. XAS spectra show a constant offset and an edge-jump (the "background" is higher after  $L_2$ -edge than before  $L_3$ ). Thus, in order to calculate the total XAS integral  $r$ , the background must be carefully corrected. Using the ratio between the orbital and the spin moment ( $m_L/m_{S_{eff}}$ ) avoids the possible error induced from the correction  $r$  and also from imprecise  $N_h$ .

### 2.6.3 X-ray photoemission electron microscopy (X-PEEM)

X-ray photoemission electron microscopy (X-PEEM) is a spatially-resolved characterization technique that records electrons emitted from the sample as a result of irradiation with an incoming photon beam from a synchrotron light source. High photon flux in combination with full polarization control makes this technique a powerful tool for space resolved element selective study of nanostructures by means of chemical maps and magnetic domain imaging.

Experiments presented in this manuscript has been performed in UE49-PGMA beamline at BESSY II synchrotron in Berlin The instrument is an Elmitec PEEM III equipped with energy filter and Helium cooled manipulator.

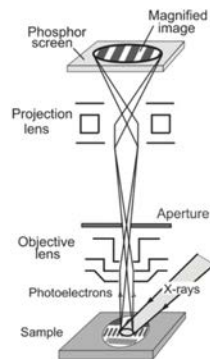


Figure 2.15: Schematics of X-PEEM setup. Reproduced from Ref. [97].

The sample is homogeneously irradiated with soft X-rays radiation (80-1800 eV) and with a spot size around the field view of the microscope. At typical working conditions the field of view is about 3-10  $\mu\text{m}$  which is of the order of the x-ray spot size (10x20  $\mu\text{m}$ ) [98]. The electrons generated from the sample are accelerated by a strong electric field between the sample and the outer electrode of the objective lens. As depicted in Figure 2.15, the objective lens is used to extract the emitted electrons, focusing them to an intermediate image. This image is further magnified by a series of electromagnetic electron lenses onto a 2D detector. Structures as small as 20 nm can be distinguished.

Photoelectrons emit in a wide range of energies. We can find core level, Auger peaks, valence band emission and secondary electron excitations. An energy analyzer allows to use X-PEEM in different modes. In this thesis we use two of them:

1. Analyzer set for detection of secondary electrons. In this case the intensity of detected electrons at the screen is proportional to the absorption of the element at the given photon energy. High photon flux in combination with full polarization control allows to obtain space resolved images in XAS, XMCD or XLD modes.
2. Analyzer set for detection of core electrons. This is equivalent to X-ray photoelectron spectroscopy (XPS) and allows to obtain information about the composition of the sample.

As explained for XAS, when a photoelectron excites electrons in core levels (*e.g.*, from  $2p$  to  $3d$  level), the emitted electron escape at an energy equal to its absorption edge (*e.g.*, 640 eV for the case of Mn). The core hole decay leads to the emission of highly energetic electrons. These electrons suffer multiple inelastic scattering events, finally leading to a secondary electron cascade. Secondary electrons that are able to reach the detector have very small kinetic energies (1-5 eV) and are the ones one detects in conventional X-PEEM mode (detecting secondary electrons). The electrons that could escape the sample without suffering scattering, which are few, are the ones used in XPS mode. The probing depth is determined by the relation between the inelastic mean free path and the kinetic energy of the electrons for the different elements. As it is depicted in Figure 2.16, for an energy of 150 eV one measures a depth circa 5 Å while for low energies around 2 eV one can probe circa 20 Å of depth. Therefore, XPS is much more surface sensitive than XAS.

### 2.6.3.1 Chemical contrast in XPS-mode in X-PEEM

An spatially resolved XPS image of a chemically heterogeneous surface can directly map the distribution of different elements selected by the corresponding photon en-



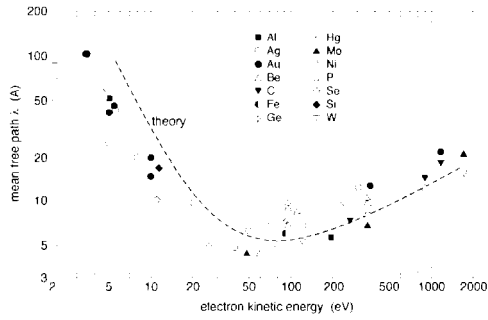


Figure 2.16: *Universal curve*: the inelastic electron mean free path (escape depth)  $\nu s$ . initial kinetic energy. Reproduced from Ref. [99].

ergy. In XPS mode in XPEEM an energy filter is used to select the  $E_K$  of the photoelectrons which enables to determine the binding energies of the emitted electrons.

The technique is based on the photoelectric effect as depicted in Figure 2.17. A highly energetic photon is capable of removing an electron from a core level conferring it enough kinetic energy ( $E_K$ ) to reach the vacuum level. Hence, the excitation energy of the photon ( $h\nu$ ) must be larger than the work function of the material ( $W_f$ ), so that the following conservation equation is obeyed:

$$h\nu = E_B + W_f + E_K \tag{2.10}$$

where  $E_B$  is the binding energy relative to the Fermi level. The  $E_B$  provide information on the chemical composition. For instance,  $E_B$  shifts give information about the oxidation state, the type of bonding, etc.

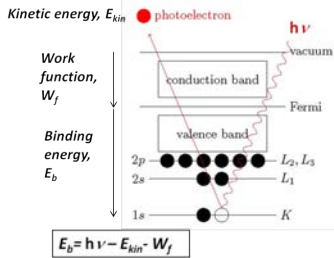


Figure 2.17: Schematic of the photoelectron emission process.

## 2.7 DEVICE FABRICATION

In this thesis nanometric and micrometric MIS junctions are fabricated. The fabrication processes is described in the following section. In order to build pillar structures,

after patterning with UV-lithography, ion milling technique is used to etch a certain thickness of material from the non-exposed areas. Once the pillar structures are isolated, another UV-lithography process is performed to open micrometric overtures. As a final step in device fabrication, in order to fill these overtures with a metal and build macrocontacts, shadow mask are applied. After fixing a shadow masks on top of the surface, the metal layer is sputtered. As an example, in Figure 2.10 we have applied a shadow mask to achieve a 3x3 matrix of Pt contacts.

### 2.7.1 *UV photolithography*

Photolithography is performed with a micro writer system that consists in a UV-beam scanning system. It has the advantage to create patterns of various size and shape over a quite large surface. The pattern designed by software is transferred to a light-sensitive film previously deposit on the sample. In our process, the pattern corresponds to the areas that we want to remove as we use a positive photoresist. This means that the resist is exposed with UV light wherever material needs to be removed. In these photoresists, UV light changes the chemical structure of the resist so that it becomes more soluble in the developer. The developer solution removes the exposed resist (positive). After etching of the exposed areas with the developer, the non-exposed areas become harder but can be easily remove with acetone.

The photolithography process consists of several steps:

- Apply photoresist coating by spin coater.
- Soft baking on a hot plate at 70°C for 1 minute.
- Sample alignment and manual focus in the UV-beam scanner.
- Pattern transfer by UV-exposure (parameters used: 1  $\mu\text{m}$  of laser spot, 180  $\text{mJ}/\text{cm}^2$  dose).
- Apply developer solution to remove exposed areas.

### 2.7.2 *E-beam lithography*

Electron beam lithography (EBL) is a versatile lithography method which enables to pattern nanometric size structures. Since the electron beam (30-100 keV) wavelengths are much smaller than interatomic distances ( $\approx 0.1 \text{ nm}$ ), the minimum size of the pattern is not fundamentally set by the beam wavelength as it is for photolithography [100]. The process is very similar to the one used for photolithography

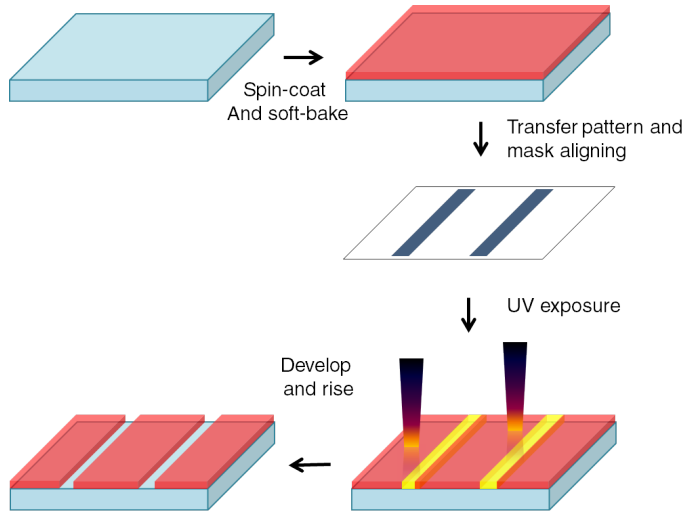


Figure 2.18: Schematic of the photolithography procedure.

but using an electron beam instead of UV-light. The electron beam exposes previously patterned areas of a sample with a resist such as PMMA. It is possible to create patterns with computer software and directly write them to the sample without any intermediate step. Scattering events and secondary electron generation can affect the resolution and generate parasitic effects. These generated electrons contribute to the exposure of the resist. Therefore proper adjustments of dose for each material is needed.

As in the case of photolithography, EBL is advantageous for designing any desired patterns without the need of shadow mask, and additionally is of great value for research in nanotechnology due to the ability to write nanometric features. However, it is slow and not practical for large area and serial writing processes needed for industry applications.

### 2.7.3 Ion milling

After a first lithography step, resin that has not been removed in the developing process becomes harder. Then, we can proceed with the ion milling step in order to etch a specific thickness of material. Prior calibration of etched thickness *vs.* exposure time is needed as etching velocity is different for each material, i.e. metals or oxides.

An ion milling system is mounted in a vacuum chamber equipped with a highly energetic ion beam source. The ionized gas used for bombardment onto the sample

is commonly Ar, which is inert. The sample is mounted on a rotating holder tilted  $5^\circ$  with respect to the incident ion beam so that it is kept in continuous rotation to provide uniform etching and prevent sputtered redeposition. Ar is introduced to the vacuum chamber at pressures around 7 mbar. Then a voltage is applied between cathode and anode to ionize Ar gas. Ions are accelerated in order to hit the sample and etch material. A previously discharged filament is immersed in the ion beam, and is used to neutralize the ion beam space charge thus, preventing the charging of the sample.



## RESULTS



# TUNNING MAGNETIC ANISOTROPY BY STRAIN IN $\text{La}_2\text{Co}_{0.8}\text{Mn}_{1.2}\text{O}_6$ THIN FILMS

---

In this chapter we present aspects of the growth and characterization of LCMO grown by RF magnetron sputtering and, in more detail, of the effect of structural strain, which appears to tune magnetic anisotropy. We have grown LCMO epitaxial thin films on top of different perovskite-oxide substrates that impose different structural strain: (001) oriented  $\text{SrTiO}_3$  (STO),  $(\text{LaAlO}_3)_{0.3}(\text{Sr}_2\text{AlTaO}_6)_{0.7}$  (LSAT) and  $\text{LaAlO}_3$  (LAO). We prove that tensile strain, produced when LCMO is grown on top of STO, is the responsible of the appearance of PMA. In addition, we study stoichiometry and valence states of our films via EPMA and XAS and we relate them with SQUID magnetometry measurements.

## 3.1 INTRODUCTION

An important motivation for the study of FM-I is the practical capability and great potential of combining magnetic and insulating functionalities in a single system for spintronics applications. Materials combining these two properties are very scarce in nature since in many cases ferromagnetic interactions are of exchange-type and driven by charge carriers. Among these rare materials we found some oxides as  $\text{EuO}$  (79 K) and simple perovskites as  $\text{YTiO}_3$  ( $T_C=29$  K),  $\text{SeCuO}_3$  ( $T_C=29$  K), and  $\text{BiMnO}_3$  ( $T_C=105$  K) [11]. Double perovskites as  $\text{La}_2\text{CoMnO}_6$  and  $\text{La}_2\text{NiMnO}_6$  have also attracted great attention as they present a rather high  $T_C$  (230 and 280 K, respectively). In this thesis we focus our attention in study  $\text{La}_2\text{CoMnO}_6$  material in the form of thin film.

In principle, in this double perovskite compound, magnetic cations should be ordered in a fully alternating way in the crystal lattice to yield to optimal FM-I behaviour. Then ferromagnetism should be explained by FM-superexchange interac-



tions between  $\text{Co}^{2+}$  and  $\text{Mn}^{4+}$  cations in base of the GKA rules, as explained in the chapter 1 [13, 14, 101]. Full cationic ordering of  $\text{Co}^{2+}/\text{Mn}^{4+}$  leads to a saturation magnetization of  $6 \mu_B/f.u.$  and a  $T_C$  of about 230 K [26, 102]). Magnetic properties in double perovskites are very sensitive to cationic ordering. In disordered samples saturation magnetization and  $T_C$  are substantially reduced [103, 104]. In this regard, a lot of discussion has been addressed on the nature of the magnetic interactions leading to ferromagnetism in bulk  $\text{La}_2\text{CoMnO}_6$  (also expressed as  $\text{LaCo}_{0.5}\text{Mn}_{0.5}\text{O}_3$ ). Most of the discrepancies and interpretations in the literature come from discussing how the degree of cationic order is achieved. Divergences of stoichiometry are a common problem in Co-based oxides. Co is a very volatile element and usually thin film growth techniques require high working temperatures. The major challenges in the growth of this materials lie in the convergence of these two delicate aspects. In particular, in our films we have found a certain degree of Co-deficiency. As it will be presented in the next sections, the exact composition of our films has been determined by EPMA measurements, showing a stoichiometry of the type  $\text{La}_2\text{Co}_{1-x}\text{Mn}_{1+x}\text{O}_6$  with  $x \approx 0.23$ . Fortunately, FM-I character in  $\text{La}_2\text{CoMnO}_6$  extends beyond the 1:1 Mn:Co ratio as reported in the literature. FM behaviour has been found in single crystals [105] and polycrystalline samples [106] of  $\text{LaCo}_y\text{Mn}_{1-y}\text{O}_3$  with  $y \approx 0.35$ . In fact, Barilo *et al.* [105] reported optimal FM properties in samples with Co content  $y=0.36$ . More importantly, Bull *et al.* [107] have recently shown, using neutron-diffraction experiments, that Co/Mn cationic order for  $y=0.35$  composition is even better than for  $y=0.50$  (i.e., stoichiometric  $\text{La}_2\text{CoMnO}_6$ ), in the sense that for the former no Co ions are present in the Mn sublattice while in the stoichiometric case about 12% of Mn sublattice sites are occupied by Co. Additionally, magnetic measurements showed a  $T_C \approx 210$  K for  $y=0.36$  very similar to that of  $y=0.50$  samples ( $T_C \approx 225$  K), and an ordered magnetic moment per cation above  $3 \mu_B$  [107]. Thus, one can consider that the  $\text{LaCo}_y\text{Mn}_{1-y}\text{O}_3$  system, in a range of  $y$  values from 0.50 down to at least 0.35 present a high degree of cationic ordering, so it must be considered as a double perovskite structure  $\text{La}_2\text{Co}_{1-x}\text{Mn}_{1+x}\text{O}_6$  (with  $x=1-2y$  for  $x=0$  to  $x=0.3$ ). We will see that the magnetic properties of our films agree with those in the literature for Co-deficient  $\text{La}_2\text{CoMnO}_6$  bulk presenting Mn/Co cationic order: they present  $T_C$  around 220 K and a saturation magnetization of  $6 \mu_B/f.u.$  (based on the double perovskite  $\text{La}_2\text{Co}_{1-x}\text{Mn}_{1+x}\text{O}_6$  f.u.) [105, 106].

Regarding LCMO thin films growth, few experimental reports have been found in literature, most of them are grown by PLD technique [103, 104, 108]. In these works, films seem to present not full cationic ordering. In another recent work it is claimed that high degree of cationic ordering can be obtained by growing LCMO on (111)STO substrates instead of the common used (001)STO [109]. The growth of LCMO on (111)STO was also explored using metal-organic aerosol deposition

(MAD) [110]. In our group, we demonstrate that highly-ordered LCMO thin films can be achieved using RF magnetron sputtering technique [111].

On the other hand, by growing LCMO film on top of different substrates that impose different structural strain we have observed that compressive strain induces IP magnetic anisotropy while tensile strain promotes PMA. It has been proved in different material systems that the easy magnetization axis can be changed from IP to OOP by means of tensile strain as in (GaMn)As [112], (IrMn)As [113], (GaMn)(PN) [114], Fe garnets [115]; or by means of compressive strain in  $\text{La}_{0.7}\text{Sr}_{0.3}\text{MnO}_3$  [116] and  $\text{SrRuO}_3$  [117]. Other examples that in particular show strain-tunable magnetocrystalline anisotropy are  $\text{Y}_3\text{Fe}_5\text{O}_{12}$ , which is widely used in microwave applications [118],  $\text{CoFe}_2\text{O}_4$  and  $\text{CoCr}_2\text{O}_4$  spinel systems that also present large magnetostriction [33, 119–122] and double perovskite systems such as  $\text{Sr}_2\text{FeMoO}_6$  [123] and  $\text{Sr}_2\text{CrReO}_6$  [124, 125]. As it will be discussed in chapter 4, we have found that in our LCMO thin films magnetic anisotropy has also a magnetocrystalline origin. Much interest is added as for LCMO/STO films it is perpendicular. Thus, the possibility of controlling PMA opens the door to the implementation of high density magnetic memory devices.

## 3.2 GROWTH AND CHARACTERIZATION OF EPITAXIAL $\text{La}_2\text{Co}_{0.8}\text{Mn}_{1.2}\text{O}_6$ ON $\text{SrTiO}_3$

As already mentioned, thin films of  $\text{La}_2\text{CoMnO}_6$  reported in literature have been mainly grown by PLD [103, 104, 108]. In there, high temperatures (700–800°C) and high oxygen pressures (200–600 mTorr) are used as growth conditions in order to achieve a high degree of cationic ordering. We have achieved high quality films using RF magnetron sputtering. Its optimization process is presented in the next section.

### 3.2.1 *Morphological, structural and magnetic characterization*

The growth of LCMO thin films by RF magnetron sputtering was accurately optimized as it is explained in Ref. [111]. In that work variations in magnetic properties were directly attributed to variation in oxygen stoichiometry. Here, we first revisit this finding as we consider it will be useful to understand the rest of the results.

The growth conditions and characteristics of all the samples analyzed in this chapter are gathered in table 3.1. All samples have been grown at a substrate temperature of 900°C and annealed at the same temperature.

Table 3.1: Growth conditions and properties of samples studied in this chapter.

Sample name	substrate	t (nm)	$T_C$	$p_{O_2}$ (Torr)	deposit time (min)	anne. $p_{O_2}$ (Torr)	anne. time (h)	cooling rate ( $^{\circ}$ /min)
LCMO-A	STO	15	225	0.4	100	400	2	10
LCMO- $\delta$ B	STO	14	150	0.4	100	$2 \cdot 10^{-6}$	1	10
LCMO- $\delta$ C	STO	15-20	120	0.3	100	0.3	0	25
LCMO- $\delta$ D	STO	15-20	220	0.4	100	400	1	10
LCMO- $\delta$ E	STO	21	228	0.4	100	400	1	1
LCMO-2	STO	2.5	200	0.4	20	400	2	10
LCMO-4	STO	4	190	0.4	25	400	2	10
LCMO-8	STO	8	223	0.4	50	400	2	10
LCMO-34	STO	34	225	0.4	200	400	2	10
LCMO-66	STO	66	223	0.4	400	400	3	10
LCMO-LAO-15	LAO	15	232	0.4	100	400	2	10
LCMO-LAO-4	LAO	4	232	0.4	25	400	2	10
LCMO-LSAT-15	LSAT	15	230	0.4	100	400	2	10
LCMO-LSAT-4	LSAT	4	207	0.4	25	400	2	10

Samples LCMO- $\delta$ B, LCMO- $\delta$ C, LCMO- $\delta$ D, LCMO- $\delta$ E are samples grown on (001)STO used for the optimization process in Ref. [111] which present different oxygen content. Best degree of oxygen content has been achieved for LCMO- $\delta$ E which only differs from growth condition of sample LCMO- $\delta$ D by the use of a slower cooling rate of  $1^{\circ}$ C/min. This cooling rate was exceedingly time consuming thus, we have proved that we can achieve almost the same degree of cationic order by increasing the annealing time to 2h (instead of 1 h) and using a cooling rate of  $10^{\circ}$ C/min (sample LCMO-A). Therefore, the optimized conditions fixed for the growth of LCMO films are the ones for LCMO-A.

Samples LCMO- $\delta$ B and LCMO- $\delta$ C are considered low-oxygenated with a high degree of cationic order. In LCMO- $\delta$ C growth and annealing is performed at lower  $p_{O_2}$  of 0.3 Torr and faster cooling rate while in LCMO- $\delta$ B annealing is performed in vacuum conditions ( $2 \cdot 10^{-6}$  Torr) but the other growth conditions are kept the same as in LCMO- $\delta$ D. Therefore, the significant reduction of  $T_C$  is attributed to a decrease of oxygen content mainly dictated by annealing conditions [111].

This argument is further confirmed by structural analysis with X-ray diffraction (XRD). High resolution XRD has been carried out in ICN2 services. Figure 3.1 shows high resolution  $\theta/2\theta$  scans of a low- and high-oxygenated film (LCMO- $\delta$ B and LCMO- $\delta$ E). The secondary oscillations observed in the scans represent thickness fringes and additionally indicate the high quality of the films.  $\theta/2\theta$  plots can be fitted in order to compute thickness and  $c$ -parameter of the film. We observe that the low-oxygenated sample is thinner ( $t_{LCMO-\delta B}=14$  nm) than the high-oxygenated one

( $t_{LCMO-\delta E}=21$  nm), and that it presents a larger  $c$ -parameter ( $c_{LCMO-\delta B}=3.878$  Å and  $c_{LCMO-\delta E}=3.865$  Å). The tendency of the  $c$ -parameter reflects the presence of oxygen vacancies. Oxygen vacancies favor the appearance of  $Mn^{3+}$  which has a larger cationic radius than  $Mn^{4+}$ , thus producing an increase of the cell parameter. This feature is further analyzed in more detail by RSM when arguing about the strain dependence on oxygen content in section 3.4.1.

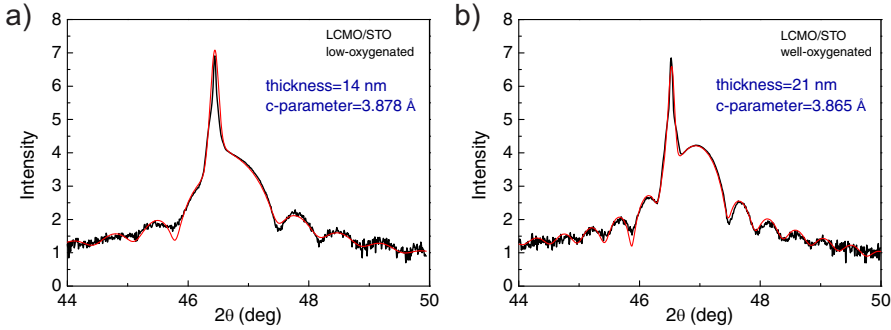


Figure 3.1: High resolution  $\theta/2\theta$  XRD scans of films LCMO- $\delta B$  and LCMO- $\delta E$ . Red lines show the fitting according to expressions given in Ref. [89]

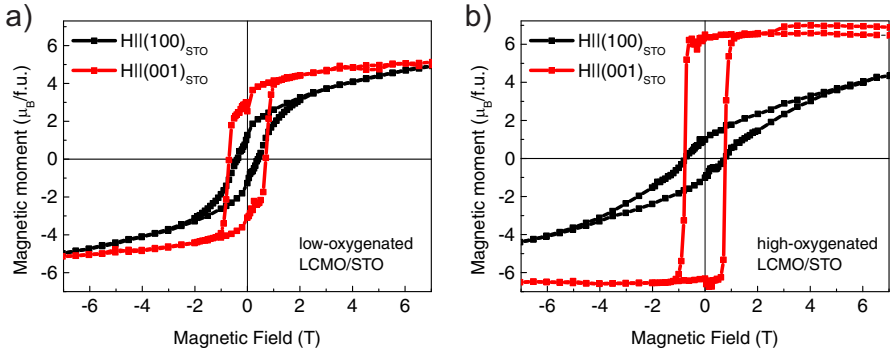


Figure 3.2: Magnetization *vs.* Field of LCMO- $\delta B$  and LCMO- $\delta E$  samples measured at 10 K with the field applied IP (red) and OOP (black)

Magnetization *vs.* field curves of these samples at 10 K are plotted in Figure 3.2. Magnetic properties have been explored using SQUID magnetometry that can operate within temperature a range of 2-300 K and up to 9 T. We have detected a great difference between measuring placing the sample perpendicular (OOP) or parallel (IP) to the applied magnetic field. Red curves corresponds to OOP configuration and black ones to IP. Thus, in Figure 3.2 its is proved that both samples exhibit PMA.  $M(H)$  data have been corrected subtracting the diamagnetic contribution of the substrate and normalized using thickness and molar density to obtain magnitudes

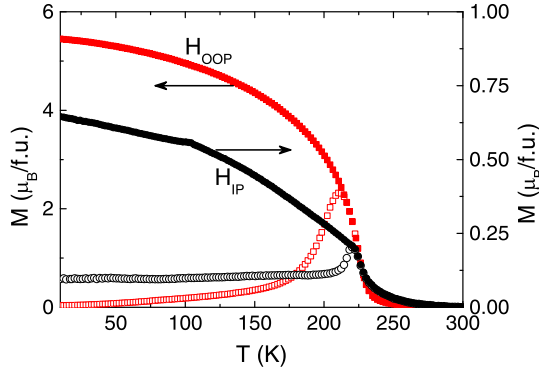


Figure 3.3: Magnetization *vs.* temperature measured after ZFC (open symbols) and FC (solid symbols) for sample LCMO-A with magnetic field of 0.1 T applied OOP (red squares, left axis) and IP (black circles, right axis)

of  $\mu_B/\text{f.u.}$ . We observe that LCMO- $\delta E$  reaches saturation magnetization of  $6 \mu_B/\text{f.u.}$ , values expected for good Co/Mn cationic ordering. In contrast, LCMO- $\delta B$  shows a saturation magnetization around  $5 \mu_B/\text{f.u.}$  In literature, low magnetization in double perovskite systems has been attributed to the presence of antisite disorder that, in this case, could induce a change of valence to  $\text{Mn}^{3+}$  and  $\text{Co}^{3+}$  [102, 126]. Hence, the presence of  $\text{Mn}^{3+}$  and  $\text{Co}^{3+}$  could produce AFM interactions which would decrease of the overall magnetization (this aspect will be clarified later). On the other hand, we also observe that magnetic anisotropy (the difference between OOP and IP magnetization loops) is greater for the high-oxygenated sample. The origin of this effect together with the possible valence changes will be discussed in sections 3.3 and 3.4.1.

In addition, Figure 3.3 shows magnetization *vs.* temperature curves of an optimized sample (LCMO-A) under an applied field of 0.1 T in both IP and OOP configurations and in FC and ZFC. The  $T_C$  value is derived from the minima of  $dM/dT$  which accounts for a  $T_C \approx 225$  K for both curves.  $T_C$  is similar to the one found in bulk samples with the similar stoichiometry [105]. The magnetization value obtained at low temperature with the field applied OOP is nearly ten times larger than when field is applied IP (note the scale of each axis magnitudes). This large difference is due to the fact that the magnetic field used (0.1 T) is considerably smaller than the coercive field ( $H_C=1$  T; see  $M(H)$  in Figure 3.2b). This means that at the end of the ZFC process, a similar number of domains with magnetization up and magnetization down must be expected, rendering a small value of the overall magnetization. The small field applied is not able to switch the domains up to a temperature near  $T_C$ . In addition, IP curve (FC branch) presents a small kink at about 100 K. Similar

kinks are also present for LCMO films grown by PLD, e.g. in [103, 104, 108], yet those works do not specify whether the measures were performed IP or OOP. In our case, this anomaly is not present neither in IP-ZFC branch nor in the OOP curve. Thus, we discard that it comes from a second phase or from a second transition and suggests that the anomaly could appear due to the competition between anisotropy and cooling field.

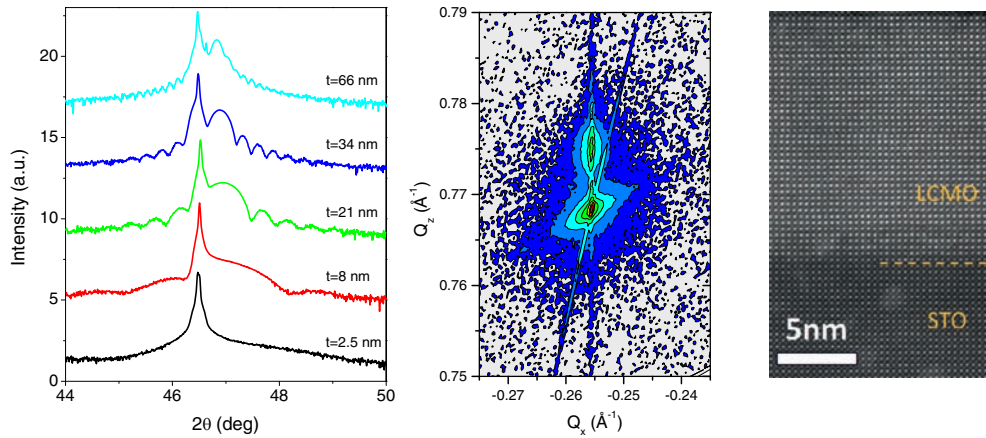


Figure 3.4: (Left) High resolution  $\theta/2\theta$  XRD scans around the (002)-STO substrate peak of films of various thickness ( $t=2.5, 8, 21, 34, 66$  nm). (Middle) RSM around  $(\bar{1}03)$ -STO peak and (right) STEM image of LCMO-15.

Following on, films in a wide range of thicknesses (from 2.5 nm to 66 nm) have been studied. It is interesting to characterize the behaviour of LCMO films as a function of thickness for two reasons. First, to examine the properties of very thin films that could be useful as active insulating barriers; and second to study whether or not the PMA found is present in thicker films. In thicker samples the total energy induced by the demagnetizing field ( $E = \vec{M} \cdot \vec{H}_d$ ) could be strong enough to put magnetization in the plane.

Good quality films were obtained for the whole thickness range proved by XRD and AFM characterization. High resolution  $\theta/2\theta$  XRD scans and RSM in Figure 3.4 (left and middle) prove that LCMO films on STO grow tensile-strained. The quality of the interface has been also checked by scanning transmission electron microscopy (STEM), as it can be seen in Figure 3.4 reproduced from Ref. [127], which reveals a sharp interface with STO substrate. AFM topography images shown in Figure 3.5 (left) prove atomically flat steps and terraces-like surfaces for  $t=4, 8, 15$  nm samples. For the thicker samples (LCMO-66) the terrace structure has disappeared. In fact, the small bumps appearing in LCMO-15 at the terrace-edges seems to indicate the starting of 3D-island formation. Therefore in LCMO-66 this could be the dominating

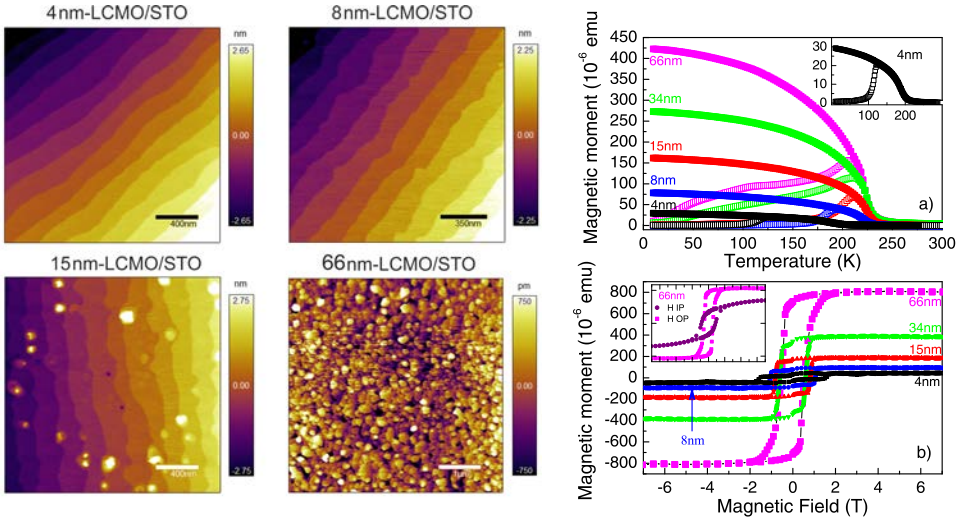


Figure 3.5: (Left) Topographies of LCMO films of  $t=4, 8, 15, 66$  nm. (Right)  $M(T)$  and  $M(H)$  for LCMO films of  $t=4, 8, 15, 35, 66$  nm.

growth mechanism. Nevertheless roughness RMS values for all samples are smaller than  $1.4(1.1)$  nm.

Figure 3.5 (top right) shows the temperature dependence of the magnetization measured with the magnetic field applied OOP for LCMO/STO films of different thicknesses. It can be appreciated that the shape of the magnetization curves is very smooth and that the  $T_C$  hardly depends on  $t$  down to 8 nm (calculated thicknesses are displayed in Table 2.1). For the thinnest samples LCMO-4 and LCMO-2 (not shown)  $T_C$  is shifted down to  $\sim 190$ -200 K. All samples present easy axis of magnetization in the OOP direction.  $M(T)$  and  $M(H)$  shown in Figure 3.5 are all measured in the OOP configuration. In the inset of Figure 3.5 (top right) the measurement corresponding to LCMO-66 for both IP and OOP is shown. PMA is also present in the thicker films confirming that the demagnetizing field is not strong enough to put magnetization in the plane. All  $M(H)$  present a remarkable square shape with a square remanence/saturation ratio very close to 1, proving the strong magnetic anisotropy of the films and that the easy axis is OOP. Coercive field remarkably grows when reducing film thickness ( $H_C=1.5$  and  $0.55$  T for  $t=4$  and  $66$  nm films respectively). Most of  $M(H)$  loops present an slight jump at  $H=0$ , an anomaly that do no decrease/increase with  $t$  (at least for  $t < 34$  nm). There are several hypothesis of where this contribution comes from: misalignment of the sample in the OOP configuration, as SQUID setup is not precise or presence of some region at the interface or at the surface with a different  $H_C$ . The later could be because interfaces may introduce disorder and changes on

Table 3.2: Quantitative compositional data for target and thin films of  $\text{La}_2\text{Co}_{1-x}\text{Mn}_{1+x}\text{O}_6$ . The percentage of each element is normalized by the atomic weight. Growth conditions of films are summarized in table 3.1.

Sample name	La (at. %)	Co (at. %)	Mn (at. %)	O (%)	La (per f.u.)	Co:Mn	$x$
<b>LCMO Target</b>	18.2(1.9)	7.3(8)	7.4(9)	67.1(3.0)	2.51(37)	1.02(9)	0.01(4)
<b>LCMO-66</b>	16.1(2)	6.1(1)	9.3(9)	68.5(4)	2.10(2)	0.65(1)	0.21(1)
<b>LCMO-A</b>	16.3(1.9)	6.1(6)	10.2(1.0)	67.4(3.4)	2.01(4)	0.50(2)	0.25(2)
<b>LCMO-<math>\delta</math>C</b>	8.1(5)	3.0(6)	4.7(3)	84.2(1)	2.12(6)	0.65(2)	0.22(1)
<b>LCMO-<math>\delta</math>D</b>	12.0(2)	4.2(1)	7.1(1)	76.6(5)	2.12(2)	0.59(1)	0.25(1)
<b>LCMO-<math>\delta</math>X</b>	15.4(6)	6.0(2)	9.9(3)	68.8(1.0)	1.94(4)	0.61(1)	0.25(1)

the strength of magnetic interactions and anisotropy due to translational symmetry breaking and other interface effects. Those effects could be especially relevant when the material is strongly anisotropic as in the present case.

### 3.2.2 Stoichiometry of the films

We have performed electron probe micro-analysis to determine the composition of LCMO thin films and the target. Measurements have been carried by Dr. X. Llovet in Scientific and Technological Center of the University of Barcelona with a CAMECA SX-50 electron microprobe equipped with four wavelength-dispersive X-ray spectrometers. Details about the technique are explained in the Experimental Methods chapter.

Quantitative data about the composition of several samples and the target are gathered in Table 3.2. The first four columns correspond to atomic percentage of each element. In the other columns we calculate the proportion of La for unit formula (f.u.), the Co:Mn ratio and the  $x$ . Oxygen concentration is not computed, as its very difficult to separate oxygen coming from the substrate from the one coming from the film. The same issue is found with La in samples with LAO and LSAT as substrates. Anyway if we impose the nominal stoichiometry of La and oxygen in order to obtain a good fitting for Co and Mn, we find similar values as for samples grown on STO ( $x \approx 0.22$  for LCMO-LSAT-15 and  $x \approx 0.16$  for LCMO-LAO-15).

We observe that all thin films present a 1:1 La:(Co+Mn) atomic ratio, hence obeying a stoichiometry of the type  $\text{La}_2\text{Co}_{1-x}\text{Mn}_{1+x}\text{O}_6$ . The Co:Mn ratio is clearly below 1:1 (except the target one) meaning that films have a certain degree of Mn excess. Within the bar of error of the technique, all films shown here present  $x$  between 0.21-0.25 and no relation is found with the oxygen content. On the other hand, EPMA results show that LCMO target possess good stoichiometry, with Co:Mn  $\approx 1$ . There-



fore, we can conclude that off-stoichiometry must be ascribed to the growth process. A possible origin could be the high temperatures used during the growth that can lead to volatilization of Co. However, 900°C are necessary to obtain good magnetic properties and lowering the temperature to 800°C, does not improve stoichiometry but has significant effects on magnetic properties. This is the case of LCMO- $\delta$ X, a film grown at 800°C (with standard  $p_{O_2}$  of 400 mTorr and 1h annealing) that present a  $T_C \approx 140$  K, and a off-stoichiometry similar to the other films (Co:Mn=0.61)<sup>1</sup>.

Although Co:Mn relation is not 1:1, we do not expect cationic vacancies of Co as La:(Co+Mn) relation is indeed equal to one. This suggests that a fraction of Mn has substituted Co sites. XAS experiments have been used to shed light into this hypothesis by examining which is the valence of the substituting Mn and in which proportion is found.

### 3.3 VALENCE STATE STUDIED WITH X-RAY ABSORPTION SPECTROSCOPY

As mentioned in the introduction of this chapter (section 3.1), FM-I character in  $La_2CoMnO_6$ -based compound extends beyond the 1:1 Mn:Co ratio [105]. In our films, despite the non-stoichiometry, optimized LCMO samples present  $T_C$  around 225 K and saturation magnetization of 6  $\mu_B$ /f.u. Assuming that ferromagnetism is driven by superexchange interactions between  $Co^{2+}$  and  $Mn^{4+}$ , FM-I behaviour can be complex to interpret in off-stoichiometric LCMO films. A deficiency of Co should imply a redistribution of charge in order to fulfill charge neutrality, and the most reliable mechanism is indeed the reduction of a part of  $Mn^{4+}$  to  $Mn^{3+}$ . This would be formally expressed as:  $La_2^{3+}Co_{1-x}^{2+}Mn_{1-x}^{4+}Mn_{2x}^{3+}O_6^{2-}$ .  $Mn^{3+}$  ion is bigger in size than  $Mn^{4+}$ , thus it would preferentially be placed at Co sublattice, as  $Co^{2+}$  ion is also bigger than  $Mn^{4+}$  ions. Therefore,  $Mn^{3+}$  ions would be placed in both Co-sublattice and randomly distributed in the Mn sublattice. In this scenario, the FM-I state displayed by this system cannot be directly understood as driven by superexchange interactions between  $Co^{2+}$  and  $Mn^{4+}$ .

To clarify the actual valence states of Co and Mn in our films, we have performed XAS experiment in BL29-BOREAS beamline at ALBA Synchrotron (Barcelona). XAS spectra are very sensitive to valence states: different valences produce clearly differentiated final states in the  $2p^63d^m$  to  $2p^53d^{m+1}$  absorption process which are translated into shifts in the energy position of the absorption peaks of the spectra. Measurements were performed in both TEY and TFY modes under a vacuum of  $2 \cdot 10^{-10}$

<sup>1</sup> LCMO- $\delta$ X sample is not included in Table 3.1 because the rest of the samples are grown at 900°C and this samples is only used for EPMA)

mbar at room temperature. As explained in chapter 2, TEY is mainly sensitive to the outermost layers, just few nanometers below the sample surface, while TFY detects across a deeper region, thus giving information about the bulk of the film. Although TFY mode is sensitive to an inner region of the sample, it gives a much smaller signal than TEY. Besides, fluorescence measurements in thin films prone to self-absorption artifacts. Therefore to recover the real signal of absorption coefficient, it is important to apply correction procedures to the fluorescence spectra. As explained in chapter 2, this can be done by measuring at different incidence angles and applying the formalism described by Eisebitt *et al.* [92].

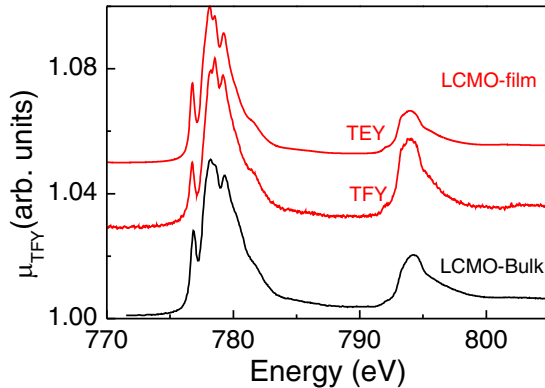


Figure 3.6: Co  $L_{2,3}$ -edge XAS of sample LCMO-66 (red lines, comparing TFY and TEY signals) and LCMO bulk (as extracted from Ref. [128], black line) at 300 K. Spectra have been vertically shifted for clarity.

We first compare XAS spectra of a thick film of LCMO with bulk XAS data from literature. Figure 3.6 shows the TFY and TEY spectra around Co  $L_{2,3}$ -edge of sample LCMO-66 measured simultaneously together with the LCMO bulk sample spectra taken from Ref. [128], that corresponds to a stoichiometric and highly ordered sample with  $T_C \approx 225$  K. TEY and TFY spectra of LCMO-66 are very similar between them but also to that of stoichiometric bulk LCMO, for which  $\text{Co}^{2+}$  in HS state is settled [128]. From this comparison, we can conclude that the non-stoichiometry introduced in our films does not alter significantly Co valence state: Co ions are in  $2+$  oxidation state and in HS configuration. Moreover, we prove that regarding the Co electronic structure, there are no significant differences between surface and bulk of the sample.

Now we proceed with Mn-edge evaluation. Figure 3.7 shows XAS spectra around Mn  $L_{2,3}$ -edge in both TFY and TEY detection modes, of  $\text{LaMnO}_3$ ,  $\text{La}_{0.7}\text{Sr}_{0.3}\text{MnO}_3$ , LCMO-66, and  $\text{CaMnO}_3$  films. Samples of  $\text{LaMnO}_3$ ,  $\text{La}_{0.7}\text{Sr}_{0.3}\text{MnO}_3$  and  $\text{CaMnO}_3$

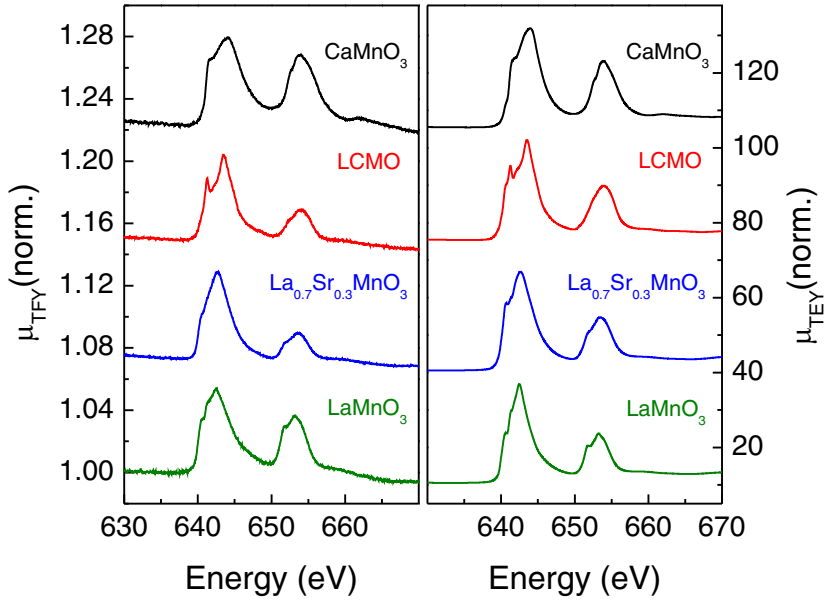


Figure 3.7: Absorption-corrected TFY-detected Mn  $L_{2,3}$ -edge XAS spectra of  $\text{CaMnO}_3$ , LCMO-66, LSMO and  $\text{LaMnO}_3$  at 300 K. Spectra have been vertically shifted for clarity.

have been purposely grown and used as references for Mn-valence analysis, representing compound with oxidation states of  $\text{Mn}^{3+}$ , mixed-valence and  $\text{Mn}^{4+}$ , respectively. In Figure 3.7, a progressive shift of the  $L_3$  peak with the series of samples can be clearly appreciated in both sets of spectra. One can observe that  $L_3$  absorption peak for LCMO-66 takes place at an energy value lying between those of  $\text{LaMnO}_3$  and  $\text{CaMnO}_3$ . If we consider that  $\text{LaMnO}_3$  absorption peak at 642.5 eV corresponds to  $\text{Mn}^{3+}$  and  $\text{CaMnO}_3$  one at 644.1 eV to  $\text{Mn}^{4+}$  then, LCMO-66 peak centred at 643.6 eV should correspond to a valence state of +3.7 (considering a linear relation). For its part,  $L_3$  peak of  $\text{La}_{0.7}\text{Sr}_{0.3}\text{MnO}_3$  lies at 642.7 eV between those of LCMO-66 and  $\text{LaMnO}_3$  so corresponds to a mixed valence state of +3.3. In conclusion, the shift of the center of  $L_3$  peak follows an increase of Mn valence from +3 towards +4.

Regarding the line shape of Mn  $L_{2,3}$ -edge absorption peaks of LCMO-66, we found that they are very similar to that published by Burnus *et al.* [128] for the high- $T_C$  LCMO bulk sample where they establish that their material was formed essentially by  $\text{Mn}^{4+}$ . Nevertheless, there are some features that lead us to conclude that our films present a small quantity of  $\text{Mn}^{3+}$  such as the small bump at the Mn  $L_3$  pre-edge and the shallower valley at  $\approx 641.5$  eV. In fact, as depicted in Figure 3.8, we can reproduce spectrum of LCMO-66 by a linear superposition of bulk  $\text{LaMn}_{0.5}\text{Co}_{0.5}\text{O}_3$

( $T_C \approx 225$ ) and  $\text{LaMnO}_3$  spectra from Ref. [128] with weights of 80 % and 20 %, respectively. This must not be considered as an absolute quantification of the balance between  $\text{Mn}^{3+}/\text{Mn}^{4+}$ , as different correcting (unknown) factors are needed, but as an evidence of the presence of extra  $\text{Mn}^{3+}$ .

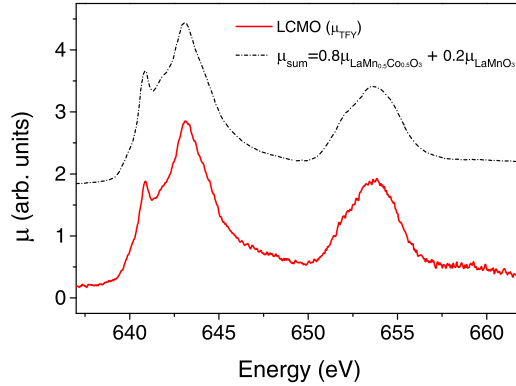


Figure 3.8: Comparison of Mn  $L_{2,3}$ -edge XAS spectra in TFY mode of LCMO-66 with a linear superposition of LCMO and LMO spectra from Ref. [128] with weights of 80 % and 20 % ( $\mu_{sum} = 0.8 \cdot \mu_{\text{LaMn}_{0.5}\text{Co}_{0.5}\text{O}_3} + 0.2 \cdot \mu_{\text{LaMnO}_3}$ ).

It is also interesting to compare TFY and TEY measurements in Figure 3.7. In general, the only significant difference between both sets of spectra (specially for LCMO-66 and LSMO ones) is a feature appearing at about 640.5 eV. This typically reflects the appearance of a small amount of  $\text{Mn}^{2+}$  on the film surface [129].

We focus now on the series of thinner ( $t \approx 15$  nm) samples prepared under different conditions resulting in different degrees of oxygenation, and on different substrates (Table 3.1). Figure 3.9 shows TEY signal around Co  $L_{2,3}$ -edge obtained for LCMO- $\delta$ C, LCMO- $\delta$ D, LCMO- $\delta$ E, LCMO-LSAT-15, LCMO-LAO-15 at RT. Except for LCMO- $\delta$ C, the shape of the absorption edge is almost identical to that found for LCMO-bulk samples [128], and to that found for LCMO-66. Thus, we can conclude that it corresponds to  $\text{Co}^{2+}$  ion in HS configuration.

We examine in more detail Co and Mn spectrum of the low-oxygenated sample LCMO- $\delta$ C, following the same procedure used in Ref. [128] to analyze the spectrum of a bulk sample with poor Co/Mn ordering ( $T_C \approx 150$  K). Figure 3.10 presents the difference spectra resulting from the subtraction of LCMO- $\delta$ E one from that of LCMO- $\delta$ C. A scale factor ( $\times 0.75$ ) has been applied to LCMO- $\delta$ E, enough for making the difference non-negative within the errors. This curve resembles that of  $\text{LaCoO}_3$  at low temperature [128] and indicates that  $3d$  orbitals occupation of a fraction of Co ions, around 25 %, is  $\text{Co}^{3+}$  in LS state. For the sake of comparison, the spectra

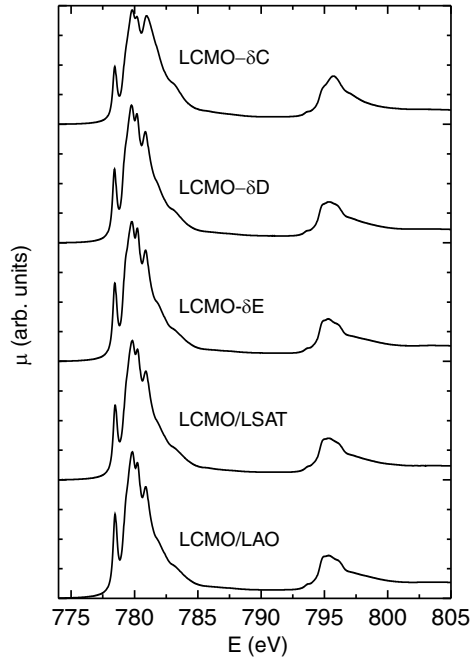


Figure 3.9: Co  $L_{2,3}$ -edge XAS spectra of LCMO- $\delta$ C, LCMO- $\delta$ D, LCMO- $\delta$ E, LCMO-LSAT-15 and LCMO-LAO-15 samples measured by TEY at 300 K. Spectra have been vertically shifted for clarity.

of LCMO- $\delta$ D and LCMO- $\delta$ E are compared in the inset of Figure 3.10a. In this case, they are very alike. So, the difference in Co valence state between LCMO- $\delta$ D and LCMO- $\delta$ E, if any, is clearly much smaller than between LCMO- $\delta$ C and LCMO- $\delta$ E.

The fraction of trivalent Co ions found in LCMO- $\delta$ D is expected to be compensated by a reduction of dominating  $Mn^{4+}$  ions towards  $Mn^{3+}$ . Therefore Mn spectra have been examined accordingly. Figure 3.10b shows the comparison of Mn  $L_{2,3}$ -edge of LCMO- $\delta$ C, LCMO- $\delta$ D and LCMO- $\delta$ E. The difference spectrum has its maximum displaced to a lower energy value (indicated by the vertical line in Figure 3.10b). In accordance with Ref. [128], this proves that  $Mn^{4+}$  in LCMO- $\delta$ C is reduced with respect to LCMO- $\delta$ E.

As already mentioned, the origin of these valence changes has been attributed to the presence of antisite disorder in the double perovskite structure [102, 126]. This would place a certain amount of Co ions in  $Mn^{4+}$  sites. As the size of  $Mn^{4+}$  (0.530 Å) is considerably smaller than that of  $Co^{2+}$  in both HS (0.745 Å) or LS (0.65 Å) states, it is forced to move to  $Co^{3+}$  in LS (0.545 Å). Besides, Mn ions moving to Co sites would have enough space to accommodate one extra electron becoming  $Mn^{3+}$  (0.645 Å) [130]. This would imply that cationic order in LCMO- $\delta$ C is deficient while

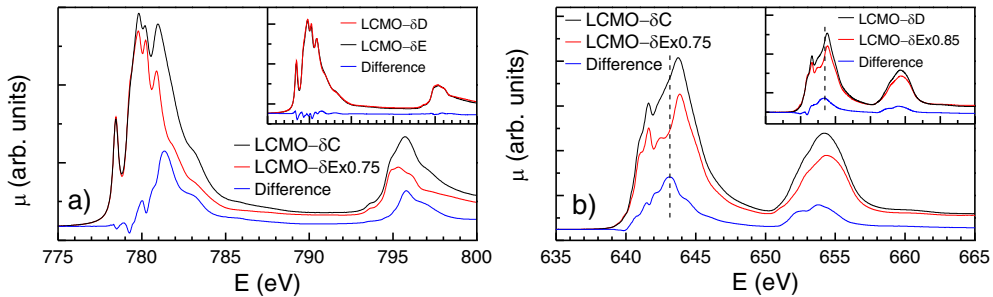


Figure 3.10: a) Co- $L_{2,3}$  XAS of LCMO- $\delta$ C and LCMO- $\delta$ E (the last scaled by a factor 0.75) and the difference between them. The inset compares Co- $L_{2,3}$  spectra of LCMO- $\delta$ D and LCMO- $\delta$ E and plots its difference. (b) Mn- $L_{2,3}$  XAS of LCMO- $\delta$ C and LCMO- $\delta$ E (the last scaled by a factor 0.75) and the difference between these two lines. The inset compares Mn- $L_{2,3}$  spectra of LCMO- $\delta$ D and LCMO- $\delta$ E (this last scaled by a factor 0.85) and the difference between these two. All plotted spectra were collected at 300 K.

in LCMO- $\delta$ E it is optimal. Here we recall that the main difference in the preparation conditions between LCMO- $\delta$ C and the other samples is the annealing process. This would mean that cationic ordering improves during the annealing at 900°C in oxygen atmosphere, in contradiction with studies in bulk that suggest that cationic ordering process freezes below 1000°C [131]. We conclude that the only film presenting a small  $T_C$  ( $\approx 150$ K), due to low oxygen content, has a significant amount ( $\approx 25\%$ ) of trivalent Co ions in LS state. This fact is pointed out as an alternative explanation to the lowering of saturation magnetization found in sample LCMO- $\delta$ B (depicted in Figure 3.2): Co(III) is non-magnetic. On the other hand, in optimized films, divalent Co, high  $T_C$ , and high saturation magnetization rule out a disordered arrangement of Co and Mn ions in the double perovskite structure, which reinforce that FM is induced by superexchange interactions.

### 3.4 SUBSTRATE MISMATCH STRAIN EFFECTS ON MAGNETIC ANISOTROPY

In this section we focus on examining the dependence of the magnetic anisotropy of LCMO films on their strain state. Firstly, we study the evolution of PMA in LCMO films grown on top of STO (tensile case) with different oxygen content. Then we discuss the compressive case: films grown on LSAT and LAO that present IP anisotropy. Secondly, we explore the thickness dependence of the anisotropy on both compressive and tensile strain and quantify anisotropy fields using torque magnetometry.

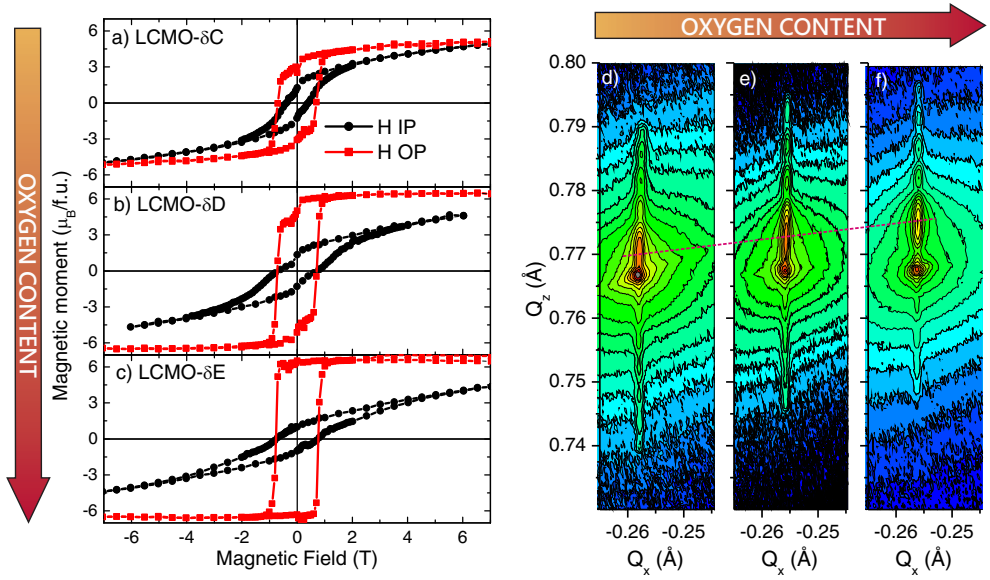


Figure 3.11: (Left) Magnetic moment *vs.* field curves of LCMO- $\delta$ C, LCMO- $\delta$ D and LCMO- $\delta$ E. Curves are taken at  $T=10$  K with the magnetic field applied IP (black) and OOP (red). (Right) RSM around  $(\bar{1}03)$  reflection measured by synchrotron X-ray diffraction for the same samples (LCMO- $\delta$ C, LCMO- $\delta$ D and LCMO- $\delta$ E).

### 3.4.1 Tensile strain case: LCMO/STO

In this section we discuss about the origin of PMA found in samples grown on top of STO, already introduced in section 3.2.1. We have explained that the change of the oxygen stoichiometry promotes the change in the OOP parameter of LCMO on top of the STO substrates (Figure 3.1). This is also proved by RSM performed with synchrotron diffraction on samples with different oxygen content as we can observe in Figure 3.11. Here, additionally, we relate structural properties of these samples with their magnetic properties. Therefore, in Figure 3.11 we show RSM of the  $(\bar{1}03)$  diffraction peak with respect to STO (reproduced from [132]) of LCMO- $\delta$ C, LCMO- $\delta$ D and LCMO- $\delta$ E (right) and their corresponding  $M(H)$  taken with the magnetic field applied both IP and OOP (left). The oxygen content follows the arrow direction.

RSMs prove that the films are epitaxial with the same IP lattice parameters as STO, meaning that films were fully strained and no relaxation was produced. On the other hand, OOP lattice parameter can be derived: 3.901  $\text{\AA}$  for LCMO- $\delta$ C, 3.881  $\text{\AA}$  for LCMO- $\delta$ D and 3.868  $\text{\AA}$  for LCMO- $\delta$ E. This reveals that oxygen content shortens the *c*-parameter.

This change in the cell parameter is a consequence of the lattice volume shrinkage as oxygen approaches the nominal stoichiometric value. As mentioned in section 3.2.1, this is linked to a change in oxidation state: oxygen vacancies promote the appearance of  $\text{Mn}^{3+}$  ions with ionic radius larger than  $\text{Mn}^{4+}$  ions. This volume shrinkage additionally produces an increase of the lattice mismatch as lattice is under tensile strain (lattice mismatch would be +0.6 % for full oxygen stoichiometry).

Regarding the magnetic properties we clearly observe in the hysteresis loops that when the field is applied OOP the magnetization is higher than when it is applied IP. On the other hand, the difference between the two directions is enhanced for films with larger oxygen content. Hence, these results prove that the three samples exhibit PMA and that the strength of the anisotropy changes with oxygen content: the larger the oxygen content the stronger the anisotropy. Besides it is worth to note that saturation magnetization also increases with oxygen content, indicating once more that oxygen deficiency promotes the formation of Co(III) that would imply a lowering of the overall magnetization.

All this observations leads us to formulate the hypothesis that the change of the anisotropy could be attributed to the change in the OOP lattice parameter, so to a change in the strain state of the films. In fact, the shortening of OOP lattice parameter implies shorter Mn-Co distances in the perpendicular direction. This reduction of cationic distances could alter the SOC interaction and consequently, the magnetic anisotropy. We will follow this discussion in chapter 4.

#### 3.4.1.1 Torque measurements

In this section we explore which are the contributions to anisotropy in LCMO films grown on STO by means of torque measurements. Magnetic torque is a useful technique to quantitatively determine the anisotropy field. The experimental procedure consist in gluing a sample to a torque-lever chip mounted on a PPMS holder that enables rotation. We continuously rotate the sample with respect to the magnetic field directions moving from OOP ( $\psi = 0^\circ, 180^\circ$ ) to IP ( $\psi = 90^\circ, 270^\circ$ ). Therefore, at every angle, we measured the torque that the field  $\vec{B}$  makes on the sample due to its magnetic moment  $\vec{m}$ . By means of a piezoelectric system, torque magnetometry measures the torsion of the torque-lever (depicted in Figure 3.12) that appears due to torque force:  $\vec{\tau} = \vec{m} \times \vec{B}$ .

We compare torque measurements of samples of LCMO/STO with different oxygen content (LCMO- $\delta$ C and LCMO-A) and with different thickness (LCMO-A and LCMO-66). The torque as a function of the position of LCMO- $\delta$ C and LCMO-A is plotted in Figure 3.12 for three different temperatures. They exhibit the typical shape corresponding to a system with uniaxial anisotropy [133]. These measurements cor-



robortate that the easy magnetization axis is perpendicular to the film plane and that the magnetic anisotropy is stronger in high-oxygenated sample (LCMO-A).

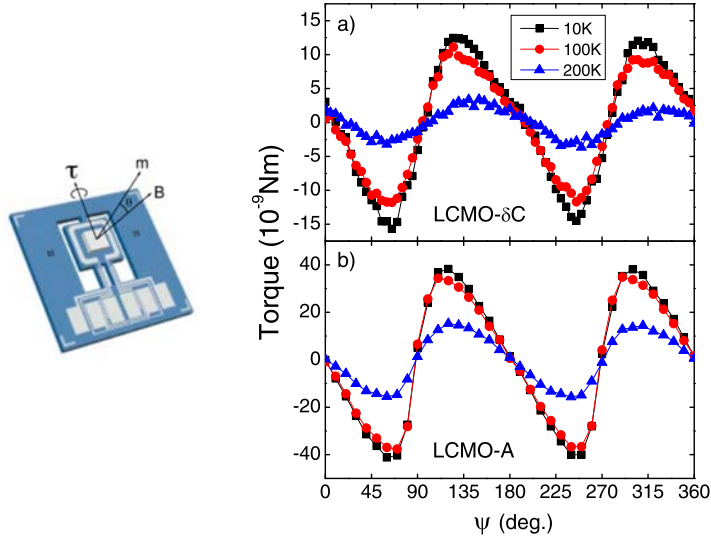


Figure 3.12: (Left) Schematic of the torque-lever chip used in *Quantum Design* PPMS. (Right) Torque needed to rotate samples (a) LCMO- $\delta$ C and (b) LCMO-A in a magnetic field of  $\mu_0 H = 8$ T at different temperatures.

The anisotropy field can be inferred from the maximum value of the torque, and the saturation magnetization through the following expressions:

$$K_1 = \tau_M / V_S \quad (3.1)$$

$$H_A = 2K_1 / M_S \quad (3.2)$$

being  $\tau_M$  the maximum torque,  $V_S$  the sample volume,  $K_1$  the effective anisotropy constant and  $M_S$  the saturation magnetization [133].

In Figure 3.13 we show torque measurements for LCMO-A ( $t=15$  nm) and LCMO-66 ( $t=66$  nm) samples. Using the expressions above we can calculate the anisotropy fields that render  $\mu_B H_A = 6.71$  and 2.75 T for LCMO-A and LCMO-66, respectively. Besides, LCMO-66, gives a  $K_1$  value smaller than LCMO-A (values are 1.64 vs. 1.16 MJ/m<sup>3</sup> for LCMO-A and LCMO-66, respectively). This reduction can be ascribed to the smaller contribution of  $K_s$  term in the thicker sample. The values of  $K_1$  found indicate that  $K_v \approx 1.02$  MJ/m<sup>3</sup> and  $K_s \approx 9.18$  mJ/m<sup>2</sup>. The volumetric term  $K_v$  takes into account the magnetocrystalline, strain, and shape anisotropy terms.

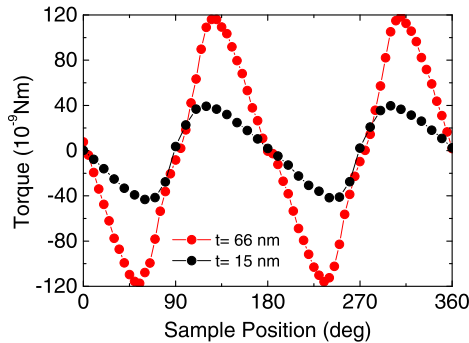


Figure 3.13: Torque needed to rotate LCMO-66 ( $t \approx 66$  nm) and LCMO-A ( $t \approx 15$  nm) in a magnetic field of  $\mu_0 H = 8$  T and at  $T = 10$  K.

The latter term always tends to place the magnetization IP and never OOP.

To clarify the role of structural strain on the magnetic anisotropy, we have grown LCMO films on substrates with different IP lattice parameter LSAT and LAO, with lattice mismatch of  $-0.3\%$  and  $-2.3\%$  respectively.

### 3.4.2 Compressive strain case: LCMO/LSAT and LCMO/LAO

LCMO/LSAT and LCMO/LAO samples have been grown under the same conditions used for growing optimized LCMO/STO samples (see Table 3.1). As a first inspection, morphology has been checked by AFM and structural features have been studied by XRD. Topography images in Figure 3.14a,b reveal step-like surfaces with well defined terraces with RMS values of  $1.7(6)$  nm and  $1.2(6)$  nm for LCMO-LSAT-15 and LCMO-LAO-15, respectively. We also observe the appearance of small mounds similar to the ones found in 15 nm-thick LCMO/STO depicted in Figure 3.5. On the other hand, RSM around  $(\bar{1}03)$  substrate peaks in Figure 3.14c,d show that LCMO/LSAT sample is fully strained (IP lattice parameter estimated from RSM is  $3.87$  Å) while LCMO/LAO sample is partially relaxed (IP parameter is about  $3.84$  Å).

Additionally, high resolution  $\theta/2\theta$  scans around  $(002)$  substrate peak have also been analyzed. In Figure 3.15 observed and calculated intensities, and the difference between both, are plotted. Fitting of the data allows estimating OOP lattice parameters that are about  $3.906(3)$  Å and  $3.912(3)$  Å for LCMO-LSAT-15 and LCMO-LAO-15, respectively. These values are, in both cases, larger than their respective IP parameters and larger than  $c$ -parameter obtained for low-oxygenated LCMO- $\delta C$  [ $3.901(3)$  Å].

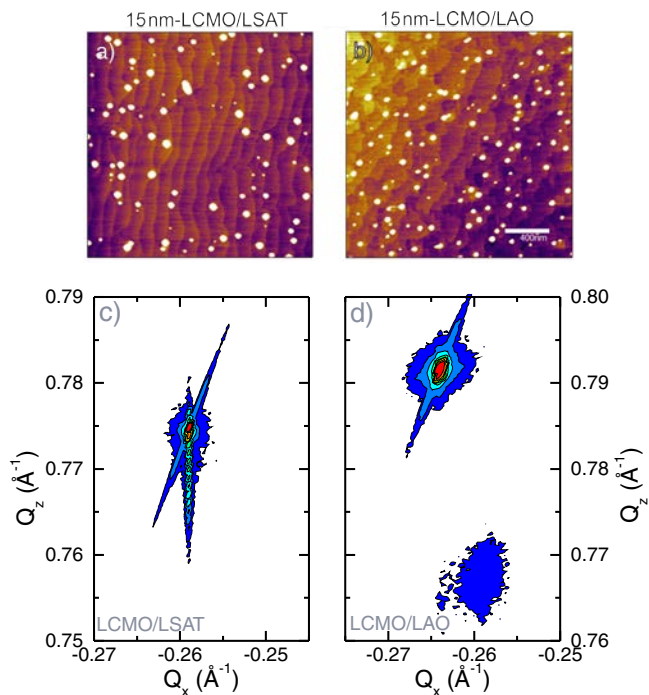


Figure 3.14: Topography image and RSM collected around  $(\bar{1}03)$  diffraction peak of (a,c) LCMO-LSAT-15 and (b,d) LCMO-LAO-15 samples.

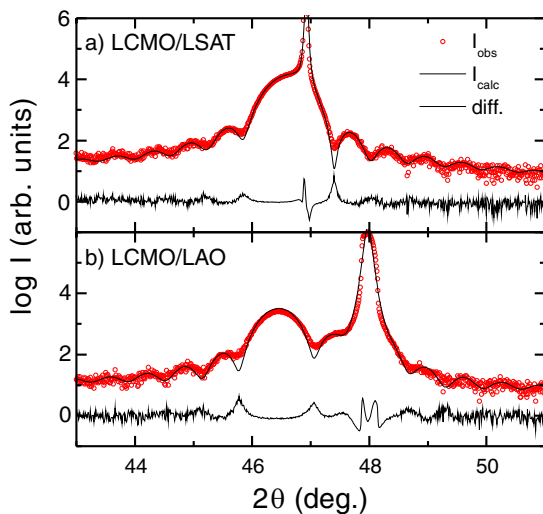


Figure 3.15: Refinement of the high resolution  $\theta/2\theta$  scans collected for (a) LCMO-LSAT-15 and (b) LCMO-LAO-15 samples.

Magnetization *vs.* temperature curves have been measured for both samples in OOP and IP configurations, as it is shown in Figure 3.16. In both cases, the  $T_C$  is around 230 K indicating an optimum oxygen content and film quality. It is also evident that the magnetization IP reaches values much larger than OOP, implying an IP orientation of the easy magnetization axis. Magnetic hysteresis loops also confirm that the magnetization measured IP is always larger than that measured OOP [Figure 3.16 (right)]. In addition, both  $M(T)$  and  $M(H)$  curves suggest that the IP anisotropy is larger in LCMO/LAO than in LCMO/LSAT. This would be in accordance with the larger OOP parameter of the former. On the other hand, Figure 3.16 shows that saturation magnetization reaches  $6 \mu_B/f.u.$ , the expected value for films displaying a good Co/Mn cationic ordering. Coercive fields for IP  $M(H)$  curves are around 0.7 T and 0.8 T for samples LCMO-LSAT-15 and LCMO-LAO-15, respectively, while OOP ones are of 0.045 and 0.06 T. Values of the  $H_C$  for the hysteresis loops measured with  $H$  along the hard magnetization axis are much smaller than in the case of LCMO/STO (as it can be observed in Figure 3.11 the  $H_C$ s for easy and hard axis are nearly the same, e.g. 0.7 T for sample LCMO- $\delta E$ ).

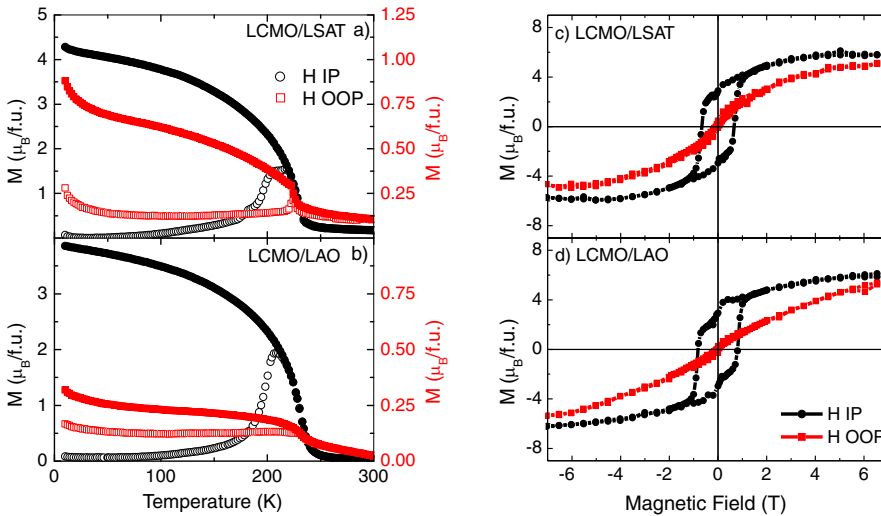


Figure 3.16: Magnetization *vs.* temperature measured under a field of 0.1 T after ZFC (open symbols) and FC (solid symbols) for samples (a) LCMO-LSAT-15 and (b) LCMO-LAO-15 with magnetic field IP (black circles, left axes) and applied OOP (red squares, right axes). Magnetic moment *vs.* field measured at  $T = 10$  K, for samples (c) LCMO-LSAT-15 and (d) LCMO-LAO-15 with magnetic field IP (black squares) and applied OOP (red squares).

### 3.4.3 Thickness dependence

We have examined how the anisotropy varies with film thickness. Samples that present IP anisotropy (compressive case) are candidates to suffer from surface anisotropy when thickness is drastically reduced. As explained in section 1.5 of the Introduction, in thin films the effective anisotropy constant can be expressed as the sum of two terms,  $K_1 = K_v + 2K_s/t$ , where  $K_v$  is the volume,  $K_s$  the surface term and  $t$  the film thickness. The surface term takes into account the anisotropy appearing due to the interfacial and its intrinsic translational symmetry breaking [31]. This term becomes more relevant for thinner films, and usually favors OOP orientation of the magnetic moment.

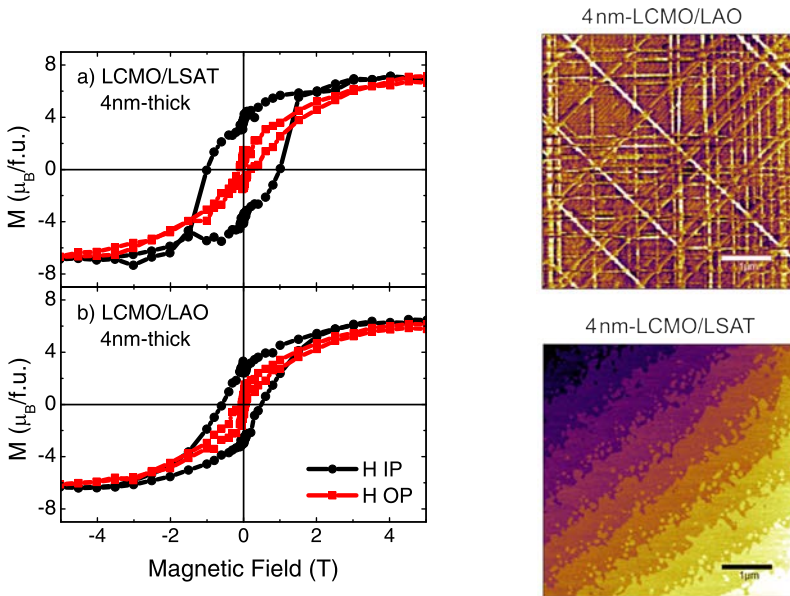


Figure 3.17: Magnetization *vs.* field measured at  $T = 10$  K, for samples (a) LCMO-LSAT-4 and (b) LCMO-LAO-4 with magnetic field IP (black squares) and applied OOP (red squares). Topography for samples (c) LCMO-LSAT-4 and (d) LCMO-LAO-4.

In order to explore the effect of shape anisotropy, very thin samples ( $t=4$  nm) of LCMO grown on top of LSAT and LAO are examined. In Figure 3.17  $M(H)$  curves and topographies for LCMO-LSAT-4 and LCMO-LAO-4 are plotted. Topography images reveal very high quality surfaces. LCMO-LSAT-4 surface reproduces the step terraces of the LSAT substrate with a RMS of 0.6(5) nm. The creation of dislocations formed to release the stress from the lattice, are perfectly visualized in LCMO-LAO-4 image. Nonetheless, step-like structure is also revealed in between dislocations and

it presents a roughness with a RMS value of 0.4(3) nm.  $M(H)$  curves prove that the IP orientation of the easy magnetization axis prevails. Even though magnetization IP reaches larger values than OOP, the difference between both is not as relevant as it is in the case of thicker samples, the differences in the  $H_C$  and remanent magnetization reinforce that the easy axis lays IP. In conclusion, when LCMO suffers compressive strain the effective anisotropy  $K_1$  is negative as anisotropy lies IP, hence  $K_1^{4\text{ nm}} > K_1^{15\text{ nm}}$  (less negative as it has less anisotropy). This implies that  $K_s$  is positive (thus favoring OOP magnetization for the thinnest samples) and  $K_v$  is negative (therefore favoring IP magnetization for the thickest films), being  $K_v$  dominant in all the cases studied.

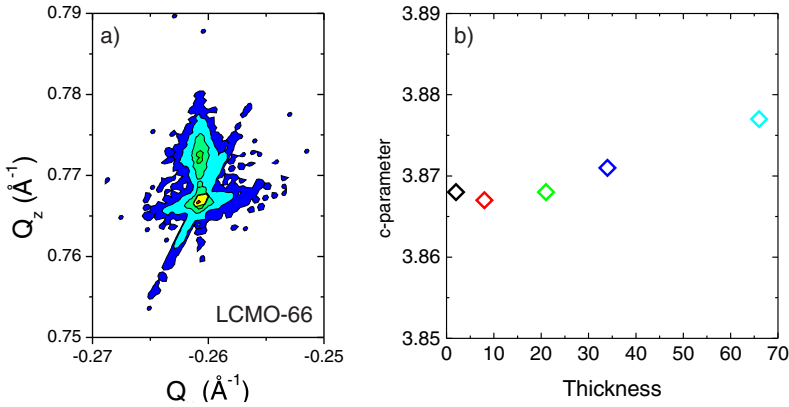


Figure 3.18: (a) RSM around  $(\bar{1}03)$ -STO peak of LCMO-66 and (b)  $c$ -parameter  $vs.$  thickness calculated from  $\theta/2\theta$  XRD scans in Figure 3.4.

With regard to LCMO on STO, we have already presented in section 3.2.1 the characterization of samples with different thicknesses. In order to analyze the strain state as a function of the thickness, here we compute  $c$ -parameter (see Figure 3.18b) obtained from the fitting  $\theta/2\theta$  scans in Figure 3.4. We observe that  $c$ -parameter goes from 3.868 Å for  $t=2.5$  nm to 3.877 Å for  $t=66$  nm thus, a maximum variation of 0.01 Å. We can ascribe the slight increase of  $c$ -parameter for thicker samples ( $t=34$  and 66 nm) to a not optimal oxygenation (not long enough annealing time). The decrease of  $c$  also explains the increase of  $H_C$  in Figure 3.5: the thinner the sample, the higher the strain, and so the magnetic anisotropy and  $H_C$ . Moreover, the RSM shown in Figure 3.18-a reveals that sample LCMO-66 is fully strained by the substrate. Thus, we conclude that no lattice relaxation occurs in the range studied and that all samples present strong PMA, even the thickest one (see Figure 3.5). This is another evidence demonstrating that shape anisotropy does not play an important role in our system.

### 3.5 SUMMARY

In this chapter we have presented a detailed study of structural, compositional and magnetic properties of LCMO thin films grown with different deposition conditions (implying variations in oxygen content) and on different substrates. Both conditions lead to differences in epitaxial strain which dominates the magnetic anisotropy: we found a strong PMA for tensile strain and IP easy-axis for compressive strain.

Regarding the composition of the films we show with EPMA that our films present a deficiency of Co and a real composition  $\text{La}_2\text{Co}_{1-x}\text{Mn}_{1+x}\text{O}_6$  with  $x \approx 0.23$ . However, we confirm through XAS measurements that in optimized LCMO films (with high  $T_C \approx 225\text{K}$ ), off-stoichiometry does not seem to affect the valence of Co ions which is essentially +2, independently of their strain state. Actually, XAS measurements indicate that part of Mn reduces from +4 to +3 to fulfil charge neutrality.

Regarding magnetic properties, strain-dependent anisotropy has been carefully characterized. Remarkably, PMA, that appears in LCMO thin films grown on top of (001)STO substrates, is very strong. By torque measurements we could determine an anisotropy field of  $\sim 7$  T for a LCMO film with  $t=15$  nm. Moreover, torque measurements reveal that the anisotropy field is closely correlated with the degree of oxygen content of the films: the larger the oxygen content, the larger the anisotropy field. We have related this fact to the change in the OOP cell parameter of LCMO with the oxygen content (the larger the oxygen content, the larger the anisotropy and the shorter the OOP cell parameter). In a context of tensile mismatch between substrate and film, the shrinkage of the OOP lattice parameter implies a larger strain. To prove that strain rules magnetic anisotropy, we have further investigated its effect by growing LCMO on top of LSAT and LAO with a smaller IP parameter. This gives rise to films with a larger OOP parameter and a compressive instead of tensile strain. As a result, the easy magnetization axis of LCMO on compressive substrate lies IP.

Finally, by exploring different LCMO film thicknesses, we have determined that the origin of PMA should be magnetocrystalline rather than surface induced. Actually, good magnetic properties have been proved even for very thin films. Having accomplished this objective we can proceed to the implementation of this material in a tunnel junction device.

# 4

## THE ORIGIN OF MAGNETIC ANISOTROPY IN LCMO: XMCD AND THEORETICAL APPROACH

---

In this chapter, we continue the discussion about the origin of magnetic anisotropy in LCMO system introduced in chapter 3. Here we discuss about its magnetocrystalline origin using XMCD experiments and a theoretical approach based on first-order perturbation theory.

### 4.1 INTRODUCTION

As already introduced in chapter 3, a number of magnetic materials epitaxial films show a change in the anisotropy direction under different strain conditions. Of special relevance is the dependence on strain of the magnetic anisotropy found in  $\text{Co}^{2+}$ -containing spinels. Revisiting the example used in section 1.5 of the Introduction, in  $\text{CoCr}_2\text{O}_4$  a compressive strain favors PMA, while a tensile strain favors IP anisotropy [33]. On the contrary,  $\text{CoFe}_2\text{O}_4$  spinel film system coincides with the behaviour of LCMO reported here, in the sense that a tensile stress induces PMA [119, 120], while a compressive strain induces IP anisotropy [121, 122]. In both systems, magnetic anisotropy is attributed to  $\text{Co}^{2+}$  ions.  $\text{CoCr}_2\text{O}_4$  is a normal spinel, where Cr ions occupy octahedral sites and Co ones occupy tetrahedral sites of the structure. In contrast,  $\text{CoFe}_2\text{O}_4$  is an inverse spinel, in which tetrahedral sites are occupied by Fe and octahedral ones by Fe and Co. According to theoretical calculations presented by Heuver *et al.* [33], compressive strain must favor PMA for  $\text{Co}^{2+}$  in tetrahedral environment ( $\text{CoCr}_2\text{O}_4$ ) and an IP easy magnetization axis when it is placed in octahedral environment ( $\text{CoFe}_2\text{O}_4$ ). Consistently, in LCMO, where  $\text{Co}^{2+}$  is in an octahedral environment, we found that a compressive strain favors an IP easy axis. To reach this statement, theoretical calculations in Ref. [33] for iron spinel are based on considering the SOC in  $\text{Co}^{2+}$  and the effect of the CF departing from a per-



fect octahedral environment as perturbations of the other terms of the ground state Hamiltonian. However, the argument developed in Ref. [33] do not predict the case of tensile strain. Here, we present a theoretical calculation on how, departing from a perfect octahedron, a tetragonal distortion, introduced to account for strain, must affect the magnetic anisotropy of  $\text{Co}^{2+}$  in LCMO thin film system. Firstly, in order to confirm experimentally that magnetic anisotropy in LCMO comes from SOC effects due to  $\text{Co}^{2+}$ , we performed XMCD experiments. This is a unique tool allowing studying separately, in an element-specific way, the orbital and spin contributions to the atomic magnetic moment [95, 122].

## 4.2 MAGNETIC ANISOTROPY STUDIED BY X-RAY MAGNETIC CIRCULAR DICHROISM

XMCD experiments have been performed in BL29-BOREAS beamline at ALBA Synchrotron (Barcelona). As a first inspection we compare XMCD data for Mn and Co  $L_{2,3}$ -edges for a standard sample (LCMO- $\delta\text{E}$ ). Thus, in Figure 4.1 we show XMCD signals measured by TEY mode for both spices. The upper part of each plot corresponds to x-ray absorption spectra (averaged over four spectra) taken with left- and right-handed circularly polarized light ( $\mu_+$  and  $\mu_-$ ); the lower part to XMCD spectra obtained from the subtraction  $\mu_+ - \mu_-$  and the dashed line (right axis) to the integral of the XMCD spectra.

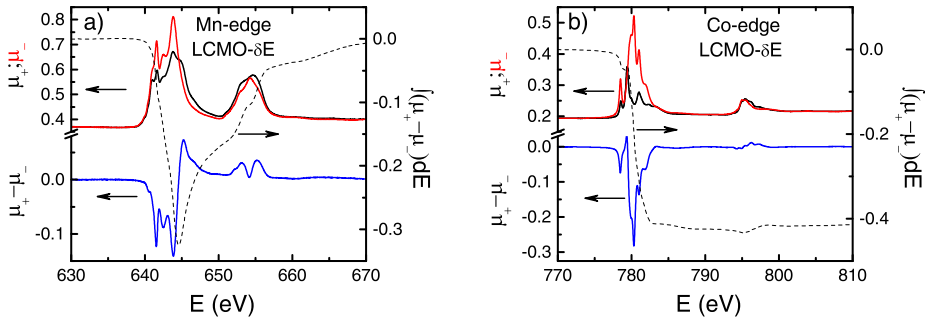


Figure 4.1: Mn- $L_{2,3}$  (left) and Co- $L_{2,3}$  (right) XMCD spectra of sample LCMO- $\delta\text{E}$  at  $T = 20$  K and normal incidence.

The integral curves are used to set the correct limits to calculate integrals for sum rules (see Experimental section). From sum rules we derive the ratio:

$$\frac{m_L}{m_{S_{eff}}} = \frac{\langle L_z \rangle}{\langle 2S_z + 7T_z \rangle} = \frac{-2 \int_{(L_3+L_2)} (\mu_+ - \mu_-) dE}{3[\int_{L_3} (\mu_+ - \mu_-) dE - 2 \int_{L_2} (\mu_+ - \mu_-) dE]} \quad (4.1)$$

where  $L_z$  and  $S_z$  denote the projections of angular and spin magnetic moment over the magnetic field direction.  $T_z$  is the magnetic dipole moment and has been estimated to be negligible in front of  $S_z$  for  $\text{Co}^{2+}$  in octahedral environment [134].

As a first result from Figure 4.1, we observe that the value of the integral  $\int_{(L_3+L_2)} (\mu_+ - \mu_-) dE$  is nearly negligible for Mn (two orders of magnitude smaller than in Co). This is an evidence that magnetic anisotropy must come from Co ions. Therefore, from now on, we center the attention on studying the Co-edge.

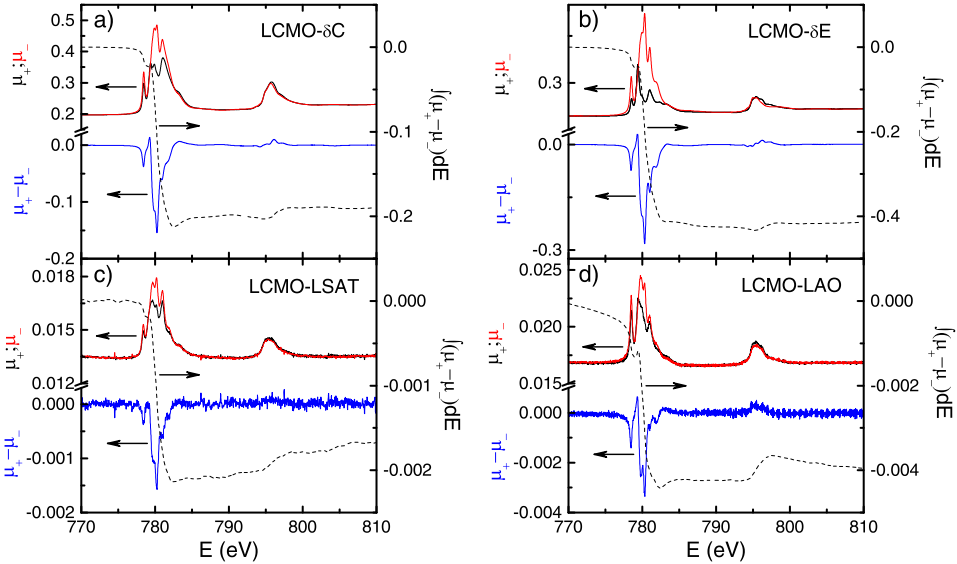


Figure 4.2: Co- $L_{2,3}$  XMCD spectra of (a) LCMO- $\delta\text{C}$  and (b) LCMO- $\delta\text{E}$  (over STO) and samples (c) LCMO-LSAT-15 and (d) LCMO-LAO-15 at  $T=20$  K and normal incidence.

In Figure 4.2 we show Co  $L_{2,3}$ -edge XMCD spectra for different samples (LCMO- $\delta\text{C}$ , LCMO- $\delta\text{E}$ , LCMO-LSAT-15 and LCMO-LAO-15); presenting oxygen-induced and substrate-induced strain variations. All spectra correspond to normal incidence geometry (i.e., with the photons' propagation vector parallel to the vector defining

the sample surface) and are taken at 20 K. It is worth noting that, despite the difference in Co valence between LCMO- $\delta$ C and LCMO- $\delta$ E (discussed in section 3.3), their XMCD signals are spectrally very similar. This fact can be easily understood as the extra Co<sup>3+</sup> detected in LCMO- $\delta$ C is in  $t_{2g}^6 e_g^0$  non-magnetic LS state.

In order to explore the dependence of XMCD signal on strain we performed measurements in normal and grazing incidence conditions (specifically at 20° with respect to the sample surface) and calculate  $m_L/m_{S_{eff}}$  for each orientation. The  $m_L/m_{S_{eff}}$  ratios derived from the analysis of the XMCD spectra obtained on the different samples at two incidence angles are listed in Table 4.1. Analyzing the spectra, its worth noting that the values of the ratio  $m_L/m_{S_{eff}}$  hardly depend on the point where the end of  $L_3$  and the start of  $L_2$  edges are taken. The uncertainty that this introduces to this value has been checked to be below 1%. This value is much smaller than the error introduced by other sources [134].

Table 4.1:  $m_L/m_{S_{eff}}$  ratios derived from the analysis of the XMCD spectra obtained on the different samples at normal (90°) and grazing (20°) incidence. OOP ( $c$ ) lattice parameter is also printed.

Sample name	$c$ -parameter (Å)	$m_L/m_{S_{eff}}$ (90°)	$m_L/m_{S_{eff}}$ (20°)
LCMO-LAO-15	3.910(5)	0.485	0.432
LCMO-LSAT-15	3.906(5)	0.456	0.558
LCMO- $\delta$ C	3.902(3)	0.567	0.581
LCMO- $\delta$ D	3.881(3)	0.608	-
LCMO- $\delta$ E	3.868(3)	0.637	0.560

The values of  $m_L/m_{S_{eff}}$  obtained at normal incidence present a monotonous increase with the strain. With the exception of LCMO-LAO-15, the enlargement (shrink) of IP (OOP) lattice parameter is accompanied by an increase of  $m_L/m_{S_{eff}}$  ratio. This could be a consequence of LCMO-LAO-15 being partially relaxed. On the contrary, at grazing incidence this ratio does not show any clear tendency and its dependence on the strain is much smaller. In particular, for compressive strain (taking into account LCMO-LSAT-15), the  $m_L/m_{S_{eff}}$  ratio found in grazing incidence is larger than that found at normal incidence, while for tensile strain this is reversed. In other words, the largest  $m_L/m_{S_{eff}}$  ratio is found when light propagation and applied field are along the easy magnetization axis.

To reinforce our observations that Mn do not significantly contribute to magnetic anisotropy in LCMO, we have also derived ratios from analysis of Mn edge which are found two orders of magnitude smaller than those of Co. In any case, according

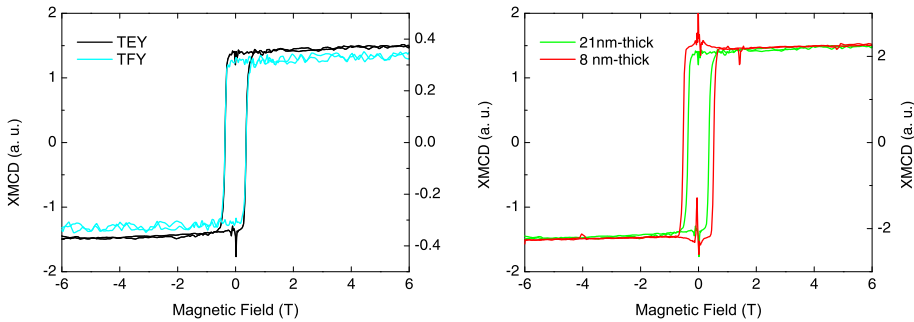


Figure 4.3: (Left) Comparison between hysteresis cycles taken in TEY (black, left axis) and TFY (blue, right axis) modes on LCMO- $\delta E$ . (Right) Comparison between hysteresis cycles taken in TEY for 21 nm-thick (green) and 8 nm-thick (red) LCMO films, LCMO- $\delta E$  and LCMO-8, respectively

to Piamonteze *et al.* [134], sum rules are not fully valid for Mn, so further analysis is not worth it.

On the other hand, hysteresis cycles can be derived from XMCD measurements while ramping the magnetic field. The hysteresis cycles are composed by 4 scans: 1) from +6 to -6T with  $C+$  polarization; 2) from -6 to +6T with  $C+$  polarization; 3) from +6 to -6T with  $C-$  polarization; 4) from -6 to +6T with  $C-$  polarization. Then the resulting cycle will result from subtracting (1) from (3) and (2) from (4). In Figure 4.3 (left) we show hysteresis loops calculated in TEY and TFY modes at  $70^\circ$  of incidence (nearly normal) on LCMO- $\delta E$  sample. The TFY measurement proved that there is no bilobe at zero field similar to the feature observed in SQUID measurements. In TEY signal, although there are some spikes at zero field, there is no sign of a bilobe. We ascribe this noise to limited sensitivity.

In addition, we have compared hysteresis loop of samples with different thicknesses [Figure 4.3 (right)], we observe an increase of  $H_C$  from LCMO-8 with  $t=8$  with respect to LCMO- $\delta E$  of  $t=21$ nm. This goes in accordance with the increase of  $H_C$  observed in SQUID measurements (Figure 3.5): more strain implies an increase of anisotropy and thus, higher coercivity.

Finally, in Figure 4.4 we show hysteresis loop taken in TFY mode at  $70^\circ$  (normal) and  $20^\circ$  (grazing) of incidence for sample LCMO- $\delta E$ , their clear difference and resemblance with SQUID measurements demonstrates one more the expected PMA.

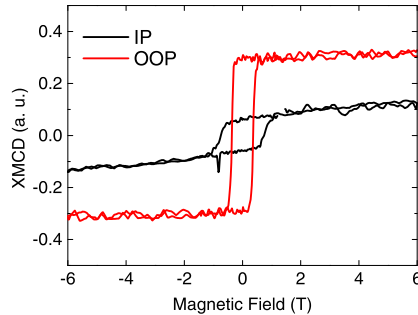


Figure 4.4: Comparison between hysteresis cycles taken in TFY mode for LCMO- $\delta E$  in 70° (red) and 20° (black) incidence.

### 4.3 THEORETICAL APPROACH: ORIGIN OF PERPENDICULAR MAGNETIC ANISOTROPY

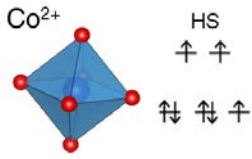
#### 4.3.1 *Effect of tetragonal CF and SOC on $Co^{2+}$ in octahedral environment*

The objective of the magnetic model we have developed is to find the magnetic anisotropy expected for the ideal case in which  $Co^{2+}$  ion is placed in an octahedron with tetragonal symmetry (compressed/expanded along one of the main axes).

As explained in section 1.3.1 in the Introduction, CFT theory consists in describing the physics of a TMO system by an interaction Hamiltonian (as the one in eq. 1.1) and treating it as a perturbative problem. Eigenstates and energy levels of this Hamiltonian are found in the basis of a specific symmetry and treating interactions as perturbation. Therefore in regard with our case of study we will introduce the tetragonal distortion of the  $Co^{2+}$  octahedron and the SOC interaction as perturbations  $H' = H_{CF} + H_{LS}$  of the Hamiltonian. Then we will calculate the matrix elements of  $H'$  in the ground state of unperturbed Hamiltonian. For this, we follow a procedure similar to that presented in Refs. [135, 136] for  $CoCl_2$  in which the octahedra lose cubic symmetry due to a trigonal distortion induced by a compression/expansion along one of the main diagonals of the cube. In our case, as already mentioned, we will consider a tetragonal distortion instead (compression/expansion along one main axis).

The ground state of a free  $Co^{2+}$  ion corresponds to a  $^4F$  term (i.e.,  $L=3$  and  $S=3/2$ ). If we consider the Co embedded in perovskite structure, we have to take into account oxygen octahedral environment. Thus, the model departs from the simplest case

where  $\text{CoO}_6$  octahedra have a perfect cubic symmetry. The cubic CF produced by a perfect octahedral environment, splits the ground state in three levels, two triplets and one singlet. The lowest level is the triplet  ${}^4T_1$  whose eigenstates are [137]:



$\text{Co}^{2+}$

HS

$\uparrow \uparrow$

$\uparrow \downarrow \uparrow \downarrow$

$$\begin{aligned} \varphi_0 &= |30\rangle \\ \varphi_+ &= \sqrt{\frac{3}{8}}|3-1\rangle + \sqrt{\frac{5}{8}}|33\rangle \\ \varphi_- &= \sqrt{\frac{3}{8}}|31\rangle + \sqrt{\frac{5}{8}}|3-3\rangle \end{aligned} \quad (4.2)$$

The triplet is easy to understand by looking the distribution of electrons of  $\text{Co}^{2+}$  in HS ( $3d^7$ ): the unpaired electron in the ground state can be in any of the three degenerate energy levels.

#### 4.3.1.1 Matrix elements of $H_{CF}$

The  $H_{CF}$  term of the perturbation Hamiltonian is the deviation of CF from cubic symmetry. According to Ref. [135], if one assumes that the potential created by neighbouring anions satisfies Laplace's equation, then it can be expanded by spherical harmonics as:

$$V = \sum_{l,m} A_l^m r^l Y_m^l(\theta, \phi) \quad (4.3)$$

where  $l$  and  $m$  are indexes ranging over  $l=0,1,2,3,\dots$  and  $m=-l, -l+1, \dots, l-1, l$ .

Then, a general tetragonal CF is expressed as:

$$H_{CF}^{tet} = A_2^0 r^2 Y_2^0 + A_4^0 r^4 Y_4^0 + r^4 \left( A_4^4 Y_4^4 + (A_4^4)^* Y_4^{-4} \right) \quad (4.4)$$

while for a cubic symmetry it reduces to:

$$H_{CF}^{cub} = A_4^0 r^4 \left[ Y_4^0 + \left( \frac{5}{14} \right)^{1/2} (Y_4^4 + Y_4^{-4}) \right] \quad (4.5)$$

By introducing some considerations the number terms in eq. 4.4 can be reduced. Thus, the tetragonal field differs from cubic one in a term on  $Y_2^0$  and on the fact that of  $A_4^0$  and  $A_4^4$  are no longer related. We have, in a first approximation, ignored this second fact and considered only the first one. Using this approximation, to calculate  $H_{ij}^{CF} = \langle \varphi_i | H_{CF} | \varphi_j \rangle$  matrix elements we have to calculate  $\langle \varphi_i | A_2^0 r^2 Y_2^0 | \varphi_j \rangle$ .

The radial part ( $r$ ) is the same for all the matrix elements as it does not depend on  $m$  but only on  $n$  and  $l$  quantum numbers. Moreover, this term is different from zero, as the integral will only contain positive terms.

Concerning the angular part, by conservation of the third component of the angular moment the unique terms that can be different from zero are those coming from:  $\langle 3\ 0|Y_2^0|3\ 0\rangle$ ,  $\langle 3\ 1|Y_2^0|3\ 1\rangle$ ,  $\langle 3\ -1|Y_2^0|3\ -1\rangle$ ,  $\langle 3\ 3|Y_2^0|3\ 3\rangle$ , and  $\langle 3\ -3|Y_2^0|3\ -3\rangle$ . Their angular parts are given by the integrals  $\int_{\Omega} Y_3^{-m} Y_2^0 Y_3^m d\Omega$  (with  $m=0,1,3$ ) that can be calculated through the Wigner 3- $j$  symbols<sup>1</sup>:

$$\int_{\Omega} Y_{j_1}^{m_1} Y_{j_2}^{m_2} Y_{j_3}^{m_3} d\Omega = \sqrt{\frac{(2j_1+1)(2j_2+1)(2j_3+1)}{4\pi}} \begin{pmatrix} j_1 & j_2 & j_3 \\ 0 & 0 & 0 \end{pmatrix} \begin{pmatrix} j_1 & j_2 & j_3 \\ m_1 & m_2 & m_3 \end{pmatrix} \quad (4.6)$$

The 3- $j$  symbols are an alternative to Clebsch-Gordan coefficients and are related with them as:

$$\begin{pmatrix} j_1 & j_2 & j_3 \\ m_1 & m_2 & m_3 \end{pmatrix} = \frac{(-1)^{j_1-j_2-m_3}}{\sqrt{2j_3+1}} \langle j_1\ m_1\ j_2\ m_2 | j_3\ -m_3 \rangle \quad (4.7)$$

Taking all this into account<sup>2</sup>, the unique matrix elements of  $H_{CF}$  different from zero are  $H_{00}^{CF}$ ,  $H_{++}^{CF}$  and  $H_{--}^{CF}$ . In fact, as we do not know the value of  $A_0^2$ , we will express these three elements in terms of a single parameter named  $\epsilon_{CF}$ . Then, it can be shown that

$$\begin{aligned} H_{00}^{CF} &= 2\epsilon_{CF} \\ H_{++}^{CF} &= H_{--}^{CF} = -\epsilon_{CF} \end{aligned}$$

This means that (before considering SOC),  $\varphi_0$  state, or equivalently  $|30\rangle$ , that is mainly oriented along  $z$  axis, is more affected by the tetragonal distortion of the CF than  $\varphi_{\pm}$ . The exact value of  $\epsilon_{CF}$  would involve the integrals of the radial part and the knowledge of the (unknown) parameter  $A_2^0$  in eq. 4.4. Nonetheless, we can easily deduce the correspondance between the sign of the  $\epsilon_{CF}$  and the type of strain. In the case of tensile strain, where basal distances of the octahedra are larger than apical ones,  $|30\rangle$  must be the state with higher energy and  $\epsilon_{CF}$  must be positive while the

1 Different online tools allow calculating 3- $j$  symbols: e.g. [www-stone.ch.cam.ac.uk/wigner.shtml](http://www-stone.ch.cam.ac.uk/wigner.shtml)

2 Using Clebsch-Gordan (e.g. [www.volya.net/index.php?id=vc](http://www.volya.net/index.php?id=vc)), the angular parts are simplified to:

$$\begin{aligned} \int_{\Omega} Y_3^{-m} Y_2^0 Y_3^m d\Omega &= \sqrt{\frac{1}{12\pi}} \frac{4 \cdot (-1)^{1-m}}{\sqrt{7}} \langle 3\ -m\ 2\ 0 | 3\ -m \rangle \\ &= A(-1)^{1-m} \langle 3\ -m\ 2\ 0 | 3\ -m \rangle \end{aligned}$$

other two states of  ${}^4T_1$  triplet have lower energy. This is in agreement with the expected degeneration of the ground state under tensile stress stated by Heuver *et al.* [33]. In the case of compressive strain  $\epsilon_{CF}$  is negative, and  $|30\rangle$  becomes the ground state (CF only). In Figure 4.5 an scheme illustrating the distribution of energy levels is plotted. It is shown that for the ground state, the unpaired electron in the compressive case is found in a non-degenerated energy level while in tensile case it is in a degenerated one.

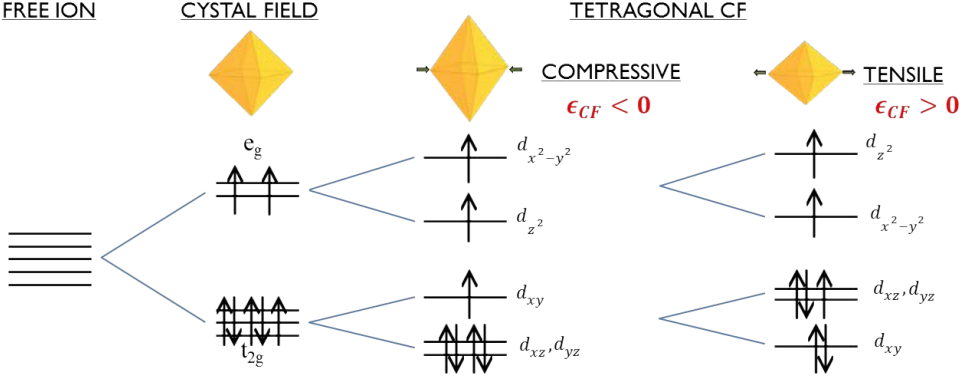


Figure 4.5: Energy level scheme illustrating the effect of a tetragonal distortion of the CF (compressive or tensile) on  $\text{Co}^{2+}$  ion in an octahedral environment.

#### 4.3.1.2 Matrix elements of $H_{LS}$

SOC interaction is introduced as  $H_{LS} = k\lambda\vec{L} \cdot \vec{S}$ , where  $\lambda$  is the spin-orbit constant, that is expected to be negative (for more than half filling  $d$ -shells), and  $k$  is the "orbital reduction factor" (slightly smaller than unity) [135, 136].  $H_{ij}^{LS}$  matrix elements are expressed in the basis of  $|LM_L\rangle$  and  $|SM_S\rangle$  and are calculated using:  $\vec{L} \cdot \vec{S} = L_z S_z + \frac{1}{2}(L_+ S_- + L_- S_+)$ . Then orbital and spin momentum operators must satisfy the following relations:

$$L_{\pm}|LM_L\rangle = M_L|LM_L\rangle \quad L_{\pm}|LM_L\rangle = \sqrt{(L \pm M_L + 1)(L \mp M_L)}|LM_L \pm 1\rangle \quad (4.8)$$

$$S_{\pm}|SM_S\rangle = M_S|SM_S\rangle \quad S_{\pm}|SM_S\rangle = \sqrt{(S \pm M_S + 1)(S \mp M_S)}|SM_S \pm 1\rangle \quad (4.9)$$

Note that in our system  $L=3$  and  $S=3/2$  so that  $M_L = \pm 0, \pm 1, \pm 3$  and  $M_S = \pm \frac{1}{2}, \pm \frac{3}{2}$ . As  $\vec{L}$  and  $\vec{S}$  operators act on different subspaces, the different matrix elements can be obtained by the Kronecker product of the  $L$  and  $S$  matrices:  $L_z \otimes S_z + \frac{1}{2}(L_+ \otimes S_- + L_- \otimes S_+)$ . That is, for instance, in terms of momentum



operator  $L_z$ :

$$\langle \varphi_i | L_z | \varphi_j \rangle = 0 \quad \text{if } i \neq j$$

Then<sup>3</sup>,

$$\langle \varphi_0 | L_z | \varphi_0 \rangle = 0$$

$$\langle \varphi_+ | L_z | \varphi_+ \rangle = 3/2$$

$$\langle \varphi_- | L_z | \varphi_- \rangle = -3/2$$

and all other elements vanish.

The rest of the matrix elements are easily calculated:

$$L_z = \begin{pmatrix} \frac{3}{2} & 0 & 0 \\ 0 & 0 & 0 \\ 0 & 0 & -\frac{3}{2} \end{pmatrix} \quad S_z = \begin{pmatrix} -\frac{3}{2} & 0 & 0 & 0 \\ 0 & -\frac{1}{2} & 0 & 0 \\ 0 & 0 & \frac{1}{2} & 0 \\ 0 & 0 & 0 & \frac{3}{2} \end{pmatrix} \quad (4.10)$$

$$L_+ = \begin{pmatrix} 0 & \frac{3}{2}\sqrt{2} & 0 \\ 0 & 0 & \frac{3}{2}\sqrt{2} \\ 0 & 0 & 0 \end{pmatrix} \quad S_+ = \begin{pmatrix} 0 & 0 & 0 & 0 \\ \sqrt{3} & 0 & 0 & 0 \\ 0 & 2 & 0 & 0 \\ 0 & 0 & \sqrt{3} & 0 \end{pmatrix} \quad (4.11)$$

$$L_- = \begin{pmatrix} 0 & 0 & 0 \\ \frac{3}{2}\sqrt{2} & 0 & 0 \\ 0 & \frac{3}{2}\sqrt{2} & 0 \end{pmatrix} \quad S_- = \begin{pmatrix} 0 & \sqrt{3} & 0 & 0 \\ 0 & 0 & 2 & 0 \\ 0 & 0 & 0 & \sqrt{3} \\ 0 & 0 & 0 & 0 \end{pmatrix} \quad (4.12)$$

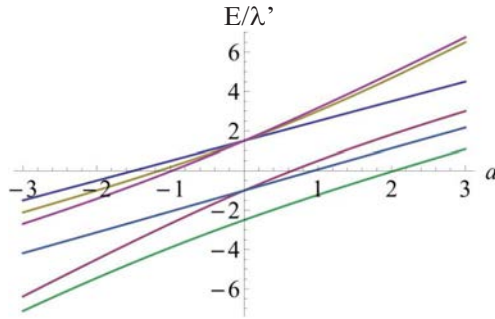
#### 4.3.1.3 First-order perturbation theory

Finally, we use all the matrix elements just calculated to obtain the total matrix elements of  $H'$ . By combining the three states of  ${}^4T_1$  with the four possible spin states we obtain the matrix given in Table 4.2 in terms of parameter  $a = \frac{\epsilon_{CF}}{\lambda'}$  (where  $\lambda' = \frac{-3k\lambda}{2}$ ) that directly relates CF and SOC.

<sup>3</sup> e.g.,  $L_z |\varphi_+\rangle = -1 \cdot \sqrt{\frac{3}{8}} |3-1\rangle + 3 \cdot \sqrt{\frac{5}{8}} |33\rangle \Rightarrow \langle \varphi_+ | L_z | \varphi_+\rangle = \frac{-3}{8} + 3 \cdot \frac{5}{8} = \frac{3}{2}$

Table 4.2: Matrix elements of the perturbation Hamiltonian  $H' = H_{CF} + H_{LS}$  (divided by a common factor  $\lambda' = \frac{-3k\lambda}{2}$ )

	$ \varphi_- -3/2\rangle$	$ \varphi_- -1/2\rangle$	$ \varphi_- 1/2\rangle$	$ \varphi_- 3/2\rangle$	$ \varphi_0 -3/2\rangle$	$ \varphi_0 -1/2\rangle$	$ \varphi_0 1/2\rangle$	$ \varphi_0 3/2\rangle$	$ \varphi_+ -3/2\rangle$	$ \varphi_+ -1/2\rangle$	$ \varphi_+ 1/2\rangle$	$ \varphi_+ 3/2\rangle$
$\langle\varphi_- -3/2 $	$-a-3/2$	0	0	0	0	$-\sqrt{3/2}$	0	0	0	0	0	0
$\langle\varphi_- -1/2 $	0	$-a-1/2$	0	0	0	0	$-\sqrt{2}$	0	0	0	0	0
$\langle\varphi_- 1/2 $	0	0	$-a+1/2$	0	0	0	0	$-\sqrt{3/2}$	0	0	0	0
$\langle\varphi_- 3/2 $	0	0	0	$-a+3/2$	0	0	0	0	0	0	0	0
$\langle\varphi_0 -3/2 $	0	0	0	0	$2a$	0	0	0	0	$-\sqrt{3/2}$	0	0
$\langle\varphi_0 -1/2 $	$-\sqrt{3/2}$	0	0	0	0	$2a$	0	0	0	0	$-\sqrt{2}$	0
$\langle\varphi_0 1/2 $	0	$-\sqrt{2}$	0	0	0	0	$2a$	0	0	0	0	$-\sqrt{3/2}$
$\langle\varphi_0 3/2 $	0	0	$-\sqrt{3/2}$	0	0	0	0	$2a$	0	0	0	0
$\langle\varphi_+ -3/2 $	0	0	0	0	0	0	0	0	$-a+3/2$	0	0	0
$\langle\varphi_+ -1/2 $	0	0	0	0	$-\sqrt{3/2}$	0	0	0	0	$-a+1/2$	0	0
$\langle\varphi_+ 1/2 $	0	0	0	0	0	$-\sqrt{2}$	0	0	0	0	$-a-1/2$	0
$\langle\varphi_+ 3/2 $	0	0	0	0	0	0	$-\sqrt{3/2}$	0	0	0	0	$-a-3/2$


 Figure 4.6: Splitting of the ground state triplet due to the SOC ( $\lambda'$ ) and the CF ( $\epsilon_{CF}$ ), represented by  $a = \frac{\epsilon_{CF}}{\lambda'}$ 

We have solved the secular equation to diagonalize this matrix with *Mathematica*. The eigenvalues as a function of  $a$  are plot in Figure 4.6. We observe that the twelve possible states are split into six spin doublets (Kramers' doublets). The ground state Kramers' doublet is that corresponding to (assuming  $\lambda < 0$ ):

$$\begin{aligned}
 \psi_- &= \alpha|\phi_- \frac{3}{2}\rangle + \beta|\phi_0 -\frac{1}{2}\rangle + \gamma|\phi_+ \frac{1}{2}\rangle \\
 \psi_+ &= \alpha|\phi_+ \frac{3}{2}\rangle + \beta|\phi_0 \frac{1}{2}\rangle + \gamma|\phi_- -\frac{1}{2}\rangle
 \end{aligned} \tag{4.13}$$

being  $\alpha$ ,  $\beta$  and  $\gamma$  coefficients that only depend on parameter  $a$ :

$$\begin{aligned}\alpha &= \frac{1}{N} \left[ -\frac{2}{\sqrt{3}} + \frac{1}{2\sqrt{3}} (1 + 2a + 2\Xi)(2a - \Xi) \right] \\ \beta &= -\frac{1}{N} \frac{1}{2\sqrt{2}} (1 + 2a + 2\Xi) \\ \gamma &= \frac{1}{N}\end{aligned}\quad (4.14)$$

With  $N$  being the appropriate normalization factor and  $\Xi$  the smallest real solution of the equation:

$$-15 - 20a - 16a^2 - 8a^3 + \Xi(-11 - 8a + 12a^2) + 8\Xi^2 + 4\Xi^3 = 0 \quad (4.15)$$

#### 4.3.1.4 Prediction of magnetic anisotropy

In order to address the magnetic anisotropy, one must consider the additional application of a magnetic field. To do so we include in our calculation a Zeeman term that will add a splitting to the Kramers' doublet. Zeeman term is much smaller than other terms and thus, usually introduced as a second perturbation and first-order perturbation theory can be applied to the subspace formed by the Kramers' doublet.

For simplicity, we consider that the field is applied in an arbitrary direction of the  $x$ - $z$  plane :  $\vec{H} = H(\cos\theta, 0, \sin\theta)$ . Then, Zeeman Hamiltonian is expressed as:

$$\begin{aligned}H_Z &= \mu_B(k\vec{L} + 2\vec{S}) \cdot \vec{H} \\ &= \mu_B H \{ (kL_z + 2S_z)\sin\theta + [k\frac{1}{2}(L_+ + L_-) + (S_+ + S_-)]\cos\theta \}\end{aligned}\quad (4.16)$$

Matrix elements within Karmers' doublet subspace are:

$$L_z = \frac{3}{2}(\alpha^2 - \gamma^2) \begin{pmatrix} -1 & 0 \\ 0 & 1 \end{pmatrix} \quad S_z = (\frac{3}{2}\alpha^2 + \frac{1}{2}\beta^2 - \frac{1}{2}\gamma^2) \begin{pmatrix} -1 & 0 \\ 0 & 1 \end{pmatrix} \quad (4.17)$$

$$L_+ = \gamma\beta 3\sqrt{2} \begin{pmatrix} 0 & 0 \\ 1 & 0 \end{pmatrix} \quad S_+ = (2\sqrt{3}\alpha\gamma + 2\beta^2) \begin{pmatrix} 0 & 0 \\ 1 & 0 \end{pmatrix} \quad (4.18)$$

$$L_- = \gamma\beta 3\sqrt{2} \begin{pmatrix} 0 & 1 \\ 0 & 0 \end{pmatrix} \quad S_- = 2\sqrt{3}\alpha\gamma + 2\beta^2 \begin{pmatrix} 0 & 1 \\ 0 & 0 \end{pmatrix} \quad (4.19)$$

and so,

$$H_Z = \mu_B H \begin{pmatrix} -\zeta_1 & \zeta_2 \\ \zeta_2 & \zeta_1 \end{pmatrix} \quad (4.20)$$

with

$$\begin{aligned} \zeta_1 &= \left[ \left( 3 + \frac{3}{2}k \right) \alpha^2 + \beta^2 - \left( 1 + \frac{3}{2}k \right) \gamma^2 \right] \sin \theta \\ \zeta_2 &= \left[ 2\alpha\gamma\sqrt{3} + k\beta\gamma\frac{3}{2}\sqrt{2} + 2\beta^2 \right] \cos \theta \end{aligned} \quad (4.21)$$

The eigenvalues of eq. 4.20 are:

$$\begin{aligned} E_1 &= -\mu_B H \cdot \sqrt{\zeta_1^2 + \zeta_2^2} \\ E_2 &= \mu_B H \cdot \sqrt{\zeta_1^2 + \zeta_2^2} \end{aligned}$$

Then the ground state is the linear combination:

$$\xi = \frac{1}{N} (\psi_- + \Delta\psi_+) \quad (4.22)$$

with  $\Delta = \frac{\zeta_2}{\zeta_1 + \sqrt{\zeta_1^2 + \zeta_2^2}}$  and  $N = \sqrt{1 + \Delta^2}$ .

Finally to relate this solution to magnetic anisotropy in our system, we define the gyromagnetic factor for a field applied along the fourfold axis of the distorted octahedra ( $g_z$ ) and for a field applied in a perpendicular direction ( $g_x$ ). Gyromagnetic factors are defined as  $g = \Delta E / \mu_B H$  for each direction.

According to eq. 4.21, for  $H$  applied OOP ( $\theta = \pi/2$ ),  $\zeta_2 = 0$  and thus,  $E_1^{OOP} = -\mu_B H \zeta_1$  while for  $H$  applied IP ( $\theta = 0$ ),  $E_1^{IP} = -\mu_B H \zeta_2$ . Hence, the ratio between  $g_z$  and  $g_x$ , will be obtained by the ratio between these energy differences and will render:

$$\frac{g_z}{g_x} = \frac{\left( 3 + \frac{3}{2}k \right) \alpha^2 + \beta^2 - \left( 1 - \frac{3}{2}k \right) \gamma^2}{2\alpha\gamma\sqrt{3} + 2k\beta\gamma\frac{3}{2}\sqrt{2} + 2\beta^2} \quad (4.23)$$

Then Figure 4.7 shows the plot of the ratio of these gyromagnetic factors in front of  $a = \frac{2\epsilon_{CF}}{-3k\lambda}$  for  $k = 0.94$  calculated after finding  $\alpha$ ,  $\beta$  and  $\gamma$  coefficients numerically. This ratio crosses the value  $\frac{g_z}{g_x} = 1$  when  $a$  (and then  $\epsilon_{CF}$ ) changes its sign. So under tensile strain, with positive values of  $\epsilon_{CF}$ , we find that  $g_z > g_x$ , and thus PMA is predicted, while for compressive strain, with negative values of  $\epsilon_{CF}$ ,  $g_x > g_z$ , and an IP anisotropy must be expected.

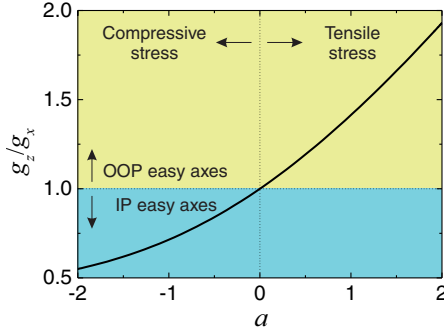


Figure 4.7: Coefficient of gyromagnetic factors in perpendicular ( $g_z$ ) and parallel ( $g_x$ ) directions as a function of the ratio  $a$  relating tetragonal CF and SOC.

#### 4.3.1.5 Prediction of $m_L/m_S$ and comparison with XMCD results

The knowledge of the ground state  $\xi$  (eq.4.22) allows the calculation, for an arbitrary  $\theta$ , of the predicted values of  $m_L/m_S$ . These magnitudes correspond to the expected value of the projections of  $\vec{L}$  and  $\vec{S}$  over the direction of the light propagation (parallel to the applied field) in a XMCD experiment. Using eq. 4.16 we can define  $\langle L_\theta \rangle = \langle L_x \cos\theta + L_z \sin\theta \rangle$ .

This is calculated as follows:

$$\begin{aligned} \langle \xi | L_\theta | \xi \rangle &= \langle \psi_- + \Delta \psi_+ | L_x \cos\theta + L_z \sin\theta | \psi_- + \Delta \psi_+ \rangle \\ &= \Delta \cos\theta [\langle \psi_- | L_x | \psi_+ \rangle + \langle \psi_+ | L_x | \psi_- \rangle] + \sin\theta [\langle \psi_- | L_z | \psi_- \rangle + \Delta^2 \langle \psi_+ | L_z | \psi_+ \rangle] \end{aligned}$$

All the matrix elements can be easily obtained. For  $L_x$  we use the relation  $L_x |LM_L\rangle = \frac{1}{2}(L_+ + L_-)|LM_L\rangle$  and eqs. 4.18 and 4.19 and for  $L_z$  we use eqs. 4.8 and 4.17. Doing the equivalent procedure for  $\langle S_\theta \rangle$ , we arrive to:

$$\begin{aligned} \frac{m_L}{m_S} &= \frac{\langle L_x \cos\theta + L_z \sin\theta \rangle}{\langle S_x \cos\theta + S_z \sin\theta \rangle} \\ &= \frac{\Delta 3\gamma\beta\sqrt{2}\cos\theta + (\Delta^2 - 1)\frac{3}{2}(\alpha^2 - \gamma^2)\sin\theta}{\Delta\left(2\alpha\gamma\sqrt{3} + 2\beta^2\right)\cos\theta + (\Delta^2 - 1)\left(\frac{3}{2}\alpha^2 + \frac{1}{2}\beta^2 - \frac{1}{2}\gamma^2\right)\sin\theta} \end{aligned} \quad (4.24)$$

In order to compare with  $m_L/m_{S_{eff}}$  ratios derived from XMCD experimental data we need to estimate how  $\epsilon_{CF}$  varies with structural parameters. We recall that  $\epsilon_{CF}$  parametrizes the deviation of Co octahedra from a perfect cubic environment. As far as the film cell is tetragonal, when films are fully strained to cubic substrates (STO and LSAT cases), we can, at least for low values of the distortion, consider  $\epsilon_{CF}$  to be proportional to  $(a_{\text{film}} - c_{\text{film}})/a_{\text{film}}$  (where  $a_{\text{film}}$  and  $c_{\text{film}}$  are the IP and OOP cell

parameters of the film). The idea behind this approximation is that for low values of the distortion the most important effect of it is to contract/expand Co-O bond distances instead of inducing a bond bending. As the film cell is tetragonal when films are fully strained to cubic substrates, this parameter renders the tetragonal distortion of the cell. In other words, we assume that octahedra are cubic ( $\epsilon_{CF} = 0$ ) when  $c_{\text{film}} = a_{\text{film}}$ , while a tensile stress makes  $c_{\text{film}} < a_{\text{film}}$  and  $\epsilon_{CF} > 0$  and a compressive strain makes  $c_{\text{film}} > a_{\text{film}}$  and  $\epsilon_{CF} < 0$ .

Figure 4.8 plots the values of the ratio  $m_L/m_{S_{\text{eff}}}$  found by XMCD as a function of  $(a_{\text{film}} - c_{\text{film}})/a_{\text{film}}$  calculated from the cell parameters obtained by XRD (top  $x$ -axis) as compared to  $m_L/m_S$  values calculated from the previous expression which, as mentioned, is a function of  $\frac{2\epsilon_{CF}}{-3k\lambda}$  (bottom  $x$ -axis). For these calculations, we use  $k=0.94$ .

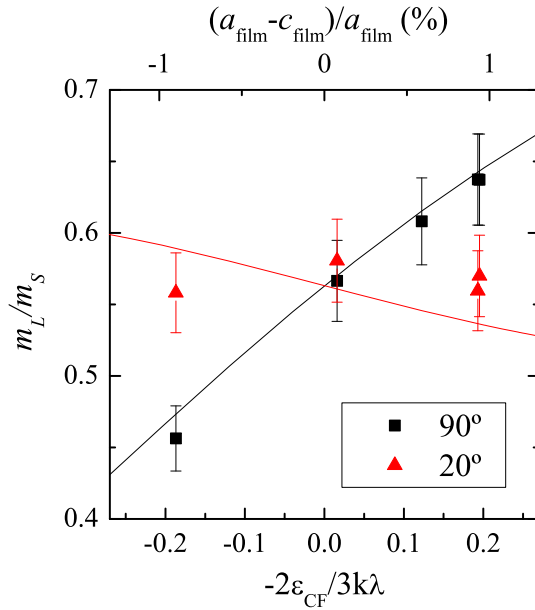


Figure 4.8: Comparison between measured  $m_L/m_{S_{\text{eff}}}$  ratios (symbols) as a function of  $(a_{\text{film}} - c_{\text{film}})/a_{\text{film}}$  (top  $x$ -axis) and predicted  $m_L/m_S$  (solid lines with colour according to symbols' one) as a function of  $a$  ( $= \frac{2\epsilon_{CF}}{-3k\lambda}$ ) parameter (bottom  $x$ -axis).

The comparison of theoretically calculated and XMCD-derived ratios is remarkably good for the normal incidence case. The intersection of the normal and grazing  $m_L/m_S$  curves coincides with the point where the sign of the CF term is inverted. Therefore, it predicts that  $m_L/m_S(90^\circ)$  will be smaller (larger) than  $m_L/m_S(20^\circ)$  for compressive (tensile) strain.

## 4.4 SUMMARY

In summary, we have provided evidence that anisotropy phenomena in LCMO are mainly driven by SOC of  $\text{Co}^{2+}$ . Firstly, XMCD measurements for the different samples in either normal or grazing incidence conditions, evidence a large contribution from the orbital angular moment of Co ions, as expected for  $\text{Co}^{2+}$ , but no contribution from Mn. On the other hand,  $m_L/m_{S_{eff}}$  ratios are computed from XMCD data. We observe a strong dependence of this ratio on the film strain, notably for the normal incidence case.

In addition, we discuss about the possible origin of PMA through simple theoretical approximation. A magnetic model, based on first order perturbation theory, gives a simple description of the relation between the crystallographic structure and the magnetic properties. It is based on considering an idealized case in which strain mainly introduces a tetragonal distortion in an otherwise cubic crystal field. Then adding the effect of spin-orbit coupling acting on  $\text{Co}^{2+}$  in this distorted octahedra enables to predict a strain-dependent magnetic anisotropy (described by gyromagnetic coefficients in each direction). Additionally, we derive spin and orbital magnetic moments from theoretical calculations to obtain a prediction of the dependence of  $m_L/m_S$  with the strain. Finally we make connection between theoretical  $m_L/m_S$  and by  $m_L/m_{S_{eff}}$  determined by XMCD.

# 5

## SPIN DEPENDENT TRANSPORT ACROSS $\text{La}_2\text{Co}_{0.8}\text{Mn}_{1.2}\text{O}_6$ -BASED TUNNEL JUNCTIONS

---

The following chapter comprises the fabrication and evaluation of tunneling transport on a device composed by LCMO barrier sandwiched between non-magnetic electrodes: metal/LCMO/Nb:SrTiO<sub>3</sub>. As the barrier presents strong PMA various phenomena that depend on the orientation of the applied magnetic field appear. In particular, spin filter, tunneling anisotropic magnetoresistance and anisotropic memory effects are analyzed. In order to confirm the transport mechanism to be tunneling, temperature dependent and thickness dependent measurements are performed. Besides two-current model is used to estimate spin filter efficiency. Then the angular dependence on magnetoresistance is analyzed. Finally we report a non-volatile bistable resistive state that can be switched by applying a magnetic field pulse in the out-of-plane or in the in-plane directions conferring the device magnetic memory functionalities.

### 5.1 INTRODUCTION

The generation and control of highly spin-polarized currents is the key ingredient of spintronics in the sense that full polarization enables to manipulate the electron spin as a unit of information. The most straightforward way to get spin polarized currents is to use FM metals. However, the spin polarization degree ( $\approx 40\%$ ) achievable with FM metals is simply too low to obtain high-performance competitive devices [138]. Fully spin polarized currents can be obtained using some complex oxides exhibiting half metallic character, i.e. full spin polarization, although their relatively low resistances compromise their use as spin injectors [139, 140]. Another versatile way is through spin filtering, i.e. spin selective tunneling through a barrier sensitive to spin orientation. In contrast to a non-magnetic insulator, a



ferromagnetic insulating (FM-I) barrier provides two different barrier heights for spin-up and spin-down electrons [141]. Since the tunneling probability depends exponentially on the barrier height, spin selection can be very efficient. In this context FM-I materials have attracted great interest over the past years as spin sources and spin filters [139, 142]. Eu chalcogenides were the first materials used as FM-I barriers convincingly demonstrating spin filtering tunneling effects in magnetic tunnel junction (MTJ)-like structures, even though they suffer from very low ferromagnetic transition temperatures.[141, 143] On the search for magnetic (either ferromagnetic or ferrimagnetic) insulating materials few perovskites ( $\text{BiMnO}_3$ ) [144] and various spinels ( $\text{NiFe}_2\text{O}_4$  [145],  $\text{MnFe}_2\text{O}_4$ [146],  $\text{NiCo}_2\text{O}_4$  [147],  $\text{CoFe}_2\text{O}_4$ [54], and  $\text{CuCr}_2\text{O}_4$  [148]) have been tested for spin-filtering purposes. In most of these cases, spin polarization is measured through Jullière's method by collecting the transmitted current with a ferromagnetic electrode on top of the FM-I barrier. The Meservey-Tedrow technique is another way used to measure the spin polarization employing a superconductor instead of a ferromagnetic collector [54]. Some other works exploit the magnetic field dependence of the tunneling current through the barrier formed in ferromagnet/semiconductor-electrode systems, e.g.  $\text{Fe}_3\text{O}_4/\text{Nb:SrTiO}_3$  and  $\gamma\text{-Fe}_3\text{O}_4/\text{Nb:SrTiO}_3$  systems [55–57]. In these cases the two-current model is used to estimate the spin filtering efficiency. This model assumes two differentiated tunneling channels for the spin-down and spin-up electrons and an additional splitting of the bands due to a Zeeman term when an external magnetic field is considered.

PMA in LCMO-based device confers the material prospects to exhibit tunneling anisotropic magnetoresistance (TAMR). Then TAMR in a NM/FM-I/OS (NM=non-magnetic metal, OS=oxide semiconductor) structure that could operate without magnetic electrodes represents an alternative of much easier technological implementation than conventional MTJs, avoiding the need of two independently controlled ferromagnetic electrodes.

## 5.2 GROWTH AND FABRICATION OF THE JUNCTION

LCMO thin films grown on (001) $\text{Nb:SrTiO}_3$  (Nb:STO) substrates are under tensile strain and exhibit strong PMA (as discussed in chapter 3 for STO case). Nb:STO is a widely used conducting substrate which enable good epitaxy with a large number of oxides, such as  $\text{La}_{0.9}\text{Ca}_{0.1}\text{MnO}_{3+\delta}/\text{Nb:STO}$  [149] or  $\text{La}_{0.7}\text{Sr}_{0.3}\text{MnO}_3/\text{Nb:STO}$  [150, 151] manganite systems. We have fabricated Pt/LCMO/Nb(0.7 %):STO heterostructures with different LCMO insulating barrier thickness (2, 4, 6 nm and without barrier). A capping layer of 3-4 nm of Pt (also tested with Au) has been deposited *in-situ* after annealing, at room temperature, in an Argon atmosphere of 5 mTorr.

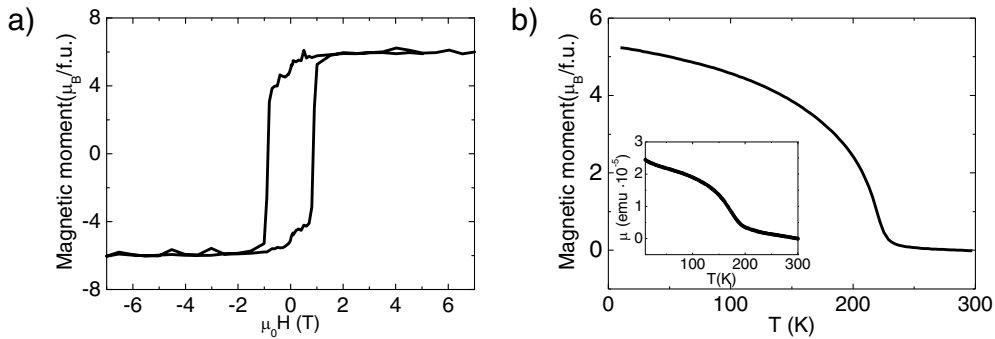


Figure 5.1: Magnetic properties of a 9 nm-thick Pt/LCMO/Nb:STO. The film exhibits bulk-like saturation magnetization, i.e.  $6 \mu_B/\text{f.u.}$ . (Left)  $M(H)$  curve at  $T=10$  K, but with a slightly reduced transition temperature of 220 K ( $T_C \approx 230$  K). (Right) Temperature dependence of the magnetization after a zero field cooling-field cooling process at 0.1 T.

Very thin films show bulk-like magnetic properties with a small reduction of  $T_C$ . In Figure 5.1 magnetic properties for a film of 9nm-thick Pt/LCMO/Nb:STO are shown. Magnetic properties of very thin films (of the order of a tunnel barrier) are difficult to measure via SQUID magnetometry because the magnetic signal of such thin layer is very small, as it is revealed by the  $M(T)$  curve of 2nm-thick Pt/LCMO/Nb:STO sample plotted in the inset of Figure 5.1. Nevertheless, we could prove PMA in 4nm-thick junction by low-temperature (77 K) magnetic force microscopy (MFM) imaging (Figure 5.2b) performed with an Attocube system. In Figure 5.2b the zero-magnetization ferromagnetic domain configuration in the virgin state, after zero-field cooling is visualized. The greater part is composed by an almost equal distribution of up (blue colour) and down (red colour) domains, confirming that the magnetization is perpendicular to the film. The thin white regions (indicating in-plane magnetization) correspond to the domain walls. Figure 5.2a also demonstrates the excellent quality of the surface of the heterostructure with a smooth and terrace-step landscape.

### 5.2.1 Fabrication of nanopillars

Once Pt/LCMO/Nb:STO heterostructure stack has been grown, we proceed with the fabrication process of current-perpendicular-to-plane MTJ device. Two lithographic techniques have been employed: Photolithography and electron beam lithography. Details of the process are explained in chapter 2. E-beam lithography has been used to pattern very small nanopillars (ranging from hundred of nm to few  $\mu\text{m}$  of diame-

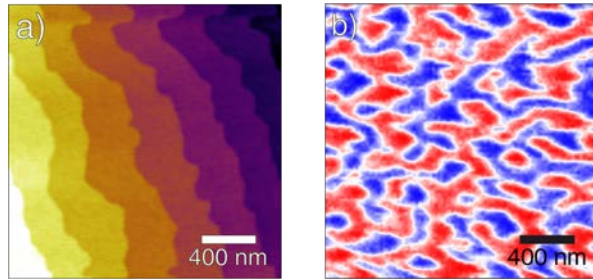


Figure 5.2: (a) Topography and (b) MFM image of Pt/4nm-LCMO/Nb:STO. MFM is measured at 77 K after zero-field cooling. An equal distribution of up (blue) and down (red) domains is observed.

ter). E-beam enables sub-micron structures with more resolution than photolithography while the later is a much faster procedure.

So firstly, we fabricate smaller nanopillar so we can characterize the quality of the junction and the ion milling time using AFM. Once we have optimized the etching process in nanopillars patterned by e-beam, photolithography is used for patterning micrometric patterns for MTJs as there is no need of e-beam resolution.

In the designing of our junctions two photolithographic stages have been performed. First one consist in patterning a 3x3 matrix of 9 rectangular isolated squares from 8-20  $\mu\text{m}$  of side (as the one shown by optical microscopy in Figure 5.3). Afterwards we remove a certain thickness of the exposed material through ion milling. Then we process with the second photolithography stage. We deposit the photoresist in order to electrically insulate the pillars. Then conducting paths to the junction are opened with a microwriter by exposing a micrometric overture ( $\approx 5 \mu\text{m}^2$ ) on each nanopillar. Finally, Pt macrocontacts are deposited by sputtering applying a shadow mask of 9x9 squares on top. Also Pt macrocontact has been sputtered on bottom of Nb:STO in order to ensure good contact when gluing the sample with silver paste on PPMS or C-AFM holders. Figure 5.3 shows and schematic of the device and the optical microscope top view of a nanopillar before depositing the macrocontacts of Pt. The oberture where platinum must contact the nanopillar is observed.

### 5.3 CHARACTERIZATION OF THE TUNNEL JUNCTION BY AFM

AFM enable to characterize the sharpness, the deepness and the electrical isolation of the nanopilars without the need of using further and time consuming lithographic procedures (deposition of macrocontacts and cables). We also wanted to check if

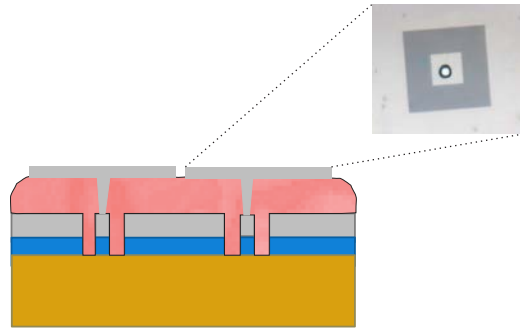


Figure 5.3: Schematic of the device and the optical microscope top view of a nanopillar before depositing the macrocontacts

there is any effect due to the size of the nanostructures and for that AFM (with conducting or magnetic tips) is a technique to exploit.

#### 5.3.0.1 *C-AFM characterization of the pillars*

Firstly we have patterned pillars of sizes ranging from 170 nm to 6  $\mu\text{m}$  diameter using e-beam lithography and ion milling etching. The pattern is depicted in Figure 5.4. We also show the optical microscope image from the AFM set-up and a topography image of a large area of 50x50  $\mu\text{m}$ . In order to optimize the ion milling procedure we compare two different etching conditions: i) eliminating only the Pt capping (3-3.5 nm thick) and ii) penetrating until the substrate (which is 6-8 nm deep). From now on we call the first structure dot and the second one pillar. As a first inspection, analysis of our heterostructure by AFM reveals a very smooth surface (Figure 5.5). The deposition 3.5nm-thick layer of Pt at room temperature on LCMO yields a very flat featureless surface with a RMS of 0.2 nm that perfectly follows LCMO terrace structure. Profile analysis in Figure 5.5c evidences that only Pt layer has been etched in the first lithography process (i). On the other hand, profile analysis in Figure 5.6e, after the second lithography process, shows etched holes of 11 nm deep in a 4nm-thick LCMO heterostructure, proving that the etching procedure has reached the Nb:STO substrate.

Additionally, current maps of a dot (Figure 5.5b) and pillars (Figure 5.6b-d) are measured to prove that structures are electrically isolated. C-AFM has been performed using TiIr and CrPt conducting tips and in a set-up configuration where Nb:STO substrate is contacted with silver paste on the bottom, voltage is applied to the substrate and current is collected by the tip and read by amplifiers are placed in the tip holder.

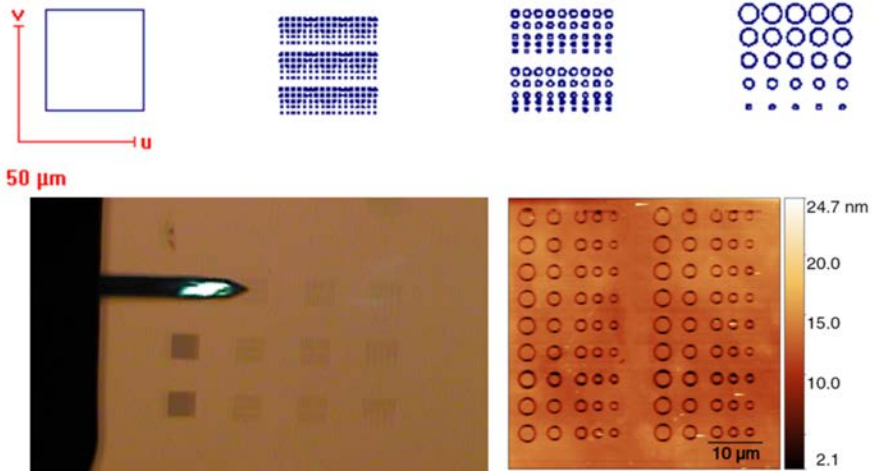


Figure 5.4: (Top) E-beam lithography patterned mask, (bottom left) optical image from AFM revealing a set of lithographed nanopillars under the AFM cantilever and (bottom right) 50x50  $\mu$  m topography AFM image.

Figure 5.7 shows  $I$ - $V$  curves of different positions on Pt/LCMO/Nb:STO and Pt/Nb:STO samples. All curves are composed by various cycles. Here the positive part represents the substrate of Nb:STO and the negative the Pt electrode. Nb:STO is an n-type semiconductor and Pt is a high-work function metal. Based on energy band theory, Ohmic contacts showing linear  $I$ - $V$  curves shape between n-type (p-type) semiconductors and metals with low (high) work function, while Schottky contacts showing rectifying  $I$ - $V$  behaviour between n-type (p-type) semiconductors and metals with high (low) work function [152]. Indeed, the  $I$ - $V$  curve on Pt extension (Figure 5.7a) shows rectifying behaviour more conductive on the positive side. This indicates that the higher resistance encountered in this current path, so the one we measured, is the bottom contact (Pt macrocontact deposited at the bottom of Nb:STO). On the contrary, the  $I$ - $V$  curve on a Pt dot on bare Nb:STO shows (Figure 5.7c, black curve) rectifying behaviour for the negative polarity revealing the Schottky barrier formed between the Pt and the Nb:STO. In Figure 5.7c same curves are plotted recorded with two different amplifiers simultaneously (Dual ORCA cantilever holder from Asylum Research), with a gain of 10  $\mu$ A/V (c-inset) and for a gain of 10 nA/V (c). In the plot in the range of nA the Pt dot curve revealing a different forward and backward curve within the cycle. This is related to interfacial induced resistive switching between Pt and Nb:STO [153]. For pillar structure, where LCMO barrier has been grown, resistive switching phenomena is not observed the curves are reversible over cycling. On the other hand,  $I$ - $V$  curves for dots on LCMO (green

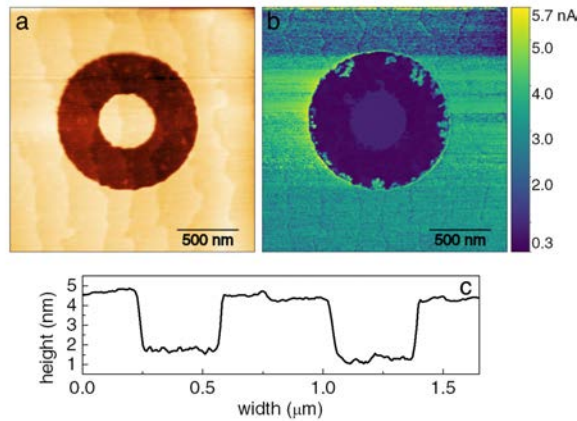


Figure 5.5: Topography (a) and C-AFM characterization (b) of a dot from 4 nm-thick Pt/LCMO/Nb:STO. (c) Profile of line marked in (a) revealing a height around 3.3 nm and a width of 460 nm. C-AFM is performed with a CrPt tip with a  $V_{SetPoint}=0.5$  V and  $V_{Sample}=100$  mV.

curves) are much more resistive and show some inhomogeneous hysteresis cycle for the negative polarity. Therefore current is much more reproducible and stable for pillar structures.

$I$ - $V$  curves on LCMO, on dots and on pillars (Figure 5.7b-c) all show similar rectifying behaviour much more conductive for the negative polarity. Then by comparison we observe that bare LCMO is less conductive than a dot which is less conductive than a pillar. This can be understood as electric field confinement: electric field lines under the dot expand through LCMO while electric field lines in the pillar are limited to the extension of LCMO, having the same lateral size of the contact. Moreover, dots in (b) and (c) have different diameter and thus, the biggest contact (c) (of 1.5 μm) is more conductive than (c) (of 400 nm).

### 5.3.0.2 Low-temperature MFM

In this section we present a magnetic characterization of Pt/LCMO/NbSTO pillars by means of cryogenic MFM. MFM mode enables to map micrometric magnetic features of magnetic films. MFM experiments have been performed in collaboration with Dr. K. Bouzouane at Thales group in CNRS at Unité Mixte de Physique in Paris using an Attocube AFM system that allows reaching temperatures of 77 K when working with liquid  $N_2$ . Since our film has high magnetization and high coercive field ( $M_s \approx 6 \mu_B$  and  $H_C \approx 1$  T), we choose AsyMFM-HC tips from Asylum Research, which has a high coercive field ( $>0.5$ T). These tips have a tip coating of 30nm of CoPt/FePt. In

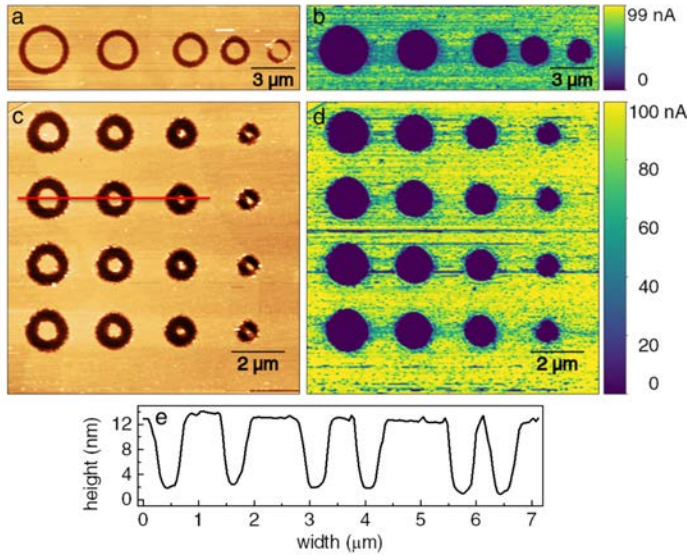


Figure 5.6: Topography (a,c) and C-AFM characterization (b,d) of pillars from 4 nm-thick Pt/LCMO/Nb:STO sample with diameters between 2.5-0.9  $\mu\text{m}$  (a,b) and 750nm to 170 nm (c,d). (d) Profile of line marked in (a) revealing a height around 11 nm and a width of 750, 500 and 300 nm for the three pillar. C-AFM is performed with a TiIr tip with a  $V_{SetPoint}=1$  V and  $V_{Sample}=50$  mV.

Attocube system, the AFM is mounted inside a tube which is introduced into a cryostat after a pumping process to achieve a high vacuum ( $\sim 10^{-6}$  Torr). High vacuum is needed to avoid ice formation when the system is cooled down. For performing our experiment before cooling down and after pumping down we have introduced around 16 mbar of Helium gas. At low temperatures and in vacuum, dissipation of the tip is minimum, Q factor increases orders of magnitude so it is very difficult to follow amplitude changes. In this situation frequency modulation AFM mode is often used. We chose to work in AM-AFM instead, therefore, the introduction of He gas (that will not freeze at 77 K) produces some damping to the tip so the bandwidth in the resonance curve is wider and amplitude changes can be monitored.

In Figure 5.8 we show topography and phase shift images in MFM mode of 4 nm-thick LCMO junction pillars having a diameter of (a) 2.5  $\mu\text{m}$ , (d) 700 nm, (g) 500 and 300 nm. Different scale windows must be used to visualize the magnetic structure on the dot or on its surroundings as MFM signal always appears lower on the dots. This effects could appear due to electrostatic forces that are mixed with the magnetic signal. Electrostatic and magnetic forces are both long range forces and it is very tricky to compensate them. A solution that can solve this issue is to measure

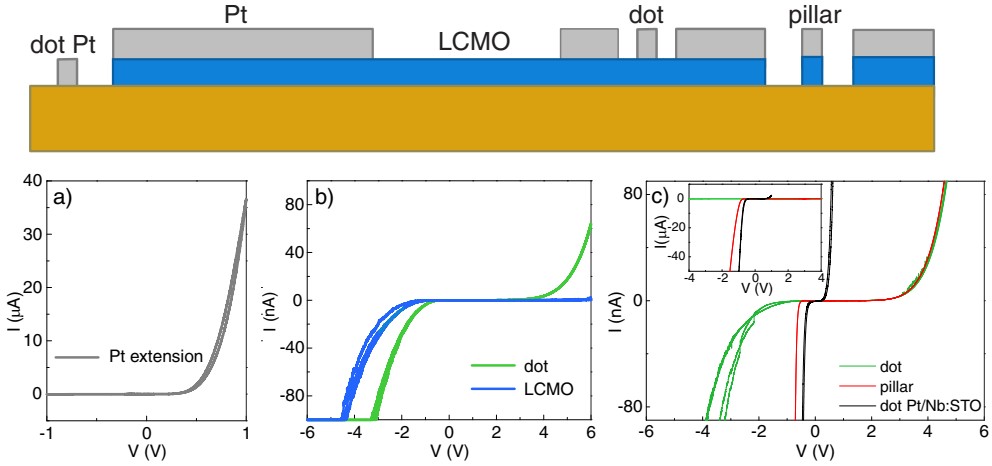


Figure 5.7: Comparison of  $I$ - $V$  curves measured on (a) extension of Pt, (b) on LCMO, (b-c) on dots (only Pt etched) and (c) on pillar (deeper etching, until Nb:STO). In (c) and (c-inset) same  $I$ - $V$  curves are measured with two different current amplifiers with gains of 10 nA/V and 10  $\mu$ A/V, respectively. Dots have different diameters so the bigger is more conductive: 400 nm (b) and 1.5  $\mu$ m (c). Diameter of the pillar is also 1.5  $\mu$ m.

Kelvin probe force microscopy simultaneously in order to vanish surface potential. This is not possible in Attocube system used in here. MFM images of the surrounding (Figure 5.2b) and the larger dot (Figure 5.2c) exhibit a maze patterned composed of alternating blue and red domains similar to the one found in Cu/Ni/Cu/Si [154] and  $\text{Tm}_3\text{Fe}_5\text{O}_{12}/\text{GGG}$  [115] systems possessing PMA. This domain structure is understood as the result of a competition between the magnetostatic energy which favors small domains and the energy cost associated with the creation of domain walls [155]. For the 2.5  $\mu$ m pillars (Figure 5.8c), the diameter is well above the domain width, which is around 200-500 nm. Therefore, the pillar structure exhibits a well defined domain pattern. The domains are the same as for the continuous film (Figure 5.2). Besides, no edge effects are observed, meaning that domains closer to the edge of the pillar do not seem to curve along the side of the structure. Thales laboratory Attocube capabilities enable to apply a relatively weak in-plane magnetic field of (0.4 T, not reaching coercive field of LCMO film). We have checked some pillar images with and without magnetic field applied and no change in the orientation of domains is observed. This could be a prove that no secondary phase near zero field is present in the samples (that could explain the feature around zero field of the  $M(H)$  hysteresis loops).

As the diameter of the pillar is reduced, its size approaches the domain width. In Figure 5.8f, for a pillar of 700 nm we observe red and blue domains with the majority



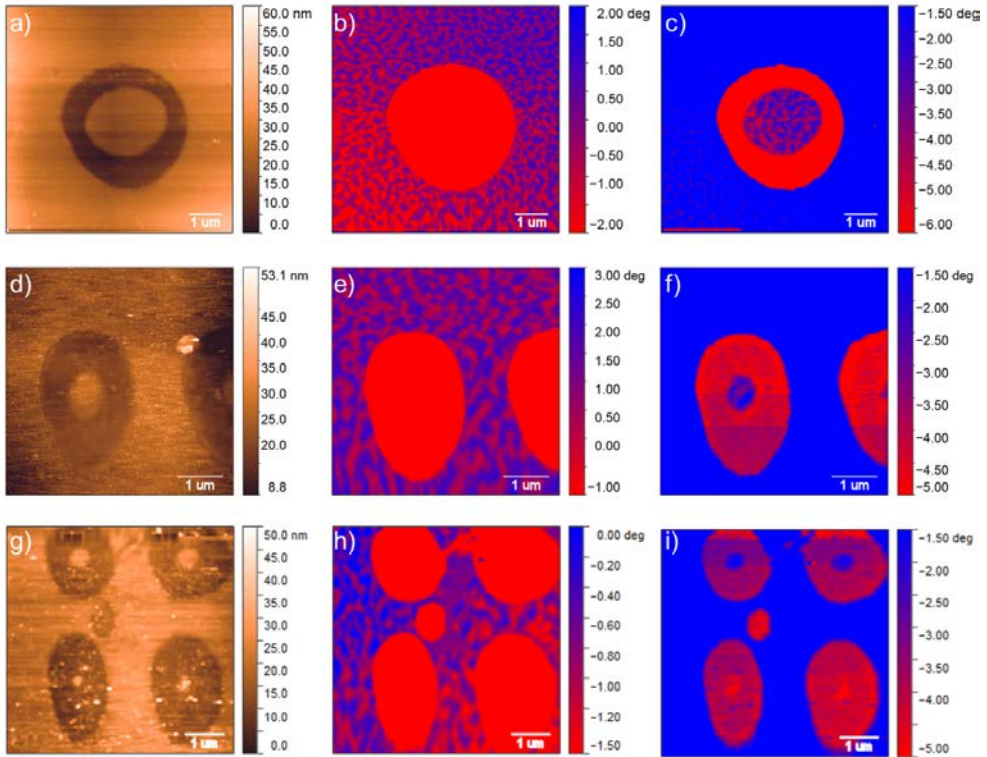


Figure 5.8: (a,d,g) Topography and MFM phase images of pillars of different lateral size: 2.5  $\mu\text{m}$  , 700, 500 and 300 nm diameter)

area covered by blue. Then, for the 500 nm-diameter pillars in Figure 5.8g we observe blue mono-domains and for the smallest pillars (2nd line) of 300 nm of diameter only red contrast is observed. With this MFM characterization, we have exemplified the possibility to engineer the magnetic properties in patterned magnetic nanostructures. That is, having mono-domain nanometric structures, spintronic functionalities as spin filtering could be exploit in this system. For example, having a bottom ferromagnetic layer with the magnetic moment OOP-pinned, we could grow a ferromagnetic metal on top exhibiting PMA, as for instance a thin layer of CoFeB, and by patterning current-perpendicular-to-plane MTJs of less than 500 nm lateral diameter, we could have a device so that smaller magnetic field than 1 T will be sufficient to control top electrode magnetization direction, thus the spin filter effect.

## 5.4 TRANSPORT CHARACTERIZATION OF THE JUNCTION BY PPMS

Measurements are performed in a commercial physical property measurement system (PPMS) where a field up to 9T and a temperature down to 2K can be achieved. A sample holder (as the one shown in 2.5) is mounted in a rotator system. Therefore we use a two-point configuration setup where the current is applied perpendicular to the film plane and the sample is rotated from OOP to IP with respect to an applied magnetic field parallel to [001]. To avoid Joule heating effects the measuring currents has been limited to 1000  $\mu\text{A}$ .

In Figure 5.9 we plot  $I$ - $V$  curves measured on Pt/LCMO/Nb:STO tunneling junctions and a Pt/Nb:STO (without the insulating LCMO barrier) junction at 10 K. The Pt/Nb:STO junction shows a rectifying behaviour characteristic of a metal-semiconductor Schottky junction. Dissimilar electrodes will result in asymmetric  $I$ - $V$  characteristics that depend on the polarity of the voltage applied. In the PPMS measurements we use a contrary in sign of voltage than the one used for C-AFM. We will define forward voltage for positive bias and reverse for negative biased. As Nb:STO is an n-type semiconductor, forward bias corresponds to electrons being injected from the semiconductor to the metal electrode [156]. The insertion of the LCMO insulating barrier implies an increase of the barrier height, i.e. an enhancement of the breakdown threshold voltage. Increasing the thickness ( $t$ ) of the LCMO barrier further increases the barrier width. From the shift of the breakdown voltage evidenced in Figure 5.9, we conclude that the limiting factor for conduction in the Pt/LCMO/Nb:STO system must not be attributed to Nb:STO but to the LCMO barrier itself.

The  $I$ - $V$  characteristic curves of the 2-nm-thick junction measured at different temperatures are shown in Figure 6.7a. The aforementioned rectifying behaviour is observed over the whole range of temperatures (10-300 K).

The behaviour of the forward  $I$ - $V$  characteristics is more clearly displayed in the  $\ln(J)$  vs.  $V$  curves depicted in the inset of Figure 5.10a for some selected temperatures. It is evident from the inset that the curves are linear over several orders of magnitude.

We can analyze these curves taking into account thermionic field emission theory presented in the Introduction of the thesis. Looking at current expressions (eqn. 1.20 and eqn. 1.18) for field emission and thermionic emission and considering  $V > 0$ , we can expand their exponential terms and find a linear dependence of the current with the voltage:

$$\ln(J) = \ln(J_S) + \frac{eV}{nk_B T} \quad (5.1)$$

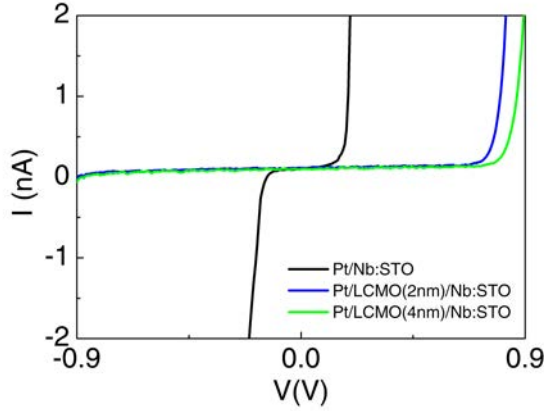


Figure 5.9:  $I$ - $V$  characteristic of junctions of Pt/LCMO/Nb:STO with a LCMO barrier of 2 nm and 4 nm and without barrier taken at 10K. The schematic of the device and measurement configuration is depicted in the inset. Lateral size of the pillars is around  $200 \mu\text{m}^2$ .

$$\ln(J) = \ln(J_S) + \frac{eV}{E_{00}} \quad (5.2)$$

Note that in both cases, the current density depends exponentially on the barrier height but, for thermionic emission, also on the temperature.

We can calculate the slope of the  $\ln(J)$  vs.  $V$  curves. Hence, the temperature dependence of the slope of the  $\ln(J)$  vs.  $V$  curves (with and without applied magnetic field) is depicted in Figure 5.11. We observe that below 50 K the slope is almost constant, above this point it increases with temperature until reaching a maximum at about 150 K and then progressively decreases, entering to a region dominated by thermionic emission. Then, in accordance with the expressions, the constant slope observed at low temperatures indicates that the dominant conduction process in this temperature range is field emission, and demonstrates tunneling through the barrier.

In addition, the field emission process depends on the applied voltage. In fact, at high voltages, it is well described by Fowler-Nordheim tunneling (FNT). As explained in the Introduction, FNT expression can be expressed as:

$$\ln \frac{J}{V^2} \propto \frac{8\pi t \sqrt{2m^*} \Phi_0^{\frac{3}{2}}}{3eh} V^{-1} \quad (5.3)$$

The  $\ln(J/V^2)$ - $V^{-1}$  curve at  $T=10$  K is shown in Figure 5.12. The linear dependence in the high voltage bias regime is indicative of FNT and it is evident above 800 mV. The barrier height can be estimated from the slope obtaining a value of 1.2 eV.

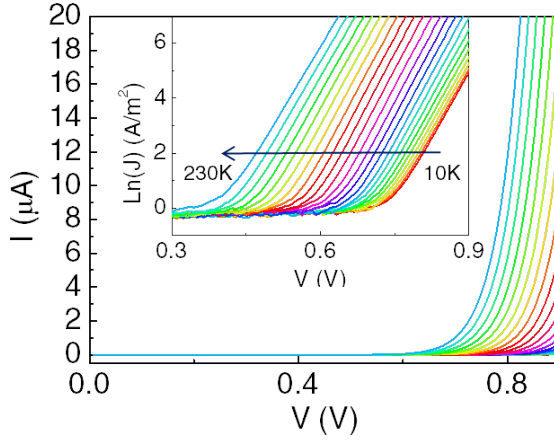


Figure 5.10:  $I$ - $V$  and corresponding  $\ln(J)$ - $V$  (inset) curves of the 2nm-thick junction (with a lateral size of  $200 \mu\text{m}^2$ ) at different temperatures at zero magnetic field ( $T$  from 10 K to 230 K every 10 K are represented).

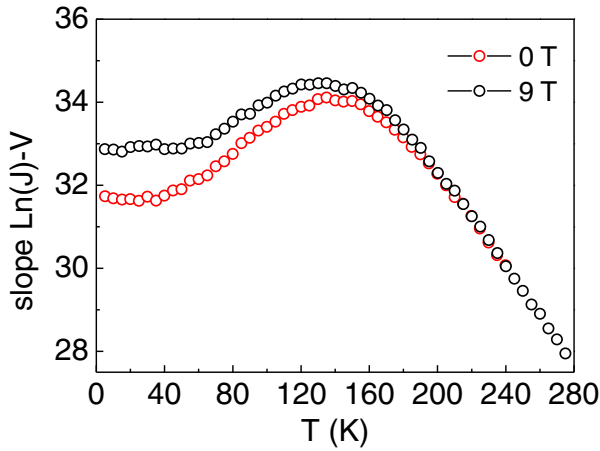


Figure 5.11:  $\ln(J)$ - $V$  slope of the 2 nm-thick junction  $I$ - $V$  curves as a function of temperature at zero field (red) and under 9 T OOP (black).

Finally, in Figure 5.11, we also plot the slope of  $I$ - $V$  measured under a magnetic field of 9 T. We observe that the two sets of measurements (without and with applied magnetic field) start to separate below  $T_C$  ( $\approx 190\text{K}$ ), indicating, as a first inspection, magnetoresistive effects.

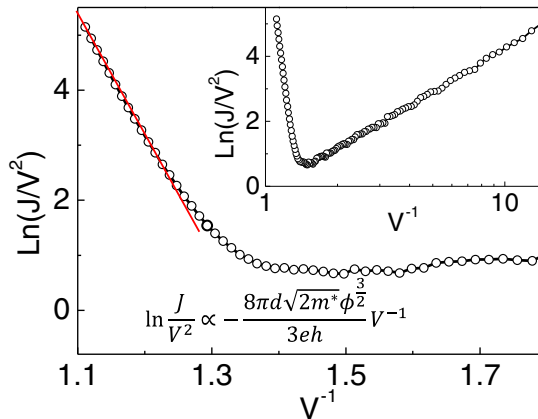


Figure 5.12:  $\ln(J/V^2)-V^{-1}$  plot from the curve at 10 K (from Figure 5.10) to determine the tunnelling transport mechanism. The straight slope in the high voltage region indicates Fowler–Nordheim tunneling.

## 5.5 MAGNETOTRANSPORT PHENOMENOLOGY

In the next section we address the effects of the magnetic field on the transport properties of the junctions. We have explored three spin-dependent effects. The first one is spin-filtering. It describes the spin selective tunneling through a barrier that is sensitive to spin orientation. The second effect is TAMR. It is defined as the dependence of the electrical resistivity on the magnetization orientation of the magnetic field with respect to the sample. Finally, the third spin-dependent phenomena we explore is the capability of our device as a magnetic memory.

These effects are derived from certain features found in magnetoresistance curves. In Figure 5.13 we show the magnetic field dependence of the resistance of a  $200 \mu\text{m}^2$  junction with a 2-nm-thick LCMO barrier at 10 K for a field applied both IP and OOP.

As mentioned in above, the OOP case corresponds to the easy magnetization direction. With the field applied OOP the junction resistance exhibits a large negative MR of about 20% at  $\mu_0 H=9$  T. The hysteretic behaviour shown in the low field regime mimics the features of the magnetization curve: its maxima correspond to the coercive fields. The same behaviour is observed in the IP case. However, a much more modest value of the negative MR is found (2% for  $\mu_0 H=9$  T).

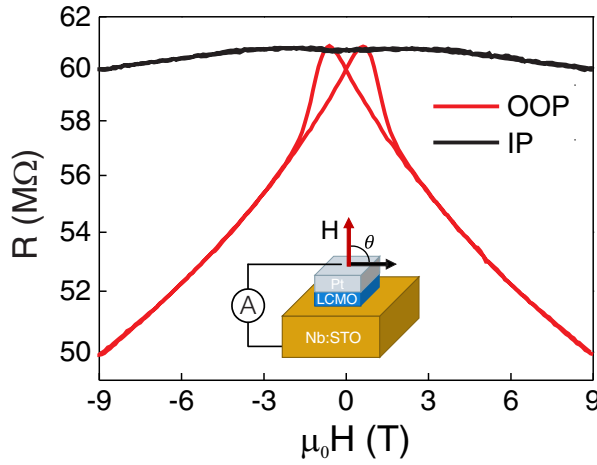


Figure 5.13: Resistance versus field of a  $200 \mu\text{m}^2$  junction of Pt/2nm-LCMO/Nb:STO with the field applied OOP and IP to the sample at 10 K and  $V = 850 \text{ mV}$ .

### 5.5.1 Estimation of spin filtering efficiency

To analyze the dependence of the MR on the applied magnetic field the two-current model was used [56, 57]. According to this model spin-down and spin-up conduction bands of the LCMO lie at different energies. The model has been introduced in the first part of the thesis. The band diagram of the system under study (with forward bias applied) is depicted in Figure 5.14.

When a positive bias  $V$  is applied the Fermi level of the semiconducting electrode increases by  $eV$  [156], accompanied by the corresponding reduction in the bending of the valence and conduction bands. According to two-current model the tunneling barrier  $\Phi_0$  splits into  $\Phi_\uparrow$  and  $\Phi_\downarrow$  due to the exchange splitting  $\Delta$ . At the same time spin-down and spin-up bands are modified by  $\Phi_H$  when a magnetic field is applied. The splitting of the conducting band position into majority and minority spin bands is confirmed by first principles calculations.

In the framework of the two-current model, Equation 1.22 describing the tunneling current density in FNT regime can be rewritten as:

$$J = J_\uparrow + J_\downarrow = A \left[ \frac{1}{\Phi_\uparrow} \exp\left(-c\Phi_\uparrow^{\frac{3}{2}}\right) + \frac{1}{\Phi_\downarrow} \exp\left(-c\Phi_\downarrow^{\frac{3}{2}}\right) \right] \quad (5.4)$$

where  $A = \frac{e^3 V^2}{8\pi \hbar t^2}$  and  $c = \frac{d}{V} \frac{8\pi t \sqrt{2m^*}}{3eh}$  and  $J_\uparrow$  ( $J_\downarrow$ ) is the current density of spin up (down) electrons. In a rigid band approximation, the overall dependence of the  $\Phi_\uparrow$  and  $\Phi_\downarrow$  sub-bands on the applied magnetic field  $H$  ( $\Phi_H$ ) should be described by a Zeeman energy term, namely  $\Phi_H \approx \mu_0 H$ . This linear dependence and the fact

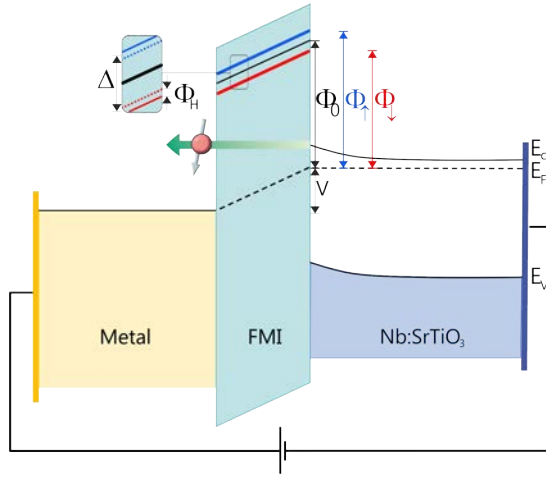


Figure 5.14: Schematics of the band diagram of our experimental configuration with forward applied bias.  $\Phi_0$  is the tunneling barrier and splits into  $\Phi_\uparrow$  and  $\Phi_\downarrow$ . In the zoom  $\Delta$  is the exchange splitting and  $\Phi_H$  is the additional splitting under an applied magnetic field.

that this term is small compared with  $\Phi_0 \pm \Delta/2$  lead to a linear dependence of the  $R(H)$  curve [56]. Note in Figure 5.15a that the dependence in the OOP case is clearly non-linear. Consequently, in the fitting of Eq. (3) to our experimental data (in OOP configuration) higher order terms in the field dependence of the barrier height have been taken into consideration.

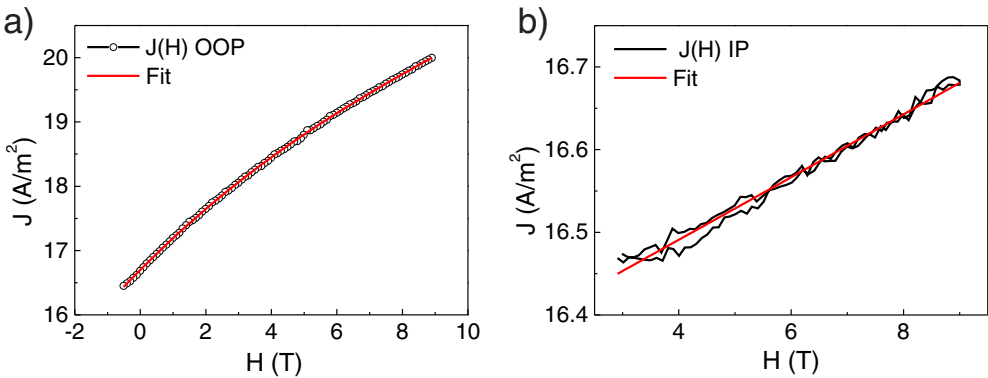


Figure 5.15: Fitting of  $J(H)$  to the two-current model extracted from measurements in 5.13 OOP field in main panel and IP field in the inset

The best fit results from testing  $\Phi_H = \alpha B + \beta B^2 + \gamma B^3$ , as shown in Figure 5.15b, although an acceptable fit is obtained for  $\Phi_H = \alpha B + \beta B^2$ . We first introduced just

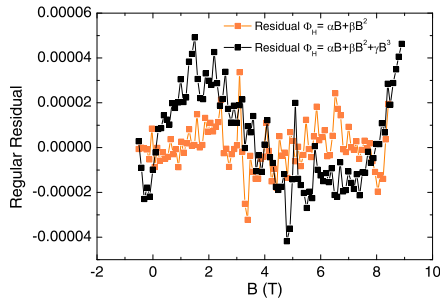


Figure 5.16: Comparison of residuals of the fitting of  $J(H)$  with OOP field applied using  $\Phi_H = \alpha B + \beta B^2$  or  $\Phi_H = \alpha B + \beta B^2 + \gamma B^3$  (orange).

the square term, and it produced a huge improvement of the fitting to  $J(H)$  but we realized that difference (measured-fitted) curve had a cubic-polynomial shape (see Figure 5.16). This made us to introduce a cubic term that further improved very significantly the fitting by reducing the  $\chi^2$  by a factor of 4. Further adding a fourth power term did not significantly improve the refinement.

We also find an estimation of the Schottky barrier of 1.27 eV for the 2-nm-thick barrier in accordance with the value found from FNT fitting of the curve at 10K. The resulting value of the exchange splitting  $\Delta$  is 0.2 eV, in good agreement with values reported in the literature [27] and with our first principles calculations (0.21 eV). The coefficient for the linear term,  $\alpha$  is around 1 meV/T. In contrast, the in-plane configuration actually exhibits the aforementioned linear dependence due to the Zeeman effect (see Figure 5.15 (inset)). In this case, the fitted barrier height and exchange splitting are 1.27 eV and 0.2 eV, respectively, while we obtain  $\alpha = 0.08$  meV/T. The dependence on field of  $\Phi_H$  in IP configuration is similar to the expected value for a pure Zeeman term ( $\mu_B \sim 0.05$  meV/T [57]). For the OOP configuration, it is twenty times bigger.

Explaining the strong difference in the field dependence of the junction resistance observed between the IP and OOP configurations is challenging. We tentatively attribute these differences to the magnetocrystalline anisotropy. As analyzed in chapter 4, LCMO, magnetic anisotropy can be described by the gyromagnetic ratio, this means that at an intra-atomic level, Zeeman energy depends on the direction of the applied magnetic field. It is thus easy to understand that  $\Phi_H$  must depend on the field direction, but it is difficult to understand why the difference is so high and why it introduces non-linear terms. Data regarding this remarkably different behaviour are very scarce in the literature. Nevertheless, related phenomenology can be found in  $\text{Fe}_3\text{O}_4/\text{spinel}/\text{La}_{2/3}\text{Sr}_{1/3}\text{MnO}_3$  magnetic junctions with differ-



ent compounds:  $\text{CuCr}_2\text{O}_4$  [148] and  $\text{CoCr}_2\text{O}_4$  [157]. In these systems the magnetic anisotropy of the ferromagnetic insulating barrier seems to strongly affect the MR.  $\text{CuCr}_2\text{O}_4$  is magnetically isotropic while  $\text{CoCr}_2\text{O}_4$  presents strain-induced magnetocrystalline anisotropy [33]. In these systems, regions where the magnetization of the electrodes/spinel is constant (i.e. no switching of the electrodes/FM-barrier is involved) have very different dependence of the MR on the field. In the case of the  $\text{CoCr}_2\text{O}_4$  barrier, with the magnetic field applied along the easy [001] direction Hu and Suzuki [157] observe a non-linear variation of the MR of 10% within 4 T. Comparatively, for the  $\text{CuCr}_2\text{O}_4$  case with no magnetic anisotropy a variation of only 0.8% is found within 2 T with a nearly linear dependence. Comparing with our experiment, we extract a variation of MR of 12% (OOP curve within 4 T) and 0.5% (IP curve within 2 T) from Figure 5.13.

On the other hand, the analysis of the tunneling current density in the FNT regime by using the two-current model, as given by Eq. (3), allows to estimate both  $J_\uparrow$  and  $J_\downarrow$  and to obtain the spin filtering efficiency of the LCMO barrier,  $P$ , which is given by:

$$P = \frac{J_\uparrow - J_\downarrow}{J_\uparrow + J_\downarrow} \quad (5.5)$$

Fitted parameters render nearly fully spin polarized current with absolute polarization values above 99.7% for the 2-nm-thick sample.

### 5.5.2 Theoretical calculations

To check the validity of our analysis we have explored the electronic structure of  $\text{La}_2\text{CoMnO}_6$  by means of density functional theory (DFT). This calculation have been done by Dr. H. Arramberry from ICMA B.

In more details, density functional theory (DFT) calculations have been performed within the local density approximation (LDA) as implemented the SIESTA-GREEN package [158, 159], employing norm-conserving Troullier-Martins pseudopotentials [160]. The electron-electron interaction is introduced through the LDA+U approach [161, 162], which describes electron correlations through a single effective parameter  $U_{\text{eff}}=U-J$ . We set  $U_{\text{eff}}$  to 3.0 eV for Co and Mn  $d$  shells, as usually employed in the literature for similar compounds [163–165]. SOC was taken into account in the calculations following the self-consistent fully-relativistic pseudo-potential formalism implemented within the SIESTA framework [166]. Self-consistent DOS calculations were performed in a  $12 \times 12 \times 9$   $k$ -point grid using a fine mesh cutoff of 1000 Ry for three-center integrals. We employed a double- $\zeta$  polarized basis set with confinement energies of 100 meV, and the electronic temperature in the Fermi-Dirac distribution was set to  $k_B T=10$  meV in the calculations. When the SOC or the Hubbard terms are

not included in the calculation, the system shows a metallic character meaning that  $\text{La}_2\text{CoMnO}_6$  is a Coulomb-assisted SOC insulator.

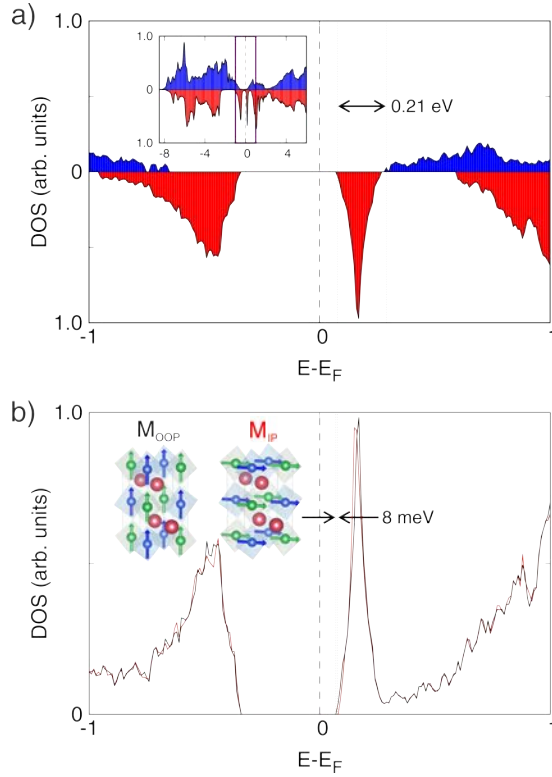


Figure 5.17: (a) Spin resolved DOS obtained by DFT calculations (red filled curve corresponds to spin down and blue one to spin up). The inset shows a view of a wider region in energy. (b) Total DOS obtained by DFT after forcing spins to be oriented in the (001)-direction (OOP, black line) and along (100)-direction (IP, red line). The conduction band minimum lies 8 meV lower when the magnetization points OOP, as indicated.

The obtained spin-resolved DOS for the magnetization perpendicular to the sample plane (OOP configuration), is depicted in Figure 5.17a. It is worth to note that the barrier heights for spin-up and spin down electrons will be determined by the lowest available bands above the Fermi level with the corresponding spin polarization. The polarization of the conduction band (lowest band above Fermi level) will in general depend on the material. In our case, the lowest band comes from unoccupied  $\text{Co}^{2+}$  levels that are spin down because  $\text{Co}^{2+}$   $d$ -levels are more than half filled.

Therefore, spin-resolved DOS renders an insulating ground state with a gap of  $\sim 0.4$  eV. Moreover, the lowest available states in the conduction band are 0.21

eV higher for the spin up species than for the spin down species. The origin of the discrepancy between the obtained gap and the value estimated for the barrier height (1.27 eV) can be two-fold. On one hand, it is well known that DFT calculations within the LDA approximation suffer from a discontinuity in the derivative of the exact exchange correlation energy [167], that drives to an underestimation of the band gap that can be as large as 80% [168, 169]. On the other hand, the value of the electron correlation  $U$ , must affect the gap.

Then, to account for the effect of magnetic field we have performed the calculations with a predetermined axis of magnetization (IP or OOP). In Figure 5.17b we show the total DOS for the system with IP magnetization (red line) and OOP magnetization (black line). While the valence band maximum (VBM) is at the same energy in both cases, the conduction band minimum (CBM) for the OOP magnetization case lies 8 meV below its in-plane counterpart. The conduction band states with lower energy correspond to spin down Co states. Co states are strongly affected by spin-orbit interaction that is at the origin of this energy difference. Although, at a first glance this energy difference could seem very small, it is practically the same as the change in  $\Phi_H$  between the IP and OOP configurations derived from the two-current model (9 meV at 9 T). In conclusion, theoretical calculations confirm that the direction of the magnetization must affect the tunnel resistance, thus predicting the existence of TAMR, and reinforcing the role of the magnetic anisotropy in this system.

## 5.6 ANGULAR DEPENDENCE OF THE TUNNELING JUNCTION RESISTANCE.

The angular dependence of the tunneling junction resistance with respect to the direction of the applied magnetic field 2-nm-thick sample is depicted in Figure 5.18. The right axis of this figure corresponds to the TAMR ratio, which is defined as  $TAMR(\theta)=[R(\theta)-R(90)]/R(90)$ , where  $\theta$  is the position of the sample with respect to the field, and reveals a maximum variation of 20% in the tunneling resistance. The magnetic field is continuously rotated from OOP to IP. A magnetic field of 9T, large enough to ensure full saturation of the magnetization in the field direction, has been used. The expected uniaxial anisotropy is found with the junction resistance reaching a minimum when the magnetic field is applied along the easy axis ( $\theta = 0, 180$ ).

The significant correlation between resistance and the orientation of the sample with respect to the magnetic field, confers the device possibilities to be used as an angular position or rotation sensor. The most commonly used material for sensor using anisotropic magnetoresistance effect is permalloy, which typically has anisotropic magnetoresistance (also known as magnetoresistive coefficient) of 1.5-3%

[170]. Therefore, in our device, the magnetoresistive coefficient reaches 20 %. Additionally, from Figure 5.18 we determine a sensitivity of 3 nA/rad. For magnetic field detection, from Figure 5.13, we obtain sensitivity around 3 nA/T when the magnetic field is parallel to the easy axis of the sensor, thus perpendicular to it. These sensitivity values could be triggered by changing the lateral size of the device.

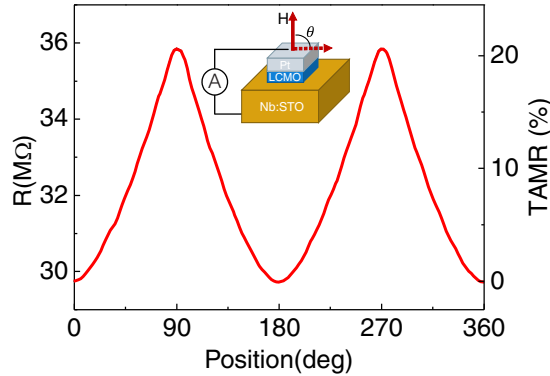


Figure 5.18: Resistance and TAMR *vs.* position of the 2-nm-thick junction with the field rotating from OOP,  $\theta=0^\circ, 180^\circ$  to IP  $\theta=90^\circ, 270^\circ$ . Measurement configuration is depicted in the inset. Measurement is performed at 900mV, 9T and 10K.

#### *Angular dependence in IP configuration*

We have also analyzed the angular dependence of the tunneling junction resistance when the magnetic field is rotated within the plane of the film, as depicted in Figure 5.19. In this configuration the tunneling current is perpendicular to the magnetic field that is rotated. We obtain a fourfold dependence of the TAMR as shown in Figure 5.19. The resistance is lower when the magnetic field is applied along the (100) and (010) crystallographic directions of Nb:STO, corresponding to the (110) and (1-10) directions of LCMO. This result indicates the existence of two in-plane easy magnetization axes along these directions. Nevertheless the TAMR found in the IP configuration is around 1%, much smaller than in the OOP to IP case (20%), confirming the relevance of the magnetocrystalline anisotropy in TAMR.

#### *Temperature and thickness dependence*

The temperature dependence of the TAMR (OOP-IP case) has also been analyzed. TAMR values have been calculated from resistance *vs.* position curves at different temperatures (see Figure 5.20). The TAMR response smoothly decreases with in-

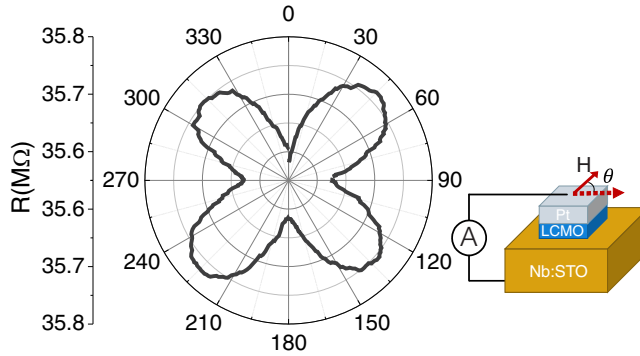


Figure 5.19: Resistance *vs.* rotation of the sample with the field applied IP. Measurement is taken at 9 T, 10 K and an applied voltage of 900 mV. Measurement configuration is depicted beside.

creasing temperature, and vanishes close to  $T_C$ , thus demonstrating that it is linked to the magnetic state of the FM-I barrier.

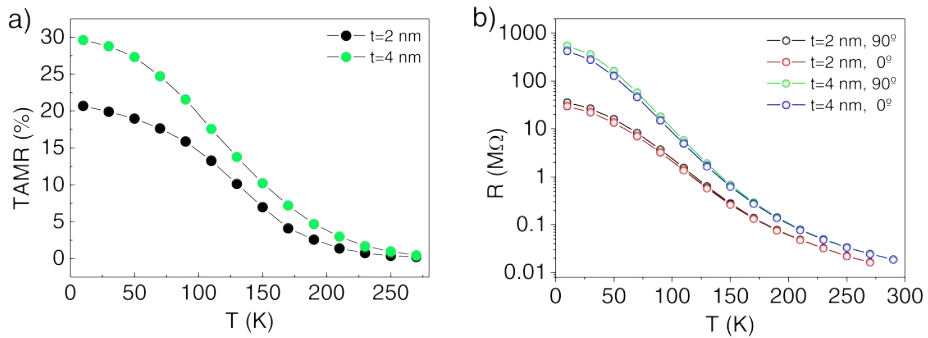


Figure 5.20: (a) TAMR *vs.* temperature (calculated from resistance *vs.* rotation curves) and (b) resistance *vs.* temperature of 2 nm and 4 nm-thick barrier samples with magnetic field applied OOP (red, blue) and IP (black, green).

We have also investigated the TAMR in the 4 nm-thick barrier heterostructure. The results corresponding to Pt/LCMO(4nm)/Nb:STO junction are presented in Figure 5.21. The very same anisotropic behaviour is found irrespective of  $t$ , rendering values of about 30 % for  $t = 4$  nm at  $T = 10$  K. It's worth noting that TAMR response is maximum for low temperatures and vanishes around  $T_C$ .

Besides, as it is observed in Figure 5.20 the difference in resistance between the  $t = 2$  nm and  $t = 4$  nm barriers is of one order of magnitude, proving the exponential dependence of the tunneling current on  $t$ .

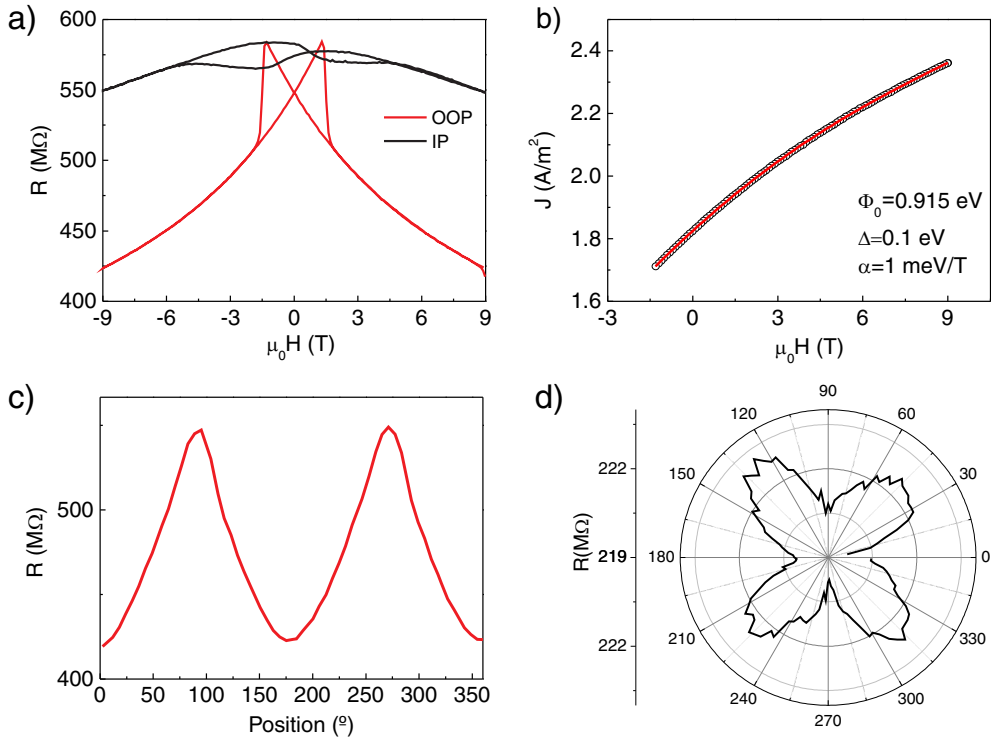


Figure 5.21: (a) Resistance *vs.* field of a  $120 \mu\text{m}^2$  junction of Pt/4nm-LCMO/Nb:SrTiO<sub>3</sub> with the field applied perpendicular the sample at 10K an applied bias voltage of 900 mV. (b) Fitting of  $J(H)$  to two-current model extracted from measurements in (a) for the OOP case. (c) Resistance versus position of the sample with respect to the magnetic field of 9T.

### Voltage dependence

Additionally, we have inspected the TAMR voltage dependence. Firstly, we have measured TAMR for different positive voltages around the voltage where the other measurements were performed (850-900 mV). Figure 5.22 shows a maximum response at  $V$  of 900 mV and then progressively decreases as the applied voltage increases. This reduction of the TAMR as the voltage increases is expected for the FNT regime and the double channel expressions. A similar behaviour is generally found in MTJs and is usually attributed to spin excitations localized at the interfaces between the magnetic electrodes and the tunnel barrier [171].

Secondly, we have explored transport with opposite polarity (reverse voltage) thus, when electrons are injected into the Nb:STO semiconductor. Figure 5.23a shows an asymmetric  $I$ - $V$  curve from -6 V to 1.7 V. TAMR values in Figure 5.23b

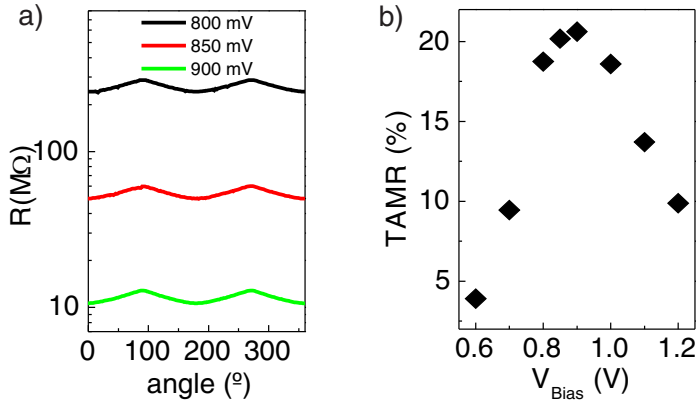


Figure 5.22: (a) Resistance *vs.* rotation of the Pt/2nm-LCMO/Nb:STO sample within a magnetic field of 9T (OOP configuration). (b) TAMR *vs.* applied bias voltage from values extracted from (a).

has been extracted from resistance *vs.* position curves (as the one depicted in the inset) taken at different voltages, at 10 K with 9T of magnetic field applied. It is worth noting that values of resistance at 10 K are: at -6 V around 147 K $\Omega$  and at -1.5 V around 4.7 G $\Omega$ . Voltages around -1.7 give the highest TAMR value of 4.7 % but are highly resistive (1.7 G $\Omega$  at -1.7 V). TAMR decreases with the applied voltage as occurs for positive voltages over 900 mV.

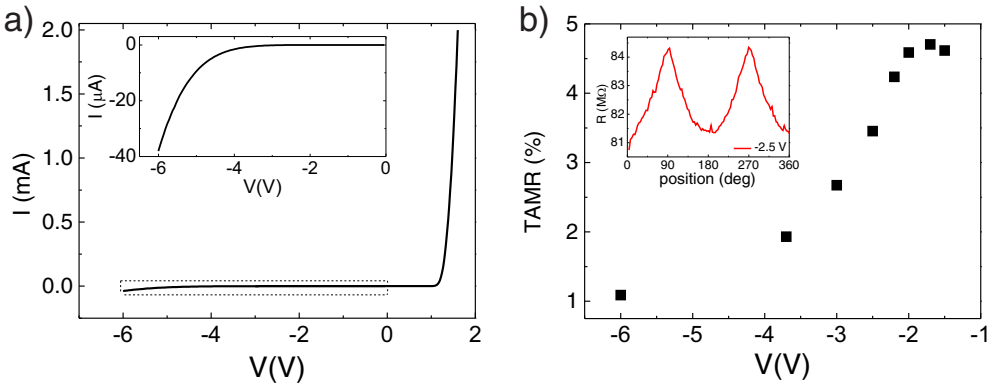


Figure 5.23: (a)  $I$ - $V$  curve from -6 V to 1.7 V on Pt/2nm-LCMO/Nb:STO (dashed area is zoomed-in in the inset). (b) TAMR *vs.* voltage extracted from Resistance *vs.* position curves (inset) with the field rotating from OOP ( $\theta=0^\circ, 180^\circ$ ) to IP ( $\theta=90^\circ, 270^\circ$ ), a negative voltage applied and measured at  $T=10K$  and  $\mu_0H=9T$ .

### Electrode material dependence

We have examined the possibility that magnetoresistive effects are produced by spin-orbit interaction arising from Pt which is a heavy metal known to possess strong SOC. For that we have prepared junctions with Au instead of Pt as the top electrode. In comparison with Pt, Au has much smaller spin orbit coupling [47]. Using metals such as Cu or Al would be much more conclusive than Au for the comparison. The problem for using these metals is that our samples can present a deficient oxygen stoichiometry and these metals can easily oxidize by capturing oxygen from the film. Au is a noble metal which should not give problems of oxidation. Therefore, possessing less spin orbit coupling than Pt gives the same phenomenology, even of the same order of magnitude (see Figure 5.24).

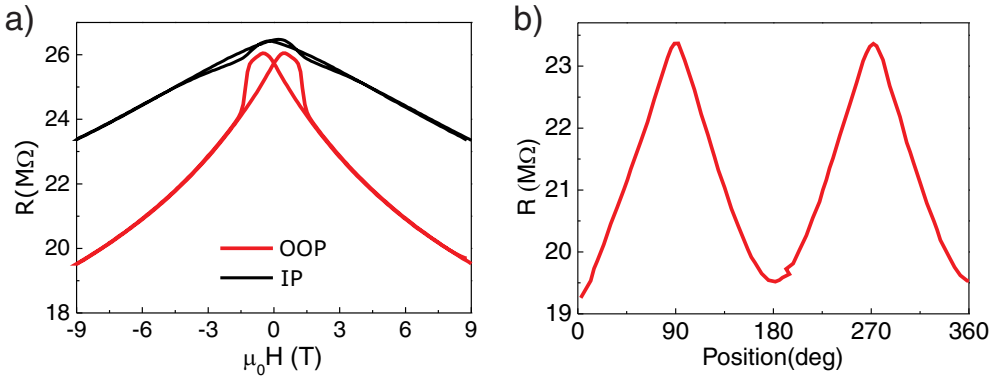


Figure 5.24: (a) Magnetic field dependence of the resistance of a  $200 \mu\text{m}^2$  junction of Au/2nm-LCMO/Nb:STO. with the field applied perpendicular (red) and parallel (black) to the sample plane. (b) Dependence of the resistance on the relative orientation of the sample with respect to the magnetic field of 9T. Measurement performed at  $T=10$  K and  $V=800$  mV.

### 5.6.1 Memory device

Revisiting Figure 5.13a we observe a clear difference between the zero-field resistance of the IP and OOP configurations. We examine the possibility of designing a memory device exploiting these two distinct remanent states.

In Figure 5.25a we plot the results of successive cycles of applying/releasing field along the IP and OOP directions. A field applied parallel or perpendicular to the sample surface ( $H_{IP}$  and  $H_{OOP}$ ) is ramped to 5 T and back to zero, and then, the resistance



is measured in zero field during 300 s. Two resistance states are clearly differentiated and reproducible over several repetitions.

The stability of those states has been tested by measuring the relaxation of the resistance for long periods of time, as it is shown in Figure 5.25b. We found that the variations in the resistance after relaxation times of about  $10^5$  s are nearly negligible in both cases, thus demonstrating high retention power.

Therefore, we have proved that Pt/LCMO/Nb:STO structures present two well defined stable memory states separated by up to 1-2 % in resistance. The magnitude of this effect is small but comparable to other bistable resistance memory systems [172]. Nonetheless this system is unique and much simpler, in the sense that it is based on only one ferromagnetic insulating layer.

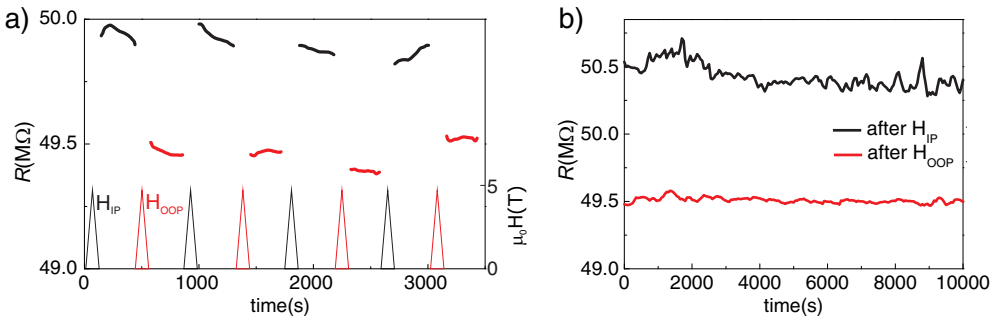


Figure 5.25: (a) Resistance measured during 300 s after applying/releasing a field of 5 T along the OOP direction (black lines) and IP direction (red lines). (b) Long time measurement ( $10^5$  s) of the two resistance states after a 9 T pulse OOP and IP.

## 5.7 SUMMARY

In the present chapter, we report a spintronic device based on a ferromagnetic insulating barrier of LCMO sandwiched between non-magnetic electrodes. The structure consist of a very thin film (2-4 nm thick) of LCMO grown on a semiconducting Nb:STO substrate and capped with a thin layer of metal (Pt or Au). As proved in previous chapters, uniquely, LCMO presents strong perpendicular magnetic anisotropy.

Various spin functionalities have been explored. Firstly, we discuss about the possibility of estimating spin-filtering effect using Fowler-Nordheim and two-current models from the analysis of the magnetoresistance curves. We obtain an estimation of spin-filtering efficiency of 99.7%.

Magnetoresistance curves evidence a strong non-linear dependence of the resistance on the applied magnetic field when this is along the easy axis (OOP) while a linear and much smaller dependence when the field is applied IP. This gives the device capabilities for position sensor applications. As a result, the tunneling MR is highly anisotropic leading to TAMR values of about 20-30% when the magnetization is rotated from OOP to IP. TAMR of 20% is obtained for 2nm-thick barrier while 30% is reached for 4nm-thick one. However, this brings with it an increase of the resistance of one order of magnitude, evidencing the exponential dependence of the tunneling current on barrier height. Besides, temperature dependence gives a maximum response of TAMR at 10 K which vanishes around  $T_C$  following de magnetization *vs.* temperature expected dependence.

These results are corroborated by DFT-based calculations. We demonstrate that the density of states of LCMO has a fully polarized spin-down character above the Fermi level. On the other hand, we estimate a difference in the tunnel barrier height of 8 meV when magnetization changes from OOP to IP, and an exchange splitting of 0.2 eV, in good agreement with values fitted experimentally.

Furthermore, we have shown that the junction can operate as a magnetic memory device by probing the existence of a non-volatile bistable resistive state that can be switched by applying magnetic field pulses in perpendicular or parallel directions. Notwithstanding that our device works below room temperature and using high magnetic fields, it is a prove of concept of a single layer ferromagnetic memory with electrical read-out. These findings heighten the potential of using ferromagnetic insulators with strong magnetic anisotropy for spin filtering, sensing and data storage applications.



# SURFACE CHEMICAL STRUCTURATION IN $\text{La}_{0.7}\text{Sr}_{0.3}\text{MnO}_3$ FILMS: STUDY OF THE LOCAL TRANSPORT PROPERTIES

---

In this chapter we present a study of the formation of two coexisting chemical terminations on the surface of LSMO on (001)STO:  $\text{La}_{0.7}\text{Sr}_{0.3}\text{O}$  and  $\text{MnO}_2$ . The two terminations have been identified by means of spatially resolved techniques, as AFM and X-ray photoemission electron microscopy (X-PEEM), correlating morphological, compositional and electrical measurements. On the other hand, we also study local transport properties (measured by C-AFM) and how they are linked with work function and electronic properties at the surface (measured by X-PEEM). Finally, we discuss about the appearance of RS phenomena and how it is influenced by the termination.

## 6.1 INTRODUCTION

The fabrication of epitaxial oxide thin films with well-defined atomically sharp interfaces relies on the successful realization of atomically flat and single-terminated substrate surfaces. On one hand, it is known that good quality epitaxial oxide thin film growth requires the use of single crystalline substrates with the appropriate lattice parameter. On the other hand, the stoichiometry of the topmost surface plane of the substrate determines the atomic stacking sequence of the deposited films and, therefore, the use of substrates having a unique chemical termination is a critical issue for obtaining sharp heteroepitaxial interfaces. Nevertheless, increasing interest in these issues arises from the possibility of modulating the interface properties, to control their impact on the films grown on top. Albeit a wise approximation consists in using substrates with nanostructured chemical terminations[173–178], simpler

procedures without the need of substrate structuration are desired. In this context, we present a way to obtain nanostructured 3D architectures in which both chemically sharp (bottom) and modulated (top) interfaces can be integrated within the same fabrication process. During epitaxial growth on vicinal surfaces, presenting atomic steps due to the substrate miscut, most atoms impinging the surface diffuse long enough to attach to the step edges. In this scenario nucleation of islands on the terraces may be neglected and growth proceeds by step flow. However, ideal step flow may break for specific values of the parameters governing surface evolution (temperature, diffusion length, etc.) provoking growth instabilities [179, 180]. Some of the consequences of such a situation are: i) step meandering leading to terraces of modulated width, ii) island nucleation at the surface terraces if atomic diffusion is reduced and, iii) mound formation in which 3D growth occurs due to a sufficiently inhibited interlayer mass transport. In practice, meandering and islands nucleation develop nearly simultaneously. As instabilities tend to appear as more material is deposited, deviation from the ideal 2D growth occurs easier for increasing thickness complicating the controlled fabrication of thick epitaxial films. Nevertheless, some benefits may result from this phenomenon and getting away from the ideal behaviour constitutes a way to obtain spontaneously formed nanostructures leading to modulated local functional properties at the surface.

In this chapter, LSMO thin films presenting double-terminated surfaces have achieved using RF magnetron sputtering without the need of special substrate preparation. The capability of confining properties at the nanoscale is of major interest for many challenging applications (e.g. confined electron gas, confined chemical reactions,...). Therefore the presented results appear as a simple way to create new functionalities at the surface, particularly, the formation of local electronic nanostructures.

## 6.2 SrTiO<sub>3</sub> SUBSTRATES TREATMENT

Employing substrates presenting a unique and well defined chemical termination is convenient for obtaining atomically sharp interfaces and good quality layers in thin film growth. Therefore appropriate substrate surface preparation before film deposition is always the initial step and has become essential in thin film preparation. Substrate treatment enables the removal of surface contaminants and also might allow the control of the surface defects density and microstructure.

The perovskite oxide STO, with lattice parameter equal to 0.391 nm [181], is the most common substrate for epitaxial growth of complex oxide thin films and constitutes an ideal substrate in the case of LSMO (pseudo-cubic unit cell, u.c., with lattice

parameter of 0.389 nm) because the resulting lattice mismatch for LSMO/STO is only of 0.39 %. STO (001)-oriented substrates are formed by alternate stacking sequence of TiO<sub>2</sub> or SrO planes along the *c*-axis with inter-plane distance of  $\approx 2$  nm ( $\frac{1}{2}$  u.c.). Therefore, STO has two possible surface termination planes, i.e., SrO and TiO<sub>2</sub>.

Commercially available substrates (from for Crystec, GmbH) are mechanically polished single-crystal and surfaces usually contain a mixture of these two terminations (commonly SrO termination is the minority, being about 5–25% of the total surface area). After appropriate preparation methods single terminated (SrO or TiO<sub>2</sub>) [182, 183], or two-terminated self-separated (SrO and TiO<sub>2</sub>) surfaces can be obtained [173].

#### *TiO<sub>2</sub>-terminated substrates*

TiO<sub>2</sub> termination is in principle energetically more stable than SrO termination [184]. In order to obtain TiO<sub>2</sub>-terminated substrates, chemical etching and thermal annealing are required. Ultrasonication in deionized water is the first step for selective etching of SrO top most layer. It yields to the formation of Sr(OH)<sub>2</sub>.

A more severe SrO etching procedure is the use of an acidic solution after the bath in deionized water. The most conventionally used one is buffered hydrofluoric acid which selectively reacts with SrO [182]. However this acid is extremely toxic and corrosive with lethal risk and need careful manipulation in a clean room (i.e. HF molecule is able to penetrate deeply into the body by non-ionic diffusion and result in destruction of soft tissues and even bones by binding to cations such as Ca<sup>2+</sup> and Mg<sup>2+</sup>). Nevertheless, we have found that same good results can be obtained by using *aqua regia* [HCl-HNO<sub>3</sub> (3:1)] [185]. After sonicating the substrates in deionized water at 70°C for 20 minutes, we soaked them in the aqua regia solution diluted at 50 % during 5 minutes.

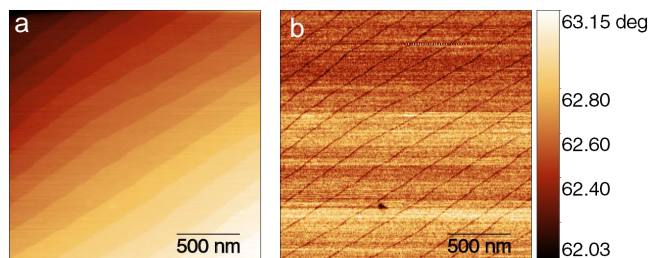


Figure 6.1: (a) Topography and (b) phase lag of single TiO<sub>2</sub>-terminated surface of (001)STO substrate.

After chemical treatment, the substrates were sonicated in acetone and ethanol bath to remove the hydroxide, followed by annealing up to 1000°C for 2 hours in a furnace tube in air for recrystallization. In Figure 6.1 an AFM image of a  $\text{TiO}_2$  surface consisting of atomically flat terraces is depicted. The lack of contrast in the corresponding phase-lag image confirms that the overall surface exhibits a single termination. On the contrary, in Figure 6.2 we show the case where etching process using just deionized water has not been sufficient to remove all SrO, resulting in a high density of SrO island along the  $\text{TiO}_2$ -terraces. These two terminations are clearly revealed by the phase-lag image.

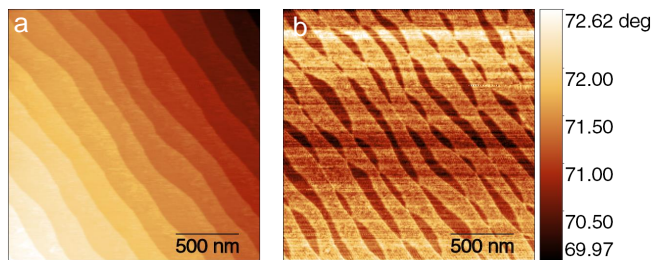


Figure 6.2: (a) Topography and (b) phase lag of surface of (001)STO substrate with mixture of  $\text{TiO}_2$  and SrO terminations.

### *SrO-terminated substrates*

SrO-terminated substrates can be obtained by a longer annealing of 72 hours at 1300°C (procedure used in Ref. [173]). The resulting SrO-terminated surface consists of atomically flat terraces with step edges faceted along the [100] and [010] directions, as it is observed in Figure 6.3.

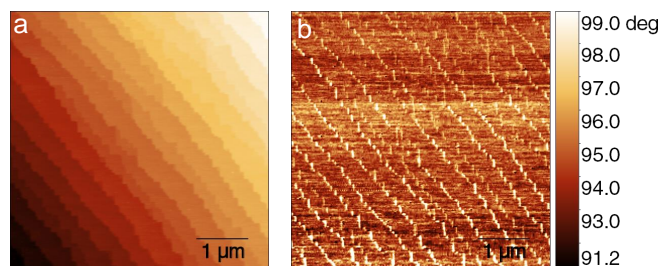


Figure 6.3: (a) Topography and (b) phase lag of SrO-terminated surface of (100)STO substrate.

### 6.3 GROWTH OF $\text{La}_{0.7}\text{Sr}_{0.3}\text{MnO}_3/\text{SrTiO}_3$ FILMS

Epitaxial growth of LSMO on single terminated STO will proceed such that if the topmost surface of the STO substrate is the  $\text{TiO}_2$ -plane, the created interface will be  $\text{TiO}_2/\text{La}_{1-x}\text{Sr}_x\text{O}$ . After deposition of  $n$  complete unit cells, the stacking sequence will be  $/\dots/\text{TiO}_2/(\text{La}_{1-x}\text{Sr}_x\text{O}/\text{MnO}_2)_n$ , i.e. the LSMO film will have a  $\text{MnO}_2$ -terminated surface. On the other hand, if the substrate is terminated at the SrO-plane, the stacking sequence will be  $/\dots/\text{SrO}/(\text{MnO}_2/\text{La}_{1-x}\text{Sr}_x\text{O})_n$  leading to a  $\text{La}_{1-x}\text{Sr}_x\text{O}$ -terminated surface. For an ideal growth, in both cases the global surface should replicate the surface morphological relief (obeying step flow growth) and would have laterally homogeneous properties as corresponding to single chemically terminated surfaces. Though this is clearly accomplished for few nanometers thick thin films, here we show that for thicker LSMO films (several tens of nanometers) the growth mode can be altered.

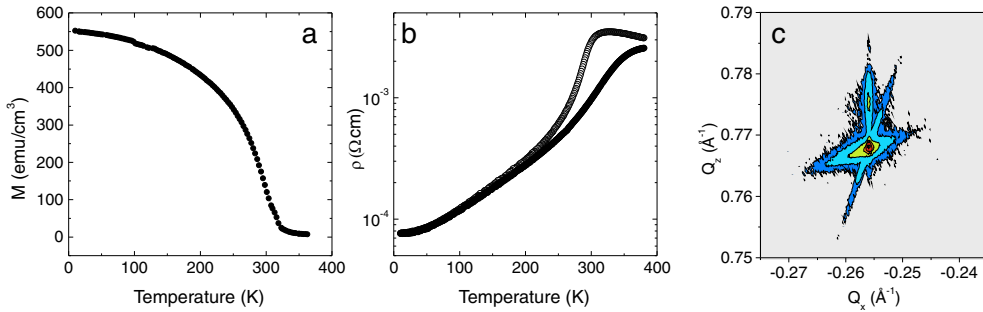


Figure 6.4: Representative measurements of (a)  $M(T)$  taken at 0.5 T, (b)  $R(T)$  with 5 T (filled dots) and without (empty dots) magnetic field applied and (c) Reciprocal space map of (103) reflection of double terminated LSMO sample.

LSMO epitaxial thin films were grown on single-crystal (001)STO substrates by RF magnetron sputtering from stoichiometric targets (purchased from Kurt J. Lesker Co), under a 190 mTorr partial oxygen pressure and at a substrate temperature of 900°C. After deposition, films were annealed *in situ* at 900°C for 60 minutes under an oxygen pressure of 400 Torr and cooled down at a rate of 25°C/min. As it can be found in previous works [186, 187], we have proved that within different oxygen pressure and annealing conditions a thorough control of the growth from 2D step flow mode to the appearance of self-organized pits can be achieved.

All LSMO films investigated here have a nominal thickness of  $\approx 18$  nm-equivalent to 46 monolayers (ML)-defining the ML as a unit cell-thick layer. The quality of the films are supported by  $M(T)$ ,  $R(T)$  and X-ray diffraction measurements (see Figure 6.4). We have observed that with the same growth conditions, the obtained LSMO



films present surfaces with a bimodal distribution in transport properties that it is not clearly detected in topography. An example of these LSMO films is depicted in Figure 6.5.

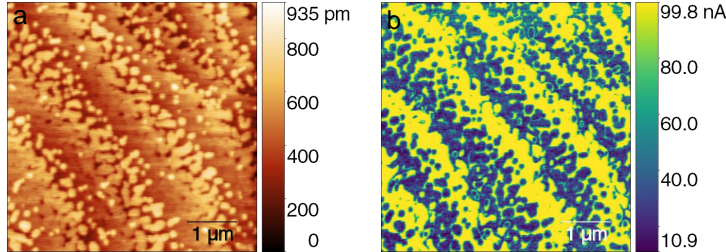


Figure 6.5: (a) Topography and (b) current map of a 18-nm thick double-terminated LSMO surface. Image taken at  $V_{sample} = 1$  V.

## 6.4 SURFACE CHARACTERIZATION USING ATOMIC FORCE MICROSCOPY

In this section, we present results obtained on different LSMO samples exhibiting two chemical terminations coexisting on the same surface. As a matter of fact, the phenomena is illustrated by the bimodal response of the surface in different magnitudes measured by diverse AFM modes. Two phases are revealed by distinct friction, phase contrast and electrical current signals. Phase lag and friction force imaging reflect tip-surface dissipative interactions as viscosity, adhesion or friction, thus indicate chemical heterogeneities regarding the LSMO surface we might relate it to planes of  $\text{La}_{0.7}\text{Sr}_{0.3}\text{O}$  and  $\text{MnO}_2$ . Additionally, C-AFM evidences domains with different conducting responses separated by step heights of half-unit cell ( $\approx 0.2\text{nm}$ ) which correlate with phase lag and friction map.

Firstly, we have explored the influence of substrate termination. In Figure 6.6 we have analyzed LSMO films of the same thickness ( $\approx 18$  nm) grown either on  $\text{TiO}_2$  or SrO single terminated STO substrates. The surface morphology of commercially available  $\text{TiO}_2$ -terminated substrates of STO (used to avoid the possibility that our etching procedure was not effective) shows well-defined atomically flat terraces separated by 1 u.c. steps with smooth edges (Figure 6.6b). The SrO-terminated surface after the treatment explained above is shown in Figure 6.6a, similarly flat terraces and steps (1 u.c. high) are separated in this case by sharp sawtooth step edges.

Along with the data for bare  $\text{TiO}_2$ - and SrO-terminated substrates, Figure 6.6 includes topography (c,d) and current maps (e,f) simultaneously measured for the

LSMO films grown on each substrate. C-AFM is treated in more detail in section 2.2.3.

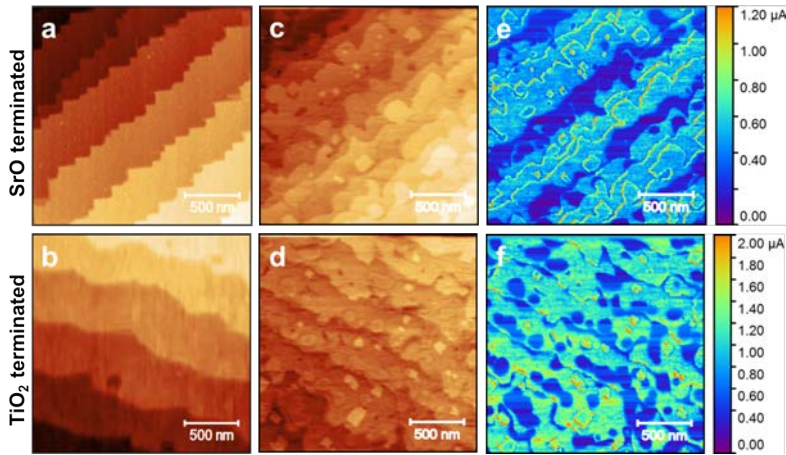


Figure 6.6: Topographic images of (a) SrO and (b) TiO<sub>2</sub> single terminated STO(001) substrates, also referred as SrO-STO and TiO<sub>2</sub>-STO, respectively, in the text. Topography (c, d) and current maps (e, f) of LSMO films grown respectively on the substrates. Current maps were obtained with a TiIr tip at  $V_{\text{sample}}=1$  V.

After deposition of the LSMO layers, the fairly straight and well defined initial step edges of the substrate have disappeared and highly meandered ledges coexist with island nucleation on the terraces.

In both cases, the LSMO films have a relatively similar apparent relief (see Figures 6.6c and d) and current readout displaying a bimodal response with mean values for both termination of 19 and 320 nA for Figure 6.6e and 29 and 700 nA for Figure 6.6f. As a remarkable difference between films, we note that the one grown on the SrO-STO substrate (Figure 6.6c) exhibits fully separated stripes of low and high conducting regions. Even more insightful results the fact of observing small isolated regions of conducting response, the height of those islands corresponds to  $\frac{1}{2}$  u.c. In all cases, the step height between terraces with identical conduction coincides with 1 u.c. ( $\approx 0.4$  nm) while the vertical separation between neighboring levels with different conduction is  $\frac{1}{2}$  u.c. ( $\approx 0.2$  nm). The first corresponds to the distance between LSMO layers of identical chemical composition (either La<sub>0.7</sub>Sr<sub>0.3</sub>O or MnO<sub>2</sub> planes) and the second corresponds to the inter-plane distance between consecutive La<sub>0.7</sub>Sr<sub>0.3</sub>O and MnO<sub>2</sub> atomic layers in LSMO. Indeed, as it has been already reported [188], the bimodal response in surface properties is an indication of chemical separation, therefore signaling that the terraces correspond to alternated (001) planes of the LSMO film.

The origin of the bimodal conduction is cleared up by lateral force imaging (FFM in contact mode presented in more detail in section 2.2.1) and phase lag imaging (in dynamic AM-AFM; see section 2.2.2) that altogether support the hypothesis of a surface with two chemical terminations. Typical results for two STO substrates with different step density are presented. Figure 6.7 shows the topography (left), friction force (central) and current (right) maps for a LSMO film grown on a  $\text{TiO}_2$ -terminated substrate with a miscut angle of around  $0.05^\circ$  with respect to the (001)STO. In the friction map, regions of lower friction appear as dark patches in

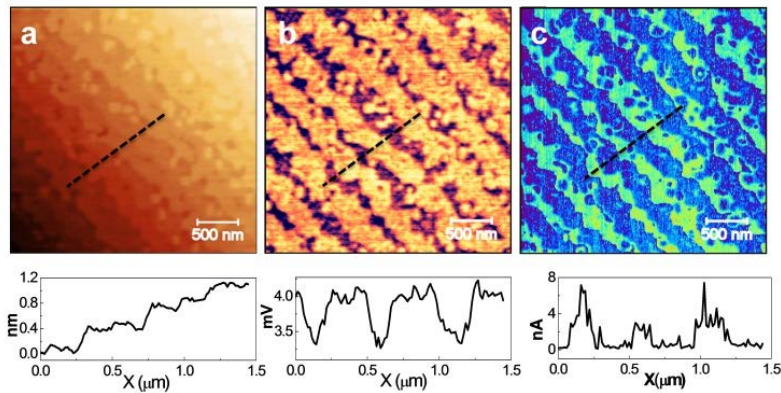


Figure 6.7: Topography (a), friction (b) and current (c) images obtained for LSMO on a  $\text{TiO}_2$ -terminated substrate, in contact AFM at  $V_{\text{sample}}=1$  V using a TiIr coated tip. Below each image the corresponding profiles (dashed segments in the images) are shown.

Figure 6.7b. Comparison of the whole data set confirms a strong correlation and definitively the differentiated regions correspond to areas vertically separated  $\frac{1}{2}$  u.c. and therefore to planes with different chemical composition.

Surface nanostructuration due to the development of regions with different nature is also observed in substrates presenting a slightly larger miscut ( $\approx 0.09^\circ$ ). Figure 6.8 shows consecutive AM-AFM (top) and contact AFM (bottom) measurements taken on different surface locations of the same sample. comparing Figure 6.8a-b and 6.8c-d the same characteristics are observed throughout the whole surface: important step meandering and rounded islands nucleated at terraces. Moreover, incipient mound formation is also noticed (black dashed circles). While the wandering topographic appearance of the steps ledges imaged in Figures 6.8a and 6.8c nearly conceals the existence of islands on the narrow terraces, these islands are otherwise clearly distinguished in the secondary channels (white arrows in Figure 6.8d). Once again, the most notable fact results when comparing topography (a, c) with the corresponding

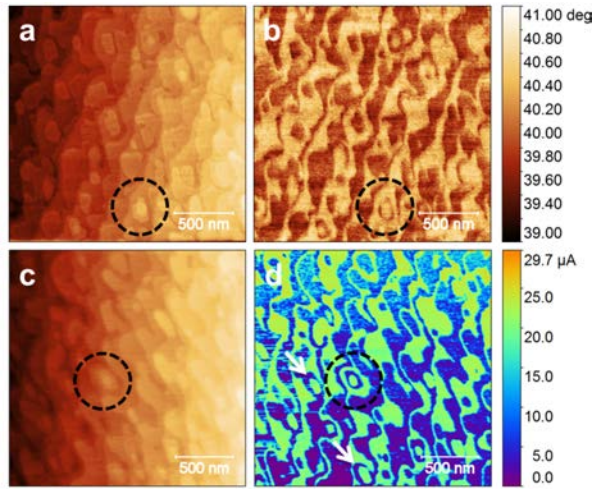


Figure 6.8: Top: Topography (a) and phase lag (b) images in AM-AFM of LSMO film. Middle: Topography (c) and current map (d) obtained at  $V_{sample} = 2$  V in contact mode AFM using a TiIr coated tip. Marks on the images are to emphasize the existence of isolated conducting regions: islands [white arrows in (d)] and small mounds (encircled in all panels).

phase lag (b) and current (d), respectively. Both phase and current exhibit bimodal signals measured at topographic levels separated by a height equal to  $\frac{1}{2}$  u.c. ( $\sim 0.2$  nm). In particular, regions with a diverse phase shift coincide with current differences of about  $18 \mu\text{A}$  ( $\approx 90\%$  increase at  $V_{sample} = 2$  V). Remarkably, this is true even in the case of isolated mounds (encircled in the images) with more than one visible level, because C-AFM enables measuring electrical properties at a very local scale, only limiting the measurement to the contact area of the tip that should not be larger than tens of  $\text{nm}^2$ . The existence of surface regions of high conductivity which are laterally isolated has important implications since the properties of perovskite oxide devices can be tuned through interface effects such as spin exchange interactions [189], charge transfer [190], and band alignment [191].

Finally, in order to confirm that instabilities tend to appear for thicknesses over 40 ML, we have grown a thinner film of LSMO ( $\leq 10$  nm) onto single terminated STO substrate. As observed in Figure 6.9, this film presents homogeneous surface with terraces exhibiting the same conducting response, thus only one chemical termination is identified. This indicates that the growth follows an ideal layer-by-layer (lbl) mode in which complete unit cells (u.c.) are piled up. Similarly, in other works it was proved that ultrathin films grown on substrates presenting laterally modulated SrO-TiO<sub>2</sub> chemical composition follow the stacking sequence of the underlying sub-

strate at each termination and, therefore, two terminated LSMO films are obtained [188].

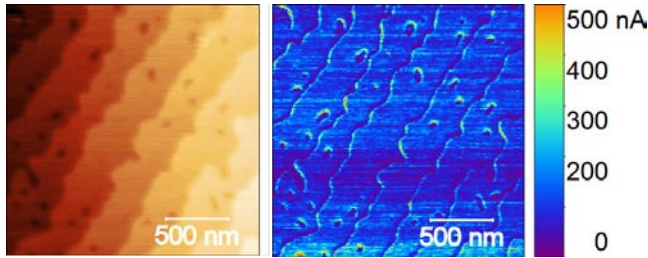


Figure 6.9: Topography (a) and current maps (b) of a  $\leq 10\text{nm}$  LSMO film grown on a  $\text{TiO}_2$ -terminated substrate and showing homogeneous conductivity. Image taken at  $V_{\text{sample}}=1\text{ V}$ .

In spite of the diverse general appearance of the LSMO film surfaces presented in Figures 6.6, 6.7 and 6.8, in all cases neighbor terraces with distinct friction, phase contrast and, notably, different read out current would correspond to  $\text{La}_{0.7}\text{Sr}_{0.3}\text{O}$  and  $\text{MnO}_2$  composition. To gain a deeper insight into the termination assignation X-PEEM has been used.

## 6.5 SURFACE CHARACTERIZATION USING X-PEEM

As presented in chapter 1, LSMO electrical properties are mainly determined by the electrons in the  $3d$  shell of the manganese atoms. Taking into account that conduction in LSMO arises from a double-exchange mechanisms between  $\text{Mn}^{3+}$  and  $\text{Mn}^{4+}$  ions, we expected that  $\text{MnO}_2$  termination would be the most conductive one. Nevertheless, our X-PEEM experiments point towards another explanation discussed in the next section.

In order to correlate the transport properties with the chemical termination X-PEEM experiments have been performed in collaboration with by Dr. Sergio Valencia in UE49-PMGa beamline at BESSY synchrotron in Helmholtz-Zentrum in Berlin. X-PEEM technique renders space resolved spectroscopic information and enables different working modes such as XAS and XPS. XAS signal is obtained collecting the emitted secondary electrons at different incoming photon energies (0.2 eV step) across the Mn  $L_3$  (641.8 eV) and  $L_2$  edges (652.8 eV). XPS is obtained from the detection of photoelectrons at selected kinetic energies ( $E_k$ ) across the Mn  $3p$  core-level ( $E_k = 145.8\text{ eV}$ ) for a fixed energy of the incoming photons ( $E_{ph}=200\text{ eV}$ ).

In Figure 6.10 we explore the Mn  $L_{3,2}$ -edge in XAS mode. XAS image reveals a bidomain structure similar to that measured by AFM based techniques thus giving

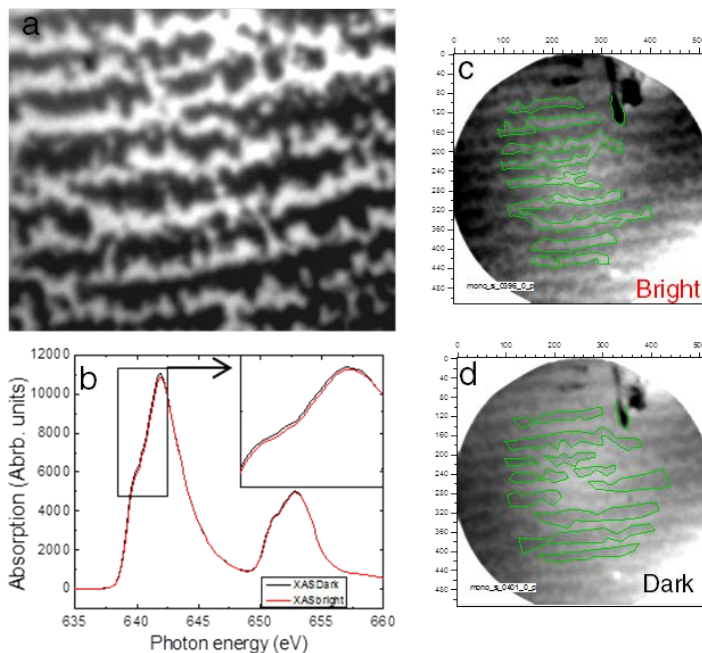


Figure 6.10: (a) XAS images obtained in TEY with X-PEEM at the pre-edge region of Mn  $L_{3,2}$ -edge. (b) Mn  $L_{3,2}$ -edges spectrum obtained after averaging the intensity *vs.* photon energy of bright and dark region encircled with green lines in (c) and (d), respectively. A constant factor has been applied to match the spectrum at pre- and post-edge regions.

an additional evidence of the double termination structure of the surface. In particular, in Figure 6.10a, we show a image corresponding to a slice of the pre-edge spectrum at 630 eV. We observe that two types of intermixed domains having different intensity of emitted photoelectrons, thus showing different contrast. The source for the contrast observed by X-PEEM in XAS mode may arise from different mechanisms including topographic features, work function or chemical nature [192, 193].

To answer this question, we have explored a wide energy range centred in the peak of absorption of Mn (630-670 eV). We have defined two region regions in the pre-edge images of a field of view of  $8 \mu\text{m}$ , named "bright" and "dark", as depicted in Figure 6.10c-d. By comparing spectrums of the two regions we observe that the difference in intensity between them prevails for the whole energy range, highlighting the fact that the difference in intensity of photo emitted electrons between both regions is remaining as a constant factor. The same intensity difference between terminations is measured for similar energy ranges around La and  $O_2$  edges. Indeed,

normalization of the XAS images by that obtained at the pre-edge leads to the loss of contrast between domains. Same result is obtained through pre-edge normalization for the three spices. This observation excludes compositional variations as the source for the contrast observed by X-PEEM.

Then we are left with two other possible primary contrast mechanisms: i) topographic and ii) work function differences. Topography variations should also be ruled out as it has been proved by AFM that samples are ultra flat under the resolution of X-PEEM. The high resemblance between C-AFM (Figure 6.8) and X-PEEM images suggests a common origin so that the most plausible explanation is that the contrast observed by X-PEEM originates from differences in the work function between both regions likely related to  $\text{La}_{0.7}\text{Sr}_{0.3}\text{O}$  and  $\text{MnO}_2$  planes. Higher work function limits the emission of low energy secondary electrons and will therefore appear darker in XAS images.

Besides, in Figure 6.10b we depict the averaged Mn  $L_{3,2}$ -edge XAS spectra of the bright (red) and dark (black) regions after normalizing them by the pre-edge. We can observe that the two sets of spectra are almost identical in shape but differentiated by a small energy shift in the absorption edge (less than  $-0.2$  eV). Indeed, the dark region local spectrum is shifted towards lower energies with respect to the bright region one. Note that even if resolving this energy shift is at the detection limit of X-PEEM, we have measured the same difference even away from edge regions (note the Figure 6.10b inset), thus we can rely on its signal-to-noise ratios. As discussed in chapter 2, the probing depth of the XAS signal is approximately  $30 \text{ \AA}$  [194] (i.e.  $\approx 7$  u.c. of LSMO) thus, the signal coming from the  $\text{MnO}_2$  buried layers is likely to be representative of the bulk since  $\text{La}_{0.7}\text{Sr}_{0.3}\text{O}$  planes cover all  $\text{MnO}_2$  planes within the probing depth. Since the stacking sequence of  $\text{La}_{0.7}\text{Sr}_{0.3}\text{O}$  and  $\text{MnO}_2$  planes is identical in both regions the only possible explanation for the observed shift at the  $\text{MnO}_2$  terminated-plane areas is that the Mn oxidation state of the uppermost  $\text{MnO}_2$  plane must be different from that of the buried  $\text{MnO}_2$  planes. This issue will be discussed later once chemical identification is realized.

Although the XAS data allows identifying regions that one can ascribe to larger or smaller work function, it is not a feasible technique to identify each surface termination because its rather large probing depth. In order to determine the chemical composition of the uppermost layer for each surface region, we make use of energy filtered X-PEEM signal in XPS mode which is known to be much more sensitive to the surface [192, 195]. In this case the probing depth when measuring across the Mn  $3p$  core-levels is ca.  $5 \text{ \AA}$  ( $\approx 1$  u.c. of LSMO).

Figure 6.11 shows the spectra of the Mn  $3p$  core level and the corresponding images obtained at (b) the pre-edge ( $E_k=150$  eV) and (c) at the edge ( $E_k=145.8$  eV). The pre-edge image showed a uniform contrast, i.e. no domains, thus supporting our

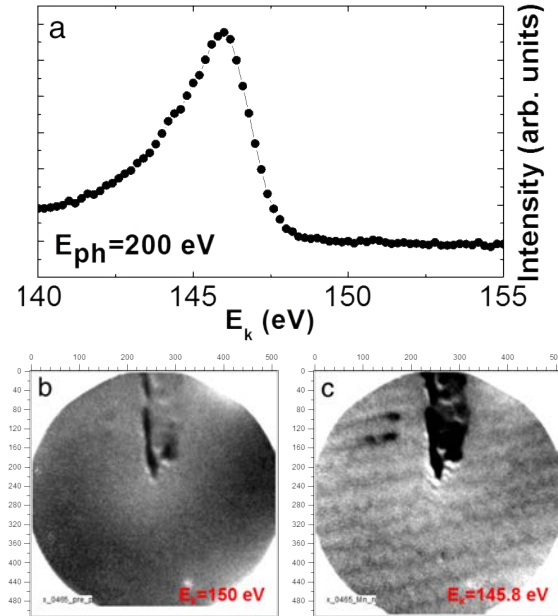


Figure 6.11: (a) Spectra of Mn 3p core level taken by X-PEEM working in XPS mode with a photon energy of 200 eV. (c) X-PEEM image working in XPS mode obtained at the pre-edge region ( $E_k = 150$  eV) and (d) at the edge ( $E_k = 145.8$  eV) of the spectra.

interpretation of the XAS image that contrast originates from work function differences. This is, topography would also be present in XPS no matter  $E_k$ , while work function contrast is only expected to appear at kinetic energies around the photoemission threshold.

The resulting XPS image obtained from normalizing Figure 6.11c to Figure 6.11b is shown in Figure 6.12b. The image obtained at the Mn 3p edge shows a clear binary modulation of contrast, before and after normalization. Since the stacking sequence of  $\text{La}_{0.7}\text{Sr}_{0.3}\text{O}$  and  $\text{MnO}_2$  planes is identical in both regions, higher intensity in XPS arises from regions exhibiting an uppermost  $\text{MnO}_2$  plane while, in the other regions, the buried  $\text{MnO}_2$  planes have an intensity attenuated by the  $\text{La}_{0.7}\text{Sr}_{0.3}\text{O}$  plane on top.

In Figure 6.12 we correlate the X-PEEM image obtained in (b) XPS mode with the corresponding one obtained in (a) XAS mode. Comparison between line profiles (Figure 6.12c) taken in both XPS and XAS images allows correlating the work function information with the atomic termination of the domains.  $\text{MnO}_2$  planes (bright XPS and dark XAS domains) show higher work function than  $\text{La}_{0.7}\text{Sr}_{0.3}\text{O}$  ones (dark XPS and bright XAS domains).



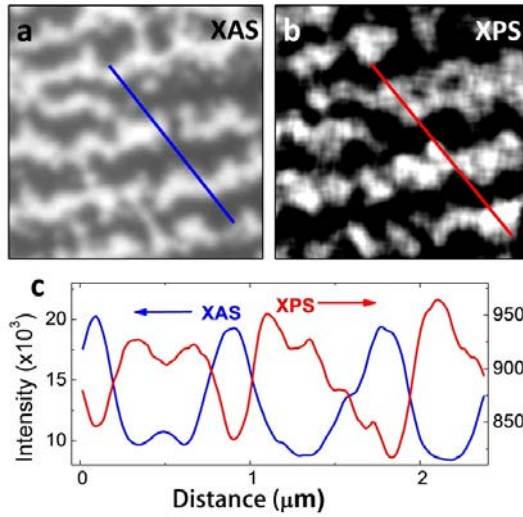


Figure 6.12: a) X-PEEM image working in XAS mode obtained at the pre-edge region of Mn  $L_{3,2}$ -edges, 630 eV. b) XPS image obtained at the Mn 3p core level ( $E_k=145.8$  eV) and normalized to a pre-edge image ( $E_k=150$  eV). Due to the low counts in the XPS mode a filter has been applied so that each pixel is the average of a  $9 \times 9$  pixel matrix. c) Profiles marked in (a) and (b).

All things considered, we get back to clarify the energy shift observed in the XAS spectra in Figure 6.10b. As mentioned, the slight shift points toward a change in the Mn oxidation state of the uppermost  $\text{MnO}_2$  plane. As less emitting (dark) areas in XAS spectra are ascribed to  $\text{MnO}_2$ , according to XPS, we attribute the shift towards lower energies to an increase of the  $\text{Mn}^{3+}$  contribution in  $\text{MnO}_2$  terminated planes.  $\text{Mn}^{3+}$  might be created to compensate the absence of apical oxygen at the surface and this should substantially impede conduction. Therefore, we conclude that lower work function in  $\text{MnO}_2$  regions should correspond to lower conductivity in C-AFM maps.

## 6.6 MONTE CARLO SIMULATIONS

The formation of two differentiated surface regions of different compositions is attributed to deviations from ideal epitaxial growth. The most likely atomistic process at the origin of the surface organization has been interpreted by Monte Carlo simulations performed by Dr. J.J. de Miguel (from Universidad Autónoma de Madrid). A full account of the results of these simulations is nevertheless beyond the scope of the thesis and can be found in Ref. [196]. Here we concentrate on getting some in-

sight on the evolution of the thin film surface under specific conditions that, though do not pretend mimic the employed growth conditions, use specific parameters leading to instabilities that provide an scenario reproducing the experimentally observed surface morphology.

The simulations render that the formation of double-terminated surfaces is independent of the initial STO termination and occur for relatively thick films (>40ML) indicating that, contrary to that expected for an ideal layer-by-layer or step flow growth, they might be interpreted as due to long range instabilities throughout growth. During deposition by RF magnetron sputtering, the different elements ejected from the target arrive to the surface and, depending on the growth parameters and substrate characteristics (deposition rate, temperature, substrate mis-cut, Schowebel barrier,...) diffuse until reaching the step edges or nucleating at the terraces. Actually, theoretical studies predict that films over a certain thickness might present instabilities on vicinal surfaces provoking the meandering of the initially straight steps and the formation of multilayer islands [179]. As illustrated in Ref. [196] by Monte Carlo simulations, our observations cannot be understood in terms of different element diffusion provoking element segregation on the surface but most plausibly due to stacking fault formation, in which the sequence  $\text{La}_{0.7}\text{Sr}_{0.3}\text{O}/\text{MnO}_2/\text{La}_{0.7}\text{Sr}_{0.3}\text{O}$  is locally changed to  $\text{La}_{0.7}\text{Sr}_{0.3}\text{O}/\text{MnO}_2/\text{MnO}_2$ . Once the stacking fault is formed, further growth maintaining the ideal local stacking leads to local energetically favorable configurations and provides a natural mechanism for the self-organized inhomogeneities over the nanometer scale.

In Figure 6.13 we present some examples of Monte Carlo simulation of LSMO surfaces in a series of limiting cases which would correspond to different experimental conditions. One can notice a qualitative agreement between C-AFM maps and simulation. The main feature is the appearance of islands and mounds exhibiting both terminations (dark and bright areas).

As shown in Figure 6.13a, for high temperature and high monomer mobility, islands formation is prevented and step flow with smooth edges takes place: free monomers rapidly join the steps. Reducing the time available for the monomers to diffuse before the arrival of new ones results in the nucleation of islands (Figure 6.13b). Thanks to the high temperature these islands have relatively smooth edges and the film grows layer-by-layer with low roughness. High mobility and low temperature leads to the appearance of patches with both surface terminations. The island sizes are large and corresponds to the long average diffusive length, thus Figure 6.13c represents the case that better reproduce our experimental results. Lower mobility (shorter diffusive length) maintaining the low temperature will cause the nucleation of many small islands (Figure 6.13) avoiding the step moving forward and increasing roughness still presenting two terminations.

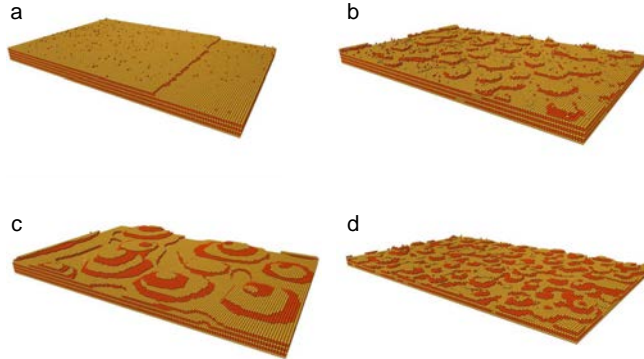


Figure 6.13: Examples of Monte Carlo simulated surfaces representative for different limiting conditions: (a) High temperature and high monomer mobility. (b) High temperature and low monomer mobility. (c) Low temperature and high monomer mobility. (d) Low temperature and low monomer mobility.

In summary, with Monte Carlo simulations developed in Ref. [196] what we have tried to demonstrate is: i) Instabilities are produced during the deposition so that the growth process deviated from the ideal case. These instabilities enable to obtain a double-terminated surface independently of the initial termination of the substrate. Until now, two-terminated surfaces have only been reported in case of very thin films grown on substrates that already present double termination. ii) It is very complicated to know the actual parameters provoking the growth instabilities as growth processes have numerous degrees of freedom (non-homogeneous composition of the target, instabilities in temperature or pressure conditions, substrate surface variations...). Therefore we remark that these simulations do not pretend to reproduce the experimental growing conditions but simulate extreme conditions to demonstrate that once instabilities take place, triggering the deviation from ideality, the final system can evolve to the two-terminations surface.

Knowing that it is possible to obtain two-terminated systems with different local properties, it is interesting to explore in more detail transport properties. It is well known that LSMO system present RS phenomenology. Therefore in the next section we investigate how the conformation of our surfaces affects this phenomena.

## 6.7 TRANSPORT PROPERTIES: RESISTIVE SWITCHING PHENOMENA.

*I-V* characteristics taken at specific location of each termination by means of C-AFM reveal distinct behaviours depending on the type of conductive probe. In Figure 6.14 *I-V* curves have been obtained with a PtSi-coated probe while in Figure 6.16 we have used a doped-diamond tip. PtSi probe has a smaller tip radius ( $R_{tip} \sim 20$  nm) than diamond-doped one ( $R_{tip} \sim 150$  nm) hence, the smaller enables to differentiate between the different terminations. Curves are performed by applying successive voltage cycles between  $V_{sample}=0$  V  $\rightarrow$  -4 V  $\rightarrow$  4 V  $\rightarrow$  -4 V  $\rightarrow$  0 V and inversely (starting at 4 V). The first curve is the black one (representing the virgin state) and it is followed by red-green-blue-cian-pink curves.

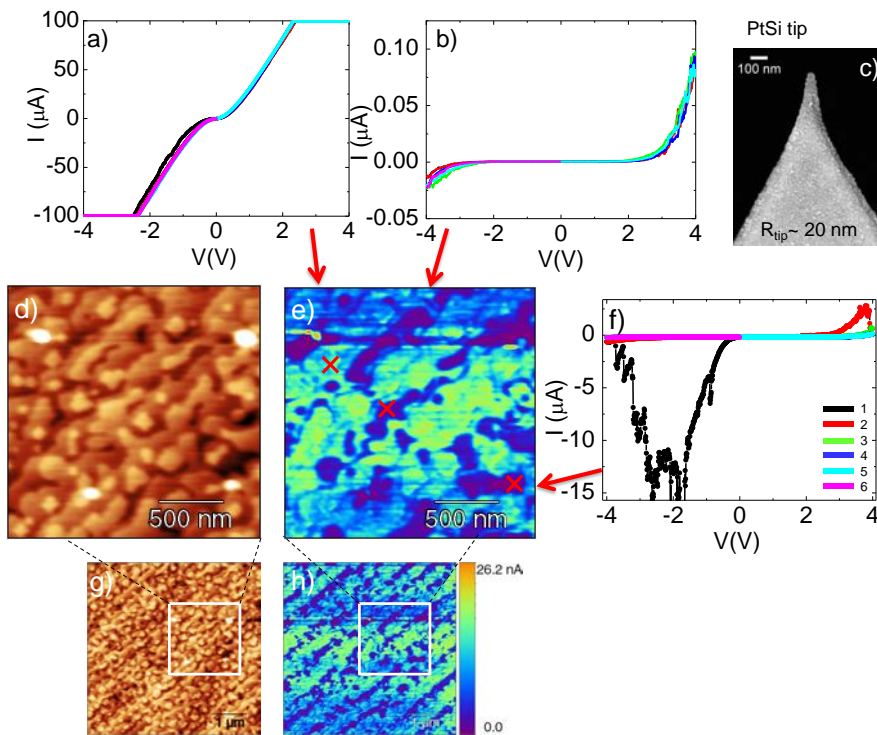


Figure 6.14: (a,b,f) *I-V* characteristic taken at diverse regions of the surface (d,g) of double terminated LSMO films (marked by crosses in current map (e), corresponding to the *I-V* where the arrows point from). (c) SEM image of a PtSi tip, as the one used for doing these measurements, revealing a  $R_{tip} \sim 20$  nm. (SEM image reproduced from Nanosensors specifications).

Regarding  $I$ - $V$  characteristics recorded with a PtSi tip, at high conductive regions, a nearly linear  $I$ - $V$  curve is measured (Figure 6.14a) indicating that the local tip-surface system in these regions can be regarded as close to a metal-metal contact. The curve is slightly non-linear and symmetric, suggesting the appearance of a very small barrier. This could evidence a very thin insulating layer that could act as tunneling barrier or contact resistance. For instance, the half unit cell formed by the top-most  $\text{La}_{0.7}\text{Sr}_{0.3}\text{O}$  plane could act as a barrier. At low conductive regions, a highly rectifying and asymmetric behaviour is observed (Figure 6.14b) suggesting the appearance of a Schottky barrier between the conductive tip and the surface. One possible explanation is the one mentioned for explaining the lowering of emissivity in  $\text{MnO}_2$  planes in X-PEEM measurements: the conduction in these regions could be impeded by the presence of  $\text{Mn}^{3+}$  created to compensate the absence of apical oxygen at the surface.

We conclude that transport seems to be more effective if it is produced by tunneling from  $\text{MnO}_2$  layer through  $\text{La}_{0.7}\text{Sr}_{0.3}\text{O}$  barrier. In this case the first  $\text{MnO}_2$  layer beneath either has no symmetry breaking promoting the appearance of  $\text{Mn}^{3+}$ .

Some locations revealed  $I$ - $V$  with large hysteresis switching to more resistive state as the one presented Figure 6.14f. We ascribe this to imprecise location on frontiers between conducting and insulating areas or also to possible electrochemical reactions with adsorbates (always present on the surfaces exposed to air).

In fact, film modification between LR and HR state can be performed over an extended area during scanning. Current map measurements in Figure 6.15 are performed using the same PtSi tip than in Figure 6.14 with a tip radius small enough to differentiate between terminations.

The procedure consists of two steps: i) writing or changing from LR to HR by scanning at high negative voltages, ii) reading or visualizing the modification by imaging at low positive voltage. In Figure 6.15, we write an area with negative voltage of  $V_{\text{sample}} = -3$  V (a,b) and afterwards we map a larger area (c,d) with a reading voltage of  $V_{\text{sample}} = 500$  mV. We observe that the negative applied voltage is large enough to induce an insulating state so that the whole written area becomes insulating (note that the two terminations are not differentiated in this area). Moreover, the switching to a higher resistance state is accompanied by a topographic change which is neat (no morphological variation) and higher in height, revealing an inflated area. This can be associated with a change in the electrostatic potential that affects deflection of the tip. We know from other works [68] that the change of the electrostatic force can be as significant as one volt.

Since STO substrate is insulating, the contact with the sample is established through a metallic clamp fixed on the surface of LSMO. In this experimental configuration, when RS to HR state is produced at some point, conducting region

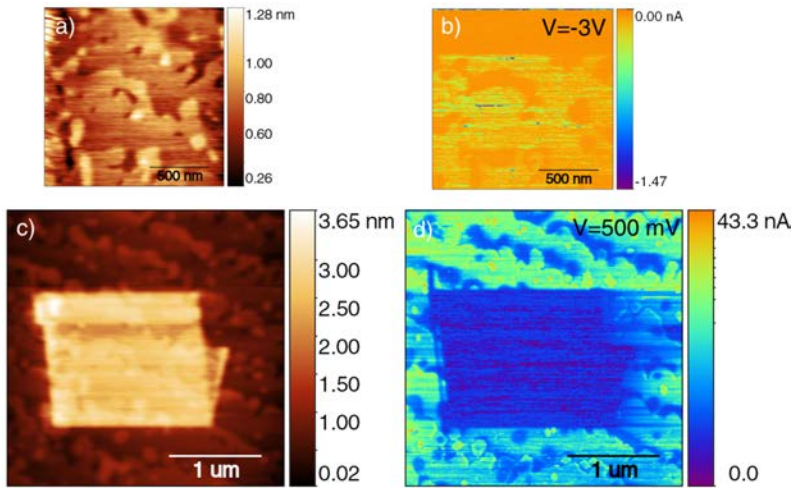


Figure 6.15: C-AFM imaging of the double-terminated LSMO film from Figure 6.14. (a) Topography and (b) current map of  $1.5 \times 1.5 \mu\text{m}^2$  area written with a voltage of  $V_{\text{sample}} = -3\text{V}$ . (c) Topography and (d) current map of  $3 \times 3 \mu\text{m}^2$  image of the same area at a reading voltage of  $V_{\text{sample}} = 500 \text{ mV}$ .

(as the ones resulting in ohmic  $I$ - $V$  curves in 6.14) that are surrounded by switched areas do not give current reading: either these conducting regions have become isolated or they have switched. Hence, we can interpret that RS to HR state at certain region expands in some degree through the thickness of the films and consequently conducting regions cannot be detected or have also suffered RS. Indeed, as it is discussed in other works in Ref. [68, 70, 197], RS creates a surface modification of the film that penetrates throughout the volume of the film in some extent.

On the other hand, the expected RS phenomena for LSMO is revealed by  $I$ - $V$  curves taken with diamond-doped conductive tips (Figure 6.16). As mentioned, diamond-doped tips are much larger than the PtSi and somehow lose the surface resolution, but the system returns to show RS curves at any location when cycling from positive to negative voltage and viceversa. It represents bipolar RS case, where a resistance changing from LR to HR occurs at certain voltage polarity, with an inverse process from HR to LR state. A voltage of at least the same magnitude and opposite polarity should be applied to cycle between HR and LR states. These set and reset voltage have always the same sign independently of the cycle direction, as it is proved by comparing (c) and (f) from Figure 6.16. Consequently, when the voltage cycles are restricted to one polarity, after reaching the HR (for negative polarity; Figure 6.16a) or the LR state (for positive polarity; Figure 6.16d), same state is maintained over several cycles (red, green and blue curves overlap). For the LR case

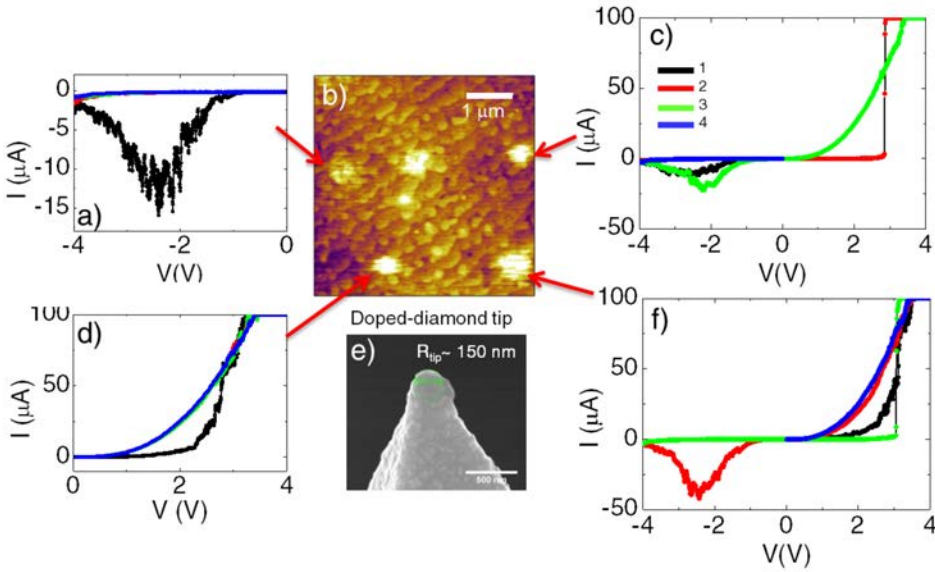


Figure 6.16: (a,c,d,f)  $I$ - $V$  characteristic taken at diverse regions of the surface (b) (marked by arrows). (e) SEM image of a diamond-doped tip, as the one used for doing these measurements, revealing a  $R_{tip} \sim 150$  nm. (SEM image reproduced from Ref. [198])

(d), the black curve reveals a small insulating barrier that is overcome in the second cycle. Then LR state is maintained in the subsequent cycles. These results highlight the fact that transport, and in particular RS phenomenon, is very sensitive to the different work functions and reactivity of the conductive coating of the tip and the local surface as well as to the contact area.

Sawa *et al.* [199], among others, explored RS in a manganite system and stated that the phenomena originates at the interface and can be manipulated by modifying the interface barrier. The work highlights the role that insulating properties of certain perovskite manganite play to trigger RS effect. They insert a thin layer of  $\text{Sm}_{0.7}\text{Ca}_{0.3}\text{MnO}_3$  (SCMO), which is an insulating manganite, at the interface of Ti/LSMO system and observed that IV curves transit from metal-metal contact for Ti/LSMO junction to Schottky-like contact for Ti/SCMO/LSMO. The insertion of one unit cell the insulating SCMO induces RS behaviour very similar to the one found in our system. Then, a plausible picture for explaining the phenomenon we report is that the presence  $\text{Mn}^{3+}$  at the  $\text{MnO}_2$  surface planes could be acting as an insulating layer enabling RS. Regions where RS is induced are active in some extension beneath the surface, promoting the insulation of surrounding material.

## 6.8 SUMMARY

The presented results show that the nanoscale structuration of the LSMO surface is consequence of chemical self-organization. The formation of two differentiated surface regions of different compositions is attributed to deviations from ideal epitaxial growth. Whereas in layer by layer growth similar chemical nanostructuration originates from the replica of patterned substrates, here instabilities during growth is proposed to be the origin of the double-terminated LSMO surfaces found experimentally. Both situations offer different ways for obtaining frameworks of metal and insulator two dimensional domains.

Due to the lack of knowledge on the true factors at the basis of the instabilities taking place in our experiments, the Monte Carlo simulations have been performed for a series of extreme and specific conditions. In such a way, these simulations should be taken as a proof of how alterations during growth, leading to the formation of stacking faults, can be responsible of the appearance of the two chemical terminations independently of the initial characteristics of the substrate.

Composition differences have been detected with different AFM approaches: in tapping mode it is detected by phase lag of the tip oscillation imaging in repulsive mode while in contact mode friction imaging derived from lateral force signal is used. Both dissipative signals have been correlated with C-AFM maps evidencing that the two terminations possess different conducting states. Then, chemical identification of the two terminations ( $\text{La}_{0.7}\text{Sr}_{0.3}\text{O}$  or  $\text{MnO}_2$ ) has been possible by combining XAS and XPS measurements simultaneously measured in X-PEEM. A shift in intensity between Mn-edge XAS spectra of each terminations is detected and associated to differences in the work function. The region that produce less emission of electrons in these XAS spectra is the one that appears darker XPS image at Mn edge thus, it is linked to  $\text{La}_{0.7}\text{Sr}_{0.3}\text{O}$  termination. Additionally, a small shift in energy in Mn-edge XAS spectrum is associated to the presence of  $\text{Mn}^{3+}$  created to compensate the absence of apical oxygen at  $\text{MnO}_2$  termination. As this termination has higher work function, it is ascribed to insulating regions in C-AFM maps.

Finally, with the aim of exploring dependences of RS switching phenomena due to variable termination, we have tested  $I$ - $V$  characteristics with C-AFM at defined locations. We observe that typical RS curves are only measured when using doped-diamond tips. When using PtSi, probes whose radius is around 20 nm, RS is not observed when doing point measurements ( $I$ - $V$  curves) but when imaging. In current maps we can isolate conducting regions that did not seem to switch when measuring  $I$ - $V$  curves. As the area of contact of the tip is much smaller than the width of the terminations, we assume that the switching is an effect that penetrate into the bulk of the film in some extent. These tip dependences highlight the complexity of



understanding tip-surface interfaces (and tip-adsorbates-oxide system) that might lead to the physical mechanism behind RS phenomena.

All in all, in this chapter we highlight the use of different techniques for identification of nanostructures on surface. In the present case, the coexistence of two different conducting surface regions indicates that different electronic nanostructures emerge depending on the termination layer, which may have relevance for the design of perovskite based devices with new functionalities at the surface.

## CONCLUSIONS



## CONCLUSIONS

---

### SUMMARY

In the present thesis, two types of lanthanum manganite-based oxide materials for spintronic and memory applications have been investigated: one obtained by B-site substitution ( $\text{La}_2\text{Co}_{0.8}\text{Mn}_{1.2}\text{O}_6$ ) and the other obtained by A-site substitution ( $\text{La}_{0.7}\text{Sr}_{0.3}\text{MnO}_3$ ). High-quality growth of thin films of both oxides has been achieved by means of RF sputtering technique allowing the design of, on one side, LCMO-based tunnel structures and, on the other side, self-organized nanostructures in the form of double-terminated LSMO film surfaces.

$\text{La}_2\text{CoMnO}_6$  is a double perovskite exhibiting ferromagnetic insulating behaviour and a relatively high  $T_C$  of 230 K in bulk. The combination of magnetic and insulating functionalities in a single system gives great potential for the developing of active tunnel barriers for spintronic devices such as spin-filters. Motivated by its technological relevance as well as by the fundamental aspects, in this work we have presented a detailed study on structural, compositional and magnetic characterization of this double perovskite thin films. We show that lattice mismatch with substrate dictate the degree and sign of the magnetic anisotropy. Remarkably, we have obtained films with strong perpendicular magnetic anisotropy (PMA) (with  $\mu_0 H_C \approx 1$  T) which is tuned by tensile strain. This has been achieved for thin films on top of (001) $\text{SrTiO}_3$  (STO).

We firstly have observed that, for films grown on STO, the magnitude of the magnetic anisotropy is closely correlated with the degree of oxygen content of the films: the larger the oxygen content, the larger the anisotropy. As the increase of oxygen content implies a shrinkage of the OOP lattice parameter, changes in magnetic anisotropy have been related with changes in the strain state. This strain-dependence has been unequivocally proved by growing thin films on top of  $(\text{LaAlO}_3)_{0.3}(\text{Sr}_2\text{AlTaO}_6)_{0.7}$  (LSAT) and  $\text{LaAlO}_3$  (LAO) that produce compressive strain. Indeed, we have found that compressive strain favors in-plane easy-axis.

Regarding the composition of the films, we have shown using electron probe microanalysis that the real composition is actually  $\text{La}_2\text{Co}_{0.8}\text{Mn}_{1.2}\text{O}_6$  (LCMO), thus this films present a deficiency of Co from the expected compound  $\text{La}_2\text{CoMnO}_6$ . At this point, questions about the degree of cationic ordering of our samples and how ferromagnetism could be explained have arisen. We have proved, by means of X-ray absorption spectroscopy (XAS) measurements, that in optimized LCMO films (with high  $T_C \approx 225$  K) off-stoichiometry does not affect the valence of Co ions, which is essentially +2. Actually, those measurements point towards the reduction of a part of Mn ions from +4 to +3 to fulfil charge neutrality. Nevertheless, in optimized films, divalent Co, high  $T_C$ , and high saturation magnetization rule out a disordered arrangement of Co and Mn ions in the double perovskite structure, reinforcing the conclusion that ferromagnetism is induced by superexchange interactions.

Finally, by exploring different LCMO film thicknesses, we have determined that the origin of PMA should be magnetocrystalline rather than shape-induced. PMA is found for the whole range of thickness studied in LCMO on STO (2 to 66 nm) and, for the compressive cases, IP easy-axis persists even for very thin films (4 nm-thick). Concerning this fact, we have given direct evidence that anisotropy phenomena in LCMO are mainly driven by SOC of  $\text{Co}^{2+}$ . Firstly, X-ray magnetic circular dichroism (XMCD) measurements reveal a large contribution from the orbital angular moment of Co ions, but no contribution from Mn. In addition, we have computed  $m_L/m_{S_{eff}}$  ratios for a set of samples with different strain states. We observe a strong dependence of this ratio on the film strain, particularly notable for the normal incidence case.

Secondly, we have developed an atomistic model based on first order perturbation theory intended to describe the relationship between the crystallographic structure and the magnetic properties. The theoretical approximation departs from the ground state of  $\text{Co}^{2+}$  ion in a cubic (undistorted) octahedral environment, and considers as perturbations: i) a tetragonal distortion on a cubic crystal field to account for strain and ii) the spin-orbit coupling of  $\text{Co}^{2+}$ . We have obtained a prediction of the strain-dependent magnetic anisotropy described by the ratio of gyromagnetic coefficients in each direction. Additionally, we have also predicted the dependence of  $m_L/m_S$  with the strain and we have compared it to experimental values of  $m_L/m_{S_{eff}}$  determined by XMCD.

Encouraged by the findings of strong PMA in LCMO/STO system, we have explored the possibility of using LCMO in a spintronic device. We have built magnetic tunnel junctions based on a single magnetic layer of LCMO sandwiched between non-magnetic electrodes, a thin layer (2-4 nm thick) of LCMO grown on a semi-

conducting Nb:STO substrate capped with a thin layer of metal (Pt or Au). We have obtained an accurate description of the transport through the barrier by fitting the magnetoresistance curves using Fowler-Nordheim tunneling and two-current models. This analysis allows estimating the exchange splitting ( $\Delta$ ) in the LCMO layer that defines the different barriers height for spin-down and spin-up electrons, as well as the additional variation of the barrier height due to the application of a magnetic field ( $\Phi_H$ ). The variation of  $\Phi_H$  has been found to be very different for the field applied along the easy or the hard axes. The values obtained render a remarkably high spin-filtering efficiency with a polarization of the current of 99.7 % at worst. The fitted values have been additionally confirmed by first-principles theoretical calculations. Furthermore, the large difference between the magnetoresistance curves measured with the field applied OOP or IP renders tunneling anisotropic magnetoresistance (TAMR) values of about 20-30%. This result suggest that the underlying phenomena for the TAMR is dictated by the large strain-induced PMA. Finally, magnetic memory capabilities of the junction have been explored by probing the existence of a non-volatile bistable resistive state that can be switched by applying a magnetic field pulses in the out-of-plane or in the in-plane directions.

The findings of this chapter heighten the potential of using ferromagnetic insulators with strong magnetic anisotropy for spin filtering, magnetic field sensing and data storage applications. Notwithstanding that our device works below room temperature and using high magnetic fields, it represents, to the best of our knowledge, the first report of a single layer ferromagnetic memory with electrical read-out.

The last part of the thesis has been focused on the study of the transport properties in structures laterally smaller than tunnel junctions, such as self-organized surfaces. In particular, we have characterized double-terminated surfaces of  $\text{La}_{0.7}\text{Sr}_{0.3}\text{MnO}_3$  (LSMO) thin films; in this case, a metallic ferromagnetic manganite. We point out that deviation from the ideal epitaxial growth constitutes a way to obtain spontaneously formed nanostructures that lead to modulated local functional properties of thin film surfaces. Hence, the formation of two differentiated surface regions of different compositions, on non-patterned substrates or on single terminated substrates, has been attributed to instabilities during the growth process. Due to the nanometric size of the different terminations at the surface, scanning probe microscopy seems a very suitable tool to characterize these structures. Different conducting responses detected by C-AFM have been associated to differences in the surface composition by relating them to dissipative signals in different AFM approaches: phase lag maps in tapping mode and friction imaging in contact mode. The two terminations ( $\text{La}_{0.7}\text{Sr}_{0.3}\text{O}$  or  $\text{MnO}_2$ ) have been chemically identified by correlating XAS and XPS maps simultaneously measured in X-PEEM. In particular, intensity differ-

ence between XAS spectrum of each terminations is detected and associated to the corresponding chemical composition revealed by XPS. This, together with C-AFM results, leads us to conclude that transport is more effective if the film termination is  $\text{La}_{0.7}\text{Sr}_{0.3}\text{O}$  instead of  $\text{MnO}_2$ . A possible explanation could be that  $\text{La}_{0.7}\text{Sr}_{0.3}\text{O}$  plane prevents the appearance of extra  $\text{Mn}^{3+}$  which impedes conduction rather harshly.

Finally, we have additionally performed  $I$ - $V$  curves in C-AFM for characterizing transport at the surface.  $I$ - $V$ s taken with small enough tip radius can distinguish between the different conducting behaviour of each termination without inducing resistive switching (RS) phenomena typical from LSMO. Other measuring conditions, such as scanning or using wider diamond-doped probes produce the expected switching and evidence the extended nature of RS effect in LSMO.

## OUTLOOK

Here we enumerate some open questions and research lines that can derive from the results presented in this thesis:

- The role of the off-stoichiometry of LCMO films is still an open question. It must be mentioned that films in the literature do not show magnetic properties as good as our films but, at the same time, may not present off-stoichiometry. At the present, a Ph.D. thesis on course has, as one of its objectives, to study the possible effect of this off-stoichiometry by preparing, by chemical solution method, films of LCMO with controlled Co-Mn ratio. Stoichiometric films with good magnetic properties have already been achieved.
- The study of double perovskite thin film oxide, being of particular interest ferromagnetic insulating ones, is an active developing field. At the moment, another Ph.D. thesis is devoted to optimize the growth of a similar FM-I double perovskite:  $\text{La}_2\text{NiMnO}_6$ . Films are grown by sputtering and present similar stoichiometry deviations as LCMO: the best magnetic properties have been found for films with a certain degree of nickel deficiency. Therefore, a better understanding of the dependence of magnetic properties on composition could help to build a better picture of the factors that impact on cationic ordering.
- Our findings on LCMO-based tunnel junctions stress out the possibility of using ferromagnetic insulating materials with PMA in sensor and memory applications. This opens a new platform for exploring other highly anisotropic FM-I materials with higher transition temperatures. Pointing in this direction, the result reported based on the first order perturbation theoretical approach

should be general and applicable to other oxides with  $\text{Co}^{2+}$ . Therefore, we propose to explore new materials conformed by  $\text{Co}^{2+}$  in octahedral environment that can develop strong PMA when grown as thin films.

- Regarding open lines for tunnel junction, we have made some attempts to build a spin-valve, that is, substituting Pt electrode by a ferromagnetic metal with PMA. The device requires two magnetic layers, one fixed and one free. With a softer ferromagnetic electrode we could easily control the magnetization direction. The ferromagnetic electrodes we tested were CoFeB/Ta and CoFeB/Pd multilayers. Actually, CoFeB may present interfacial PMA at certain thickness and in contact with transition metal with  $5d$  metals.
- Spin efficiency found for the device is actually an estimation derived from magnetoresistance curves, as Pt or Au are non-magnetic metals. Therefore another arisen question is if we can have a direct measurement of the polarization. A way to do so could be using the Anomalous Hall Effect (AHE) induced on Pt. The idea consist in defining a track on Pt/LCMO/Nb:STO structure with three contacts, one in the middle and others in the sides. Then inject current between Nb:STO and the contact in the center (at low T and with magnetic field applied) and measure the voltage between contacts at the sides. If the injected current is polarized, electrons will be deflected to one side of the track due to the AHE and hence, a potential difference should be created.
- Designing magnetic structures with dimensions in the nanometer scale represent an exciting field of research. The nanosized pillar structures reported in the thesis are a starting point for the improvement of the performance of the junctions. The influence of defects on electron transport could be reduced, and, by confining single magnetic domains, pinned magnetization states could be obtained without the need of using high magnetic fields.
- Concerning the self-organized nanostructures on LSMO surfaces, it would be interesting to have a better control of the growth parameters in order to tailor nanosized functional domains in perovskite thin films. Moreover, by growing metals or other oxides on top of a well-controlled double-terminated surface, we could deeply investigate the role of the termination on the interface emerging properties.





# LIST OF PUBLICATIONS

---

The publications related to the topics of the thesis are:

- R. Galceran, C. Frontera, Ll. Balcells, J. Cisneros-Fernández, **L. López-Mir**, J. Roqueta, J. Santiso, N. Bagués, B. Bozzo, A. Pomar, B. Martínez "Engineering the microstructure and magnetism of  $\text{La}_2\text{CoMnO}_6$  thin films by tailoring oxygen stoichiometry", *Applied Physics Letters* 105, 242401 (2014).
- **L. López-Mir**, Ll. Balcells, S. Valencia, F. Kronast, B. Martiñez, J.J. de Miguel and C. Ocal "Growth Instabilities as a Source of Surface Chemical Structuration in Functional Perovskite Thin Films", *Crystal Growth & Design* 16(9), 5479-5486 (2016).
- R. Galceran\*, **L. López-Mir\***, B. Bozzo, J. Cisneros-Fernández, J. Santiso, Ll. Balcells, C. Frontera, and B. Martínez "Strain-induced perpendicular magnetic anisotropy in  $\text{La}_2\text{CoMnO}_{6-\epsilon}$  thin films and its dependence on film thickness", *Physical Review B* 93, 144417 (2016).
- **L. López-Mir**, R. Galceran, J. Herrero-Martín, B. Bozzo, J. Cisneros-Fernández, E. V. Pannunzio Miner, A. Pomar, L. Balcells, B. Martínez, and C. Frontera "Magnetic anisotropy and valence states in  $\text{La}_2\text{Co}_{1-x}\text{Mn}_{1+x}\text{O}_6$  ( $x \approx 0.23$ ) thin films studied by x-ray absorption spectroscopy techniques" *Physical Review B* 95, 224434 (2017).
- **L. López-Mir**, C. Frontera, H. Aramberri, K. Bouzehouane, J. Cisneros-Fernández, B. Bozzo, L. Balcells, B. Martínez, and C. Frontera "Anisotropic sensor and memory device with a ferromagnetic tunnel barrier as the only magnetic element" *Scientific Reports*, 8, 861, (2018).

Other works published during the period of the thesis, but not related to its topic are:

- P. Miranzo, **L. López-Mir**, B. Román-Manso, M. Belmonte, M. I. Osendi, C. Ocal "Prominent local transport in silicon carbide composites containing in-situ synthesized three-dimensional graphene networks", *Journal of the European Ceramic Society* 36, 13, 3073-3081 (2016).

- R. Galceran, I. Fina, J. Cisneros-Fernández, B. Bozzo, C. Frontera, **L. López-Mir**, H. Deniz, K.-W. Park, B.-G. Park, L. Balcells, X. Martí, T. Jungwirth, and B. Martínez, "Isothermal anisotropic magnetoresistance in antiferromagnetic metallic IrMn", *Scientific Reports*, 6, 35471, (2016).
- G. García, I. Preda, M. Díaz-Híjar, V. Tormo-Márquez, O. Peña-Rodríguez, J. Olivares, F. Bosia, N.M. Pugno, F. Picollo, L. Giuntini, A. Sordini, P. Olivero, **L. López-Mir** and C. Ocal "Micro and nano-patterning of single-crystal diamond by swift heavy ion irradiation", *Diamond and Related Materials* 69, 1-7, (2016).
- A. Pomar, Z. Konstantinović, N. Bagués, J. Roqueta, **L. López-Mir**, Ll. Balcells, C. Frontera, N. Mestres, A. Gutiérrez-Llorente, M. Šćepanović, N. Lazarević, Z.V. Popović, F. Sandiumenge, B. Martínez and J. Santiso "Formation of self-organized Mn<sub>3</sub>O<sub>4</sub> nanoinclusions in LaMnO<sub>3</sub> films", *Frontiers in Physics* 4:41 (2016).
- D. Preziosi, **L. López-Mir**, X. Li, K. Bouzehouane, S. Valencia, A. Gloter, A. Barthélémy and M. Bibes, "Direct mapping of phase separation across the metal-to-insulator transition of NdNiO<sub>3</sub>", *submitted*.
- S. Valencia, M.J. Calderón, **L. López-Mir**, Z. Konstantinović, E. Schierle, E. Weschke, L. Brey, B. Martínez, and Ll. Balcells, "Spin-orbit effects surfacing on manganites", *submitted*.

# BIBLIOGRAPHY

---

- [1] M. Lorenz and *et al.* The 2016 oxide electronic materials and oxide interfaces roadmap. *Journal of Physics D: Applied Physics*, 49(433001), 2016.
- [2] Y. Tokura. Critical features of colossal magnetoresistive manganites. *Reports on Progress in Physics*, 69:797–851, 2006.
- [3] S. A. Wolf, D. D. Awschalom, R. A. Buhrman, J. M. Daughton, S. von Molnár, M. L. Roukes, A. Y. Chtchelkanova, and D. M. Treger. Spintronics: A Spin-Based Electronics Vision for the Future. *Science*, 294(5546):1488–1495, 2001.
- [4] L. Brey, C. Tejedor, and J. Fernández-Rossier. Tunnel magnetoresistance in GaMnAs: Going beyond Jullière formula. *Applied Physics Letters*, 85(11):1996–1998, 2004.
- [5] M. Tanaka and Y. Higo. Large Tunneling Magnetoresistance in GaMnAs/AlAs/GaMnAs Ferromagnetic Semiconductor Tunnel Junctions. *Physical Review Letters*, 87(2):026602, 2001.
- [6] A. B. Shick, F. Máca, J. Mašek, and T. Jungwirth. Prospect for room temperature tunneling anisotropic magnetoresistance effect: Density of states anisotropies in CoPt systems. *Physical Review B - Condensed Matter and Materials Physics*, 73:024418, 2006.
- [7] C. O. Avci, A. Quindeau, C.-F. Pai, M. Mann, L. Caretta, A. S. Tang, M. C. Onbasli, C. A. Ross, and G. S. D. Beach. Current-induced switching in a magnetic insulator. *Nature Materials*, 16:309–314, 2016.
- [8] H. Y. Hwang, Y. Iwasa, M. Kawasaki, B. Keimer, N. Nagaosa, and Y. Tokura. Emergent phenomena at oxide interfaces. *Nature Materials*, 11(2):103–113, 2012.
- [9] <http://wps.prenhall.com/wps/media/objects/3085/3159106/blb2406.html>, chapter 24, section 6.
- [10] J. N. Lalena and D. A. Cleary. *Principles of Inorganic Materials Design*. John Wiley & Sons, Inc., 2005.

- [11] N. Spaldin. *Magnetic materials: fundamentals and device applications*. Cambridge University Press, 2003.
- [12] J. B. Goodenough. *Magnetism And The Chemical Bond*. John Wiley & Sons, 1963.
- [13] J. Kanamori. Superexchange interaction and symmetry properties of electron orbitals. *Journal of Physics and Chemistry of Solids*, 10(2-3):87–98, 1959.
- [14] P. W. Anderson. Antiferromagnetism. Theory of Superexchange Interaction. *Physical Review*, 79(2):350–356, 1950.
- [15] Y. Shimakawa, M. Azuma, and N. Ichikawa. Multiferroic compounds with double-perovskite structures. *Materials*, 4:153–168, 2011.
- [16] C. Zener. Interaction between the  $d$ -shells in the transition metals. ii. ferromagnetic compounds of manganese with perovskite structure. *Physical Review Letters*, 82:403–405, 1951.
- [17] M. Opel. Spintronic oxides grown by laser-MBE. *Journal of Physics D: Applied Physics*, 45:033001, 2012.
- [18] E. Dagotto. Nanoscale Phase Separation and Colossal Magnetoresistance. In *Springer Series in Solid State Sciences*, volume 136, page 459. Springer Berlin Heidelberg, 2003.
- [19] P. M. Woodward. Octahedral Tilting in Perovskites. II. Structure Stabilizing Forces. *Acta Crystallographica Section B Structural Science*, 53:44–66, 1997.
- [20] A. M. Glazer. The classification of tilted octahedra in perovskites. *Acta Crystallographica Section B: Structural Crystallography and Crystal Chemistry*, 28:3384–3392, 1972.
- [21] N. S. Rogado, J. Li, A. W. Sleight, and M. A. Subramanian. Magnetocapacitance and magnetoresistance near room temperature in a ferromagnetic semiconductor:  $\text{La}_2\text{NiMnO}_6$ . *Advanced Materials*, 17:2225–2227, 2005.
- [22] H. Kato, T. Okuda, Y. Okimoto, Y. Tomioka, Y. Takenoya, A. Ohkubo, M. Kawasaki, and Y. Tokura. Metallic ordered double-perovskite  $\text{Sr}_2\text{CrReO}_6$  with maximal Curie temperature of 635 K. *Applied Physics Letters*, 81(2):328–330, 2002.
- [23] K.-I. Kobayashi, T. Kimura, H. Sawada, K. Terakura, and Y. Tokura. Room-temperature magnetoresistance in an oxide material with an ordered double-perovskite structure. *Nature*, 395(6703):677–680, 1998.

- [24] M. Azuma, K. Takata, T. Saito, S. Ishiwata, Y. Shimakawa, and M. Takano. Designed ferromagnetic, ferroelectric  $\text{Bi}_2\text{NiMnO}_6$ . *Journal of the American Chemical Society*, 127:8889–8892, 2005.
- [25] Y. H. Huang, R. I. Dass, J. C. Denyszyn, and J. B. Goodenough. Synthesis and characterization of  $\text{Sr}_2\text{MgMoO}_{6-\delta}$ . *Journal of the Electrochemical Society*, 153(7), 2006.
- [26] A. J. Barón-González, C. Frontera, J. L. García-Muñoz, B. Rivas-Murias, and J. Blasco. Effect of cation disorder on structural, magnetic and dielectric properties of  $\text{La}_2\text{CoMnO}_6$  double perovskite. *Journal of physics: Condensed matter*, 23:496003, 2011.
- [27] S. Baidya and T. Saha-Dasgupta. Electronic Structure and Phonons in  $\text{La}_2\text{CoMnO}_6$ : A Ferromagnetic Insulator Driven by Coulomb-assisted Spin-Orbit Coupling. *Physical Review B*, 84:035131, 2011.
- [28] R. Skmoski. *Simple Models of Magnetism*. Oxford University Press, 2008.
- [29] A. Lisfi and C. M. Williams. Magnetic anisotropy and domain structure in epitaxial  $\text{CoFe}_2\text{O}_4$  thin films. *Journal of Applied Physics*, 93:8143–8145, 2003.
- [30] M. T. Johnson, P. J. H. Bloemen, F. J. A den Broeder, and J. J. de Vries. Magnetic anisotropy in metallic multilayers. *Reports on Progress in Physics*, 59:1409–1458, 1999.
- [31] L. Néel. Anisotropie magnétique superficielle et surstructures d’orientation. *Journal de Physique et le Radium*, 15(4):225–239, 1954.
- [32] P. Bruno. Tight-binding approach to the orbital magnetic moment and magnetocrystalline anisotropy of transition-metal monolayers. *Physical Review B*, 39(1):865–868, 1989.
- [33] J. A. Heuver, A. Scaramucci, Y. Blickenstorfer, S. Matzen, N. A. Spaldin, C. Ederer, and B. Noheda. Strain-induced magnetic anisotropy in epitaxial thin films of the spinel  $\text{CoCr}_2\text{O}_4$ . *Physical Review B - Condensed Matter and Materials Physics*, 92:214429, 2015.
- [34] T. R. McGuire and R. I. Potter. Anisotropic Magnetoresistance in Ferromagnetic 3d Alloys. *IEEE Transactions on Magnetism*, 11(4), 1975.
- [35] W. Thomson. On the electro-dynamic qualities of metals: Effects of magnetization on the electric conductivity of nickel and of iron. *Proceedings of the Royal Society of London*, 8:546–550, 1856.

- [36] M. N. Baibich, J. M. Broto, A. Fert, F. Nguyen Van Dau, F. Petroff, P. Etienne, G. Creuzet, A. Friederich, and J. Chazelas. Giant Magnetoresistance of (001)Fe/(001)Cr Magnetic Superlattices. *Physical Review Letters*, 61(21):2472–2475, 1988.
- [37] G. Binasch, P. Grünberg, F. Saurenbach, and W. Zinn. Enhanced magnetoresistance in layered magnetic structures with antiferromagnetic interlayer exchange. *Physical Review B*, 39(7):4828–4830, 1989.
- [38] U. Hartmann. *Magnetic Multilayers and Giant Magnetoresistance - Fundamentals and Applications*. Springer Berlin Heidelberg, 1999.
- [39] A. B. Granovsky, M. Ilyn, A. Zhukov, V. Zhukova, and J. Gonzalez. Giant magnetoresistance of granular microwires: Spin-dependent scattering in intergranular spacers. *Physics of the Solid State*, 53(2):320–322, 2011.
- [40] C. W. Searle and S. T. Wang. Studies of the ionic ferromagnet (LaPb)MnO<sub>3</sub>. V. Electric transport and ferromagnetic properties. *Canadian Journal of Physics*, 48(17):2023–2031, 1970.
- [41] R. von Helmolt, J. Wecker, B. Holzapfel, L. Schultz, and K. Samwer. Giant negative magnetoresistance in perovskitelike La<sub>2/3</sub>Ba<sub>1/3</sub>MnO<sub>x</sub> ferromagnetic films. *Physical Review Letters*, 71:2331–2333, 1993.
- [42] S. Jin, T. H. Tiefel, M. McCormack, H. M. O’Bryan, L.H. Chen, R. Ramesh, and D. Schurig. Thickness dependence of magnetoresistance in La-Ca-Mn-O epitaxial films. *Applied Physics Letters*, 67(4):557–559, 1995.
- [43] K. Li, L. Liu, J. Sun, X. J. Xu, J. Fang, X. W. Cao, J. S. Zhu, and Y. H. Zhang. The power-law magnetic-field-dependence of the giant magnetoresistance ratio in La<sub>0.67</sub>Ca<sub>0.33</sub>MnO<sub>Z</sub> thin film. *Journal of Physics D: Applied Physics*, 29:14–19, 1996.
- [44] Y. Tokura, A. Urushibara, T. Arima, Y. Moritomo, A. Asamitsu, G. Kidō, and N. Furukawa. Giant Magnetotransport Phenomena in Filling-Controlled Kondo Lattice System: La<sub>1-x</sub>Sr<sub>x</sub>MnO<sub>3</sub>. *Journal of the Physical Society of Japan*, 63(11):3931–3935, 1994.
- [45] S. Yuasa, T. Nagahama, A. Fukushima, Y. Suzuki, and K. Ando. Giant room-temperature magnetoresistance in single-crystal Fe/MgO/Fe magnetic tunnel junctions. *Nature Materials*, 3:868–871, 2004.

- [46] A. Matos-Abiague, M. Gmitra, and J. Fabian. Angular dependence of the tunneling anisotropic magnetoresistance in magnetic tunnel junctions. *Physical Review B*, 80:045312, 2009.
- [47] E. Tsybal and I. Žutić. *Handbook of Spin Transport and Magnetism*. Chapman and Hall/CRC, 2011.
- [48] A. N. Chantis, K. D. Belashchenko, E. Y. Tsybal, and M. van Schilfhaarde. Tunneling anisotropic magnetoresistance driven by resonant surface states: First-principles calculations on an Fe(001) surface. *Physical Review Letters*, 98:046601, 2007.
- [49] B. G. Park, J. Wunderlich, D. A. Williams, S. J. Joo, K. Y. Jung, K. H. Shin, K. Olejník, A. B. Shick, and T. Jungwirth. Tunneling anisotropic magnetoresistance in multilayer-(Co/Pt)/AlO<sub>x</sub>/Pt structures. *Physical Review Letters*, 100(087204):1–4, 2008.
- [50] J. Moser, A. Matos-Abiague, D. Schuh, W. Wegscheider, J. Fabian, and D. Weiss. Tunneling anisotropic magnetoresistance and spin-orbit coupling in Fe/-GaAs/Au tunnel junctions. *Physical Review Letters*, 99:056601, 2007.
- [51] C. Gould, C. Rüster, T. Jungwirth, E. Girgis, G. M. Schott, R. Giraud, K. Brunner, G. Schmidt, and L. W. Molenkamp. Tunneling Anisotropic Magnetoresistance: A Spin-Valve-Like Tunnel Magnetoresistance Using a Single Magnetic Layer. *Physical Review Letters*, 93(11):117203, 2004.
- [52] J. S. Moodera, T. S. Santos, and T. Nagahama. The phenomena of spin-filter tunnelling. *Journal of Physics: Condensed Matter*, 19:165202, 2007.
- [53] R. Meservey and P. M. Tedrow. Spin-polarized electron tunneling. In *Physics Reports*, volume 238, pages 173–243. North-Holland, 1994.
- [54] A. V. Ramos, T. S. Santos, G. X. Miao, M. J. Guittet, J. B. Moussy, and J. S. Moodera. Influence of oxidation on the spin-filtering properties of CoFe<sub>2</sub>O<sub>4</sub> and the resultant spin polarization. *Physical Review B - Condensed Matter and Materials Physics*, 78:180402, 2008.
- [55] Y. Z. Chen, J. R. Sun, Y. W. Xie, D. J. Wang, W. M. Lu, S. Liang, and B. G. Shen. Rectifying properties of magnetite-based Schottky diode and the effects of magnetic field. *Applied Physics Letters*, 90:143508, 2007.
- [56] P. Li, C. Xia, Z. Zhu, Y. Wen, Q. Zhang, H. N. Alshareef, and X. Zhang. Ultra-thin Epitaxial Ferromagnetic  $\gamma$ -Fe<sub>2</sub>O<sub>3</sub> Layer as High Efficiency Spin Filtering



- Materials for Spintronics Device Based on Semiconductors. *Advanced Functional Materials*, 26(31):5679–5689, 2016.
- [57] M. Ziese, U. Köhler, A. Bollero, R. Höhne, and P. Esquinazi. Schottky barrier and spin polarization at the  $\text{Fe}_3\text{O}_4 - \text{Nb} : \text{SrTiO}_3$  interface. *Physical Review B*, 71:180406, 2005.
- [58] Y. J. Park, M. C. Hickey, M. J. Van Veenhuizen, J. Chang, D. Heiman, and J. S. Moodera. Analysis of current-voltage characteristics of fe/mgo/gaas junctions using self-consistent field modeling. *Phys. Rev. B*, 80:245315, 2009.
- [59] E. I. Rashba. Theory of electrical spin injection: Tunnel contacts as a solution of the conductivity mismatch problem. *Phys. Rev. B*, 62:R16267–R16270, 2000.
- [60] J. G. Simmons. Electric Tunnel Effect between Dissimilar Electrodes Separated Effect between Dissimilar Electrodes by a Thin Insulating Film. *Journal of Applied Physics*, 34:2581, 1963.
- [61] J. G. Simmons. Potential barriers and emission-limited current flow between closely spaced parallel metal electrodes. *Journal of Applied Physics*, 35(8):2472–2481, 1964.
- [62] V. Garcia and M. Bibes. Ferroelectric tunnel junctions for information storage and processing. *Nature Communications*, 5(4289), 2014.
- [63] M. Lenzlinger and E. H. Snow. Fowler-Nordheim tunneling into thermally grown  $\text{SiO}_2$ . *Journal of Applied Physics*, 40:278–283, 1969.
- [64] J. J. Yang, D. B. Strukov, and D. R. Stewart. Memristive devices for computing. *Nature Nanotechnology*, 8:13–24, 2013.
- [65] A. Sawa. Resistive switching in transition metal oxides. *Materials Today*, 11(6):28 – 36, 2008.
- [66] R. Waser and M. Aono. Nanoionics-based resistive switching memories. *Nature Materials*, 6(11):833–840, 2007.
- [67] A. Sawa and R. Meyer. From fundamentals of nanoionic redox processes to memristive device applications. In *Resistive Switching*. Wiley-VCH, 2016.
- [68] C. Moreno, C. Munuera, S. Valencia, F. Kronast, X. Obradors, and C. Ocal. Reversible resistive switching and multilevel recording in  $\text{La}_{0.7}\text{Sr}_{0.3}\text{MnO}_3$  thin films for low cost nonvolatile memories. *Nano letters*, 10(10):3828–35, 2010.

- [69] Y. W. Xie, J. R. Sun, D. J. Wang, S. Liang, and B. G. Shen. Reversible electroresistance at the Ag/La<sub>0.67</sub>Sr<sub>0.33</sub>MnO<sub>3</sub> interface. *Journal of Applied Physics*, 100(3):033704, 2006.
- [70] J. C. Gonzalez-Rosillo, R. Ortega-Hernandez, J. Jareño-Cerulla, E. Miranda, J. Suñe, X. Granados, X. Obradors, A. Palau, and T. Puig. Volume resistive switching in metallic perovskite oxides driven by the metal-insulator transition. *Journal of Electroceramics*, 39(1-4):185–196, 2017.
- [71] M. Hasan, R. Dong, H. J. Choi, D. S. Lee, D.-J. Seong, M. B. Pyun, and H. Hwang. Uniform resistive switching with a thin reactive metal interface layer in metal-La<sub>0.7</sub>Ca<sub>0.3</sub>MnO<sub>3</sub>-metal heterostructures. *Applied Physics Letters*, 92(20):202102, 2008.
- [72] A. Sawa, T. Fujii, M. Kawasaki, and Y. Tokura. Hysteretic current-voltage characteristics and resistance switching at a rectifying Ti/Pr<sub>0.7</sub>Ca<sub>0.3</sub>MnO<sub>3</sub> interface. *Applied Physics Letters*, 85(18):4073–4075, 2004.
- [73] R. Yasuhara, T. Yamamoto, I. Ohkubo, H. Kumigashira, and M. Oshima. Interfacial chemical states of resistance-switching metal/Pr<sub>0.7</sub>Ca<sub>0.3</sub>MnO<sub>3</sub> interfaces. *Applied Physics Letters*, 97(13):132111, 2010.
- [74] F. Borgatti, C. Park, A. Herpers, F. Offi, R. Egoavil, Y. Yamashita, A. Yang, M. Kobata, K. Kobayashi, J. Verbeeck, G. Panaccione, and R. Dittmann. Chemical insight into electroforming of resistive switching manganite heterostructures. *Nanoscale*, 5(9):3954, 2013.
- [75] L. Yao, S. Inkinen, and S. Van Dijken. Direct observation of oxygen vacancy-driven structural and resistive phase transitions in La<sub>2/3</sub>Sr<sub>1/3</sub>MnO<sub>3</sub>. *Nature Communications*, 8(14544):1–9, 2017.
- [76] P. R. Willmott. Deposition of complex multielemental thin films. *Progress in Surface Science*, 76(6):163 – 217, 2004.
- [77] D. Oka and T. Fukumura. Crystal engineering for novel functionalities with oxide thin film epitaxy. *CrystEngComm*, 19:2144–2162, 2017.
- [78] G. Binnig, C. F. Quate, and Ch. Gerber. Atomic force microscope. *Physical Review Letters*, 56:930–933, 1986.
- [79] Y. Seo and W. Jhe. Atomic force microscopy and spectroscopy. *Reports on Progress in Physics*, 71(1):016101, 2008.

- [80] Asylum Research Oxford Instruments. SPM Applications Guide. *User Guide* 3, 13, 2013.
- [81] C. D. Frisbie, L. F. Rozsnyai, A. Noy, M. S. Wrighton, and C. M. Lieber. Functional group imaging by chemical force microscopy. *Science*, 265(5181):2071–2074, 1994.
- [82] A. San Paulo and R. García. Tip-surface forces, amplitude, and energy dissipation in amplitude-modulation (tapping mode) force microscopy. *Physical Review Letters* B, 64:193411, 2001.
- [83] D. Y. Abramovitch, S. B. Andersson, L. Y. Pao, and G. Schitter. A tutorial on the mechanisms, dynamics, and control of atomic force microscopes. *2007 American Control Conference*, pages 3488–3502, 2007.
- [84] A. Schirmeisen, B. Anczykowski, and H. Fuchs. *Dynamic Force Microscopy*. Springer Berlin Heidelberg, 2005.
- [85] C. Barth, A. S. Foster, C. R. Henry, and A. L. Shluger. Recent trends in surface characterization and chemistry with high-resolution scanning force methods. *Advanced Materials*, 23(4):477–501, 2011.
- [86] C. Teichert and I. Beinik. *Conductive Atomic-Force Microscopy Investigation of Nanostructures in Microelectronics*. Springer Berlin Heidelberg, Berlin, Heidelberg, 2011.
- [87] O. Iglesias. *Advances in Magnetic Force Microscopy*. PhD thesis, Universitat Autònoma de Madrid, 2014.
- [88] [http://www.xtal.iqfr.csic.es/Cristalografia/parte\\_06\\_2-en.html](http://www.xtal.iqfr.csic.es/Cristalografia/parte_06_2-en.html).
- [89] D. Pesquera, X. Marti, V. Holy, R. Bachelet, G. Herranz, and J. Fontcuberta. X-ray interference effects on the determination of structural data in ultrathin  $\text{La}_{2/3}\text{Sr}_{1/3}\text{MnO}_3$  epitaxial thin films. *Applied Physics Letters*, 99(22):221901, 2011.
- [90] Essential Knowledge Briefings. *Electron probe microanalysis*. John Wiley & Sons, 2015.
- [91] Quantum Design. Hardware Reference Manual. In *Magnetic Property Measurement System - MPMS XL*. LOT-Oriel Group Europe, 2011.
- [92] S. Eisebitt, T. Böske, J. E. Rubensson, and W. Eberhardt. Determination of absorption coefficients for concentrated samples by fluorescence detection. *Physical Review B*, 47(21):14103–14109, 1993.

- [93] G. van der Laan and A. I. Figueroa. X-ray magnetic circular dichroism—a versatile tool to study magnetism. *Coordination Chemistry Reviews*, 277-278:95 – 129, 2014.
- [94] B. T. Thole, P. Carra, F. Sette, and G. Van Der Laan. X-ray circular dichroism as a probe of orbital magnetization. *Physical Review Letters*, 68(12):1943–1946, 1992.
- [95] P. Carra, B. T. Thole, M. Altarelli, and X. Wang. X-ray circular dichroism and local magnetic fields. *Physical Review Letters*, 70:694–697, 1993.
- [96] C. T. Chen, Y. U. Idzerda, H.-J. Lin, N. V. Smith, G. Meigs, E. Chaban, G. H. Ho, E. Pellegrin, and F. Sette. Experimental confirmation of the x-ray magnetic circular dichroism sum rules for iron and cobalt. *Physical Review Letters*, 75:152–155, 1995.
- [97] J. Stöhr and H. C. Siegmann. X-rays and Magnetism: Spectroscopy and Microscopy. In *Magnetism From Fundamentals to Nanoscale Dynamics*, page 460. Springer, 2006.
- [98] Helmholtz-Zentrum Berlin für Materialien und Energie. SPEEM: The photoemission microscope at the dedicated microfocus PGM beamline UE49-PGMa at BESSY II. *Journal of large-scale research facilities*, 2:A90, 2016.
- [99] <http://www.globalsino.com/micro/TEM/TEM9923.html>.
- [100] June W. L. and Justin M. S. Magnetic nanostructures for advanced technologies: fabrication, metrology and challenges. *Journal of Physics D: Applied Physics*, 44(30):303001, 2011.
- [101] J. B. Goodenough. Theory of the role of covalence in the perovskite-type manganites [La, M(II)]MnO<sub>3</sub>. *Physical Review*, 100(2):564, 1955.
- [102] R. I. Dass and J. B. Goodenough. Multiple magnetic phases of La<sub>2</sub>CoMnO<sub>6-δ</sub> ( $0 \leq \delta \leq 0.05$ ). *Physical Review B*, 67(1):014401, 2003.
- [103] H. Z. Guo, A. Gupta, T. G. Calvarese, and M. A. Subramanian. Structural and magnetic properties of epitaxial thin films of the ordered double perovskite La<sub>2</sub>CoMnO<sub>6</sub>. *Applied Physics Letters*, 89(26):2–5, 2006.
- [104] M. P. Singh, S. Charpentier, K. D. Truong, and P. Fournier. Evidence of bidomain structure in double-perovskite La<sub>2</sub>CoMnO<sub>6</sub> thin films. *Applied Physics Letters*, 90(21):2005–2008, 2007.

- [105] S. N. Barilo, V. I. Gatal'skaya, S. V. Shiryayev, L. A. Kurochkin, S. N. Ustinovich, H. Szymczak, R. Szymczak, and M. Baran. Magnetic behavior of single crystal-  
sof the perovskite oxides  $\text{LaMn}_x\text{Co}_{1-x}\text{O}_3$ . *Physica Status Solidi (a)*, 199(3):484–  
490, 2003.
- [106] I. O. Troyanchuk, L. S. Lobanovsky, D. D. Khalyavin, S. N. Pastushonok, and  
H. Szymczak. Magnetic and magnetotransport properties of Co-doped man-  
ganites with perovskite structure. *Journal of Magnetism and Magnetic Mate-  
rials*, 210(1-3):63–72, 2000.
- [107] C. L. Bull, H. Y. Playford, K. S. Knight, G. B. G. Stenning, and M. G. Tucker.  
Magnetic and structural phase diagram of the solid solution  $\text{LaCo}_x\text{Mn}_{1-x}\text{O}_3$ .  
*Physical Review B*, 94(1):014102, 2016.
- [108] H. Z. Guo, A. Gupta, Jiandi Zhang, M. Varela, and S. J. Pennycook. Effect of  
oxygen concentration on the magnetic properties of  $\text{La}_2\text{CoMnO}_6$  thin films.  
*Applied Physics Letters*, 91(2007):202509, 2007.
- [109] J. E. Kleibeuker, E.-M. Choi, E. D. Jones, T.-M. Yu, B. Sala, B. A. Mac-  
Laren, D. Kepaptsoglou, D. Hernandez-Maldonado, Q. M. Ramasse, L. Jones,  
J. Barthel, I. MacLaren, and J. L. MacManus-Driscoll. Route to achieving  
perfect B-site ordering in double perovskite thin films. *NPG Asia Materials*,  
9(7):406, 2017.
- [110] R. Egoavil, S. Hühn, M. Jungbauer, N. Gauquelin, A. Béché, G. Van Tende-  
loo, J. Verbeeck, and V. Moshnyaga. Phase problem in the B-site ordering of  
 $\text{La}_2\text{CoMnO}_6$ : impact on structure and magnetism. *Nanoscale*, 7(21):9835–43,  
2015.
- [111] R. Galceran, C. Frontera, Ll. Balcells, J. Cisneros-Fernández, L. López-Mir,  
J. Roqueta, J. Santiso, N. Bagués, B. Bozzo, A. Pomar, F. Sandiumenge, and  
B. Martínez. Engineering the microstructure and magnetism of  $\text{La}_2\text{CoMnO}_{6-\delta}$   
thin films by tailoring oxygen stoichiometry. *Applied Physics Letters*,  
105:242401, 2014.
- [112] X. Liu, Y. Sasaki, and J. K. Furdyna. Ferromagnetic resonance in  $\text{Ga}_{1-x}\text{Mn}_x\text{As}$ :  
Effects of magnetic anisotropy. *Physical Review B*, 67(20):205204, 2003.
- [113] X. Liu, W. L. Lim, Z. Ge, S. Shen, M. Dobrowolska, J. K. Furdyna, T. Woj-  
towicz, K. M. Yu, and W. Walukiewicz. Strain-engineered ferromagnetic in  
 $\text{In}_{1-x}\text{Mn}_x\text{As}$  films with in-plane easy axis. *Applied Physics Letters*, 86(11):1–3,  
2005.

- [114] P. R. Stone, L. Dreher, J. W. Beeman, K. M. Yu, M. S. Brandt, and O. D. Dubon. Interplay of epitaxial strain and perpendicular magnetic anisotropy in insulating ferromagnetic  $\text{Ga}_{1-x}\text{Mn}_x\text{P}_{1-y}\text{N}_y$ . *Physical Review B - Condensed Matter and Materials Physics*, 81(20):205210, 2010.
- [115] M. Kubota, K. Shibuya, Y. Tokunaga, F. Kagawa, A. Tsukazaki, Y. Tokura, and M. Kawasaki. Systematic control of stress-induced anisotropy in pseudomorphic iron garnet thin films. *Journal of Magnetism and Magnetic Materials*, 339:63–70, 2013.
- [116] J. Dho and N.H. Hur. Thickness dependence of perpendicular magnetic anisotropy in  $\text{La}_{0.7}\text{Sr}_{0.3}\text{MnO}_3$  films on  $\text{LaAlO}_3$ . *Journal of Magnetism and Magnetic Materials*, 318(1-2):23–27, 2007.
- [117] C. U. Jung, H. Yamada, M. Kawasaki, and Y. Tokura. Magnetic anisotropy control of  $\text{SrRuO}_3$  films by tunable epitaxial strain. *Applied Physics Letters*, 84(14):2590–2592, 2004.
- [118] H. Wang, C. Du, C. Hammel, and F. Yang. Strain-tunable magnetocrystalline anisotropy in epitaxial  $\text{Y}_3\text{Fe}_5\text{O}_{12}$  thin films. *Physical Review B*, 89(13):134404, 2014.
- [119] P. C. Dorsey, P. Lubitz, D. B. Chrisey, and J. S. Horwitz.  $\text{CoFe}_2\text{O}_4$  thin films grown on (100) $\text{MgO}$  substrates using pulsed laser deposition. *Journal of Applied Physics*, 79(8):6338, 1996.
- [120] A. Lisfi, C. M. Williams, L. T. Nguyen, J. C. Lodder, A. Coleman, H. Corcoran, A. Johnson, P. Chang, A. Kumar, and W. Morgan. Reorientation of magnetic anisotropy in epitaxial cobalt ferrite thin films. *Physical Review B - Condensed Matter and Materials Physics*, 76(5):054405, 2007.
- [121] G. Hu, J. Choi, C. Eom, V. Harris, and Y Suzuki. Structural tuning of the magnetic behavior in spinel-structure ferrite thin films. *Physical Review B*, 62(2):779–782, 2000.
- [122] C. Gatel, B. Warot-Fonrose, S. Matzen, and J.-B. Moussy. Magnetism of  $\text{CoFe}_2\text{O}_4$  ultrathin films on  $\text{MgAl}_2\text{O}_4$  driven by epitaxial strain. *Applied Physics Letters*, 103(9):092405, 2013.
- [123] C. Du, R. Adur, H. Wang, A. J. Hauser, F. Yang, and P. C. Hammel. Control of magnetocrystalline anisotropy by epitaxial strain in double perovskite  $\text{Sr}_2\text{FeMoO}_6$  films. *Physical Review Letters*, 110(14):1–5, 2013.

- [124] J. M. Lucy, M. R. Ball, O. D. Restrepo, A. J. Hauser, J. R. Soliz, J. W. Freeland, P. M. Woodward, W. Windl, and F. Y. Yang. Strain-tunable extraordinary magnetocrystalline anisotropy in  $\text{Sr}_2\text{CrReO}_6$  epitaxial films. *Physical Review B*, 90:180401(R), 2014.
- [125] A. J. Hauser, J. M. Lucy, H. L. Wang, J. R. Soliz, A. Holcomb, and P. Morris. Electronic and magnetic tunability of  $\text{Sr}_2\text{CrReO}_6$  films by growth-mediated oxygen modulation. *Applied Physics Letters*, 102:032403, 2013.
- [126] T. Kyômen, R. Yamazaki, and M. Itoh. Correlation between Magnetic Properties and Mn/Co Atomic Order in  $\text{LaMn}_{0.5}\text{Co}_{0.5}\text{O}_{3+\delta}$ . I. Second-Order Nature in Mn/Co Atomic Ordering and Valence State. *Chemistry of Materials*, 15(25):4798–4803, 2003.
- [127] R. Galceran, L. López-Mir, B. Bozzo, J. Cisneros-Fernández, J. Santiso, L. Balcells, C. Frontera, and B. Martínez. Strain-induced perpendicular magnetic anisotropy in  $\text{La}_2\text{CoMnO}_{6-\epsilon}$  thin films and its dependence on film thickness. *Physical Review B*, 93:144417, 2016.
- [128] T. Burnus, Z. Hu, H. H. Hsieh, V. L. J. Joly, P. A. Joy, M. W. Haverkort, Hua Wu, A. Tanaka, H.-J. Lin, C. T. Chen, and L. H. Tjeng. Local electronic structure and magnetic properties of  $\text{LaMn}_{0.5}\text{Co}_{0.5}\text{O}_3$  studied by x-ray absorption and magnetic circular dichroism spectroscopy. *Physical Review B*, 77(12):125124, 2008.
- [129] S. Valencia, A. Gaupp, W. Gudat, Ll. Abad, Ll. Balcells, A. Cavallaro, B. Martínez, and F. J. Palomares. Mn valence instability in  $\text{La}_{2/3}\text{Ca}_{1/3}\text{MnO}_3$  thin films. *Physical Review B - Condensed Matter and Materials Physics*, 73(10):104402, 2006.
- [130] R. D. Shannon. Revised effective ionic radii and systematic studies of interatomic distances in halides and chalcogenides. *Acta Crystallographica Section A*, 32(5):751–767, 1976.
- [131] T. Kyômen, R. Yamazaki, and M. Itoh. Correlation between Magnetic Properties and Mn/Co Atomic Order in  $\text{LaMn}_{0.5}\text{Co}_{0.5}\text{O}_{3+\delta}$ . 2. Magnetic and Calorimetric Properties. *Chemistry of Materials*, 16(1):179–184, 2004.
- [132] R. Galceran. *Spin-dependent transport in oxide-based tunnel junctions*. PhD thesis, Universitat Autònoma de Barcelona, 2015.
- [133] B. D. Cullity and C. D. Graham. *Introduction to magnetic materials*. John Wiley & Sons, Inc., 2009.

- [134] C. Piamonteze, P. Miedema, and F. M. F. De Groot. Accuracy of the spin sum rule in XMCD for the transition-metal L edges from manganese to copper. *Physical Review B - Condensed Matter and Materials Physics*, 80(18):184410, 2009.
- [135] M. E. Lines. Magnetic properties of  $\text{CoCl}_2$  and  $\text{NiCl}_2$ . *Physical Review*, 131(2):546–555, 1963.
- [136] D. Dai, H. Xiang, and M. Whangbo. Effects of spin-orbit coupling on magnetic properties of discrete and extended magnetic systems. *Journal of Computational Chemistry*, 29(13):2187–2209, 2008.
- [137] B. Bleaney and K. W. H. Stevens. Paramagnetic resonance. *Reports on Progress in Physics*, 16(1):304, 1953.
- [138] R. J. Soulen, J. M. Byers, M. S. Osofsky, B. Nadgorny, T. Ambrose, S. F. Cheng, P. R. Broussard, C. T. Tanaka, J. Nowak, J. S. Moodera, A. Barry, and J. M. D. Coey. Measuring the spin polarization of a metal with a superconducting point contact. *Science*, 282(5386):85–88, 1998.
- [139] M. Bibes, J. E. Villegas, and A. Barthélémy. Ultrathin oxide films and interfaces for electronics and spintronics. *Advances in Physics*, 60:5–84, 2011.
- [140] I. Žutić, J. Fabian, and S. D. Sarma. Spintronics : Fundamentals and applications. *Reviews of Modern Physics*, 76(2):323–410, 2004.
- [141] T. Nagahama, T. S. Santos, and J. S. Moodera. Enhanced magnetotransport at high bias in quasimagnetic tunnel junctions with EuS spin-filter barriers. *Physical Review Letters*, 99(016602):1–4, 2007.
- [142] Y. Kajiwara, K. Harii, S. Takahashi, J. Ohe, K. Uchida, M. Mizuguchi, H. Umezawa, H. Kawai, K. Ando, K. Takanashi, S. Maekawa, and E. Saitoh. Transmission of electrical signals by spin-wave interconversion in a magnetic insulator. *Nature*, 464(7286):262–266, 2010.
- [143] P. Leclair, J. K. Ha, H. J. M. Swagten, J. T. Kohlhepp, C. H. Van De Vin, and W. J. M. De Jonge. Large magnetoresistance using hybrid spin filter devices. *Applied Physics Letters*, 80:625–627, 2002.
- [144] M. Gajek, M. Bibes, A. Barthélémy, K. Bouzehouane, S. Fusil, M. Varela, J. Fontcuberta, and A. Fert. Spin filtering through ferromagnetic  $\text{BiMnO}_3$  tunnel barriers. *Physical Review B - Condensed Matter and Materials Physics*, 72:020406, 2005.



- [145] U. Lüders, A. Barthélémy, M. Bibes, K. Bouzehouane, S. Fusil, E. Jacquet, J.-P. Contour, J.-F. Bobo, J. Fontcuberta, and A. Fert. NiFe<sub>2</sub>O<sub>4</sub>: A Versatile Spinel Material Brings New Opportunities for Spintronics. *Advanced Materials*, 18(13):1733–1736, 2006.
- [146] S. Matzen, J. B. Moussy, G. X. Miao, and J. S. Moodera. Direct evidence of spin filtering across MnFe<sub>2</sub>O<sub>4</sub> tunnel barrier by Meservey-Tedrow experiment. *Physical Review B - Condensed Matter and Materials Physics*, 87:184422, 2013.
- [147] P. Li, C. Xia, J. Li, Z. Zhu, Y. Wen, Q. Zhang, J. Zhang, Y. Peng, H. N. Alshareef, and X. Zhang. Spin Filtering in Epitaxial Spinel Films with Nanoscale Phase Separation. *ACS Nano*, 11(5):5011–5019, 2017.
- [148] J. M. Iwata-Harms, R. V. Chopdekar, F. J. Wong, B. B. Nelson-Cheeseman, C. A. Jenkins, E. Arenholz, and Y. Suzuki. Magnetotransport in La<sub>0.7</sub>Sr<sub>0.3</sub>MnO<sub>3</sub>/CuCr<sub>2</sub>O<sub>4</sub>/Fe<sub>3</sub>O<sub>4</sub> magnetic junctions. *Applied Physics Letters*, 106:0–4, 2015.
- [149] Y. W. Xie, J. R. Sun, D. J. Wang, S. Liang, W. M. Lü, and B. G. Shen. Electronic transport of the manganite-based heterojunction with high carrier concentrations. *Applied Physics Letters*, 90:192903, 2007.
- [150] F. M. Postma, R. Ramaneti, T. Banerjee, H. Gokcan, E. Haq, D. H. A. Blank, R. Jansen, and J. C. Lodder. Epitaxial diodes of a half-metallic ferromagnet on an oxide semiconductor. *Journal of Applied Physics*, 95(11):7324–7326, 2004.
- [151] K. G. Rana, S. Parui, and T. Banerjee. Probing electron transport across a LSMO/Nb:STO heterointerface at the nanoscale. *Physical Review B*, 085116:1–5, 2013.
- [152] A. Sawa. Resistive switching in transition metal oxides. *Materials Today*, 11(6):28 – 36, 2008.
- [153] E. Mikheev, B. D. Hoskins, D. B. Strukov, and S. Stemmer. Resistive switching and its suppression in Pt/Nb:SrTiO<sub>3</sub> junctions. *Nature communications*, 5:3990, 2014.
- [154] P. J. A. van Schendel, H. J. Hug, B. Stiefel, S. Martin, and H.-J. Güntherodt. A method for the calibration of magnetic force microscopy tips. *Journal of Applied Physics*, 88(1):435–445, 2000.
- [155] O. Klein, Y. Samson, A. Marty, S. Guillous, M. Viret, C. Fermon, and H. Alloul. Magnetization process in FePd thin films. *Journal of Applied Physics*, 89(11):6781–6783, 2001.

- [156] S. M. Sze and K. K. Ng. *Physics of Semiconductor Devices*. John Wiley & Sons, Inc, 3rd edition, 2006.
- [157] G. Hu and Y. Suzuki. Negative Spin Polarization of  $\text{Fe}_3\text{O}_4$  in Magnetite/Manganite-Based Junctions. *Physical Review Letters*, 89(27):276601, 2002.
- [158] J. Cerdá, M. A. Van Hove, P. Sautet, and M. Salmeron. Efficient method for the simulation of STM images. I. Generalized Green-function formalism. *Physical Review B*, 56(24):15885–15899, 1997.
- [159] J. M Soler, E. Artacho, J. D. Gale, A. García, J. Junquera, P. Ordejón, and D. Sánchez-Portal. The SIESTA method for ab initio order-N materials simulation. *Journal of Physics: Condensed Matter*, 14(11):2745–2779, 2002.
- [160] N. Troullier and J. L. Martins. Efficient pseudopotentials for plane-wave calculations. *Physical Review B*, 43(3):1993–2006, 1991.
- [161] S. L. Dudarev, G. A. Botton, S. Y. Savrasov, C. J. Humphreys, and A. P. Sutton. Electron-energy-loss spectra and the structural stability of nickel oxide: An LSDA+U study. *Physical Review B*, 57(3):1505–1509, 1998.
- [162] M. Wierzbowska, D. Sánchez-Portal, and S. Sanvito. Different origins of the ferromagnetic order in  $(\text{Ga},\text{Mn})\text{As}$  and  $(\text{Ga},\text{Mn})\text{N}$ . *Physical Review B*, 70:235209, 2004.
- [163] X. Lv, S. and Liu, H. Li, L. Han, Z. Wang, and J. Meng. Insulator-metal transition driven by pressure and B-site disorder in double perovskite  $\text{La}_2\text{CoMnO}_6$ . *Journal of Computational Chemistry*, 33(16):1433–9, 2012.
- [164] S. Lv, Z. Wang, M. Saito, and Y. Ikuhara. Atomic and electronic structure of  $\text{La}_2\text{CoMnO}_6$  on  $\text{SrTiO}_3$  and  $\text{LaAlO}_3$  substrates from first principles. *Journal of Applied Physics*, 113(20), 2013.
- [165] M. Zhu, Y. Lin, E. W. C. Lo, Q. Wang, Z. Zhao, and W. Xie. Electronic and magnetic properties of  $\text{La}_2\text{NiMnO}_6$  and  $\text{La}_2\text{CoMnO}_6$  with cationic ordering. *Applied Physics Letters*, 100(6):062406, 2012.
- [166] R. Cuadrado and J. I. Cerdá. Fully relativistic pseudopotential formalism under an atomic orbital basis: spin-orbit splittings and magnetic anisotropies. *Journal of Physics: Condensed Matter*, 24(8):086005, 2012.

- [167] J. P. Perdew, R. G. Parr, M. Levy, and J. L. Balduz. Density-functional theory for fractional particle number: Derivative discontinuities of the energy. *Physical Review Letters*, 49:1691–1694, 1982.
- [168] J. P. Perdew. Density Functional Theory and the Band-Gap Problem. *International Journal of Quantum Chemistry*, 28(19):497–523, 1985.
- [169] G. A. Sawatzky and J. W. Allen. Magnitude and Origin of the Band Gap in NiO. *Physical Review Letters*, 53:2339–2342, 1984.
- [170] L. Jogschies, D. Klaas, R. Kruppe, J. Rittinger, P. Taptimthong, A. Wienecke, L. Rissing, and M. C. Wurtz. Recent Developments of Magnetoresistive Sensors for Industrial Applications. *Sensors (Basel, Switzerland)*, 15(11):28665–89, 2015.
- [171] J. S. Moodera, J. Nowak, and R. J. M. van de Veerdonk. Interface Magnetism and Spin Wave Scattering in Ferromagnet-Insulator-Ferromagnet Tunnel Junctions. *Physical Review Letters*, 80:2941–2944, 1998.
- [172] X. Marti, I. Fina, C. Frontera, J. Liu, P. Wadley, Q. He, R. J. Paull, J. D. Clarkson, J. Kudrnovský, I. Turek, J. Kuneš, D. Yi, J-H. Chu, C. T. Nelson, L. You, E. Arenholz, S. Salahuddin, J. Fontcuberta, T. Jungwirth, and R. Ramesh. Room-temperature antiferromagnetic memory resistor. *Nature Materials*, 13:367–374, 2014.
- [173] F. Sanchez, C. Ocal, and J. Fontcuberta. Tailored surfaces of perovskite oxide substrates for conducted growth of thin films. *Chemical Society Reviews*, 43:2272–2285, 2014.
- [174] R. Bachelet, C. Ocal, L. Garzón, J. Fontcuberta, and F. Sánchez. Conducted growth of SrRuO<sub>3</sub> nanodot arrays on self-ordered La<sub>0.18</sub>Sr<sub>0.82</sub>Al<sub>0.59</sub>Ta<sub>0.41</sub>O<sub>3</sub>(001) surfaces. *Applied Physics Letters*, 99(5):051914, 2011.
- [175] J. E. Kleibeuker, G. Koster, W. Siemons, D. Dubbink, B. Kuiper, J. L. Blok, C. Yang, J. Ravichandran, R. Ramesh, J. E. ten Elshof, D. H. A. Blank, and G. Rijnders. Atomically defined rare-earth scandate crystal surfaces. *Advanced Functional Materials*, 20(20):3490–3496, 2010.
- [176] R. Bachelet, F. Sánchez, F. J. Palomares, C. Ocal, and J. Fontcuberta. Atomically flat SrO-terminated SrTiO<sub>3</sub>(001) substrate. *Applied Physics Letters*, 95(14):141915, 2009.

- [177] R. Bachelet, F. Sánchez, J. Santiso, C. Munuera, C. Ocal, and J. Fontcuberta. Self-Assembly of SrTiO<sub>3</sub>(001) Chemical-Terminations: A Route for Oxide-Nanostructure Fabrication by Selective Growth. *Chemistry of Materials*, 21(12):2494–2498, 2009.
- [178] M. Paradinas, L. Garzón, F. Sanchez, R. Bachelet, D. B. Amabilino, J. Fontcuberta, and C. Ocal. Tuning the local frictional and electrostatic responses of nanostructured SrTiO<sub>3</sub>-surfaces by self-assembled molecular monolayers. *Physical Chemistry Chemical Physics*, 12:4452–4458, 2010.
- [179] A. Beausoleil, P. Desjardins, and A. Rochefort. Impact of nucleation on step-meandering instabilities during step-flow growth on vicinal surfaces. *Physical Review E*, 89(3):032406, 2014.
- [180] A. Pimpinelli and J. Villain. *Physics of Crystal Growth*. Collection Alea-Saclay: Monographs and Texts in Statistical Physics. Cambridge University Press, 1998.
- [181] S. N. Ruddlesden and P. Popper. New compounds of the K<sub>2</sub>NiF<sub>4</sub> type. *Acta Crystallographica*, 10(8):538–539, 1957.
- [182] M. Kawasaki, K. Takahashi, T. Maeda, R. Tsuchiya, M. Shinohara, O. Ishiyama, T. Yonezawa, M. Yoshimoto, and H. Koinuma. Atomic Control of the SrTiO<sub>3</sub> Crystal Surface. *Science*, 266(5190):1540–1542, 1994.
- [183] G. Koster, B. L. Kropman, G. J. H. M. Rijnders, D. H. A. Blank, and H. Rogalla. Quasi-ideal strontium titanate crystal surfaces through formation of strontium hydroxide. *Applied Physics Letters*, 73(20):2920–2922, 1998.
- [184] V. E. Henrich and P. A. Cox. *The Surface Science of Metal Oxides*. Cambridge University Press, 1994.
- [185] M. Kareev, S. Prosandeev, J. Liu, C. Gan, A. Kareev, J. W. Freeland, Min Xiao, and J. Chakhalian. Atomic control and characterization of surface defect states of TiO<sub>2</sub> terminated SrTiO<sub>3</sub> single crystals. *Applied Physics Letters*, 93(6):061909, 2008.
- [186] F. Sandiumenge, J. Santiso, L. Balcells, Z. Konstantinovic, J. Roqueta, A. Pomar, J. P. Espinós, and B. Martínez. Competing misfit relaxation mechanisms in epitaxial correlated oxides. *Physical Review Letters*, 110:107206, 2013.
- [187] Z. Konstantinović, J. Santiso, L. Balcells, and B. Martínez. Strain-driven self-assembled network of antidots in complex oxide thin films. *Small*, 5(2):265–271, 2009.

- [188] C. Ocal, R. Bachelet, L. Garzón, M. Stengel, F. Sánchez, and J. Fontcuberta. Nanoscale laterally modulated properties of oxide ultrathin films by substrate termination replica through layer-by-layer growth. *Chemistry of Materials*, 24(21):4177–4184, 2012.
- [189] M. Izumi, Y. Ogimoto, Y. Okimoto, T. Manako, P. Ahmet, K. Nakajima, T. Chikyow, M. Kawasaki, and Y. Tokura. Insulator-metal transition induced by interlayer coupling in  $\text{La}_{0.6}\text{Sr}_{0.4}\text{MnO}_3/\text{SrTiO}_3$  superlattices. *Physical Review Letters B*, 64:064429, 2001.
- [190] J. Chakhalian, J. W. Freeland, H.-U. Habermeier, G. Cristiani, G. Khaliullin, M. van Veenendaal, and B. Keimer. Orbital reconstruction and covalent bonding at an oxide interface. *Science*, 318(5853):1114–1117, 2007.
- [191] Y. Hikita, M. Nishikawa, T. Yajima, and H. Y. Hwang. Termination control of the interface dipole in  $\text{La}_{0.7}\text{Sr}_{0.3}\text{MnO}_3/\text{Nb}:\text{SrTiO}_3(001)$  Schottky junctions. *Physical Review Letters B*, 79:073101, 2009.
- [192] C. M. Schneider and G. Schönense. Investigating surface magnetism by means of photoexcitation electron emission microscopy. *Reports on Progress in Physics*, 65(12):1785, 2002.
- [193] L. Aballe, S. Matencio, M. Foerster, E. Barrena, F. Sánchez, J. Fontcuberta, and C. Ocal. Instability and surface potential modulation of self-patterned (001) $\text{SrTiO}_3$  surfaces. *Chemistry of Materials*, 27(18):6198–6204, 2015.
- [194] A. Ruosi, C. Raisch, A. Verna, R. Werner, B. A. Davidson, J. Fujii, R. Kleiner, and D. Koelle. Electron sampling depth and saturation effects in perovskite films investigated by soft x-ray absorption spectroscopy. *Physical Review Letters B*, 90:125120, 2014.
- [195] M. P. Seah and W. A. Dench. Quantitative electron spectroscopy of surfaces: A standard data base for electron inelastic mean free paths in solids. *Surface and Interface Analysis*, 1(1):2–11, 1979.
- [196] L. López-Mir, L. Balcells, S. Valencia, F. Kronast, B. Martínez, J. J. De Miguel, and C. Ocal. Growth instabilities as a source of surface chemical structuration in functional perovskite thin films. *Crystal Growth and Design*, 16(9):5479–5486, 2016.
- [197] L. Peña, L. Garzón, R. Galceran, A. Pomar, B. Bozzo, Z. Konstantinović, F. Sandiumenge, L. Balcells, C. Ocal, and B. Martinez. Macroscopic evidence

- of nanoscale resistive switching in  $\text{La}_{2/3}\text{Sr}_{1/3}\text{MnO}_3$  micro-fabricated bridges. *Journal of physics: Condensed matter*, 26(39):395010, 2014.
- [198] N. Domingo, L. López-Mir, M. Paradinas, V. Holy, J. Železný, D. Yi, S. J. Suresha, J. Liu, C. Rayan Serrao, R. Ramesh, C. Ocal, X. Martí, and G. Catalan. Giant reversible nanoscale piezoresistance at room temperature in  $\text{Sr}_2\text{IrO}_4$  thin films. *Nanoscale*, 7(8):3453–3459, 2015.
- [199] A. Sawa, T. Fujii, M. Kawasaki, and Y. Tokura. Interface resistance switching at a few nanometer thick perovskite manganite active layers. *Applied Physics Letters*, 88(23):232112, 2006.